

## PDF hosted at the Radboud Repository of the Radboud University Nijmegen

The following full text is a publisher's version.

For additional information about this publication click this link.

<http://hdl.handle.net/2066/175276>

Please be advised that this information was generated on 2017-12-05 and may be subject to change.

# **Neuronal Network Mechanisms of Gamma Oscillations**

## **Proefschrift**

ter verkrijging van de graad van doctor  
aan de Radboud Universiteit Nijmegen  
op gezag van de rector magnificus prof. dr. J.H.J.M. van Krieken,  
volgens besluit van het college van decanen  
in het openbaar te verdedigen op donderdag 24 augustus 2017  
om 10.30 uur precies  
door

**Atthaphon Viriyopase**

geboren op 4 november 1978  
te Bangkok, Thailand

Promotor: Prof. dr. C.C.A.M. Gielen  
Copromotor: Dr. Raoul-Martin Memmesheimer  
Frankfurt Institute for Advanced Studies,  
Duitsland

Manuscriptcommissie: Prof. dr. S.A. van Gils  
Nonlinear Analysis Department of Mathematics,  
University of Twente, Nederland

Prof. dr. P.H.E. Tiesinga

Dr. Magteld Zeitler-Geurds  
Institute of Neuroscience and Medicine,  
Forschungszentrum Jülich, Duitsland

© 2017 Atthaphon Viriyopase

ISBN: 978-94-92380-41-8

Gedrukt door Ipskamp Drukkers, Nijmegen

# **Neuronal Network Mechanisms of Gamma Oscillations**

## **Doctoral Thesis**

to obtain the degree of doctor  
from Radboud University Nijmegen  
on the authority of the Rector Magnificus prof. dr. J.H.J.M. van Krieken,  
according to the decision of the Council of Deans  
to be defended in public on Thursday, August 24, 2017  
at 10.30 hours  
by

**Atthaphon Viriyopase**

Born on November 4, 1978  
in Bangkok, Thailand

Supervisor: Prof. dr. C.C.A.M. Gielen  
Co-supervisor: Dr. Raoul-Martin Memmesheimer  
Frankfurt Institute for Advanced Studies,  
Germany

Doctoral Thesis Committee: Prof. dr. S.A. van Gils  
Nonlinear Analysis Department of Mathematics,  
University of Twente, Netherlands

Prof. dr. P.H.E. Tiesinga

Dr. Magteld Zeitler-Geurds  
Institute of Neuroscience and Medicine,  
Forschungszentrum Jülich, Germany

© 2017 Atthaphon Viriyopase

ISBN: 978-94-92380-41-8

Printed by Ipskamp Printing, Nijmegen

# Contents

<b>1</b>	<b>Introduction .....</b>	<b>1</b>
1.1	Neurons and their interactions.....	4
1.2	Brain rhythms .....	9
1.3	Gamma oscillations in local networks.....	14
1.4	Long-range synchronization of gamma oscillations.....	20
<b>2</b>	<b>Cooperation and competition of gamma oscillation mechanisms .....</b>	<b>25</b>
2.1	Introduction .....	26
2.2	Methods .....	29
2.3	Results .....	37
2.4	Discussion .....	63
2.5	Appendix .....	70
<b>3</b>	<b>Analyzing the competition of gamma rhythms with delayed pulse-coupled oscillators in phase representation.....</b>	<b>75</b>
3.1	Introduction .....	76
3.2	Phase representation of type I one-dimensional oscillators.....	80
3.3	Phase representation of type II one-dimensional oscillators .....	87
3.4	Interaction scenarios, iteration map and phase-locking equations .....	95
3.5	Regular oscillations .....	104
3.6	PING-ING interactions in networks of two oscillators .....	108
3.7	Summary and discussion .....	118
3.8	Appendix .....	124
<b>4</b>	<b>When long-range zero-lag synchronization is feasible .....</b>	<b>135</b>
4.1	Introduction .....	136
4.2	Materials and methods.....	137
4.3	Results .....	147
4.4	Discussion .....	165
4.5	Appendix .....	169
<b>5</b>	<b>Robustness of long-range zero-lag synchronization .....</b>	<b>183</b>

5.1	Introduction .....	184
5.2	Materials and methods.....	185
5.3	Results .....	193
5.4	Discussion .....	206
	<b>Summary .....</b>	<b>211</b>
	<b>References .....</b>	<b>215</b>
	<b>Dankwoord.....</b>	<b>239</b>
	<b>Curriculum Vitae .....</b>	<b>241</b>
	Publications .....	241
	Conferences, Events, and Schools.....	241

# 1

## Introduction



**T**he human brain is a complex system. It contains a huge amount of neurons between  $10^{10}$  and  $10^{12}$  neurons (Williams and Herrup, 1988; Azevedo et al., 2009; Lent et al., 2012) with synaptic connections in the range between  $10^{13}$  and  $10^{16}$  (Kandel, 2013). How do the billions of individual neurons interact to produce behavior and cognitive states, and how is the activity of this huge network influenced by the environment to respond to changes in the environment, for example in case of danger or when looking for food? Attempts to answer these questions began in the early 19th century when Franz Joseph Gall proposed that neurons in the cerebral cortex could be grouped into at least 27 distinct regions, each controlling specific functions related to for example perception, action, emotion, and the ability to evaluate causality (Gall, 1835). The current dominant view on brain function is based on the work by Ramón y Cajal (y Cajal, 1892) who championed the view of brain function called cellular connectionism. According to this view single neurons are the signaling units of the brain; they are arranged in functional groups and connect to one another in a precise fashion. Wernicke's work (Wernicke, 1910) revealed that different behaviors are produced by different interconnected brain regions. Fortunately, new tools for the empirical study of behaviors became available, and significant progress was soon made in cellular analyses of the neural mediation of vision, touch, and action in intact primates engaged in ordinary behavior. Single-neuron recording (cf. Fig. 1-1D as an example) and noninvasive neuro-imaging have allowed researchers to describe how neural activity in different sensory and motor pathways encodes sensory stimuli and plans actions. One of widely-used noninvasive imaging techniques is the electroencephalogram (EEG), cf. Fig. 1-1A as an example of measuring-EEG setups. EEG activity represents the electrical activity that is the result of the weighted activity of a large number of neurons. The electrical activity is recorded by electrodes on the human scalp (Berger, 1929), cf. Fig. 1-1B as an example of the recorded EEG signal obtained by one electrode. The scalp EEG provides large-scale and robust measures of neocortical dynamic function. Depending on the mental state of the subject, the frequency distribution of EEG activity can be broad (corresponding to noisy fluctuations in the EEG activity) or can reveal a peak in the frequency spectrum, which results from synchronized oscillations of many neurons (Jia et al., 2013), cf. Fig. 1-1C as an example of synchronized neuronal activity. In the past scientists identified various oscillatory patterns that are particularly obvious during rest (Barry et al., 2007), sleep (Siegel,

2005; Vyazovskiy and Harris, 2013), and epilepsy (Misulis and Abou-Khalil, 2014). These observations have led to many new scientific questions regarding the functional role of various brain rhythms and about the neuronal mechanisms that underlie these brain rhythms.

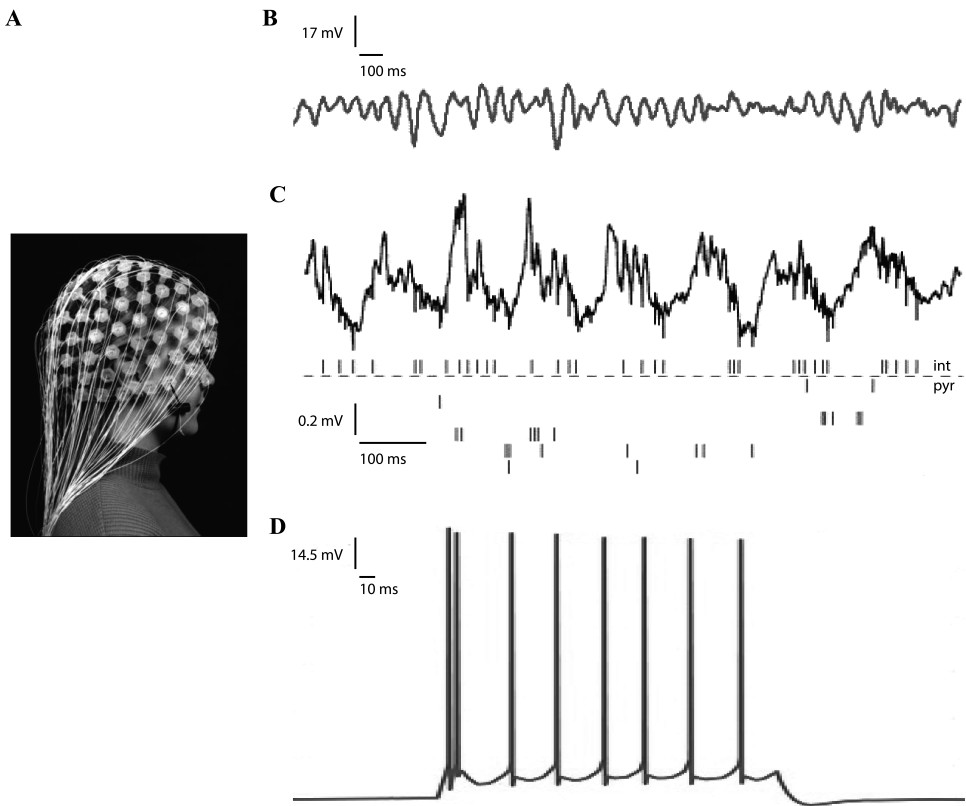


**Figure 1-1. Measuring brain activity.** A typical setup to measure the electroencephalogram activity (EEG) is illustrated in **A** (reproduced from Nunez (2002)). This setup contains 128 electrodes fixated on a well-defined set of positions on the scalp. **B** shows an EEG signal obtained by one electrode (reproduced from Nunez and Srinivasan (2006)). The EEG signal reflects synchronized firing activities of neurons (see **C** as an example reproduced from Buzsáki et al. (2003)), in which the action potentials of a neuron (**D** reproduced from Nowacki et al. (2011)) are synchronized with the oscillatory activity in **C**.

## 1.1 Neurons and their interactions

To explain how interactions between neurons may lead to synchronized oscillations, we will first give a short description of a typical neuron, cf. Fig. 1-2 for the schematic. The neuron is a cell that, like all eukaryotic cells (Hardin et al., 2012), contains a nucleus surrounded by cytoplasm. Unlike other cells, the neuron contains physical extensions called dendrites that receive incoming electrical signals, and combine them with others from different neurons (Jan and Jan, 2010). The neuron also possesses an axon that is an output channel that conveys electrical signals called action potentials to other neurons (y Cajal, 1892). The action potentials are initiated at a specialized trigger region near the origin of the axon known as an axon hillock.

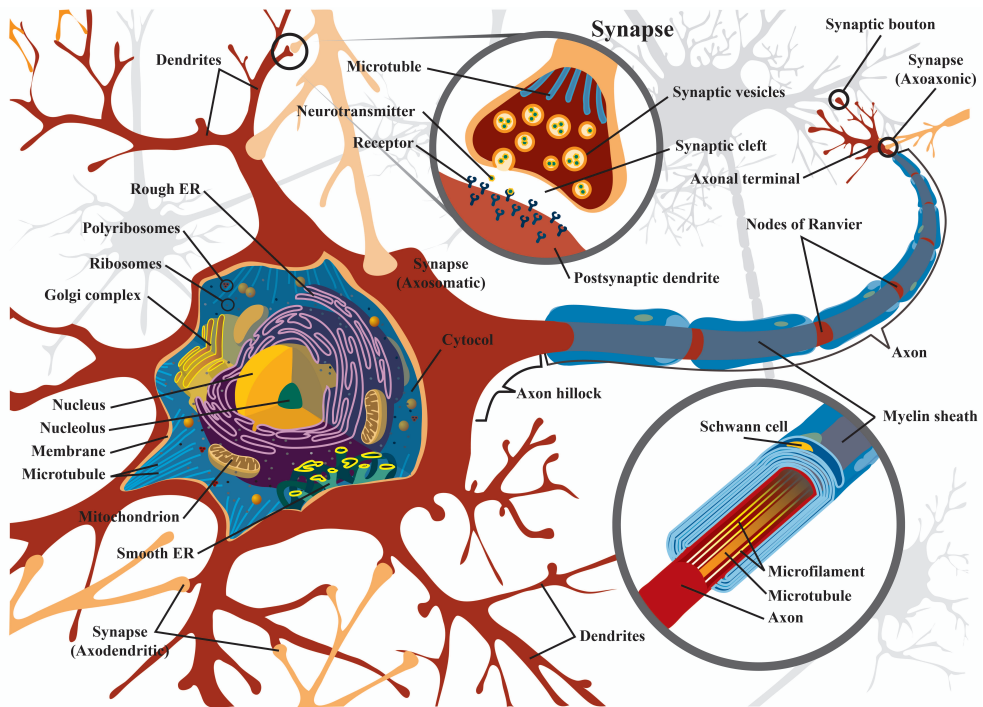


**Figure 1-2. The neuron.** Schematic overview of a typical neuron (Kandel (2013), Purves (2012), and graphics created by Mariana Ruiz Villarreal). The neuron contains a nucleus surrounded by cytoplasm and has physical extensions, called dendrites, for receiving signals from other neurons. Furthermore, it has an axon for transporting action potentials to other neurons.

Many (not all!) vertebrate axons are surrounded by a myelin sheath, which electrically insulates the segments of the axon except at regular intervals at the nodes of Ranvier (Hartline, 2008; Debanne et al., 2011). Axons can be very long up to several thousand times longer than the diameter of the cell body. For example, a motor neuron that innervates a muscle in the human leg has its cell body in the spinal cord, and its axon extends approximately a meter down to the human leg (Kandel, 2013). The myelin sheet enhances the propagation velocity of action potentials along the axon from a few meters per second to about 50 m/s (Purves, 2012). Axons terminate in structures called synaptic boutons that contact other neurons at specialized zones of communication known as synapses. For neuron-to-neuron connections, synapses usually occur between an axon and a dendrite (Gray, 1959; Walberg, 1965), but they can also occur between two dendrites (Famiglietti, 1970).

The neuron is capable of receiving action potentials from other neurons and initiating an action potential to be sent from the cell body of the neuron along its axon since its membrane is electrically and chemically excitable. Mechanisms that allow the membrane to be excitable are the following: At rest the extracellular surface of the membrane has an excess of positive charge relative to the cytoplasmic surface, cf. Fig. 1-3A. The charge separation gives rise to a difference of electrical potential or voltage across the membrane, called the membrane potential ( $V_m$ ), defined as

$$V_m = V_{in} - V_{out}, \quad (1-1)$$

where  $V_{in}$  is the potential at the inside of the cell and  $V_{out}$  the potential outside. The membrane potential of a neuron at rest is called the resting membrane potential. Since by convention  $V_{out}$  is defined as zero, the resting membrane potential is equal to  $V_{in}$ . Its usual range is between -60 mV and -70 mV. All electrical signaling involves brief changes in the resting membrane potential that are caused by electrical currents across the cell membrane. A reduction or reversal of charge separation, leading to a less negative membrane potential, is called depolarization; an increase of charge separation is called hyperpolarization.

Electrical currents across the cell membrane are created by net movement of the charges across the membrane. The charges can move through the cell membrane

through ion channels, which are a class of membrane proteins found in all cells. The ion channels of neurons open and close in response to specific electrical (voltage-gated channels by changes in membrane potential), mechanical (mechanically gated channels by pressure or stretch), or chemical (ligand-gated channels by chemical transmitters) signals. The flow of ions relies on the thermodynamic concentration and electrical gradients of ions. Such ion movements hence are termed passive transport. The flow of ions through the ion channels is very fast, up to 100 million ions passing through a single channel each second. This causes the rapid changes in

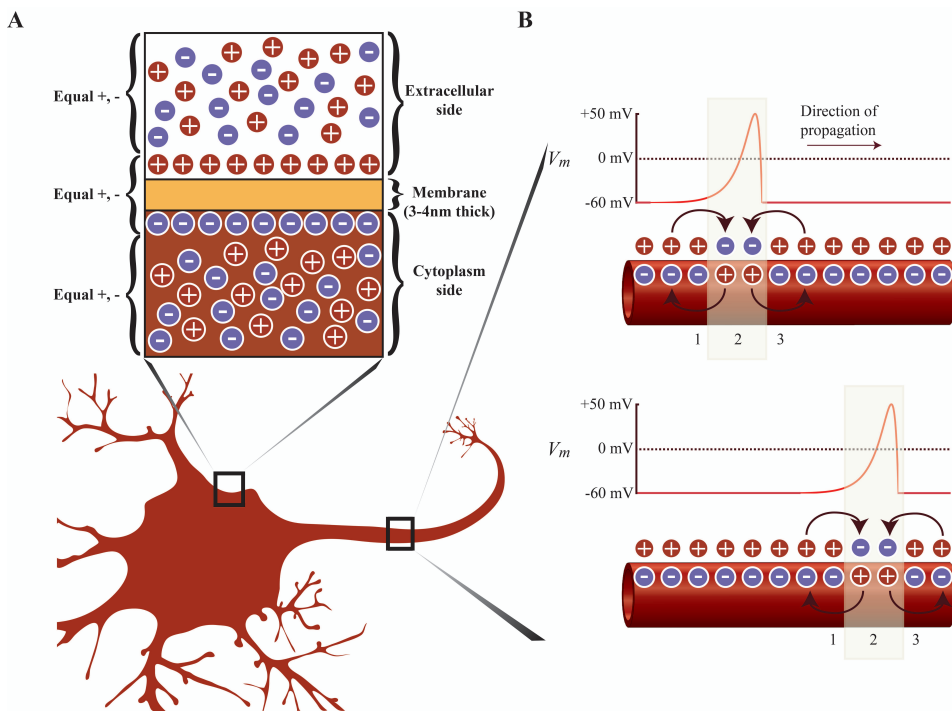


**Figure 1-3. Membrane potential and action potential.** *A* illustrates a schematic overview of the ion distribution resulting in the membrane potential of a neuron. The membrane potential is caused by the separation of net positive and net negative charges on either side of the membrane. When the neuron is excited such that its membrane potential voltage exceeds a threshold, the neuron will generate an action potential. *B* shows schematically the propagation of the action potential along the axon. Panels reproduced after Kandel (2013).

the membrane potential required for signaling. Moreover, the charges can also move through the cell membrane through proteinaceous ion pumps. Each time a pump moves an ion or a group of ions across the membrane, it must undergo a series of conformational changes. As a result, the active rate of ion flow through pumps is 100 to 100,000 times slower than the passive flow through ion channels. Ion-pump proteins do not participate in rapid neuronal signaling (generation of action potentials) but rather are important for establishing and maintaining the concentration gradients of physiologically important ions between the inside and outside of the neuron. This kind of ion movements is termed active transport because ion pumps require energy to transfer ions against electrical and/or concentration gradients.

To understand how neurons create and use action potentials to transmit signals, we must first examine how neurons generate a resting membrane potential and how the membrane potential changes during an action potential. Ions tend to diffuse from an area with a higher concentration to an area with a lower concentration. For instance, neurons usually have a high concentration of potassium ions inside and a low concentration of potassium ions outside, cf. Table 1-1 for

**Table 1-1. Distribution of the major ions across a neuronal membrane of squid neuron at rest (Purves, 2004; Kandel, 2013).**

Ion	Concentration (mM)	
	Cytoplasmic side	Extracellular side
Potassium ( $K^+$ )	400	20
Sodium ( $Na^+$ )	50	440
Chloride ( $Cl^-$ )	52	560
Calcium ( $Ca^{2+}$ )	0.0001	10
Organic anions ( $A^-$ )	385	none

details of typical ion concentrations inside and outside of the squid neuron. We refer to this uneven distribution of potassium ions as a potassium ion gradient. Given the large potassium concentration gradient, potassium ions will tend to diffuse out of the cell.

The membrane of the neurons is permeable to sodium  $\text{Na}^+$ , chloride  $\text{Cl}^-$ , and potassium  $\text{K}^+$  but not for organic anions  $\text{A}^-$ . How are the concentration gradients for the three permeant ions ( $\text{Na}^+$ ,  $\text{K}^+$ , and  $\text{Cl}^-$ ) maintained across the membrane of a neuron and how do these three gradients interact to determine the neuron's resting membrane potential? To answer these questions, we start with the diffusion of  $\text{K}^+$ , i.e. with a membrane that only allows permeation of  $\text{K}^+$  ions. Potassium ions diffuse out of the cell due to the higher  $\text{K}^+$  concentration in the cytoplasmic side (cf. Table 1-1). When the positively charged potassium ions leave the cytoplasmic side, the membrane potential will decrease. Diffusion of  $\text{K}^+$  out of the cytoplasmic side continues to a point where the outflow of  $\text{K}^+$ -ions due to the concentration gradient balances the inflow due to the membrane potential. This type of equilibrium, in which a chemical gradient is balanced with an electrical potential, is referred to as an electrochemical equilibrium. The membrane potential at the point of equilibrium is known as the equilibrium (reversal) potential. The same principles apply to sodium  $\text{Na}^+$  and chloride  $\text{Cl}^-$ . The balance of all ions inside and outside the neuron determines the resting membrane potential.

The mechanism for action potential propagation along an axon without myelin sheath is illustrated in Fig. 1-3B. When an action potential is generated at the axon initial segment (Clark et al., 2009), it will depolarize its adjacent point. The depolarization at this adjacent point is sufficient to bring the membrane potential of the point above the threshold potential, triggering the inward rush of sodium ions through voltage-gated  $\text{Na}^+$  channels, followed in time by a high permeability for potassium ions. As potassium ions rush out of the cell through voltage-gated  $\text{K}^+$  channels, that portion of the membrane returns to its resting state. In this way, an action potential does not fade away as it travels because it activates nearby membrane sides anew, as an all-or-none event, at each successive point along the axon. With addition of a myelin sheath around the axon (cf. Fig. 1-2), an action potential spreads faster than it would along a nonmyelinated axon in a jump-like manner.

When the action potential travels along the axon and arrives at the synapse, the electrical signal is converted into a chemical signal carried by a neurotransmitter. An action potential arriving at the terminal causes secretion of the neurotransmitter into the synaptic cleft. The neurotransmitter molecules then bind to either ionotropic (ligand-gated ion channels) or metabotropic receptors embedded within the membrane of the postsynaptic neuron. When neurotransmitter molecules bind to ionotropic receptors, the corresponding ion channels will open and ions flow through them. In case of metabotropic receptors, transmitter binding indirectly regulates a channel by activating second messengers. Neurotransmitter binding is converted back into electrical signals, setting in motion a sequence of events that create either excitatory (increase of the membrane potential) or inhibitory (decrease of the membrane potential) responses in the postsynaptic neuron.

When a neurotransmitter molecule binds to its receptor, the properties of the receptor are altered, and the postsynaptic neuron responds accordingly. The effect of a synaptic potential - whether it creates excitatory or inhibitory responses - is determined not by the type of neurotransmitter released from the presynaptic neuron but by the type of ion channels in the postsynaptic cell activated by the neurotransmitter. Although some transmitters can produce both excitatory and inhibitory postsynaptic potentials, by acting on distinct classes of ionotropic receptors at different synapses, most transmitters produce a single predominant type of synaptic response; that is, a neurotransmitter induces inhibition or excitation. For example, in the vertebrate brain neurons that release glutamate typically act on receptors called glutamate receptors that produce excitation; neurons that release  $\gamma$ -aminobutyric acid (GABA) or glycine act on receptors that produce inhibition.

## 1.2 Brain rhythms

Oscillations in neuronal networks are assumed to serve various physiological functions, from coordination of motor patterns to perceptual binding of sensory information. In the case of the perceptual binding problem, the shape of an apple, for example, is encoded by neurons in one portion of the visual cortex, its color in another portion, and its smell in yet another portion of the cortex. The problem how neuronal activity in these widely distributed processing areas is combined to form the percept of the apple amid other neuronal activity, e.g. coding for the apple tree,



the sky, and birds in the sky, is called the perceptual binding problem. One of the leading hypotheses is that the solution to the binding problem may lie in synchronized neuronal oscillations, which become synchronized whenever distinct regions are encoding the same object, in this case the apple (Engel et al., 1992; Singer and Gray, 1995).

In general, the benefits of particular neuronal oscillations are thought to depend on the function of the brain system that supports it. Nevertheless, there are a few universal principles, some of which are independent of the physical substrate. First, neuronal oscillations may encode the representation of phase information. Second, neuronal oscillations may be appropriate for binding neuronal assemblies, defined as distributed networks of neuronal groups that are transiently synchronized (Engel et al., 2001; Varela et al., 2001). Information in the brain has been hypothesized to be processed, transferred, and stored by flexible neuronal assemblies. The ability of neuronal assemblies to synchronize depends on the coupling strength and the distribution of natural frequencies (Mirollo and Strogatz, 1990; Winfree, 2001). As long as the frequencies of the coupled oscillating assembly of neurons remain similar, synchrony can be sustained even with very weak synaptic links (Mirollo and Strogatz, 1990; Buzsáki et al., 2004). This inherent feature of oscillations allows activated neuronal groups in distant cortical regions with sparse interconnections to become temporally linked and then activate unique sets of downstream assemblies.

### **1.2.1 Brain rhythms and their functional roles**

Neuronal networks in the mammalian brain can reveal oscillatory activity in a range of frequency bands at least covering frequencies from approximately 0.007 Hz to 200 Hz (Penttonen and Buzsáki, 2003; Noachtar et al., 2004), cf. Fig. 1-4 as examples of brain rhythms: infraslow oscillations (0.007-0.1 Hz) (Vanhatalo et al., 2004; Hiltunen et al., 2014), slow oscillations (0.1-1.5 Hz) (Compte et al., 2003), delta rhythm (1.5-4 Hz) (Nacher et al., 2013), theta rhythm (4-8 Hz) (Song et al., 2014), alpha rhythm (8-13 Hz) (Klimesch, 2012), beta rhythm (14-30 Hz) (Engel and Fries, 2010), gamma rhythm (30-80 Hz) (Fries, 2009), and high-gamma ripple frequencies (80-200 Hz) (Buzsáki et al., 1992). Neighboring frequency bands within the same neuronal network are typically associated with different brain states and may compete with each other (Klimesch, 1999; Kopell et al., 2000; Engel et al.,

2001; Csicsvari et al., 2003). On the other hand, several rhythms can temporally coexist in the same or different structures and interact with each other (Steriade, 2001; Csicsvari et al., 2003).

As a general rule, the neuronal excitability is larger in a particular phase of the oscillation period, e.g. neurons hardly respond to arriving inputs when the inputs arrive during the absolute refractory period of the neurons (Kandel, 2013). This then defines a temporal window for integration of inputs of a neuron, during which

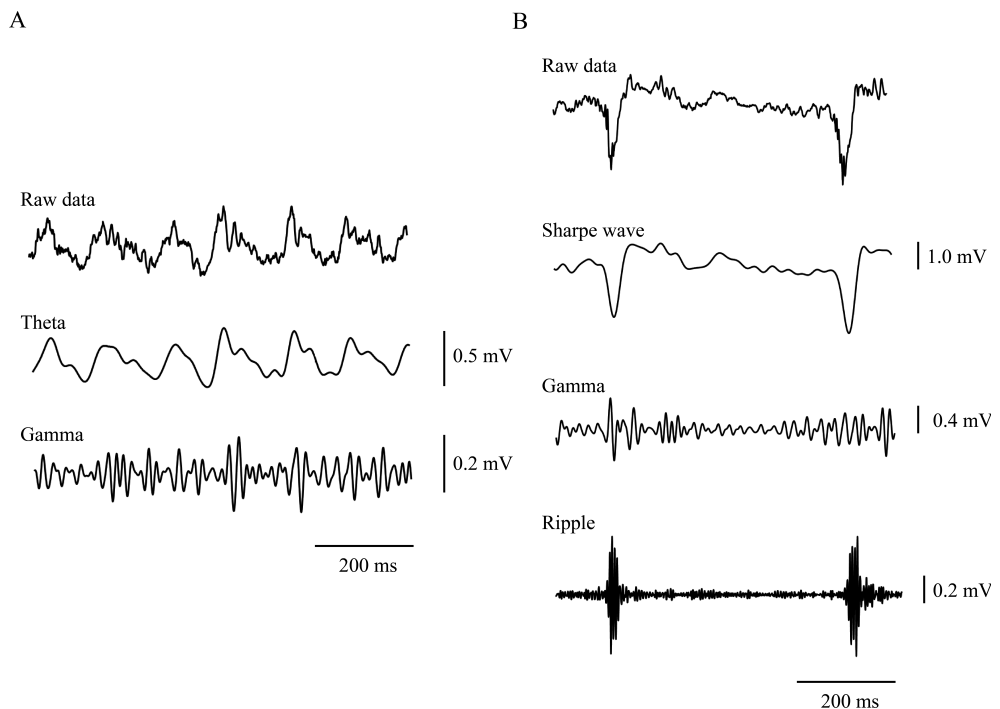


**Figure 1-4. Examples of brain rhythms.** Raw data of local field potential (LFP) in *A top* was recorded from the CA1 dorsal of rodents' hippocampus during exploratory activity of the animal. In the raw data, there are theta oscillations (*A middle*) that are superimposed by gamma oscillations (*A bottom*). Different brain rhythms dominate during their slow wave sleep. *B top* illustrates LFP recorded from hippocampus during slow wave sleep. LFP composes of gamma oscillations and sharp waves, i.e. relatively-large negative-voltage deflections in the raw data, which are associated with brief trains of high-frequency oscillations termed ripples (O'Keefe and Nadel, 1978) shown in *B bottom*. Panels reproduced from Maier et al. (2013).

receiving signals are effectively summated. Because the intervals between these activation phases and the temporal window for integration of inputs vary in proportion to the length of the oscillation period, lower frequency oscillations allow for an integration of neuronal effects with longer synaptic delays, larger variability in the delays, e.g. between hemispheres or between frontal and posterior regions (von Stein and Sarnthein, 2000; Varela et al., 2001), due to larger temporal windows for integration of inputs (Contreras and Llinas, 2001). In contrast, high frequency oscillation bands allow for a more precise and spatially limited representation of information by incorporating synaptic events from closely located regions with short synaptic delays and limited variability (Contreras and Llinas, 2001; Patel et al., 2013). This demonstrates that rhythms with different frequencies may have different functional roles.

Infraslow oscillations (0.007-0.1 Hz) with a period greater than 15 sec. have been demonstrated in conscious and lightly anesthetized cats (0.01-0.025 Hz; Norton and Jewett (1965)), unanesthetized rabbits (0.007-0.02 Hz; Aladjalova (1957)), and in drowsy and sleeping humans ( $\approx$ 0.05 Hz; Moiseeva and Aleksanian (1986)). Oscillations in the range of 0.07-0.2 Hz have been proposed to reflect changes in cortical excitability (Vanhatalo et al., 2004; Hiltunen et al., 2014) and are thought to be related to the emergence of conscious awareness (He and Raichle, 2009). Intra- and extracellularly recorded increases of activation occur with a frequency of 0.3-1 Hz during natural sleep and under anesthesia in the cat cortex (Steriade et al., 1993) and under anesthesia in the cat thalamus (Timofeev and Steriade, 1996). Oscillations in the delta band (1.5-4 Hz) have been extensively described for the neocortex, thalamus, and basal ganglia in the cat under urethane anesthesia (1-4 Hz; Amzica et al. (1992); Nunez et al. (1992)) and rabbit (Rappelsberger et al., 1982) as well as during decision making in monkey (Nacher et al., 2013) and in human (Saleh et al., 2010). The slow and delta oscillations appearing during sleep are hypothesized to play a role for memory consolidation, during which memory traces are gradually translated from short-term hippocampal to longer-term neocortical stores (Siapas and Wilson, 1998; Gais et al., 2000; Stickgold et al., 2000; Maquet, 2001; Huber et al., 2004), while the delta oscillations during awake are thought to be related to the coordination between neural activity in large-scale, distant cortical networks (Nacher et al., 2013).

Theta (4-8 Hz) oscillations have been demonstrated in hippocampal areas in cats, rabbits, and rats (Bland, 1986; Vertes and Kocsis, 1997; Buzsáki, 2002) as well as in the frontal area of the human brain (Griesmayr et al., 2010) with memory load. Whishaw and Vanderwolf (1973) showed that theta oscillations frequently begin several hundred milliseconds before the onset of movement, and that they are associated with the intention to move rather than with feedback produced by movement. During large movements (run and jump) the amplitude of theta oscillations is up to 6 times greater than during small movements (head turn, lever press) (Whishaw and Vanderwolf, 1973). It has been speculated that theta oscillations might support information transfer from neocortex to hippocampus (Buzsáki, 1996) by enhancing long-term potentiation, which is considered to be critical for hippocampal memory formation (Otto et al., 1991; Hasselmo, 2005). However, the idea is controversial (Vertes, 2004).

Oscillations in the alpha/beta band (8-30 Hz) are present in cat, rat, monkey, and man (Kandel and Buzsáki, 1997; Niedermeyer, 1997; Rougeul-Buser and Buser, 1997; Palva and Palva, 2007; Haegens et al., 2011; Klimesch, 2012). Sleep spindles at 7-18 Hz occur in the neocortex and thalamus of the cat (Steriade and Deschenes, 1984), while in the sleeping rat spindles occur in the 12-18 Hz band (Buzsáki, 1991; Kandel and Buzsáki, 1997; Siapas and Wilson, 1998). In humans, the frequency band of sleep spindles is quite similar to that in cat and rat (12-18 Hz; Steriade et al. (1990)). Studies show that sleep-related spindle oscillations are essential for memory formation (Gais et al., 2000) and demonstrate short- and middle-term synaptic plasticity (Steriade and Timofeev, 2003). In the active rat, beta oscillations occur spontaneously and in response to noxious olfactory stimulation in the olfactory bulb, piriform cortex, entorhinal cortex, and dentate gyrus in the 15-35 Hz band with a mean frequency of 19 Hz (Chapman et al., 1998; Vanderwolf and Zibrowski, 2001). The coherent burst with a peak frequency at 19 Hz propagates from the olfactory bulb to the dentate gyrus for the transmission of olfactory signals to the hippocampal formation. Engel and Fries (2010) hypothesized that beta-band activity and/or coupling in the beta-band are expressed more strongly when the maintenance of the status quo is intended or predicted, than when a change is expected (cf. Fig. 3 in Engel and Fries (2010)).

Gamma oscillations (30-80 Hz) are common in all mammals (Gray, 1994; Engel et al., 2001). In the active rat and mouse, gamma frequency is usually in the 40-70 Hz range in the hippocampus (Bragin et al., 1995; Buzsáki et al., 2003; Csicsvari et al., 2003), in olfactory structures (Woolley et al., 1966; Eeckman and Freeman, 1990; Chapman et al., 1998), and in neocortex (Maloney et al., 1997). Larger animals such as cats and monkeys display slower gamma oscillations with a modal frequency near 40 Hz during sensory binding in cortical areas (Bouyer et al., 1981; Singer and Gray, 1995) and during sniffing in the olfactory bulb (Bressler and Freeman, 1980). Gamma oscillations have been well documented in the human neocortex as well (Joliot et al., 1994). It has been suggested that gamma oscillations are involved in feature binding and associational memory (Miltner et al., 1999; Rodriguez et al., 1999), but consensus about these hypothetical functions has not been reached yet. The functional significance of evoked (phase-locked with the stimulus (Swettenham et al., 2009)) and induced (not phase-locked with stimulus (Swettenham et al., 2009)) gamma oscillations still remains unclear. However, it has been suggested that the evoked gamma band response may reflect synchronously active neural assemblies for feature binding or may signal the precise temporal relationship of concurrently incoming stimuli (Tallon-Baudry and Bertrand, 1999). Gamma oscillations are thus pivotal. However, there are several hypotheses about the function role of gamma oscillations. In this work, we thus investigated the properties of gamma oscillations from a theoretical point of view.

### **1.3 Gamma oscillations in local networks**

Network oscillations appearing in LFP (Fig. 1-4) reflect synchronized activity of large sets of neurons (Cooper et al., 1965; Whittingstall and Logothetis, 2009). An important step in understanding the role of neurons in network oscillations is to examine their spiking patterns during these oscillations. Due to a plethora of experimental studies of gamma rhythmogenesis in hippocampus, a major component of the brain, we concentrate on the firing patterns of neurons in hippocampus during gamma oscillations. We focus on two neuron classes that actively participate in gamma oscillations (Cutsuridis et al., 2010): pyramidal cells and interneurons.

### **1.3.1 Firing activity of pyramidal cells**

Analysis of firing properties of pyramidal cells participating in gamma oscillations *in vitro* (Fisahn et al., 1998; Hajos et al., 2004; Gloveli et al., 2005a; Gloveli et al., 2005b) in the CA3 area of hippocampus reveals low-frequency, <5Hz, firing of the cells. These results agree with *in vivo* observations demonstrating similar low-frequency firing of pyramidal cells (Csicsvari et al., 2003). Moreover, firing of pyramidal cells is phase-locked to the local field oscillations. In some gamma oscillations, pyramidal cells fire action potentials around the negative peak of the local field potential recorded in the pyramidal cell layer (Hajos et al., 2004). Both *in vivo* and *in vitro* observations suggest that during gamma oscillations, pyramidal cells of the CA3 area drive local interneurons in a feedback manner (Fisahn et al., 1998; Csicsvari et al., 2003; Hajos et al., 2004; Palhalmi et al., 2004), i.e. the pyramidal cells send signals to the interneurons that transfer signals back to themselves. If pyramidal cell–interneuron interactions generate gamma oscillations, the firing of pyramidal cells should precede interneuron discharges so that pyramidal cells can recruit interneuron activity in the next gamma cycle (Oren et al., 2006). Consistent with this suggestion, interneuron firing was indeed preceded by firing of pyramidal cells (Hajos et al., 2004).

### **1.3.2 Firing activity of interneurons.**

During gamma oscillations *in vivo* and *in vitro*, different classes of interneurons fire action potentials at different times and inhibit distinct subcellular domains of pyramidal cells (Gloveli et al., 2005b).

During pharmacologically induced gamma oscillations *in vitro*, basket cells (a class of interneurons) generate a predominantly gamma frequency output and are tightly coupled to the oscillations (Hajos et al., 2004; Gloveli et al., 2005b). Bistratified cells (another class of interneurons) discharge at a high frequency, phase-locked to the local field potential of the gamma oscillations (Hajos et al., 2004; Gloveli et al., 2005b; Tukker et al., 2007). Therefore, they are thought to be involved in the generation of the gamma oscillatory activity. However, the most prominent interneuronal output seen during pharmacologically induced gamma oscillations *in vitro* was associated with trilaminar interneurons (Hajos et al., 2004; Gloveli et al., 2005b). Axon collaterals of trilaminar interneurons were seen projecting into area

CA1, the subiculum, and possibly other brain areas as well (Somogyi and Klausberger, 2005). Their axonal arborization indicates that trilaminar interneurons innervate somatic and dendritic compartments of pyramidal cells locally as well as distant regions. Thus, via these cells, gamma rhythms generated locally in area CA3 could be efficiently transmitted to distal sites “downstream” in the hippocampal processing pathway.

### 1.3.3 Mechanisms of gamma oscillations

Gamma oscillations have been observed in several cortical areas, e.g. neocortex (Gray et al., 1989; Jones and Barth, 1997; Buhl et al., 1998; Cunningham et al., 2004) and hippocampus (Bragin et al., 1995; Whittington et al., 1995; LeBeau et al., 2002; Csicsvari et al., 2003), in which common denominators are the presence of inhibitory interneurons and their actions through GABA<sub>A</sub> (inhibition through GABA type A receptor) synapses. From these considerations, it is reasonable to assume that a key ingredient of gamma oscillations is GABA<sub>A</sub> receptor-mediated inhibition. Based on this speculation, several theories have been proposed for the generation of gamma oscillations (Jefferys et al. (1996) for a review). The two main mechanisms that underlie gamma oscillations are interneuron network gamma (ING), cf. Fig. 1-5A,

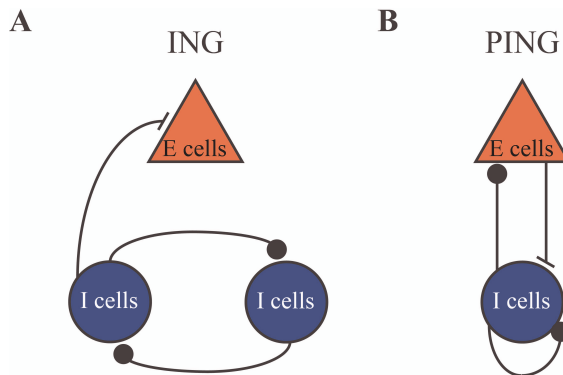


**Figure 1-5. Schematics of mechanisms to generate ING and PING.** *A* illustrates a schematic of mechanism of ING generation, in which interneurons (I cells) interact to create gamma oscillations and impose the oscillations onto pyramidal cells (E cells). *B* shows a schematic of mechanism of PING generation, in which interaction between E cells and I cells as well as interaction among I cells are important to generate gamma oscillations. Panels reproduced after Bartos et al. (2007).

in which rhythmogenesis is based solely on interneurons, and pyramidal-interneuron network gamma (PING), cf. Fig. 1-5B, in which rhythmogenesis is based on interactions between pyramidal cells and interneurons. Apart from these two main mechanisms, gamma oscillations may possibly arise from others as well (Wang, 1993; Gray and McCormick, 1996; Wang, 1999; Minlebaev et al., 2011). In this section, we will explain ING and PING in more detail.

### *ING*

In vivo and in vitro experiments provided support for the role of mutual inhibition among interneurons, essentially basket cells, for the generation of gamma rhythms (Whittington et al., 1995; Hajos et al., 2000; Fisahn et al., 2004; Bartos et al., 2007). ING is caused when a subset of interneurons begins to discharge in synchrony and generates synchronous inhibitions in the partner neurons. In turn, the inhibited neurons will spike again with increased probability when GABA<sub>A</sub> receptor-mediated hyperpolarization has decayed, and the cycle repeats. Based on experimental and modeling studies, the three most important requirements for ING to emerge are (Wang and Rinzl, 1992; Whittington et al., 1995; Traub et al., 1996a; Wang and Buzsáki, 1996): mutually connected inhibitory interneurons, the magnitude and kinetics of the GABA<sub>A</sub> receptors, and a sufficient drive to induce spiking in the interneurons. We will elaborate on each of these requirements in more details in the following.

Wang and Buzsáki (1996) demonstrated that minimal connectedness among GABAergic interneurons is required for the emergence of ING. To be precise, large-scale network synchronization requires a critical (minimal) average number of synaptic contacts per cell, which is not sensitive to the network size. This requirement is satisfied by a high degree of mutual interconnectivity among GABAergic interneurons in different cortical areas (Sik et al., 1995; Tamas et al., 1998; Gulyas et al., 1999; Ascoli and Atkeson, 2005).

Second, the magnitude of the synaptic inhibition between interneurons determines the frequency of ING. It is influenced by either the absolute magnitude changes in the postsynaptic response or the kinetics of the response itself. A broad range of chemical agents can modify the GABA receptor-mediated inhibition, and many of these have been shown to alter the frequency of gamma oscillations in



experimental models (Whittington et al., 2000a). These agents include anesthetics (Halothane, MacIver et al. (1991)), hormones (Insulin, Wan et al. (1997)), and other neuromodulators (Siarey et al., 1995). Some agents, e.g. diazepam (Traub et al., 1996b), cause a marked decrease in ING frequency to an extent that high concentrations reduce the frequency to a point where ING is no longer supported. On the other hand, some agents, e.g. morphine (Whittington et al., 1996; Whittington et al., 1998), increase the frequency of ING. These observations demonstrate the nature of ING and highlight the role played by inhibition in generating and controlling the oscillation frequency. From this a prediction can be made that any pharmacological agent or neuromodulator substance that affects the kinetics of the GABA response, the amount of GABA released at inhibitory terminals, or the excitability of interneurons themselves will affect the rhythmicity and frequency of gamma oscillations generated by inhibitory neuronal networks.

Finally, the tonic driving force causing the excitation of the interneuron networks has to be of sufficient magnitude: it must be large enough to activate a majority of the interneurons to fire in synchrony in the gamma frequency range despite the inhibitory actions between the interneurons. When the driving force decreases from optimal, a decrease in the frequency of the population oscillation can be seen until the population oscillation is no longer manifested (Traub et al., 1996b). As the driving force increases, the oscillation frequency can also increase up to approximately 80 Hz but the dependence of frequency on the drive can be non-linear (Whittington et al., 2011).

### *PING*

Gamma oscillations can also be induced in vitro by activation of muscarinic acetylcholine receptors (mAChRs, which mimic cholinergic input to pyramidal cells (Fisahn et al., 1998; Fellous and Sejnowski, 2000; Hajos et al., 2004; Palhalmi et al., 2004)) using carbachol or application of a potassium-rich solution (LeBeau et al., 2002). Oscillations in the CA3 region induced by the cholinergic agonist carbachol have different pharmacological properties. They are blocked by GABA<sub>A</sub> receptor antagonists bicuculline and by AMPA receptor antagonists (Fisahn et al., 1998; Mann et al., 2005b). Potassium-induced oscillations in both the CA1 and CA3 regions have intermediate properties, as they are completely blocked by GABA<sub>A</sub> receptor antagonists, but only partly inhibited by AMPA receptor blockers (LeBeau

et al., 2002). The induced gamma oscillations rely on both fast inhibition mediated by GABA<sub>A</sub> receptors and excitatory synaptic connections from pyramidal cells to interneurons. Because the induced gamma oscillations involve both pyramidal cells and interneurons, the oscillations in this scheme are referred to as PING.

A mechanism causing PING requires that the pyramidal cells recover from inhibition before the interneurons do. The resultant firing of the recovering pyramidal cells then causes the interneurons to fire. The involvement of pyramidal cells in the rhythm makes the network less vulnerable to a loss of coherence when there is heterogeneity in driving forces (Traub et al., 1996b; Wang and Buzsáki, 1996; White et al., 1998b). In simulations of networks involving both pyramidal cells and interneurons, assuming that the drive to the interneurons is narrowly dispersed, e.g. under 10%, the drive to the excitatory neurons can vary as much as twofold and still can generate coherence with approximate synchrony (Traub et al., 1997).

An appealing property of PING over ING is that the temporal difference between pyramidal-cell spikes and interneuron spikes is a prominent characteristic both in vivo and in vitro (Bragin et al., 1995; Csicsvari et al., 2003; Hasenstaub et al., 2005; Mann et al., 2005b; Hájos and Paulsen, 2009; Tiesinga and Sejnowski, 2009). The delay between the pyramidal cells and interneurons (~5 ms or up to 90°) is caused by axonal conduction and synaptic delays from pyramidal cells to interneurons, cf. Fig. 1-6. Additionally, having reciprocal dynamic interactions

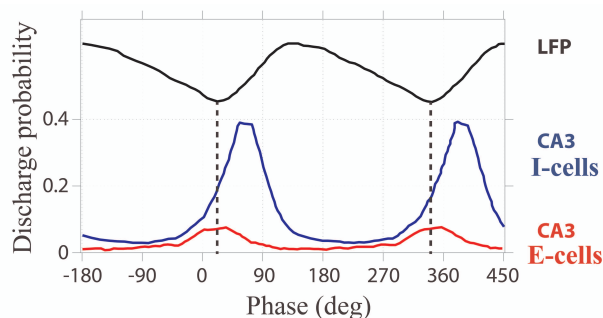


**Figure 1-6. Firing activity of pyramidal cells (E cells) and interneurons (I cells) during gamma oscillations.** The firing of CA3 pyramidal cells (red, E cells) at the negative peak of local field potentials (LFP) was followed by the discharge of interneurons (blue, I cells) by around 90° (reproduced after Hájos and Paulsen (2009)).

between interneurons and pyramidal cells has at least three important consequences for network dynamics. First, compared to the ING frequency, the PING frequency is more robust in the face of changes in network excitation and GABA<sub>A</sub> receptor kinetics (Whittington et al., 1997). Second, allowing principal projection neurons to modulate interneuron spike timing provides a robust mechanism for establishing long-range synchrony between spatially separate gamma-generating local circuits (Traub et al., 1996a; Traub et al., 1996b). Finally, the nature of synaptic plasticity at excitatory synapses onto interneurons provides a powerful means of modulating and stabilizing distributed network activity (Lamsa et al., 2007; McBain and Kauer, 2009).

In vitro experimental evidence (Whittington et al., 1995; LeBeau et al., 2002; Fisahn et al., 2004; Palhalmi et al., 2004) showed that ING and PING could co-exist in the same neuronal network (Csicsvari et al., 2003; Hájos and Paulsen, 2009). In **Chapter 2**, we investigate how ING and PING interact and how they give rise to oscillations of the network using mathematical modeling and scientific computing. We use realistic parameter values for the neurons and their connections belonging to the CA1 neuronal network of hippocampus. Furthermore, we provide a mathematical analysis of the stable modes of oscillatory activity based on a simplified version of the neural network in **Chapter 3**.

## 1.4 Long-range synchronization of gamma oscillations

Although gamma oscillations typically arise locally, patches of distant gamma networks can interact with each other and result in zero-lag synchrony (Roelfsema et al., 1997; Rodriguez et al., 1999; Varela et al., 2001; Gregoriou et al., 2009b; Gregoriou et al., 2009a). The synchrony between distant gamma networks is referred to as long-range synchronization. Long-range synchronization concerns gamma networks that are far apart in the brain, i.e. distance  $> 1$  cm or with transmission delays  $> 8$ – $10$  ms (Girard et al., 2001), such as synchronization across hemispheres (Konig et al., 1995a; Roelfsema et al., 1997; Rodriguez et al., 1999; von Stein et al., 2000; Soteropoulos and Baker, 2006; Witham et al., 2007), cf. Fig. 1-7. Roelfsema et al. (1997) recorded local field potential (LFP) from multiple electrodes implanted in cat cortex. Cats were presented with a grating that signals onset of a trial. When the orientation of the grating changed, cats had to press a key to obtain a food reward.

Analysis of LFP demonstrated that a coherent pattern in the gamma band appeared as soon as the cats focused their attention on the stimulus. This pattern further increased until the task was completed. This is a direct evidence showing that large-scale synchrony emerges as the underlying basis for an attentive behavior. Long-range synchronization was also reported in human subjects. Lachaux et al. (1999; 2000) studied patients implanted with multiple electrodes in preparation for surgical resection for epilepsy. They observed long-range synchronization between temporal

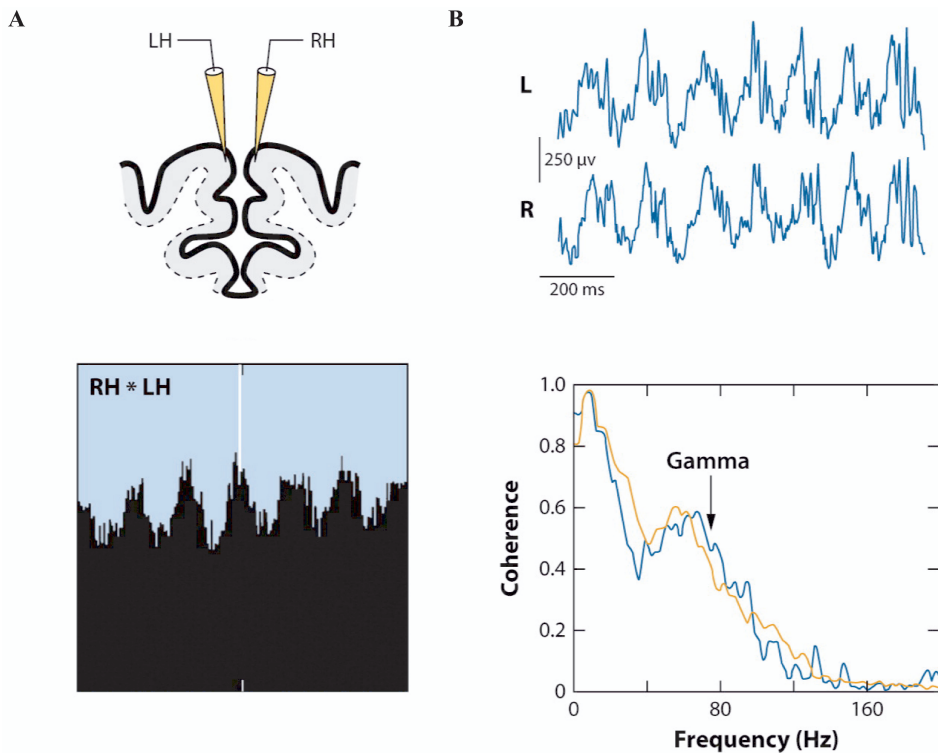


**Figure 1-7. Long-range synchronization.** *A top* shows an overview of measurements from left (LH) and right (RH) primary visual cortex of the anesthetized cat showing almost zero time lag at gamma frequency in *A bottom* (Engel et al., 1991). *B top* illustrates an example of local field potential traces from the left (L) and right (R) CA1 of mouse hippocampus during running, while *B bottom* shows coherence spectra, an indication of resemblance of the signals at each frequency, between the traces during running (orange) and REM sleep (blue) (Buzsáki et al., 2003). Panels reproduced after Buzsáki and Wang (2012).

and frontal lobes appearing only during execution of a discrimination task. Similarly, Aoki et al. (1999) provided evidences of long-range synchronization in the gamma band obtained from grids implanted over the motor cortex of patients who performed various visuomotor tasks. All patients showed an increase in gamma oscillations during performing the tasks. Long-range synchronization in the gamma band also appeared in healthy humans. Rodriguez et al. (1999) studied the perception of high-contrast human faces in healthy humans. A consistent pattern of gamma-band synchrony between occipital, parietal, and frontal areas appeared during face recognition. The synchrony was absent when the faces were presented upside down and not easily recognized.

Long-range synchronization is a surprising phenomenon since signal transmission times between involving brain regions can be up to several tens of milliseconds. A question is then how, despite such relatively long time delays, the reciprocal interactions between two brain regions can lead the associated neural populations to fire in synchrony at zero phase lag. Long-range synchronization cannot be based on local cytoarchitecture but must instead reside in distant connections, either cortico-cortical fibers or thalamocortical reciprocal pathways (Bressler, 1995; Llinas et al., 1998; Sherman and Guillery, 2002). One promising explanation that agrees with this conjecture is that long-range synchronization can be established via dynamical relaying (Vicente et al., 2008), cf. Fig. 1-8. Vicente et al. (2008) showed that two populations of neurons can become synchronized if they are coupled reciprocally to a third population. In this scheme, synchrony is maintained even when the conduction delays of the connections are up to several tens of milliseconds. The most important requirement for the dynamic relaying to

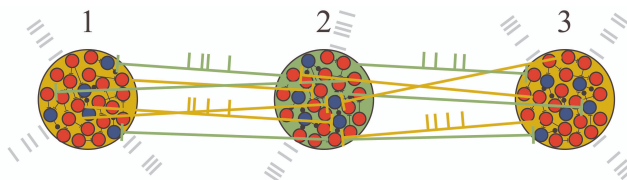


**Figure 1-8. A schematic overview of dynamical-relaying motif.** Distant populations of neurons 1 and 3 connect reciprocally with the relay population 2. Picture reproduced after Vicente et al. (2008).

work is that the relay population of neurons occupies a temporally equidistant location from the pools of neurons to be synchronized. Nevertheless, latency from the thalamus to a cortical cell is remarkably constant across the cortex (typically  $\approx 2$  ms difference) (Salami et al., 2003). Thus, in this scheme, thalamic nuclei occupy a central position for the mediation of zero phase solutions.

In **Chapter 4**, we investigate long-range synchronization using a simplified network for reasons of mathematical tractability. Our aim is to study the effect of various parameter values of a neuronal network on long-range synchronization. The most relevant parameters are the strengths of the synaptic contacts and the conduction delays. We find gamma oscillations generated in distant networks based on the dynamical-relaying motif will be in synchrony at zero phase lag as long as the conduction delays between the distant networks and the relaying network are the same. In general, temporal mismatch of the relative phase of gamma oscillations in distant networks is proportional to the difference of the conduction delays. We extend the studies in **Chapter 4** to **Chapter 5** by incorporating different types of oscillators and synaptic plasticity to study their effect on long-range synchronization.



# 2

## **Cooperation and competition of gamma oscillation mechanisms**

Atthaphon Viriyopase

Raoul-Martin Memmesheimer

C.C.A.M. Gielen

Published in *Journal of Neurophysiology* 2016, 116 (2) 232-251



## 2.1 Introduction

Neuronal oscillations in the gamma band (30–80 Hz) have been found in many cortical areas and have been associated to various sensory, motor, and cognitive tasks (see e.g. Schoffelen et al. (2005); Uhlhaas and Singer (2006); Fries (2009)). They have been linked to input selectivity (Börgers and Kopell, 2008), reference signals for temporal encoding (Buzsáki and Chrobak, 1995; Hopfield, 1995), feature binding of sensory information into a coherent percept (Gray and Singer, 1989), as well as storage and retrieval of information (Lisman and Idiart, 1995; Lisman, 1999). Numerous reviews discuss the biological processes (Gray, 1994; Whittington et al., 2000b; Laurent, 2002; Traub et al., 2002) and the synaptic mechanisms (Bartos et al., 2007; Buzsáki and Wang, 2012) underlying gamma oscillations as well as possible diseases that may be due to their malfunction (Llinas et al., 1999; Spencer et al., 2003; Lewis et al., 2005; Uhlhaas and Singer, 2006). We note that although gamma oscillations can be found in many cortical areas (Gray and Singer, 1989; Buzsáki and Draguhn, 2004), they have been particularly well studied in the hippocampus (Buzsáki et al., 1983; Bragin et al., 1995; Csicsvari et al., 2003) because of their prominent appearance (Forster et al., 2006) and their explicit role in exploratory behavior (Bragin et al., 1995).

The two major mechanisms that have been suggested to underlie gamma oscillations (Buzsáki and Wang, 2012) are interneuron network gamma (“ING”), which is thought to be related to tonic excitation of reciprocally coupled inhibitory interneurons (Lytton and Sejnowski, 1991; Friesen, 1994; Cobb et al., 1995; Whittington et al., 1995; Traub et al., 1996a; Whittington et al., 2000b), and pyramidal-interneuron network gamma (“PING”), which is mediated by coupled populations of excitatory pyramidal cells and inhibitory interneurons (Whittington et al., 2000b; Tiesinga et al., 2001; Börgers and Kopell, 2003). Gamma oscillations generated by different mechanisms may serve different biological functions. In this chapter we therefore investigate which mechanism will dominate the dynamics of a network that could in principle generate oscillations according to different mechanisms and how the dominant mechanism may switch.

The coupling between interneurons, which yields synchronized oscillations of interneuronal networks in the gamma frequency range (Tamas et al., 2000;

Whittington et al., 2000b; McBain and Fisahn, 2001; Bartos et al., 2002; Kopell and Ermentrout, 2004; Bartos et al., 2007), includes both synaptic coupling and gap junctions. Both theoretical and experimental studies have shown that inhibitory synapses alone may be sufficient for generating gamma oscillations (e.g. van Vreeswijk et al. (1994); Bartos et al. (2007)). However, gap junctions are sometimes required (Deans et al., 2001; Hormuzdi et al., 2001; Kopell and Ermentrout, 2004) and may also induce oscillations in the absence of chemical synapses (Gibson et al., 1999; Mann-Metzer and Yarom, 1999; Kopell and Ermentrout, 2004). Some studies reported that gap junctions impede synchrony of neuronal activity (Bou-Flores and Berger, 2001; Pfeuty et al., 2003). Since both gap junctions and chemical synapses are abundant in many brain areas (Fukuda and Kosaka, 2000; Galarreta and Hestrin, 2002), they should be both taken into account in order to understand ING. Gap junctions and inhibitory synapses between interneurons may be supportive or hindering, as they may contribute to both in-phase and antiphase oscillations (Long et al., 2002; Bem and Rinzel, 2004; Bem et al., 2005; Pfeuty et al., 2005). When GABA-mediated inhibition is strong, addition of a small electrical conductance can increase the degree of synchronization more than a larger increase in inhibitory conductance (White et al., 1998b; Kopell and Ermentrout, 2004).

The above studies indicate that the impact of electrical and chemical synapses on oscillatory activity is complicated and can depend on the details of the network setup and the type of oscillation. This motivated us to investigate this impact on the ING and PING oscillations in networks that are modeled according to neurobiological knowledge on hippocampal networks.

Most theoretical studies on ING rhythms have investigated oscillations in networks of interneurons with a tonic excitatory drive to the interneurons without reciprocal connections with pyramidal cells and without the input from these pyramidal cells to the interneurons. In contrast, theoretical studies on PING oscillations have mainly investigated networks with external input to pyramidal cells, which are reciprocally coupled to interneurons that do not fire on their own; thus the drive to the interneurons in these PING rhythms is weak. ING oscillations with only external input to interneurons on the one hand, and PING oscillations with a strong drive to pyramidal cells and weak input to interneurons on the other hand, are presumably two extremes of more common situations with variable amounts of

comparable input to both interneurons and pyramidal cells. We name these two extremes “pure” ING and “pure” PING and use them as reference to study how ING and PING interact in networks that could in principle generate both kinds of rhythms.

In vitro studies have addressed this topic by adding drugs that modify the excitability of pyramidal cells or interneurons or that modify the synaptic interactions between pyramidal cells and interneurons (see, e.g., Fisahn et al. (1998); Fisahn et al. (2004); Hajos et al. (2004); Palhalmi et al. (2004); Gloveli et al. (2005b)). Theoretical analyses of interactions between ING and PING rhythms are scarce. Börgers and Kopell (2003, 2005) and Börgers and Walker (2013) studied transitions from PING to irregular oscillations (e.g., the “walkthrough transition”), to asynchronous activity with or without suppressed E cells (with suppressed E cells: “suppression transition”), and to ING oscillations with suppressed E cells as another variant of the suppression transition. Most closely related to our work, Börgers and Walker (2013) studied different forms of the suppression transition, from PING to asynchronous or oscillatory activity, both with suppressed E cells.

We study the transition from PING to ING with active E cells for networks with type I interneurons and type II interneurons: For type I interneurons an excitatory input always advances their spiking, while the same input arriving soon after spiking of type II interneurons delays their next spiking (see Hansel et al. (1995) for this definition of type I and type II neurons). Considering both types of interneurons allows us on the one hand to make contact with the many network oscillation studies that have used type I interneurons. On the other hand, it accounts for the literature that suggests that interneurons relevant for gamma oscillations often belong to the class of type II neurons (see Erisir et al. (1999); Tateno et al. (2004); Tateno and Robinson (2007); Tikidji-Hamburyan et al. (2015)). Furthermore, it allows to draw conclusions on the robustness of the observed effects.

The transition between PING and ING with active pyramidal cells as considered in our study may be a biologically highly relevant one: It may allow switching between rhythms of neuronal activity related to different cognitive functions, keeping the pyramidal cells active, which are able to provide information transfer to more distant brain areas through their long-range connectivity. Indeed,

excitatory neurons are experimentally found to be active during ING oscillations (e.g., Cardin et al. (2009); Sohal et al. (2009); Whittington et al. (2011)).

As a first step toward understanding the behavior of a full network where ING and PING rhythms interact, we analyze the properties of pure ING in a reduced network that cannot generate PING and pure PING oscillations in a reduced network that cannot generate ING. To make the model biologically plausible and to facilitate experimental validation of our results, we have modeled a network of the hippocampal region CA1 using data and biologically plausible parameter values from the literature. We use CA1 as a paradigmatic region where different kinds of gamma oscillations can be generated, at least in vitro (Bartos et al., 2007). By eliminating the projections from the pyramidal cells to the interneurons, we create networks only generating ING oscillations (pure ING). By removing the external input to the interneurons, we create networks only allowing for PING (pure PING). With the complete model, including projections from pyramidal cells and with a constant drive to the interneurons, we investigate the interactions between ING and PING oscillations. To explain the results of the extensive computer simulations, we present a theoretical model that allows for a full theoretical analysis of the stable states of network oscillations when ING and PING interact. This model qualitatively reproduces and explains the results of the computer simulations.

## 2.2 Methods

### 2.2.1 Single-compartment Hodgkin-Huxley type model

In our computer simulations we use a single-compartment Hodgkin-Huxley type model for CA1 pyramidal (E) cells as suggested in Nowacki et al. (2011), with transient  $I_{Na_T}$  and persistent  $I_{Na_P}$   $Na^+$  currents, T-type ( $I_{Ca_T}$ ) and high-voltage-activated ( $I_{Ca_H}$ )  $Ca^{2+}$  currents, a delayed rectifier ( $I_{K_{DR}}$ ), an M-type ( $I_{K_M}$ )  $K^+$  current, and a leak current ( $I_L$ ). The free dynamics of the membrane potential obeys the differential equation  $C_{m,E} dV/dt = -I_{Na_T} - I_{Na_P} - I_{Ca_T} - I_{Ca_H} - I_{K_{DR}} - I_{K_M} - I_L$ , with the membrane capacitance  $C_{m,E}$ . The seven ionic currents follow  $I_\chi = g_\chi m_\chi^M h_\chi^N (V - E_\chi)$ , where  $\chi$  stands for  $Na_T, Na_P, Ca_T, Ca_H, K_{DR}, K_M$  or  $L$

with different nonnegative integer exponents  $M$  and  $N$ ;  $g_\chi$  stands for the maximal conductance,  $m_\chi$  for the activation gating variable,  $h_\chi$  for the inactivation gating variable, and  $E_\chi$  for the reversal potential. The parameters for the CA1 pyramidal cell model in Nowacki et al. (2011) yield a passive time constant  $\tau_{0,E} = C_{m,E}/g_L \approx 50$  ms. Note that  $g_{Ca_H}$  in Table 2 of Nowacki et al. (2011) should be  $2.6 \text{ mS/cm}^2$  instead of the value  $0.74 \text{ mS/cm}^2$ , which was used in that paper.

We model the fast-spiking interneurons (I cells) in CA1 hippocampus either as type I neurons, where excitatory input always gives a phase advance of the neuronal oscillator (see Krogh-Madsen et al. (2012)), or as type II neurons, where excitatory input in the early phase of the firing cycle causes a phase delay and a phase advance in later phases of the firing cycle (Ermentrout, 1996; Izhikevich, 2007). For the networks with type I interneurons, we use Wang-Buzsáki (WB) neurons (Wang and Buzsáki, 1996). These WB neurons have a transient  $Na^+$  current ( $I_{Na_T}$ ), a delayed rectifier  $K^+$  current ( $I_{K_{DR}}$ ), and leak ( $I_L$ ). The differential equation describing the membrane potential is given by  $C_{m,I} dV/dt = -I_{Na_T} - I_{K_{DR}} - I_L$ . Figure 2-1 shows the voltage trace as a function of time, the firing rate as a function of the input current, and the phase response curve (PRC). We display the standard infinitesimal PRC, i.e. the phase lead or phase lag in response to an infinitesimal positive instantaneous input, normalized by the input strength, as a function of the phase in the cycle. We adopt the standard parameter values suggested in Wang and Buzsáki (1996). With these parameter values, the time constant  $\tau_{0,I} = C_{m,I}/g_{L,I}$  equals 10 ms.

For the interneuron network with type II neurons, we use the Hodgkin-Huxley-type model proposed by Erisir et al. (1999), but modified as described by Börgers and Walker (2013). We refer to this neuron model as the Börgers-Walker neuron. Figure 2-1 shows the voltage trace as a function of time, the firing rate as a function of the input current, and the PRC for this neuron. In early stages of the firing cycle, the PRC has negative values, corresponding to a phase delay, which is typical for type II neurons. With the standard parameter values given in Börgers and Walker (2013), the passive time constant of this interneuron model is 2 ms. To facilitate a

comparison of the results for both types of interneurons, the mean external input current was adjusted in our simulations to produce the same intrinsic firing frequency for the network of inhibitory type I and type II interneurons (i.e., an input near  $1\mu\text{A}/\text{cm}^2$  for the WB neuron and near  $7\mu\text{A}/\text{cm}^2$  for the Börgers-Walker neuron to produce oscillations near 65 Hz; see Fig. 2-1B).

E and I cells are connected by AMPA synapses ( $E \rightarrow E$  and  $E \rightarrow I$ ), GABA<sub>A</sub> synapses ( $I \rightarrow E$  and  $I \rightarrow I$ ), and gap junctions ( $I \leftrightarrow I$ ). The synaptic input by the AMPA and GABA<sub>A</sub>-receptor-mediated synapses for cell  $i$  are modeled by  $-gs_i(t-t_k-\tau_l)(V_i-E_{rev})$ , where  $g$ ,  $s_i$ ,  $t_k$ ,  $\tau_l$ , and  $E_{rev}$  are the synaptic conductance, the time course of the conductance, the time of the  $k^{\text{th}}$  presynaptic action potential, latency, and the reversal potential. For AMPA synapses,  $E_{rev} = 0$  mV (Cutsuridis et al., 2010) with  $g = g_{E \rightarrow I}$  or  $g = g_{E \rightarrow E}$ . For GABA<sub>A</sub> synapses  $E_{rev} = -75$  mV (Cutsuridis et al., 2010) with  $g = g_{I \rightarrow I}$  or  $g = g_{I \rightarrow E}$ . The time course of the conductance  $s_i$  is modeled by the normalized difference between two exponential functions (Gerstner and Kistler, 2002) with rise time  $\tau_r$  and decay time  $\tau_d$ . For  $E \rightarrow E$  connections,  $\tau_l = 2.5$  ms (see Debanne et al. (1995)),  $\tau_r = 0.5$  ms, and  $\tau_d = 2.5$  ms with a peak conductance of 2.3 nS (see Memmesheimer (2010) and references therein for this and subsequent peak conductances). For  $E \rightarrow I$  connections the parameter values are  $\tau_l = 1.3$  ms,  $\tau_r = 0.45$  ms, and  $\tau_d = 1.0$  ms (Geiger et al., 1997; Brunel and Wang, 2003) with a peak conductance of 3.2 nS. For  $I \rightarrow E$ ,  $\tau_l = 0.95$  ms,  $\tau_r = 0.25$  ms, and  $\tau_d = 4.0$  ms (Bartos et al., 2002) with a peak conductance of 5 nS. For  $I \rightarrow I$ ,  $\tau_l = 0.6$  ms,  $\tau_r = 0.3$  ms, and  $\tau_d = 2.0$  ms (Bartos et al., 2002) with a peak conductance of 4 nS. Hence, with a typical total surface area of  $21,590 \mu\text{m}^2$  for a CA1 pyramidal cell (Routh et al., 2009) and  $18,069 \mu\text{m}^2$  for a CA1 basket cell (Cutsuridis et al., 2010),  $g_{E \rightarrow E} = 0.04$  mS/cm<sup>2</sup>,  $g_{E \rightarrow I} = 0.034$  mS/cm<sup>2</sup>,  $g_{I \rightarrow E} = 0.11$  mS/cm<sup>2</sup>, and  $g_{I \rightarrow I} = 0.062$  mS/cm<sup>2</sup>. The gap junctions between I cells are modeled by  $-g(V_i - V_j)$  with conductance  $g_{GJ} = 0.01$  mS/cm<sup>2</sup> (Bartos et al., 2002).

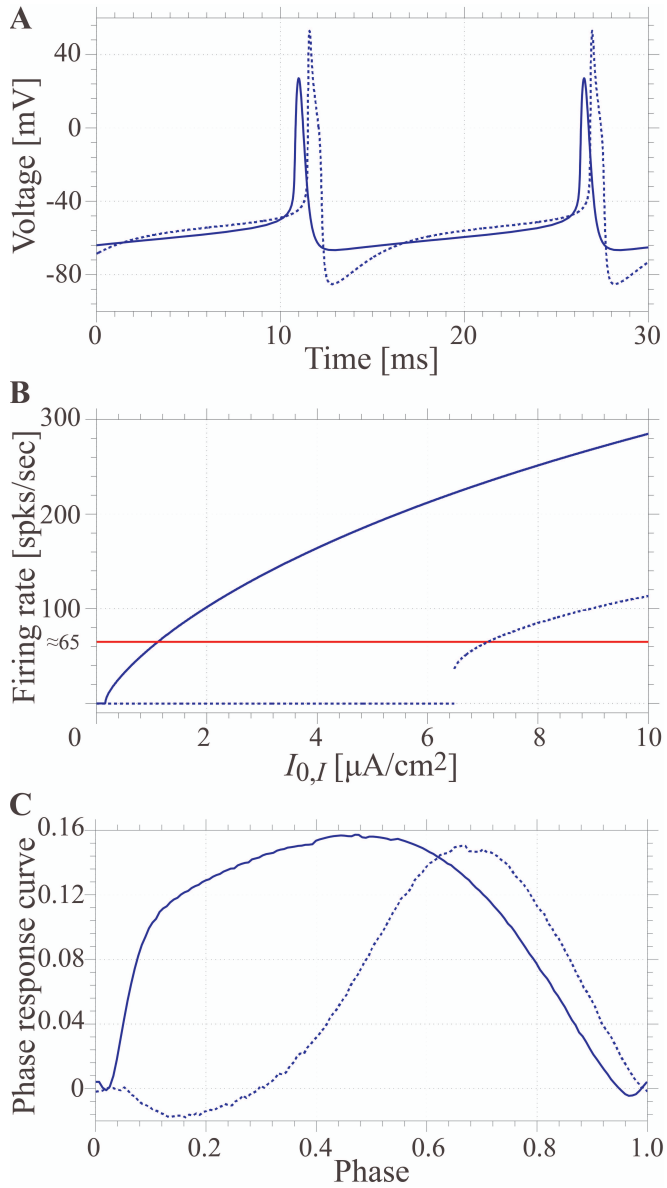


**Figure 2-1. Dynamics of the Wang-Buzsáki and Börgers-Walker interneuron.** *A*, Example of voltage traces of the Wang-Buzsáki (solid line) and Börgers-Walker (dashed line) interneuron for  $I_{0,I} = 1.1 \mu\text{A}/\text{cm}^2$  for the Wang-Buzsáki interneuron and  $I_{0,I} = 7.1 \mu\text{A}/\text{cm}^2$  for the Börgers-Walker interneuron. *B*, Firing rate versus the external current for the Wang-Buzsáki (solid line) and Börgers-Walker (dashed line)

interneuron.  $C$ , Infinitesimal phase response curves of the Wang-Buzsáki (solid line) and the Börgers-Walker (dashed line) interneuron are of type I and type II, respectively.

We assume a ratio of excitatory and inhibitory neurons  $N_E / N_I = 4$  with 5,000 neurons in total. Synaptic connectivity is random and sparse. We adopt connection probabilities reported for the CA1 region (Ascoli and Atkeson, 2005),  $E \rightarrow E$  : 0.0067,  $E \rightarrow I$  : 0.3,  $I \rightarrow E$  : 0.67, and  $I \rightarrow I$  : 0.3. I cells are connected by gap junctions with probability 0.004 (Bartos et al., 2002). See sec. 2.4 for a careful interpretation of these choices.

E cells receive external currents  $I_{app,E} = I_{0,E} + \sigma_E \left( C_{m,E} / \sqrt{\tau_{0,E}} \right) \xi(t)$ , where  $I_{0,E}$  is the mean excitatory current,  $\xi$  is independent Gaussian white noise (zero mean, unit variance),  $C_{m,E}$  denotes the membrane capacitance,  $\tau_{0,E}$  the passive time constant, and  $\sigma_E$  the standard deviation of stochastic fluctuations. Similarly, I cells receive external inputs  $I_{app,I} = I_{0,I} + \sigma_I \left( C_{m,I} / \sqrt{\tau_{0,I}} \right) \xi(t)$ .

We solve the differential equations for the membrane potential of the E and I cells using the Euler-Maruyama method with  $\Delta t = 0.01$  ms (Goldwyn and Shea-Brown, 2011), well below all relevant time scales in the model. At the start of each simulation, neurons that are driven above their spiking threshold are initialized at a uniformly drawn random point on their firing limit cycle; the remaining neurons are initialized at their resting state. After a time interval of 500 ms (to eliminate the effect of initial network conditions), we collect firing activities of the E and I cells in the time interval from 500 to 2,000 ms to calculate the oscillation frequency of the network, the mean firing rates, and the coherence  $\kappa$  among cell activity as defined in Wang and Buzsáki (1996). To estimate  $\kappa$ , we average the pairwise coherences (cf. Eq. 2.5 of Wang and Buzsáki (1996)) between all neurons in a randomly chosen set of 100 neurons. In our study, dynamics with  $\kappa > 0.08$  are classified as showing a rhythm. To calculate the oscillation frequency, the firing activities of the E and I cells are used to construct the corresponding population activity with a 1-ms time resolution (see Gerstner and Kistler (2002)). Next we remove the nonzero DC average of the population activity by subtracting the mean population activity. The



power spectral density of the resulting population activity is calculated with Welch's method (Welch, 1967) with 50% overlapping. The power spectral density is then normalized in order to have unit energy in the frequency domain. The frequency of the oscillation is determined as the frequency corresponding to the peak power in the power spectral density. All results, except for the spike raster diagrams, are averaged over 10 independent runs.

### 2.2.2 Phase model

To substantiate the results based on the single-compartment Hodgkin-Huxley-type models, we investigate the dynamics of a pair of interacting simplified E and I cells representing the dynamics of synchronized E and I neuron populations, respectively. The model allows a full analytical solution. For this simple model we assume two pulse-coupled neurons: an excitatory (E) neuron with excitatory projection  $\varepsilon_{E \rightarrow I}$  to an inhibitory (I) neuron, which reciprocally inhibits the E neuron with coupling strength  $\varepsilon_{I \rightarrow E}$ . Since the I neuron represents the synchronous activity of a population of coupled inhibitory neurons, it has self-inhibitory coupling  $\varepsilon_{I \rightarrow I}$ . All couplings have a delay  $\tau$ . The synapses are assumed to be instantaneous, in the sense that the membrane potential is incremented by an amount  $\varepsilon$  when the input arrives  $\tau$  after the spike generation in the presynaptic neuron.

We use a phase representation, where  $\varphi_E(t)$  and  $\varphi_I(t)$  represent the phases of the E and I neurons at time  $t$ . Without input, the phases increase linearly as  $d\varphi_E(t)/dt = d\varphi_I(t)/dt = 1$  until they reach the phase thresholds  $\Theta_E$  and  $\Theta_I$  and are reset to zero. We analyze the stable states of 1:1 phase-locked firing for the case where the E neuron and the I neuron are represented by leaky integrate-and-fire (LIF) neurons (model 1) and for the case where the I neuron is a so-called sine neuron (model 2), which is a paradigmatic neuron of type II (Hansel et al., 1995; Ermentrout et al., 2001; Brown et al., 2004; Izhikevich, 2007).

**Model 1** In model 1 the E and I neurons are both LIF neurons. The dynamics of the membrane potential  $V_{LIF}$  are given by

$$\frac{dV_{LIF}(t)}{dt} = -\gamma V_{LIF}(t) + I(t), \quad (2-1)$$

where we use the standard form for the dynamics of the LIF neuron (Gerstner and Kistler, 2002),  $\gamma$  is equal to  $1/\sigma$ , with the time constant of the LIF neuron  $\sigma$ . For simplicity, we assume that  $\gamma$  is the same for the E and I neurons; without loss of generality its value is set to one. Additionally, we assume that when  $V_{LIF}$  of a neuron reaches a voltage threshold defined to be 1, the neuron sends a spike, which arrives after a time delay  $\tau$ . When the voltage reaches the voltage threshold, it is instantaneously reset to zero. The voltage threshold corresponds to the phase thresholds (and free periods)  $\Theta_E$  of the E neuron and  $\Theta_I$  of the I neuron where  $V_{LIF,E}(\Theta_E) = V_{LIF,I}(\Theta_I) = 1$ . The external current applied to the E and I neurons is then  $1/(1 - e^{-\Theta})$  with  $\Theta$  referring to  $\Theta_E$  or  $\Theta_I$  for the E or I neuron, respectively. The LIF neuron represented by Eq. 2-1 is a type I neuron and an analytical expression for its PRC can be found in the literature (van Vreeswijk et al., 1994; Lewis and Rinzel, 2003; Izhikevich, 2007; Canavier et al., 2013).

The transfer function  $H_{LIF}(\varphi, \varepsilon; \Theta)$ , which gives the new phase of the LIF neuron after arrival of a spike at the synapse with coupling strength  $\varepsilon$  when the phase of the LIF neuron is  $\varphi \leq \Theta$ , is given by

$$H_{LIF}(\varphi, \varepsilon; \Theta) = \begin{cases} -\ln[e^{-\varphi} - \Gamma_{LIF}(\Theta, \varepsilon)] & \text{for } V_{LIF}(\varphi) + \varepsilon < 1, \\ 0 & \text{otherwise,} \end{cases} \quad (2-2)$$

where  $\Gamma_{LIF}(\Theta, \varepsilon) = (1 - e^{-\Theta})\varepsilon$ .

In Eq. 2-1,  $I(t)$  represents the time-dependent total input to the neuron. This implies that for pure ING oscillations, the input  $I(t)$  to an interneuron gathers the external input (which is constant in our simulations) plus the time-dependent inhibitory input from the other inhibitory neurons in the network, represented by the self-inhibition after firing. For pure PING, the input to the E neuron gathers the external (constant) input to the E neuron plus the time-dependent inhibitory input from the interneuron.

**Model 2** Motivated by experimental findings suggesting that interneurons relevant for typical gamma oscillations belong to the category of type II neurons, we also performed phase analysis for the case where the E neuron is represented by a LIF neuron and the I neuron by a sine neuron, i.e. a neuron that has an infinitesimal PRC (iPRC) given by

$$iPRC_{\text{sine}}(\varphi) = -\sin\left(\frac{2\pi}{\Theta}\varphi\right) \quad (2-3)$$

(cf., e.g., Winfree (1967); Goel and Ermentrout (2002)). Note that the neuron belongs to the category of type II neurons: The iPRC in Eq. 2-3 is negative in the first half of the cycle, such that a positive input generates a phase delay when  $0 < \varphi < \Theta/2$ , and it is positive for the second half of the cycle, i.e. a positive input generates a phase advance when  $\Theta/2 < \varphi < \Theta$ . The iPRC does not fully specify the neural dynamics as it only determines the derivative of the transfer function at  $\varepsilon = 0$ ,

$$\left. \frac{\partial H_{\text{sine}}(\varphi, \varepsilon)}{\partial \varepsilon} \right|_{\varepsilon=0} = iPRC_{\text{sine}}(\varphi). \quad (2-4)$$

We characterize the transfer function by the requirement that the response of the neuron to a large input equals the linear summation of responses of the neuron to a number of small ones that arrive separately within a short time interval. This leads to the defining differential equation

$$\frac{\partial H_{\text{sine}}(\varphi, \varepsilon)}{\partial \varepsilon} = iPRC_{\text{sine}}(H_{\text{sine}}(\varphi, \varepsilon)). \quad (2-5)$$

Note that for  $\varepsilon = 0$ , Eq. 2-5 reduces to Eq. 2-4 since  $H_{\text{sine}}(\varphi, 0) = \varphi$ . The explicit expression for  $H_{\text{sine}}(\varphi, \varepsilon)$  and the analytical expressions for the firing frequencies in various conditions can be found in Appendix 2.5. Further details and the derivations will be given in **Chapter 3**.

## 2.3 Results

### 2.3.1 Role of gap junctions and chemical synapses in ING oscillations

How do gap-junctional coupling and recurrent chemical connectivity interact to give rise to synchronous oscillations in our networks? To address this question, we focus on the interneuron networks, which possess electrical coupling, and on the resulting ING oscillations. We reduce the topology of the network described in sec. 2.2 by eliminating the projections from the excitatory pyramidal cell population (E cells) to the I cells (Fig. 2-2A). This prevents the network from generating PING oscillations.

We first study the ING oscillations in a network of WB type I neurons. Depending on the strengths of chemically synaptic and gap-junctional coupling, the network of I cells may or may not reveal oscillatory activity. The overall picture is shown in Fig. 2-2. When recurrent inhibition  $g_{I \rightarrow I}$  is very small, there is no or only weak synchronization in the I cells (Fig. 2-2B, **a** and **b**) depending on the strength of the gap-junctional coupling, which is in agreement with previous findings (Wang and Rinzel, 1992; Abbott and van Vreeswijk, 1993; Brunel and Hakim, 1999; Chow and Kopell, 2000; Traub et al., 2001; Bem and Rinzel, 2004). This is because in order to create ING, interneurons require a certain minimal amount of inhibition from other interneurons (Wang and Buzsáki, 1996). When  $g_{I \rightarrow I}$  increases, e.g., from **b** to **c** in Fig. 2-2B, firing becomes more synchronous and the firing rate decreases because of the increasing amount of inhibition (Fig. 2-2Bc) (see Kopell and Ermentrout (2004)). The mean firing rate and the coherence between firing of I cells are shown in Fig. 2-2C, **left** and **right**, respectively. We note that the coarse scaling of the coherence in Fig. 2-2C, **right**, obscures a gradual increase in coherence for increasing values of gap-junctional coupling for small values of  $g_{I \rightarrow I}$ . An increase of  $g_{I \rightarrow I}$  from **c** to **d** in Fig. 2-2B first decreases the oscillation frequency. However, at some point a transition occurs to a higher frequency of the ING network oscillations. This higher oscillation frequency co-occurs with a lower mean firing rate of the I cells, which can be explained by alternating firing of two clusters into which the I neuron population has dissociated (Fig. 2-2Bd and point **d** in Fig. 2-2C). We note that such a state may be biologically irrelevant since it is sensitive to

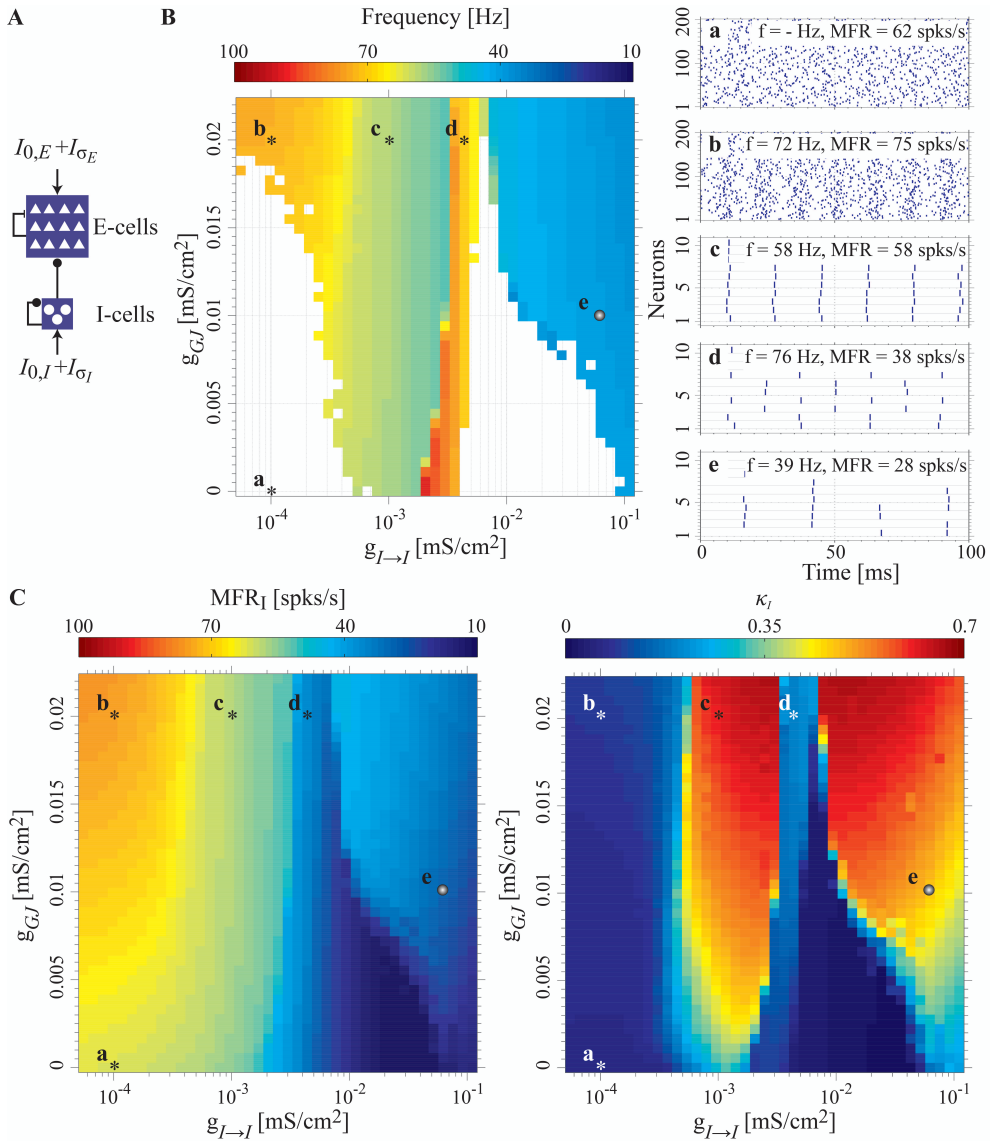


**Figure 2-2. ING oscillations for a reduced network with type I interneurons coupled by inhibitory synapses and gap junctions.** *A*, Schematic overview of the network with reduced topology to focus on ING oscillations. E cells receive inhibitory inputs from I cells, but connections from E cells to I cells are removed. *B*, Oscillation frequency in the network of interneurons for various gap-junctional ( $g_{GJ}$ ) and synaptic strengths ( $g_{I \rightarrow I}$ ). *Ba-e*, Raster plots illustrating the different modes of firing

corresponding to the combinations of  $g_{I \rightarrow I}$  and  $g_{GJ}$  labeled **a-e**: (**a**) no oscillation, (**b**) weak gamma-range oscillations generated by gap junctions, (**c-e**) strongly synchronous ING-based oscillations where neurons spike (**c**) once per cycle, (**d**) alternatingly, and (**e**) in changing synchronously firing groups. Parameter values corresponding to the spiking activities (**a-e**) are highlighted in the main panel in **B** by asterisks/gray sphere. The white area corresponds to parameter values where significant oscillatory activity was absent (sec. 2.2). The gray sphere marked **e** indicates the parameter values found in experiments in the CA1 region. Parameter values:  $I_{0,I}=1.1 \mu\text{A}/\text{cm}^2$ ,  $\sigma_I=0.5 \text{ mV}$ . Panels **Ba – Be**:  $(g_{I \rightarrow I}, g_{GJ}) = (10^{-4}, 0)$ ,  $(10^{-4}, 0.02)$ ,  $(10^{-3}, 0.02)$ ,  $(3.6 \times 10^{-3}, 0.02)$ , and  $(0.062, 0.01) \text{ mS}/\text{cm}^2$ . Panel **C** shows the mean firing rate of the interneurons (left panel) and the coherence of firing (right panel).

heterogeneity in the external currents to the neurons. Increasing  $g_{I \rightarrow I}$  even further at the same value of the gap-junctional coupling (for  $g_{GJ}$  below approximately  $0.02 \text{ mS}/\text{cm}^2$ ) yields asynchrony (see Fig. 2-2**B**). Stronger gap-junctional coupling seems to counteract the desynchronization such that the transition from the high oscillation ING synchrony to asynchrony occurs at larger values of  $g_{I \rightarrow I}$ . Interestingly, we find that when the strength of the chemical synapses increases further, ING reappears. Experimentally found values (see sec. 2.2) for chemically synaptic coupling and gap-junctional strengths are illustrated by the letter “e” in Fig. 2-2**B**.

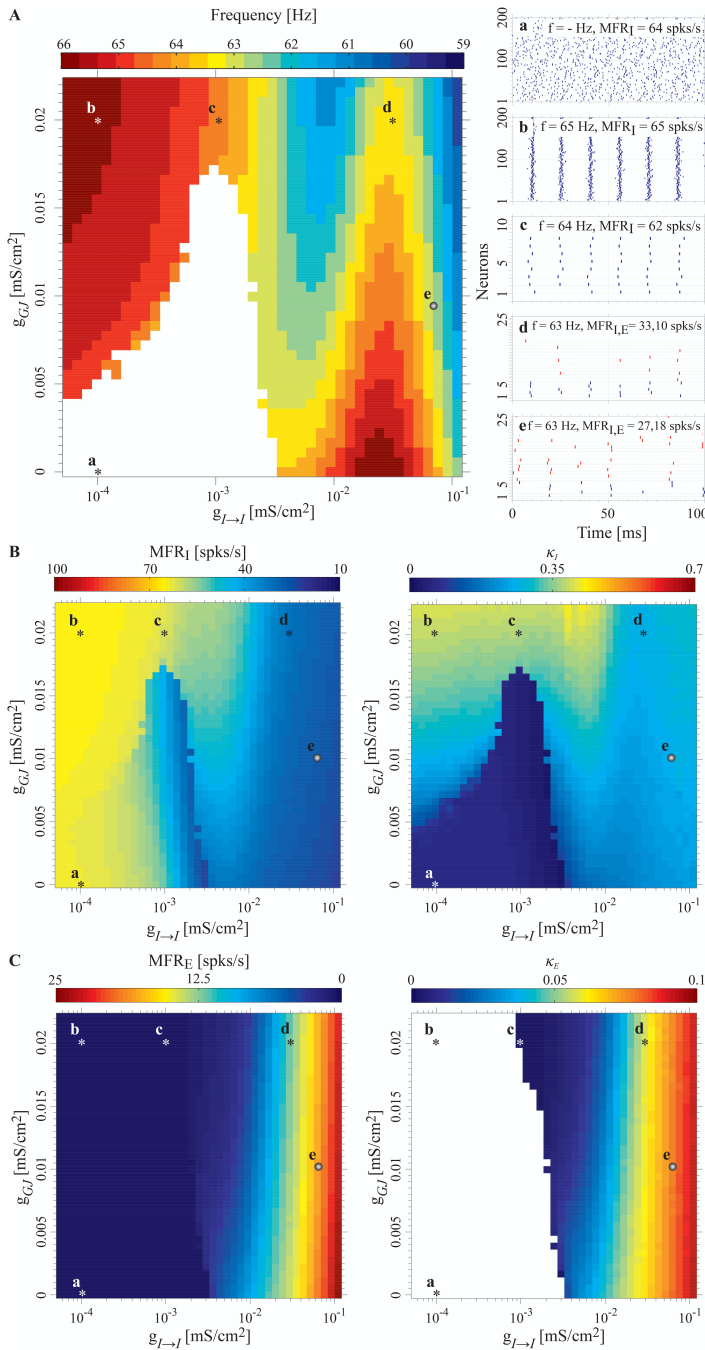
Figure 2-3 shows the results for ING oscillations when the type I WB neuron is replaced by the type II Börgers-Walker neuron. One of the characteristics of type II neurons is that the frequency-current relation is discontinuous; if the neuron starts firing, it will do so with a firing rate significantly above zero (see Fig. 2-1**B**). Moreover, type II neurons have a PRC with a phase delay for excitatory input arriving shortly after firing (Fig. 2-1**C**) and, which is equivalent, a phase advance for inhibitory inputs after firing. The phase advance accelerates the neuron in its cycle, reducing the interval to the next spike. This mechanism explains why the network and thus individual neuron firing frequencies for type II neurons in Fig. 2-3**A** do not decrease as much as for type I neurons (see Fig. 2-2**B**) when  $g_{I \rightarrow I}$  increases. (Note that the color code for ING oscillation frequency is different in Fig. 2-2**B** and Fig. 2-3**A**).

As for the type I neurons, the firing frequency of oscillations in the network of interneurons (Fig. 2-3A) and the coherence of synchronous firing in the ING network increases (Fig. 2-3B, **right**, and Fig. 2-3A, **a** and **b**) when the gap-junctional coupling strength increases for small values of  $g_{I \rightarrow I}$ . Qualitatively similar to Fig. 2-2, increasing  $g_{I \rightarrow I}$  at a constant value of the gap-junctional coupling gives rise to a decrease of the firing frequency in the network of interneurons (see Fig. 2-3A, **b** and **c**). As already mentioned, this decrease is much smaller than for type I neurons, since inhibitory input after firing of the interneuron gives rise to a phase advance or a phase delay for type II neurons, rather than only a phase delay as for type I neurons. Furthermore, we find that the increase of weak synaptic coupling has a desynchronizing effect on the synchronization by gap junctions: Synchronization disappears when weak synaptic coupling becomes stronger (transition into the white region in Fig. 2-3A, **bottom left**). In the region of parameter space where the gap-junctional coupling is not strong enough to maintain synchronization for all values of  $g_{I \rightarrow I}$  (for  $g_{GJ}$  below approximately  $0.017 \text{ mS/cm}^2$ ), the network synchronizes again as  $g_{I \rightarrow I}$  increases further to higher values. The region without synchronization can be related to a region with coexistence of stable in-phase and antiphase synchronization in simulations of two-neuron systems with inhibitory and gap-junctional coupling (cf. Bem and Rinzel (2004) for the general setup), where the parameters are adapted to match those of our large networks. When the value of  $g_{I \rightarrow I}$  is at about  $10^{-3} \text{ mS/cm}^2$  (condition **c**), a further increase (e.g., from **c** to **d** in Fig. 2-3A) gives rise to a decrease of the oscillation frequency of the ING network followed by an increase (see Fig. 2-3A). The decrease in ING frequency and mean firing rate of I cells (see Figs. 2-3, **A** and **B**) for increasing (small, **b** to **c**) values of  $g_{I \rightarrow I}$  is due to the increasing inhibitory input for larger values of  $g_{I \rightarrow I}$ . When  $g_{I \rightarrow I}$  increases to larger values, the stable mode of firing of the network changes from in-phase to antiphase. This is in agreement with previous results in two-neuron systems by Bem and Rinzel (2004) and with our own simulations of two-neuron systems with parameters adapted to match those of our large networks. The change of mode leads to an increase in network oscillation frequency. In contrast to the case of type I neurons (see Fig. 2-2B with  $g_{I \rightarrow I}$  values in the range between about  $6 \times 10^{-3} \text{ mS/cm}^2$

and  $10^{-1}$  mS/cm<sup>2</sup>), the border between the white region of asynchrony and the colored regions of synchronized firing is largely independent of the gap junctional strength (see Fig. 2-3A for  $g_{I \rightarrow I}$  values between about  $10^{-3}$  mS/cm<sup>2</sup> and  $3 \times 10^{-3}$  mS/cm<sup>2</sup>), indicating that gap junctions do not play a major role for it. This may be dependent on the chosen parameters, e.g. gap junctions may be more supportive when introducing heterogeneity in the constant inputs to the neurons. For the type I WB neurons in Fig. 2-2, the transition to a higher firing frequency of the network is abrupt because of a sudden change to alternating firing of the I neurons, i.e. the type I interneurons spike once per two oscillatory cycles, causing a discrepancy between network oscillations and mean firing rate of the I cells. For the type II Hodgkin-Huxley-type neurons in Fig. 2-3, this transition is gradual, since type II interneurons do not switch to a mode of alternating firing, although firing gets sparser. In contrast to the network with type I interneurons, we do not find a region of desynchronization for strong inhibitory synapses.

The set of parameter values that correspond to data from the experimental literature about CA1 (condition **e** in Fig. 2-3A) reveals coherent, synchronous spiking of variable subgroups of the I cells. Figure 2-3C, **left**, shows the mean firing rate of the E cells. In the current setup generating pure ING oscillations, there is no projection from the E cells to the interneurons (see Fig. 2-2A), and the E cells receive a constant external input, in addition to the inhibitory input from the network of interneurons. The coherence (Fig. 2-3C, **right**) and the mean firing rate of the E cells (Fig. 2-3C, **left**) increase with increasing values of  $g_{I \rightarrow I}$ . Because of the inhibition by the I cells, E cells fire before or near the firing of the I cells but not thereafter (Fig. 2-3A, **d** and **e**): The pure ING oscillations illustrate that the observation that the peak of spiking of the E cells precedes that of the I cells should not be interpreted as evidence for PING. When  $g_{I \rightarrow I}$  increases, the mean firing rate of the I cells decreases because of the temporal extension and shape of the postsynaptic currents, which leads to more delay than advance despite the type II PRC (Fig. 2-3B, **left**). When the mean firing rate of the I cells decreases, the inhibitory input to the E cells decreases as well, which explains the higher mean firing rate of the E cells for larger values of  $g_{I \rightarrow I}$  in Fig. 2-3C, **left**.





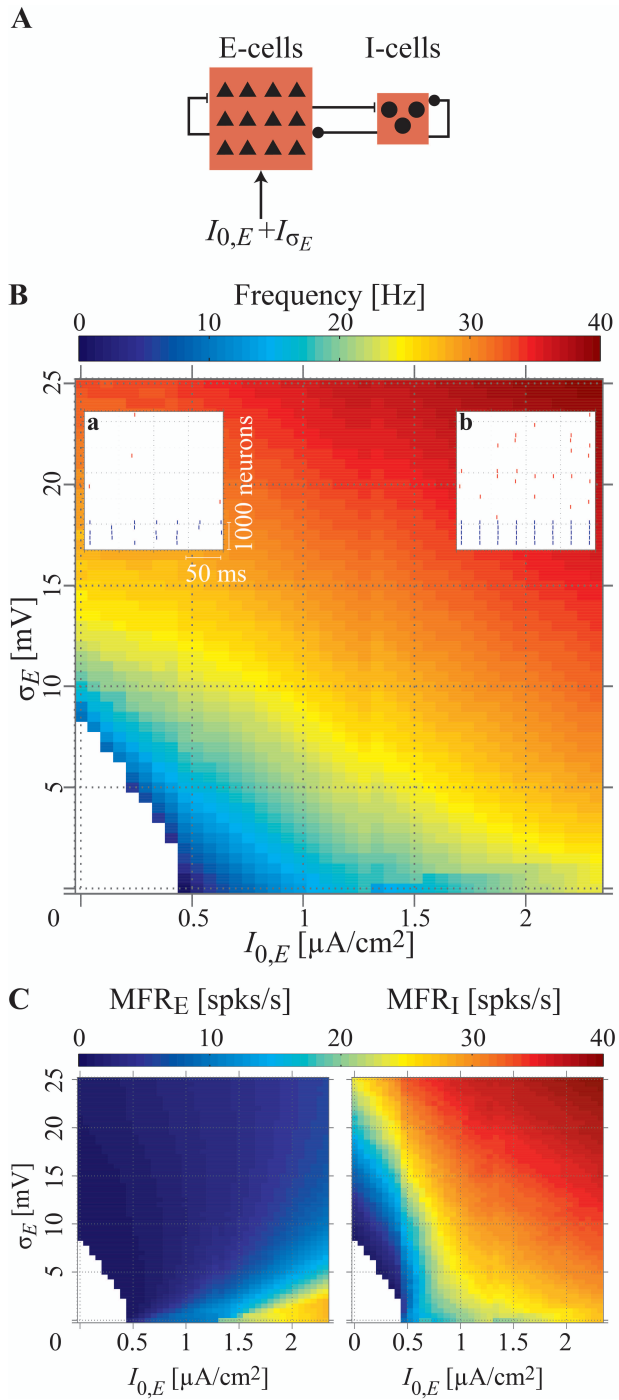
**Figure 2-3. ING oscillations for a reduced network with type II interneurons coupled by inhibitory synapses and gap junctions. The network topology is as in**

Fig. 2-2A. **A**, Frequency of network oscillation vs. gap-junctional ( $g_{GJ}$ ) and synaptic strengths ( $g_{I \rightarrow I}$ ). **Aa-e**, Raster plots illustrating the different modes of firing in **A**: **(a)** no oscillations, **(b)** gamma-range oscillations generated by gap junctions, **(c)** strongly synchronous ING-based oscillations and **(d, e)** in changing synchronously firing groups. Red vertical bars display spiking of pyramidal neurons, blue vertical bars display spiking of interneurons. In some parts of the parameter space, the E cells do not fire (as in **a**) or fire at a low rate (as in **b** and **c**; spiking not shown due to low rate). **B** and **C** show the mean firing rate (left panels) and the coherence of firing (right panels) in the network of the interneurons and of the pyramidal cells, respectively. Parameter values:  $I_{0,I} = 7.1 \mu\text{A}/\text{cm}^2$ ,  $\sigma_I = 0.5 \text{ mV}$ ,  $I_{0,E} = 5.8 \mu\text{A}/\text{cm}^2$ ,  $\sigma_E = 60 \text{ mV}$ . Panels **Aa** – **Ae**:  $(g_{I \rightarrow I}, g_{GJ}) = (10^{-4}, 0)$ ,  $(10^{-4}, 0.02)$ ,  $(10^{-3}, 0.02)$ ,  $(3 \times 10^{-2}, 0.02)$ , and  $(0.062, 0.01) \text{ mS}/\text{cm}^2$ .

### 2.3.2 PING rhythms and the firing rate of E cells

In our ING simulations, we found that E cells can spike at a low firing rate during rhythmic activity in the I cells (see in particular Fig. 2-3Ae and Fig. 2-3C, **left**), in agreement with experimental findings (Fisahn et al., 1998). In contrast, for PING oscillations in typical neural network models the firing rates are often implausibly high, reaching the network oscillation rate. We will now explore for our networks how excitatory neurons may spike during PING oscillations at a rate that is much lower than the network oscillation rate, even for highly synchronized PING rhythms. To focus on PING rhythms, we remove the constant input to the interneurons (Fig. 2-4A), which disables ING-related oscillations.

Börger and Kopell (2003) have shown that the PING mechanism can yield perfect synchronization if the  $E \rightarrow I$  synapses are sufficiently strong. In agreement with their results, our network gives almost perfect synchronization (not shown) for the biologically plausible values for  $E \rightarrow I$  synapses near  $g_{E \rightarrow I} = 0.034 \text{ mS}/\text{cm}^2$  (see sec. 2.2) without noise input to the E and I cells. In this regime, the firing rates of E and I cells agree with the frequency of the network oscillations (defined as the oscillation frequency of the population of E cells) both for type I interneurons and for type II interneurons. However, observations both in vivo (Csicsvari et al., 2003)



**Figure 2-4. Relation between PING rhythm and mean firing rate in a reduced network of E and type I I cells.** **A**, Schematic overview of the recurrent network with reduced topology to simulate PING oscillations. There is no external input to the I cells. **B**, Frequency of PING rhythm as a function of current  $I_{0,E}$  and noise  $\sigma_E$ . Insets: Raster plot (red for E cells and blue for I cells) showing the spiking activity for the same noise  $\sigma_E$  and low **(a)** and high **(b)** driving current  $I_{0,E}$ . Parameter settings:  $\sigma_E = 20$  mV and  $I_{0,E} = 0$   $\mu\text{A}/\text{cm}^2$  and  $2.3$   $\mu\text{A}/\text{cm}^2$  for insets **a** and **b**, respectively. **C**, Mean firing rate of E and I cells are shown in left and right panels, respectively. The white areas in **B** and **C** correspond to parameter values without rhythmic firing.

and in vitro (Gloveli et al., 2005b) studies have shown that the firing rate of E cells is much lower than that of I cells during gamma oscillations. Orienting at the work of Börger and Kopell (2005) and Economo and White (2012) (who investigated the effect of noise on PING rhythms) and the work of White et al. (1998a) (who proposed a role for channel noise in shaping interspike interval distributions of the pyramidal cells), we check this and investigate how our simpler Gaussian white noise input to the E cells reduces the E cell firing rate in both networks with type I and type II interneurons while still allowing for strongly synchronous PING oscillations.

For this we investigate the frequency of PING rhythms and the corresponding mean firing rates of the E and I cells as a function of the mean current  $I_{0,E}$  and the noise amplitude  $\sigma_E$ . When  $I_{0,E}$  and  $\sigma_E$  are too small, the network fails to generate periodic oscillations for type I interneurons (cf. the white region in Fig. 2-4, **B** and **C**, **bottom left**) as well as for type II interneurons (Fig. 2-5) since the small input is not sufficient to drive the E cells above their spiking threshold. If the noise increases, more E cells are activated (see Figs. 2-4**C** and 2-5**B**), thereby eliciting PING rhythms (Figs. 2-4**B** and 2-5**A**). The lower the value of  $I_{0,E}$ , the higher the value of  $\sigma_E$  that is required to generate PING rhythms (boundary between the white and colored regions in Figs. 2-4**B** and 2-5**A**). When the constant input  $I_{0,E}$  increases, the mean firing rate of the E cells increases (Figs. 2-4**C** and 2-5**B** for type I and type II interneurons, respectively). When  $I_{0,E}$  increases, passing the value of  $0.5$   $\mu\text{A}/\text{cm}^2$ , we observe relatively sharp transitions of frequency (Figs. 2-4**B** and 2-5**A**), of the

mean firing rate of the E cells ( $MFR_E$ ) (Figs. 2-4C, **left**, and 2-5B, **left**), and of the mean firing rate of the I cells ( $MFR_I$ ) (Figs. 2-4C, **right**, and 2-5B, **right**). The transitions are caused by the transition of the E cells to the intrinsically oscillatory regime at this value of driving current. When  $I_{0,E}$  increases further, so does the frequency of the PING rhythm and the firing rate of the I cells (Fig. 2-4, **B** and **C**, and Fig. 2-5, **A** and **B**, for type I and type II interneurons, respectively). For small values of noise  $\sigma_E$  the firing rate of the E cells is slightly less than that of the I cells (Figs. 2-4C and 2-5B). Increasing the noise to the E cells reduces the firing rate of the E cells but increases the firing rate of the I cells and the PING frequency. This can only be observed for relatively large values of  $I_{0,E}$ . For small values of  $I_{0,E}$  we are in the fluctuation-driven regime where the E cell firing rate slightly increases with  $\sigma_E$  (Brunel, 2000). As the external current  $I_{0,E}$  increases, the coherence among the E cells increases. For small values of  $I_{0,E}$  (E cells in the fluctuation-driven regime), the coherence weakly increases with noise; for larger values of  $I_{0,E}$  (E cells in the mean-driven regime), the coherence generally decreases with noise. For low noise and larger  $I_{0,E}$ , the coherence is near 1. The results in Figs. 2-4 and 2-5 show that PING rhythms depend on  $I_{0,E}$  and  $\sigma_E$  in a very similar way for both types of interneurons. The increase of firing of the E cells as a function of the drive  $I_{0,E}$  to the E cells will come back in Figs. 2-6 and 2-7, where we show the firing rate of the E cells, when ING and PING interact.

### 2.3.3 Interactions between ING and PING

In the previous sections, we have considered networks with a reduced topology to study ING and PING oscillations separately. We now focus on the interaction between ING and PING rhythms. More precisely, we ask the question: If according to its connectivity the network is in principle able to generate PING as well as ING rhythms, which of the two will it generate, or will it generate a mixture? To answer this question, we study the oscillation characteristics of the complete network (Fig.

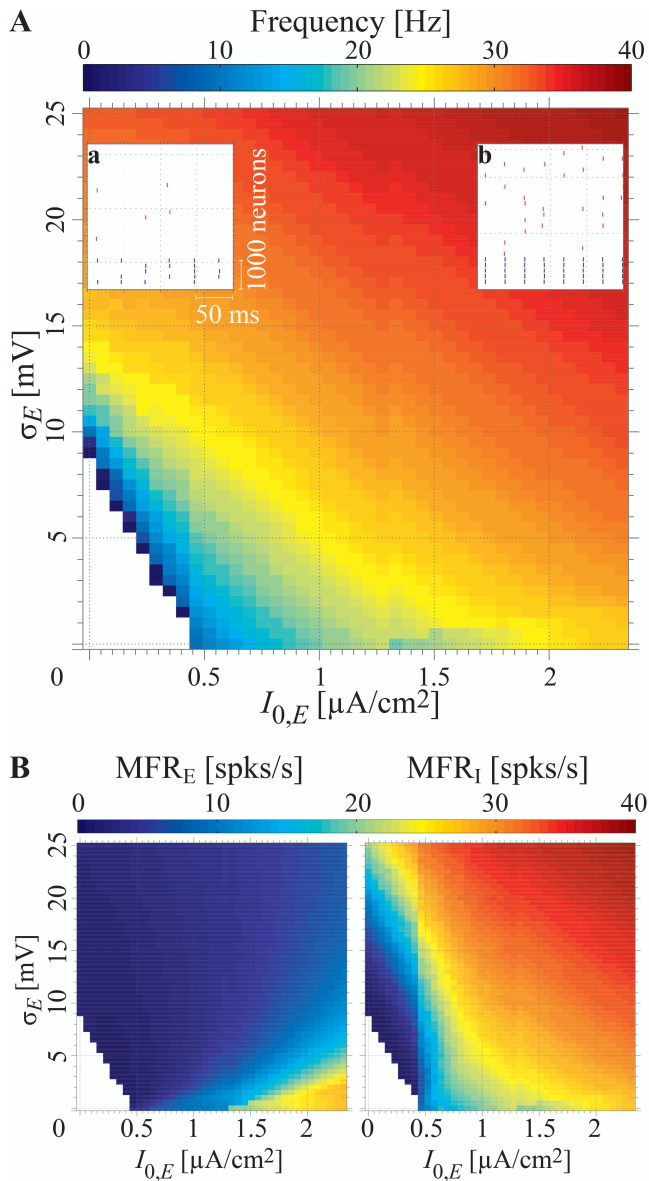


**Figure 2-5. PING rhythms and mean firing rate in a reduced network of E and type II I cells.** The network topology is as displayed in Fig. 2-4A. **A**, Frequency of PING rhythm as a function of current  $I_{0,E}$  and noise  $\sigma_E$ . **Aa** and **Ab** show raster plots (red for E cells, blue for I cells) as in Fig. 2-4B. **B**, Mean firing rate of E and I cells in left and right panels, respectively. The white area in **A** and **B** corresponds to parameter values without rhythmic

firing. Parameter settings:  $\sigma_E = 20$  mV and  $I_{0,E} = 0$   $\mu\text{A}/\text{cm}^2$  and  $2.3$   $\mu\text{A}/\text{cm}^2$  for insets **a** and **b**, respectively.

2-6A) and compare the results with the results obtained above for ING and PING rhythms in reduced networks. In other words, we investigate whether the network oscillations change when one of the mechanisms is disabled by eliminating the projections from the pyramidal cells to the inhibitory neurons (ING) or by eliminating the input to the interneurons (PING). In particular, if network oscillations are left unchanged when disabling one mechanism, and they are affected when disabling the other, we may conclude that only the other mechanism is responsible for the network oscillations in the full network.

Figure 2-6 shows the results for the network with type I WB neurons. The full model is schematically displayed in Fig. 2-6A. Figure 2-6B shows the frequency of network oscillations as a function of the external constant drive  $I_{0,E}$  to the E cells and the external constant input  $I_{0,I}$  to the I cells for 1) the ING-generating network as in Fig. 2-2A (blue surface), 2) the PING-generating network as in Fig. 2-4A (red surface), and 3) the full network as in Fig. 2-6A (green surface). The green surface in Fig. 2-6B is always equal to or slightly above the higher of the ING and PING surfaces. For small values of  $I_{0,I}$ , the oscillation frequency of the full network is slightly higher than the oscillation frequency of the PING mechanism. This is illustrated in detail in Fig. 6C, **left**, which shows the oscillation frequency for ING (blue line), PING (red line), and the full network (green line) as a function of the input  $I_{0,I}$  to the I cells for a constant input  $I_{0,E} = 2$   $\mu\text{A}/\text{cm}^2$  to the E cells, while the mean firing rate of the pyramidal cells ( $\text{MFR}_E$ , dark green line) and of the interneurons ( $\text{MFR}_I$ , light green line) corresponding to the full network (green line) are illustrated in Fig. 2-6C, **right**. The slightly higher frequency for the full model can be explained by the fact that the input from the E cells to the I cells due to the projections  $g_{E \rightarrow I}$  is not suprathreshold and does not generate a spike immediately after arrival of the input spike. Larger inputs  $I_{0,I}$  increase the excitability of the I cells, such that the interval between arrival of the spike volley from the E cells to the I cells and spiking of the I cells decreases. If the interval between firing of the E cells

and I cells decreases, the inhibition from the I cells to the E cells comes earlier in the firing cycle of the E cells and thus has a smaller impact. The earlier start and end of the inhibition explain the reduced interval between subsequent spikes for the E cells for the full network and the corresponding higher frequency. We note that we interpreted the relation between  $I_{0,I}$  and the pure PING network (red) as follows: There is no external input to the I cells, so the value of this parameter does not influence the PING dynamics. An alternative interpretation is to assume  $I_{0,I} = 0$   $\mu\text{A}/\text{cm}^2$  for pure PING. Then, the continuation of the red surface in Fig. 2-6B and the red lines in Fig. 2-6C, **left**, to nonzero values of  $I_{0,I}$  should be viewed as reference for comparison.

When  $I_{0,I}$  increases in Fig. 2-6C, **left**, the oscillation frequency of the full network approaches that of the pure ING oscillations, while the corresponding  $\text{MFR}_E$  monotonically decreases (Fig. 2-6C, **right**). The transition from PING-dominated responses to ING-dominated responses is gradual for the network with the type I interneurons, in agreement with earlier results by Börgers and Walker (2013). Although the full network generates ING-dominated oscillations for higher values of  $I_{0,I}$ , the pyramidal cells are still active (see Fig. 2-6C, **right**). The higher oscillation frequency for the full network at the transition of the blue and red curves is explained by the fact that the interneurons receive input from the pyramidal cells in the full model, and thereby receive more excitation for the same value of  $I_{0,I}$  than for the ING condition. This larger amount of excitation causes a higher oscillation frequency in the network of interneurons and thereby also a higher oscillation frequency for the full network.

Note that although  $\text{MFR}_E$  is low for high values of  $I_{0,I}$  (Fig. 2-6C, **right**), we observe clear gamma rhythms in the pyramidal cells. The  $\text{MFR}_I$  in Fig. 2-6C, **right**, varies in a more complicated way with changes in  $I_{0,I}$  than the mean firing rate of the pyramidal cells ( $\text{MFR}_E$ ). First  $\text{MFR}_I$  slightly increases, then decreases, and increases again as  $I_{0,I}$  increases. This can be understood as follows: For small values of  $I_{0,I}$ , many E cells recover from the inhibition sooner than the I cells do



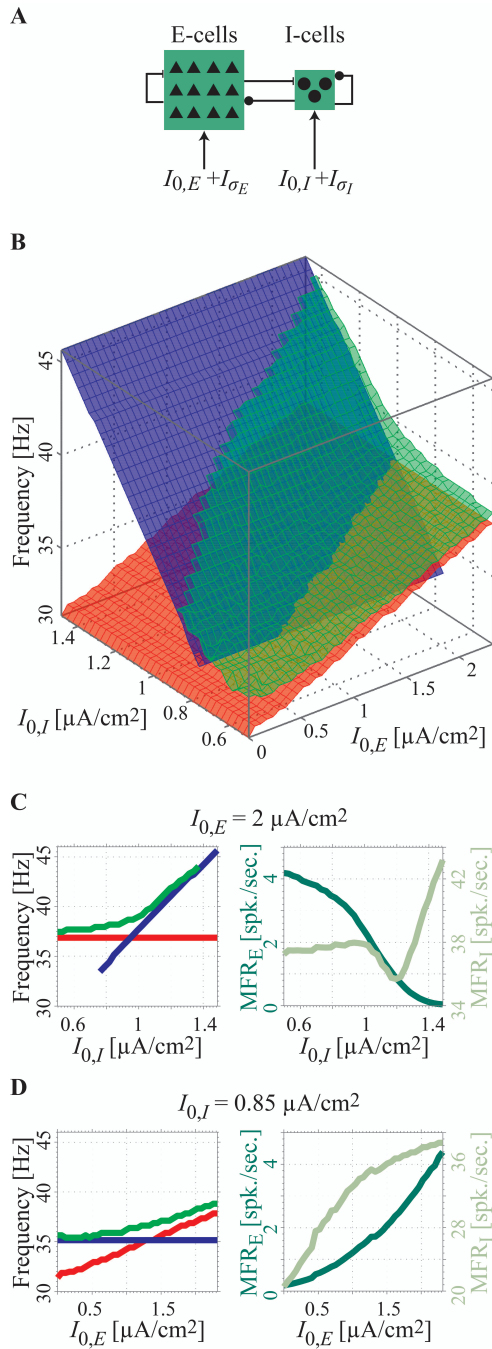


**Figure 2-6. Oscillations in a full network of reciprocally coupled pyramidal cells and type I interneurons.** *A*, Network topology of the full network. *B*, Frequency of ING rhythm

generated by the network in Fig. 2-2A (blue surface), PING rhythm generated by the network in Fig. 2-4A (red surface), and rhythms generated by the full network (green surface) as a function of mean current to E cells  $I_{0,E}$ , and to I cells  $I_{0,I}$ . When the green and blue surfaces closely overlap (for large values of  $I_{0,I}$  and small values of  $I_{0,E}$ ), only the blue surface is shown. **C** and **D**, Left-hand panels show cross sections of **B** along the  $I_{0,I}$  (**C**) and  $I_{0,E}$  (**D**) axes for fixed  $I_{0,E}$  (**C**) and fixed  $I_{0,I}$  (**D**). Right-hand panels show the corresponding mean firing rates of the interneurons (pale green color) and of the pyramidal cells (dark green color). Parameter values:  $\sigma_E = 20$  mV and  $\sigma_I = 0.5$  mV.

and start spiking to elicit spiking of the I cells. We observe a PING rhythm. The I cells spike once in each oscillatory cycle and their mean firing rate increases like the frequency of the full network as  $I_{0,I}$  increases. As  $I_{0,I}$  increases further, the increased excitation to the I cells lets some I cells recover sooner from the inhibition than the E cells. These inhibit the E cells, in particular the E cells in the population that tend to fire late. This leads to less excitation given to the I cells from the E cells and therefore to a lower mean firing rate of the I cells. We checked that the higher the noise  $\sigma_I$ , the more I cells recover early and the stronger the effect. When  $I_{0,I}$  increases even further, the I cells receive more excitation and further inhibit the E cells until the excitation from the E cells is so low that the full network behaves like pure ING, i.e. the mean firing rate of the I cells increases and the I cells skip a lower number of the oscillatory cycles as  $I_{0,I}$  increases.

Figure 2-6D, **left**, shows the oscillation frequency for ING (blue line), PING (red line), and the full network (green line) as a function of the input  $I_{0,E}$  to the E cells for a constant input  $I_{0,I} = 0.85$   $\mu\text{A}/\text{cm}^2$  to the I cells, while Fig. 2-6D, **right**, shows the mean firing rate of the pyramidal cells ( $\text{MFR}_E$ , dark green line) and of the interneurons ( $\text{MFR}_I$ , light green line) corresponding to the full network (green line in Fig. 2-6D, **left**). For small values of  $I_{0,E}$  the oscillation frequency for the full network is close to the ING oscillation frequency, while the pyramidal cells show clear gamma rhythms although  $\text{MFR}_E$  is low (see Fig. 2-6D, **right**). For larger values of  $I_{0,E}$  near the intersection of the red and blue lines, the oscillation frequency of the

full network (green line in Fig. 2-6D, **left**) exceeds that for ING and PING rhythms for the same reasons as for Fig. 2-6C, **left**. For larger values of  $I_{0,E}$ , the oscillation frequency of the full model increases with the pure PING oscillation frequency (and so does the mean firing rate of the pyramidal cells and of the interneurons) but always remains somewhat higher than the pure PING frequency. The latter is in agreement with results by Börgers and Walker (2013), who reported that increase of input to the E cells in a network of reciprocally coupled E and I cells advances firing of the I cells in each cycle when their phase response is of type I.

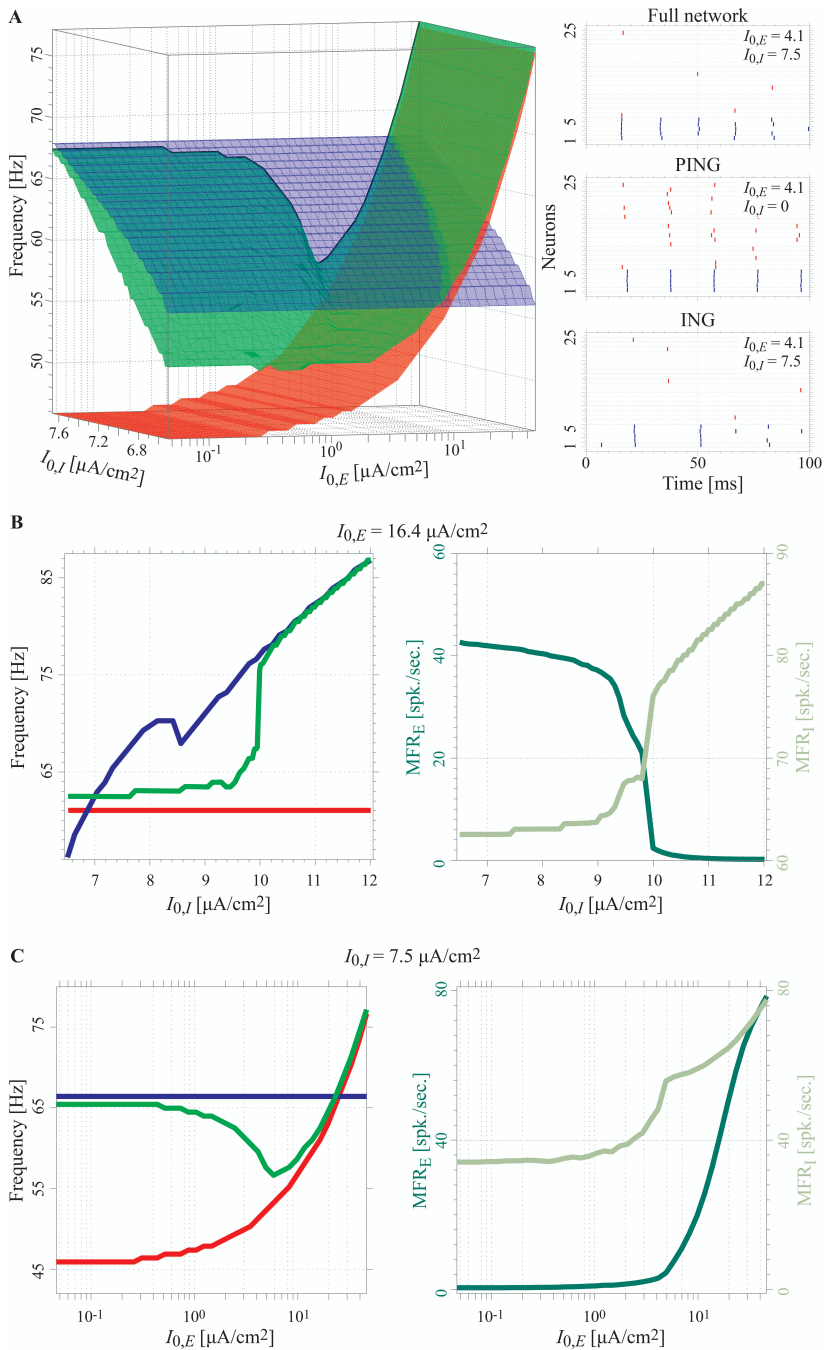
Summarizing, our results show that the oscillation frequency of the full network is equal to (or somewhat higher than) the higher of the pure ING and pure PING oscillation frequency. The reason for this is that the higher-frequency mechanism recruits the vast majority of available neurons in the two populations, such that the other mechanism cannot exist. For example, when the PING frequency is higher than the ING frequency, the E neurons recover before the I neurons; they spike and recruit the I neurons into the PING rhythm by near-suprathreshold excitation. The ING rhythm then cannot develop because the I neurons cannot reach threshold because of their intrinsic drive. In contrast, when the ING frequency is higher than the PING frequency, the I neurons recover before the E neurons and are reset when the input from nonsuppressed E neurons arrives, such that they cannot be recruited into the PING rhythm.

Figure 2-7 shows an analysis similar to Fig. 2-6 for the network with type II interneurons. As in the analogously structured Fig. 2-6, the blue, red, and green surfaces in Fig. 2-7A represent the firing frequencies for pure ING oscillations ( $g_{E \rightarrow I} = 0$  ms/cm<sup>2</sup>), for pure PING oscillations ( $I_{0,I} = 0$  μA/cm<sup>2</sup>), and for the full network, respectively, while the dark green and light green curves in Fig. 2-7B, **right**, represent the mean firing rate of the pyramidal cells and of the interneurons in the full network. The main difference between the results in Fig. 2-7A for type II interneurons and the results in Fig. 2-6B for type I interneurons is that the firing frequency of the full network can be between that of ING and PING for type II interneurons for intermediate values of  $I_{0,E}$  and  $I_{0,I}$  (compare also Figs. 2-6C, **left**, and 2-7B, **left**). The explanation for this observation is that when the ING rhythm

dominates, the E cells can only fire just before firing of the I cells, i.e. before inhibition from the interneurons comes in. The action potentials from the E cells then arrive at the I cells just after their firing, which causes a phase delay because of the type II PRC, and therefore a lower frequency of the full network compared with the pure ING frequency. When the input  $I_{0,I}$  increases to larger values, the frequency of the full network becomes fully determined by the ING frequency (Fig. 2-7, **A** and **B, left**) while the mean firing rate of the pyramidal cells of the full network strongly decreases. In that case the blue and green surfaces (Fig. 2-7**A**) or curves (Fig. 2-7**B, left**) overlap. This holds even though the E cells are still active near the transition, albeit with reduced frequency (Fig. 2-6**C, right**, and Fig. 2-7**B, right**). The blue curve for ING in Fig. 2-7**B, left**, shows some abrupt variation, which may suggest an underlying bifurcation.

When the I drive is even stronger, the E cells become suppressed (cf. Börgers and Kopell (2003, 2005); Börgers and Walker (2013)). In this sense, our transition for increasing I drive may be considered as a part of the suppression transition. Like Börgers and Walker (2013), in networks with type II interneurons we find a rather abrupt departure from PING oscillations when increasing the I drive (green curve in Fig. 2-7**B, left**). For different transition paths (increasing the E drive; see Fig. 2-7**C**), the transition is more gradual. Figure 2-7**C, left**, shows the oscillation frequency when the input to the interneurons is constant and when the input  $I_{0,E}$  to the E cells is varied; for small values of  $I_{0,E}$ , the oscillation frequency of the full network (green curve) is slightly below that for the ING rhythm (blue curve), again because of the effective delaying of I cells through E cells as explained above. When  $I_{0,E}$  increases, the oscillation frequency of the network (green line) decreases, approaching the pure PING oscillation frequency (red line) even when the pure PING oscillation frequency is lower than the pure ING oscillation frequency. From there the frequency of network oscillations follows the frequency of PING oscillations.

The reason for the fact that in intermediate input ranges in Fig. 2-7**A, left**, and Fig. 2-7**C, left**, the full network approaches the pure PING oscillation frequency as  $I_{0,E}$  increases even when the pure ING oscillation frequency is higher lies again in the phase delay in the PRC of type II interneurons: During the full network ING



**Figure 2-7. Oscillations in a full network of reciprocally coupled pyramidal cells and type II interneurons.** Network topology is as in Fig. 2-6A. **A**, Frequency of ING rhythm

generated by the network in Fig. 2-2A (blue surface), PING rhythm generated by the network in Fig. 2-4A (red surface), and rhythms generated by the full network (green surface) as a function of mean current  $I_{0,E}$  to E cells and  $I_{0,I}$  to I cells. The raster plots show the firing of the E (red) and I (blue) neurons for the full network, the reduced PING, and the reduced ING networks, at the same point in parameter space. Left-hand panels of **B** and **C** show the frequency for ING (blue line), PING (red line), and for the full network (green line), while right-hand panels of **B** and **C** show the mean firing rate of the interneurons (light green color) and of the pyramidal cells (dark green color) for variations in  $I_{0,I}$  (**B**) and  $I_{0,E}$  (**C**). Parameter values:  $\sigma_E = 60$  mV and  $\sigma_I = 0.5$  mV.

rhythm, the E cells spike such that their input arrives early in the phase of the I neurons, so it has a delaying effect and reduces the frequency of the ING rhythm. In other words, when the oscillation frequency for the full network is between pure ING and pure PING, the type II nature of the interneurons causes a lower frequency for ING in the full network than in the reduced network, such that the higher frequency is in fact PING; this dominates the network oscillations in the full network. So, as in networks with type I interneurons, we have in fact the higher frequency generating mechanism winning.

When the external input to the E cells increases, the mean firing rate of the E cells increases (see Fig. 2-7C, **right**). The higher mean firing rate of the E cells implies that the E cells provide more excitation to the I cells. This larger amount of excitation arrives at early phases in the firing cycle of the I cells and gives rise to a larger phase delay (lower firing rate) of the I cells due to their type II PRC. Because of the larger phase delay of the I cells, the interval of firing of the I cells decreases. This explains why the frequency of the full network (green line in Fig. 2-7C, **left**) decreases as  $I_{0,E}$  increases.

Given the decrease in the frequency of the full network, it may seem contradictory that the mean firing rate of the I cell increases as  $I_{0,E}$  increases (Fig. 2-7C, **right**). The explanation is that the increased firing of E cells provides more excitation to the I cells, such that more I cells fire in each cycle, which becomes longer. The frequency of the full network decreases till it approximately meets the

pure PING frequency (see Fig. 2-7C, **left**): At this point,  $I_{0,E}$  increases the excitability of the E cells high enough such that the E cells recover from the inhibition from the I cells sooner than the I cells, and the full network generates PING-dominated oscillations.

### 2.3.4 Analytical insights into the interactions between ING- and PING-driven oscillations using a phase model

The results of the computer simulations presented so far might raise the question of whether these results are generic and not due to a particular choice of parameter values in our model. To address this issue, we performed a mathematical analysis of a simple pair of neurons with an excitatory (E) and inhibitory (I) neuron (see sec. 2.2). This simple model allows for analytical expressions for the firing rate of the system for various conditions (see Appendix 2.5). Since we want to investigate the interaction between ING and PING on network oscillations, we provide input to both the E and I neurons in our simulations. From the previous sections and from the literature (e.g. Börgers and Kopell (2003, 2005); Börgers and Walker (2013)), we know that PING will dominate the network dynamics for relatively large input to the E neuron and small input to the I neuron and that ING dominates when the input to the E neuron is relatively small and the input to the I neurons is large. We are interested in intermediate regimes of transition between PING and ING, far from these extremes. More precisely, we focus on regimes where both the E and the I neuron spike once in every cycle. In particular, also during ING-dominated oscillations the E neuron should not be suppressed but it should generate a regular spike rhythm with one-to-one locking. This restricts the ranges of admissible parameters.

For an illustration of this case, see Fig. 2-8A, which shows the firing of the E neuron (red vertical lines) and I neuron (blue vertical lines) for the ING condition. The figure shows results for model 1 (see sec. 2.2), where the E and I neurons are both LIF neurons. If the E neuron (red trace in Fig. 2-8A) fires in this ING condition, either it fires just before the I neuron (blue trace) with a time lead smaller than the conduction delay  $\tau$  from the E neuron to the I neuron or the E neuron fires just after firing of the I neuron before the inhibition of the I neuron arrives at the E neuron. Figure 2-8A illustrates the latter case. The self-inhibition of the I neuron is reflected

by the inhibition in the blue trace at a time  $\tau$  ( $= 0.4$  time units) after firing of the I neuron; similarly, the excitation from the E neuron to the I neuron is reflected by the small increment in the blue trace at time 0.4 after firing of the E neuron.

Figure 2-8B shows the relative firing of the E and I neurons for the PING condition. After firing of the E neuron, the I neuron fires with a delay  $\tau$ , i.e. the

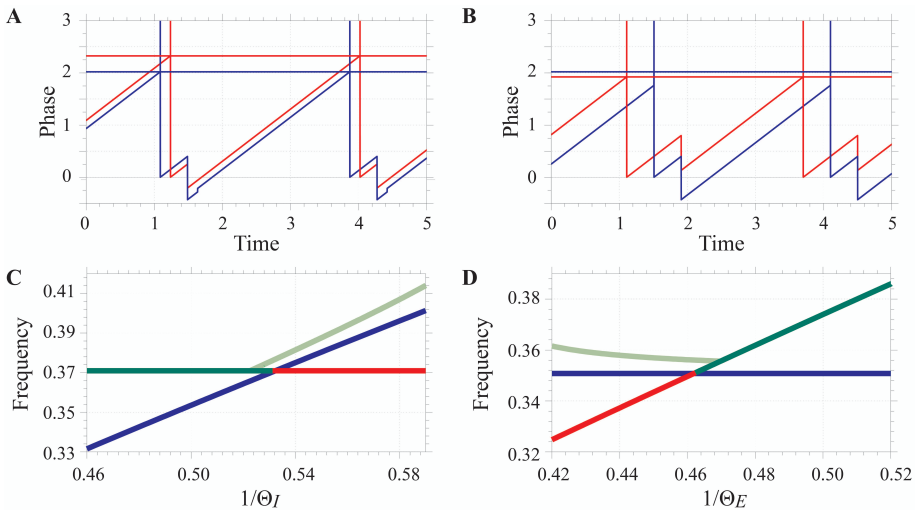


**Figure 2-8. Interactions between ING and PING oscillations for an LIF-LIF phase model.** Examples of ING-dominated phase dynamics (*A*) and PING-dominated phase dynamics (*B*) as a function of time (arbitrary units) for a network with two LIF neurons, coupled by excitation and inhibition. The firing of the E (I) neuron is highlighted by red (blue) vertical lines. The time delay from the E neuron to the I neuron is equal to that from the I neuron to the E neuron (0.4 units; if the firing rate would be 40 Hz, the delay of 0.4 units would correspond to about 3 ms). *C* shows the firing frequency of the network as a function of the input to the I neuron, while the input to the E neuron is kept constant. The blue and red curves show the network oscillations for pure ING and pure PING, respectively. The green curve shows the frequency of network oscillations for the full two-neuron network; dark green indicates full-network PING and light green full network ING. *D* similarly shows the network oscillations as a function of the input to the E neuron, while the input to the I neuron is kept constant. For the full network the parameter values for the coupling strengths are  $\varepsilon_{I \rightarrow E} = -0.5$ ,  $\varepsilon_{E \rightarrow I} = 0.1$ ,  $\varepsilon_{I \rightarrow I} = -1.0$ , and  $\tau = 0.4$ ; for the ING condition we set  $\varepsilon_{E \rightarrow I} = 0$ , which eliminates any input from the E to the I neuron. The input to the I and



E neurons is  $1/\Theta_I = 0.495$  and  $1/\Theta_E = 0.43$  for **A**,  $1/\Theta_I = 0.495$  and  $1/\Theta_E = 0.52$  for **B**,  $1/\Theta_E = 0.495$  for **C**, and  $1/\Theta_I = 0.495$  for **D**.

output from the E neuron raises the phase of the I neuron above the phase threshold  $\Theta_I$  near the value 2. The I neuron will then send inhibitory output back to the E neuron and to itself. This is illustrated by the decrease of the phase of the E and I neurons at the time  $2\tau$  after firing of the E neuron.

The frequencies of the ING and PING oscillations can be computed analytically. Figure 2-8C displays the results (Eqs. 2-A2, 2-A4, and 2-A5 with 2-A6 as well as 2-A7) as a function of the free firing frequency of the I neuron. This firing frequency is a unique, monotonically increasing function of the constant input to the I neuron. The blue line shows the network oscillation frequency for the pure ING condition ( $\varepsilon_{E \rightarrow I} = 0$ , cf. Appendix 2.5). This increases linearly when the input to the interneuron measured by  $1/\Theta_I$  increases, in agreement with previous studies (Bartos et al., 2001; Bartos et al., 2007). The red line shows the network oscillation frequency for pure/ideal PING with suprathreshold excitation of the I neuron (cf. Appendix 2.5). For the full model, the frequency of rhythmic activity for different constant inputs to the I cell is illustrated by the green curve. For small inputs to the I cell, PING dominates the behavior of the model (dark green part of the green curve), which explains why the green and red lines superimpose at the left-hand side of Fig. 2-8C. When the input to the I cell increases such that the firing frequency of the I cell exceeds that of the E cell (near  $1/\Theta_I = 0.53$ ), ING takes over (i.e. the full network generates an ING rhythm, light green part of the curve) and the frequency of the rhythm of the full model increases, similar to that of pure ING. This happens because the I cell recovers from the inhibition before the E cell does, after which the I cell delays spiking of the E cell and determines the rhythm. The firing rate of the network exceeds that of pure ING because the I cell in the full network also receives additional excitatory input from the E cell. Figure 2-8 illustrates that the network oscillation frequencies approximately follow the firing frequencies of pure ING or PING, whichever is the largest of the two. This agrees with our results from the computer simulations for the model with the single-compartment Hodgkin-Huxley type I neuron model in Fig. 2-6C, **left**. The reason for this is that the higher-

frequency mechanism recruits both available neurons just as it recruits the majority of neurons in the large two-population networks, such that the other mechanism cannot exist.

Interestingly, the theoretical analysis reveals a small region of bistability for values of  $1/\Theta_I$  between about 0.52 and 0.53 (see Fig. 2-8C): When the constant input to the I neuron gradually increases, the model generates the pure PING-firing frequency until the blue ING curve intersects the red PING curve (cf. the dark green curve). At that crossing, the model switches to ING and to the firing rates along the light green curve. When the input to the interneurons is gradually decreased starting from high values, the firing frequency follows the light green curve until it intersects the red curve. From there the firing frequency of the model follows the red pure PING curve (dark green curve). We do not observe such a region in the larger networks: this might be because effects of coupling inhomogeneity and noise do not allow a sufficient separation of the close-by frequencies.

Figure 2-8D shows the changes in frequency of the rhythmic activity when the input to the E cell is varied while the input to the I neuron is kept the same. The frequency of the rhythmic activity is obtained from Eqs. 2-A2, 2-A4, and 2-A5 with 2-A6 as well as 2-A7. The red line illustrates the increase of pure PING frequency with increasing input to the E cell (note that the green curve superimposes the red line for larger inputs). This is a direct consequence of the increase in firing rate of the E cell when it receives increasing input. Pure ING oscillations are not affected by changes in input to the E cell (blue line). For small input to the E neuron (with  $1/\Theta_E$  approximately less than 0.46) the full network generates ING-dominated oscillations with a frequency that is approximately constant despite variations in input to the E cells (light green line); this happens when the firing frequency for the pure PING case (red line) is below that for the pure ING case (blue line). As in Fig. 2-8C, the higher frequency “wins.” The frequency of the full model ING exceeds the frequency of the reduced-network ING rhythm, because the full model has projections from the E to the I cell, which provide excitatory input in addition to the constant input to the I cell. When the network frequency for reduced-network PING exceeds that of reduced-network ING, the full network adopts the PING rhythm (dark green line superimposed on red line in Fig. 2-8D). In between there is again a small region of coexistence. These results are in good agreement with the results of

the simulations of larger networks with single-compartment Hodgkin-Huxley type I neurons (cf. Fig. 2-6D, left).

Figure 2-9 shows the results for the network where the I neuron are represented by a type II sine neuron. As in Fig. 2-8, Fig. 2-9A shows the firing of the E (red) and I (blue) neurons for ING-dominated firing of the network. The firing of the E neuron precedes the firing of the I neuron, but the interval between their spikes is less than the time delay  $\tau$  from the E to the I neuron (0.4). Therefore, firing of the I neuron is due to its intrinsic firing and not an immediate consequence of excitation by the E neuron. In fact, the excitation of the I neuron by spike input from the E neuron is hardly visible because of the nature of the sine neuron: An excitatory input arriving just after the I neuron's reset causes a rather small delay in firing, not a marked depolarization. The inhibition of the E neuron after firing of the I neuron is clearly visible, simultaneous with the increase of the phase of the I neuron by self-inhibition, which, because of the type-II PRC of the sine neuron, leads to a phase advance (i.e. an increase of the membrane potential). Figure 2-9B shows the same results for a PING rhythm in the circuit.

Figure 2-9, C and D, shows the frequency of ING (blue line), PING (red line), and the full model (green line) according to Eqs. 2-A3, 2-A4, 2-A9, and 2-A11. In Fig. 2-9C we vary the input  $1/\Theta_I$  to the I neuron with fixed input  $1/\Theta_E$  to the E neuron. In Fig. 2-9D the input  $1/\Theta_E$  to the E neuron is varied, while the input  $1/\Theta_I$  to the I neuron is kept constant. In both Fig. 2-9, C and D, the frequency of the full network is between the frequencies of the pure ING and pure PING rhythms. Nevertheless, the full network generates either ING or PING depending on which mechanism (pure ING or pure PING) yields the higher-frequency oscillations in the reduced networks (cf. dark and light green parts of the green curve highlighting PING and ING oscillations in Fig. 2-9, C and D, respectively). Already for inputs to the I neuron that are smaller than those to the E neuron, the frequency of the PING rhythm exceeds that of the ING rhythm, i.e. the red curve lies above the blue curve [see the results for  $1/\Theta_I < 0.5$  ( $1/\Theta_E = 0.75$ ) in Fig. 2-9C and  $1/\Theta_E > 0.74$  ( $1/\Theta_I = 0.50$ ) in Fig. 2-9D]. We see from the detailed dynamics of the full network in Fig. 2-9B that in this case the E neuron recovers from reset and inhibition before the I neuron does, and it excites the I neuron to spiking, i.e. the full network generates

PING oscillations. The oscillation frequency is nevertheless between those of pure PING and pure ING. This can be understood from the fact that we assumed an "ideal" PING rhythm for the comparison, in the sense that the input from the E neuron to the I neuron is practically suprathreshold, causing the I neuron to fire immediately after arrival of the E spike. Our type II neuron does not allow for strictly suprathreshold input, i.e. our type II neuron requires an infinitely strong input pulse to immediately reach threshold. For the full model, the I neuron will spike shortly

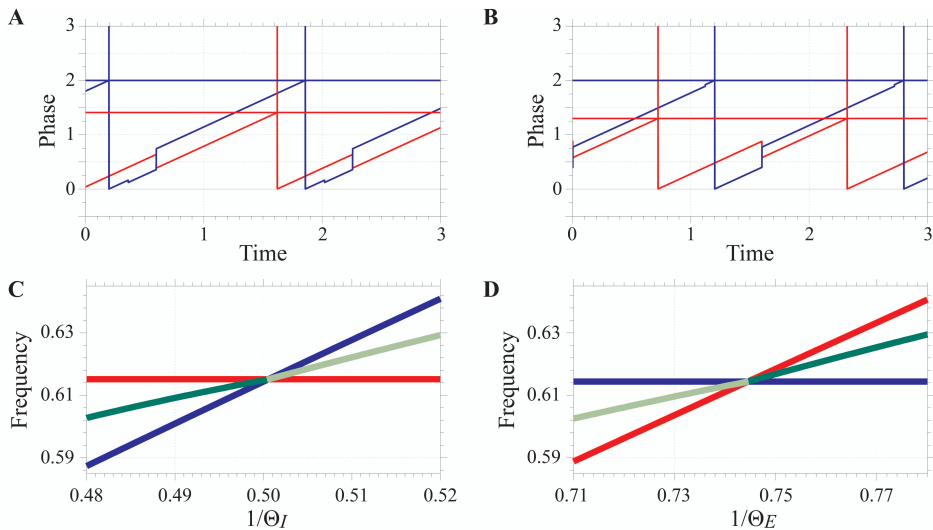


**Figure 2-9. Interactions between ING and PING oscillations for the LIF-sine phase model.** Examples of ING-dominated phase dynamics (*A*) and PING-dominated phase dynamics (*B*) as a function of time (arbitrary units) for a network with a LIF-type E neuron and a sine neuron as I cell. The firing of the E (I) neuron is highlighted by red (blue) vertical lines. The time delay from the E neuron to the I neuron is equal to that from the I neuron to the E neuron (0.4 units as in Fig. 2-8). *C* shows the firing frequency of the network when the input to the E neuron remains constant. The blue and red curves show the network oscillation frequencies for pure ING and pure PING, respectively. The green curve shows the frequency of network oscillations for the full two-neuron network; dark green indicates full-network PING, and light green for full-network ING. *D* is similar to *C*, except for the fact that the input to the I neuron is constant, while the input to the E neuron varies. For the full network, the parameter values for the strengths of the couplings are  $\varepsilon_{I \rightarrow E} = -0.2$ ,  $\varepsilon_{E \rightarrow I} = 0.1$ ,  $\varepsilon_{I \rightarrow I} = -0.42$ , and  $\tau = 0.4$ ; input from the E to the I neuron was eliminated to obtain ING by setting

$\varepsilon_{E \rightarrow I} = 0$ . The input to the I and E neurons was  $1/\Theta_I = 0.5$  and  $1/\Theta_E = 0.71$  for **A**,  $1/\Theta_I = 0.5$  and  $1/\Theta_E = 0.77$  for **B**,  $1/\Theta_E = 0.75$  for **C**, and  $1/\Theta_I = 0.5$  for **D**.

but not immediately after arrival of the E spike. The small delay in firing causes a delay in arrival of inhibition at the E neuron, a larger impact of the inhibitory input, and therefore a delay in the next spike of the E neuron. The frequency of the rhythm of the full network is then below that of the pure PING rhythm. The observation that the frequency of the full network is higher than the frequency of the pure ING rhythm may be understood from the fact that the frequency of pure PING is higher than the frequency of pure ING: This implies that during the full-network PING rhythm, the E neuron reaches the threshold for firing faster than the I neuron. When the threshold for firing of the E neuron is reached, the spike from the E neuron arrives at the I neuron in the second half of its phase cycle. This causes a phase advance for the I neuron, causing a higher firing rate for the I neuron than for the pure ING case.

For relatively large inputs to the E neuron (or small inputs to the I neuron), the phase model with type II I neuron yields results (Fig. 2-9, **C** and **D**) that are qualitatively different from the results for the network with Hodgkin-Huxley type II cells shown in Fig. 2-7: For the phase model, the frequency of the full network is lower than the frequency of PING (see Fig. 2-9, **C** and **D**), whereas it is slightly higher for the Hodgkin-Huxley-type model (see Fig. 2-7, **B** and **C**, **left**). This discrepancy stems from the fact that for the phase model with type II I neuron, the synaptic strength  $\varepsilon_{E \rightarrow I}$  from the E to the I neuron for pure PING is assumed to be larger than that for the full network to generate the “ideal” PING rhythm with practically suprathreshold input. However, the synaptic connectivity  $\varepsilon_{E \rightarrow I}$  is the same for pure PING and for the full network for the Hodgkin-Huxley-type model. When  $\varepsilon_{E \rightarrow I}$  is larger for pure PING than for the full network in the phase model, the I neuron will spike at shorter latencies after a spike by the E neuron for PING than for the full network. As a consequence, the firing rate will be higher for PING than for the full network. However, in case of the Hodgkin-Huxley-type model where the effective strength of outputs from the pyramidal cells to interneurons in PING and in the full network is approximately the same, the interval between spiking of the E and I cells is approximately the same. Frequency differences between pure PING

and full-network PING are a consequence of the additional external inputs to interneurons. Because interneurons in the full network receive additional constant inputs  $I_{0,I}$  that are not present or negligible in case of pure (reduced network) PING, the frequency of the Hodgkin-Huxley full network is higher.

For small input to the E neuron (or large input to the I neuron), the frequency of pure ING oscillations exceeds that of pure PING oscillations (see Fig. 2-9, **D** and **C**, left and right, respectively). In these cases, the full network generates ING oscillations. Again, this is because the I neuron recovers faster from the reset and excitation-inhibition than the E neuron does. The frequency of the full network is nevertheless lower than that of pure ING. This can be understood as follows. During the full-network ING rhythm, the excitatory output from the E neuron arrives at the I neuron in an early phase of the I neuron, which causes a phase delay for the type II I neuron (see, e.g., Fig. 2-9A). The period of the full network is then longer than the period of pure ING, or in other words, the frequency of the full network is lower than the frequency of pure ING. Furthermore, when the I neuron spikes, inhibition from the I neuron arrives at the E neuron at a phase less than  $2\tau$  for the full network but at the phase  $2\tau$  of its cycle for pure PING. Because of the shape of the PRC of the E neuron, inhibition generated by the I neuron then delays the spiking of the E neuron in the full network less than in case of the reduced network generating pure PING, and the E neuron in the full network recovers from the inhibition sooner than the E neuron in the pure-PING reduced network does. The period of the full network is then shorter than the period of PING, i.e. the frequency of the full network exceeds that for PING. This agrees with the studies based on the Hodgkin-Huxley-type model (see Fig. 2-7).

## 2.4 Discussion

We have investigated the interactions between gamma oscillations generated by ING and PING mechanisms, using a model inspired by neural networks in hippocampal region CA1. Usually ING oscillations have been studied in networks with input to interneurons without drive to pyramidal cells (if present at all in the network). Similarly, PING oscillations have usually been studied in networks of mutually coupled pyramidal cells and interneurons with external input to the pyramidal cells but without external input to the interneurons. In this study we have investigated

network oscillations when both ING and PING can in principle be generated because of the network connectivity and the external input to both the pyramidal cells and the interneurons. We have investigated PING and ING oscillations and oscillations in the full network where ING and PING interact. In our study we considered both networks with type I and networks with type II interneurons. Our results are derived using computer simulations of networks with pyramidal cells and interneurons, as well as analytical considerations for simple two-neuron circuits. Analyzing the similarities and differences between the dynamics of the two setups allows a better understanding of the dynamics. Furthermore, the approach demonstrates that the simulation results reflect a general behavior of networks with pyramidal cells and interneurons, rather than a particular behavior that is specific for a small niche in parameter space used in the computer simulations.

The results in Figs. 2-2 and 2-3 show that gap-junctional coupling may be sufficient to generate ING oscillations in our networks of coupled interneurons, for both type I and type II interneurons, well in agreement with previous observations (Chow et al., 1998; Galarreta and Hestrin, 1999; Gibson et al., 1999; Chow and Kopell, 2000; Galarreta and Hestrin, 2001a, b; Kopell and Ermentrout, 2004; Gibson et al., 2005). We find a richer dependence of the oscillations on the inhibitory coupling than previously reported: For type I interneurons the frequency of ING oscillations decreases when the inhibition increases, while the coherence increases (Fig. 2-2, **B** and **C**, **right**). At some value, the ING oscillation frequency abruptly increases before the oscillation disappears and reappears for larger values of synaptic strength  $g_{I \rightarrow I}$  (see Fig. 2-2**B**). Studies on two-neuron systems (see van Vreeswijk et al. (1994); Ernst et al. (1995); Ermentrout (1996); Terman et al. (1998); Di Garbo et al. (2002); Lewis and Rinzel (2003); Nomura et al. (2003); Bem and Rinzel (2004); Jeong and Gutkin (2005); Merriam et al. (2005); Nomura and Aoyagi (2005); Pfeuty et al. (2005); Di Garbo et al. (2007a); Di Garbo et al. (2007b); Meyrand et al. (2009); Oh and Matveev (2009); Terman et al. (2011); Canavier et al. (2013)) have not reported such findings, likely because they did not consider self-inhibition. Nevertheless, there are some similarities between our results and their results for intermediate values of  $g_{I \rightarrow I}$ : Lewis and Rinzel (2003) reported bistability for interneurons coupled by gap junctions and chemical synapses without self-inhibition. We also find in two-neuron simulations with self-inhibition and

parameters adapted to describe the two neuron populations in our large networks that in-phase and antiphase firing coexist for intermediate values of  $g_{I \rightarrow I}$ , related to the region without oscillations (white area) in the full network with  $g_{I \rightarrow I} = 4 \times 10^{-3} - 10^{-1}$  mS/cm<sup>2</sup> in Fig. 2-2B. Furthermore, we verified that a system of two inhibitory coupled WB neurons with self-inhibition reveals behaviors similar to those in larger networks not only for intermediate values of  $g_{I \rightarrow I}$  (range  $g_{I \rightarrow I} = 4 \times 10^{-3} - 10^{-1}$  mS/cm<sup>2</sup> in Fig. 2-2B) but also for small ( $g_{I \rightarrow I} < 4 \times 10^{-3}$  mS/cm<sup>2</sup> in Fig. 2-2B) and large ( $g_{I \rightarrow I} > 10^{-1}$  mS/cm<sup>2</sup> in Fig. 2-2B) values of  $g_{I \rightarrow I}$ , where in-phase firing between the two neurons is preferred compared to antiphase firing. In agreement with the two-neuron systems with self-inhibition, the large networks generate synchronized firing activities for small and large values of  $g_{I \rightarrow I}$ , only when  $g_{I \rightarrow I}$  is too small, e.g. on the order of  $10^{-4}$  mS/cm<sup>2</sup>, the large networks cannot generate synchronized firing because of noise. A pair of two inhibitorily-coupled Hodgkin-Huxley-type neurons with self-inhibition was also studied by White et al. (1998b). For the parameters used in their study, White et al. (1998b) always observe in-phase synchronization between the two neurons regardless of the choices of the external drive, the strength of the inhibitory chemical synapse, and the decay time constant of the synapse. We speculate that the discrepancy (no antiphase observed) might be due to the relatively long decay time constant of the synapse used in White et al. (1998b). In this context it is interesting to point out a resemblance to the results in the work by Achuthan and Canavier (2009). The authors report that full synchrony in networks of WB interneurons can fall apart into clusters of neurons that fire in antiphase, followed by asynchrony when the strength of synaptic coupling increases to large values. In addition, our simulations show that the range of values for  $g_{I \rightarrow I}$  where stable oscillations are absent becomes smaller for increasing values of gap-junctional coupling. This illustrates that synchronization by gap-junctional coupling can support oscillations by synaptic coupling, in agreement with previous results by Kopell and Ermentrout (2004) as well as Lewis and Rinzel (2003).

In sec. 2.3 we used the argument that in order to create ING, interneurons require a certain minimal amount of inhibition from other interneurons (Wang and Buzsáki, 1996) and that the role of inhibition might be to erase the “history” of the



interneurons (see also Kopell and Ermentrout (2004)). Since a population of uncoupled neurons can be synchronized by a single inhibitory pulse, this has been the general view in the research community for a while, and this mechanism is thought to underlie ING-like oscillations in the gamma frequency range (30–80 Hz) in hippocampus and neocortex. In this context, it is worth noting that Börgers et al. (2010) showed that synchronization by an inhibitory pulse may fail for populations of classical Hodgkin–Huxley neurons, more likely when the hyperpolarizing inhibitory pulse is strong or long-lasting. Recently, Tikidji-Hamburyan et al. (2015) demonstrated that synchronization in resonator neurons can be robust even when the hyperpolarizing inhibition is strong, as long as the time constant of the inhibitory synapse is short enough. Both results are consistent with our study, which finds for type II neurons and hyperpolarizing inhibition variations in synchronization and coherence as a function of the strength of the inhibitory coupling, cf. Fig. 2-3.

For networks with type II interneurons, the dependency of ING oscillations on  $g_{I \rightarrow I}$  and  $g_{G/I}$  is quantitatively and qualitatively different from that in a network with type I interneurons. The first quantitative difference is that ING oscillations occur at smaller values of gap-junctional coupling in networks with type II interneurons than in networks with type I interneurons when chemical synapses are weak or absent (see Figs. 2-2B and 2-3A). Exploratory simulations indicate that these and following observations of loss of synchrony are related to coexisting stable in-phase and antiphase oscillatory states in corresponding two-neuron systems. Another difference is that chemical synapses compete with the gap junctions to generate stable ING oscillations for type II neurons (Fig. 2-3) when the chemical synaptic coupling strength is small. More specifically, when the synaptic coupling increases, the value required for gap-junctional coupling to obtain ING oscillations increases.

The dynamics of PING oscillations has been addressed in many studies. Variations in external drive can create or abolish PING rhythms (see Börgers and Kopell (2003); Börgers et al. (2005); Börgers and Kopell (2005); Börgers and Walker (2013)). The set of parameter values taken from experimental data on CA1 networks yields stable PING oscillations in our model for both type I and type II interneurons. Moreover, the raster plots in Fig. 2-4B and Fig. 2-5A show that for sufficiently noisy conditions the population of pyramidal cells reveals a clear gamma

rhythm, whereas each pyramidal cell fires once every few cycles, in agreement with experimental observations. The explanation for the finding that the firing rate of pyramidal cells in biological neural networks is considerably lower than the oscillation frequency of PING has not yet been set unambiguously. Various explanations have been suggested: Kopell and LeMasson (1994) showed that in a network with coupled excitatory and inhibitory neurons, hyperpolarization-activated inward currents can help to produce population rhythms in which individual cells participate sparsely and randomly. A shift in the activation curve of such a current changes the fraction of the cells participating in any given cycle of the population rhythm. Conceptually related approaches assume cholinergic modulation, by variations in adaptation currents to produce intermittent spiking of pyramidal cells in PING rhythms (Kilpatrick and Ermentrout, 2011; Krupa et al., 2014). This mechanism is related to the long-lasting afterhyperpolarization observed in pyramidal cells (Mann et al., 2005a). Another suggestion was that noise can cause low and intermittent spike discharges in pyramidal cells that interact with interneurons in PING-like rhythms (see Börgers et al. (2005); Börgers and Kopell (2005)). In the present study we have used a model belonging to the second class of explanations, using Gaussian white input current noise, to yield firing rates of E cells well below the frequency of the PING rhythm. This noise input can be considered as the arguably simplest approximation to the effects of random external spike trains and as an implementation of other noise sources such as channel noise (Goldwyn and Shea-Brown, 2011).

Since the main focus of our study was on the interaction between ING and PING rhythms, we showed the characteristics of ING and PING oscillations separately only for some network parameters, such as gap-junctional coupling, synaptic coupling strength, connection heterogeneity, and time-dependent input noise. A full analysis of ING and PING responses for other network parameters, such as variability in the constant drive to I and E cells, would be outside the scope of this study. However, it is relevant to mention that ING rhythms are sensitive to variations in the constant drive to the I cells and in the number of synaptic inputs. Our exploratory simulations show that the straightforward ING rhythm disappears when the variability in constant drive becomes too large. This happens more easily

in the full than in the reduced network and provides another path of transition between ING and PING.

In our study we assumed connection probabilities between I cells and between E and I cells as reported in anatomical and neurophysiological studies (see sec. 2.2). This requires some attention, since it is important to realize that connection probabilities per se are not useful. What matters more is the number of synaptic inputs per cell (see for instance Golomb and Hansel (2000); Tiesinga et al. (2002); B"orgers and Kopell (2003)). In most computer simulations, the number of neurons in the network is much smaller than in the neurophysiological substrate. Previous studies (see e.g. Golomb and Hansel (2000); B"orgers and Kopell (2003)) have shown that a minimum number of synaptic inputs per cell is required to obtain synchronization. In particular, synchronous firing becomes unstable when the number of inputs per cell is below a threshold value, which is independent of network size. If the number of neurons in the simulated network is relatively small, the number of synaptic inputs to a cell may become small and may fall below the critical value for synchrony (which can be about 100 synaptic inputs or more, see Golomb and Hansel (2000)). To compensate for the small network, one has to increase the connectivity probabilities to unrealistically high values. Since we obtained clear ING and PING oscillations with the connection probabilities from the literature (see sec. 2.2), we did not modify the values for connectivity probability since unrealistically high values might raise new questions about the proper values that should have been used in this study.

It is a long-standing question to what extent gamma oscillations in networks with coupled excitatory and inhibitory neurons are determined by the ING or PING mechanism or by mixtures of both, e.g. during spatial visual attention (Buia and Tiesinga, 2006; Tiesinga and Sejnowski, 2009). Our results show that for highly synchronous oscillations only one mechanism, the one with the higher frequency, determines the network oscillation frequency. This is because the higher frequency mechanism recruits the vast majority of available neurons in the network, such that the other mechanism cannot exist. In sec. 2.3 we analyzed this behavior for networks with type I and type II interneurons, using both computer simulations for a network with many neurons (Figs. 2-6 and 2-7) and theoretical analyses for simple networks with two interacting neurons (Figs. 2-8 and 2-9).

While in both types of networks the dominating rhythm will be the one of ING or PING that generates the higher frequency, the results of our study also reveal a clear difference for the behavior of a network with coupled pyramidal cells and interneurons for type I and type II interneurons: For type I interneurons, the frequency of network oscillations will be slightly above the higher of the reduced-network ING and reduced-network PING oscillation frequencies, whereas for type II interneurons the frequencies of the network oscillation can be between the frequencies for reduced-network ING and reduced-network PING. Figure 2-6C, **left**, for the network with type I interneurons shows that for increasing drive to the interneurons, ING suppresses the PING-driven oscillation in the network and takes over for larger input values to the interneurons. The opposite occurs for increase of drive to the E cells (Fig. 2-6D). In both cases, the oscillation frequency smoothly increases. For a network with type II interneurons (Fig. 2-7, **B** and **C, left**) the transition is more complex with a rapid transition from PING-driven oscillations to ING-driven oscillations (green line in Fig. 2-7B, **left**) or nonmonotonous changes of frequency (Fig. 2-7C, **left**). The more rapid transition from PING to ING in networks with type II interneurons is in agreement with results presented by Börgers and Walker (2013) for the suppression transition from PING to ING with suppressed E neurons. They find that the transition tends to be both narrower and more orderly for networks with type II interneurons than when the I cells are of type I.

Our results suggest possible approaches to experimentally distinguish between ING and PING oscillations with active E cells in in vitro studies. In the first approach, the external drive to the E cells should be kept constant while the external drive  $I_{0,I}$  to I cells is varied. When the oscillations are dominated by PING, the *rate of change* in the frequency of the rhythm will increase when the external drive  $I_{0,I}$  to the I cells increases (cf. Fig. 2-6C, **left**, and Fig. 2-7B, **left**). In contrast, the rate of change of the oscillation frequency decreases with increasing  $I_{0,I}$  when the oscillations are dominated by ING. Note that the oscillation frequency itself increases in both cases with  $I_{0,I}$ , so an observation of frequency increase cannot be used to distinguish PING and ING. If the PING rhythm dominates the network dynamics and the interneurons are of type I, the frequency varies similarly with changes in  $I_{0,E}$ . In networks with type II interneurons, the nonmonotonic

dependence near the ING-PING transition may be a characteristic hallmark to detect the oscillation character: Decrease of the frequency when increasing  $I_{0,E}$  indicates ING; increase indicates PING. If the variation range of the driving current covers the transition region itself, it will be marked by a strong change in the E-cell firing frequency (cf. also Börgers and Walker (2013)). Some experimental evidence is in line with these predictions. For example, Craig and McBain (2015) reported that optogenetic silencing of pyramidal cells in CA3, where the dominant form of gamma observed in vitro is PING, led to a significant increase in the peak frequency of the oscillation, as predicted by our results (cf. the curves in Fig. 2-7C, **left**, at intermediate values of  $I_{0,E}$ ). With the newly developed step-opsins (Prakash et al., 2012), one could selectively apply currents to neurons from specific populations over longer times. Thereby results as in Fig. 2-6, **B-D**, and Fig. 2-7, **A-C**, could be obtained experimentally. This will allow a test of our simulation results and predictions in this chapter, and it may reveal how ING and PING oscillations interact.

## 2.5 Appendix

In this appendix we will give a summarized derivation of the oscillation frequency of the phase model described in sec. 2.3, with an excitatory and inhibitory neuron. The text in this appendix is an extension of the description provided in sec. 2.2: further details are given in **Chapter 3**.

Integrating Eq. 2-5 in the case of  $iPRC_{\text{sine}}$  given in Eq. 2-3 yields the transfer function for our sine neuron,

$$H_{\text{sine}}(\varphi, \varepsilon; \Theta) = \begin{cases} \frac{\Theta}{\pi} \arctan \left[ \tan \left( \frac{\pi}{\Theta} \varphi \right) e^{\frac{2\pi\varepsilon}{\Theta}} \right] & \text{for } \varphi \in \left] 0, \frac{\Theta}{2} \right[ , \\ \frac{\Theta}{\pi} \arctan \left[ \tan \left( \frac{\pi}{\Theta} \varphi \right) e^{\frac{2\pi\varepsilon}{\Theta}} \right] + \Theta & \text{for } \varphi \in \left] \frac{\Theta}{2}, \Theta \right[ , \\ \varphi & \text{for } \varphi \in \left\{ 0, \frac{\Theta}{2}, \Theta \right\}. \end{cases} \quad (2-A1)$$

Since we are interested in the relative firing of the E and I neurons, the relevant variable is the relative phase  $\Delta\varphi = \varphi_E - \varphi_I$  between the E and I neurons. We derive the transition from  $\Delta\varphi$  to the phase difference  $\Delta\tilde{\varphi}$  in the next cycle of firing. In particular, we derive an analytical expression for the firing frequency for the periodic state of the model, i.e. when  $\Delta\tilde{\varphi}$  equals  $\Delta\varphi$ . We do so for three conditions for each of the two models: 1) for the dynamics of the I neuron without input from the E neuron (i.e.  $\varepsilon_{E \rightarrow I} = 0$ ) (oscillations of the I neuron in this condition will henceforth be referred to as “pure” ING oscillations) and 2) for the dynamics of the E neuron with suprathreshold excitation of and feedback from an otherwise (nearly) silent I neuron. This condition is referred to as “pure” PING. The third condition refers to the dynamics of the full network.

The firing frequencies of the model for various conditions follow directly from the transfer functions, cf. Eq. 2-2 for the LIF neuron in sec. 2.2 and Eq. 2-A1 for the sine neuron. For pure ING, the expression for the firing frequency of the interneuron is given by

$$f_{LIF,ING}(\tau, \varepsilon_{I \rightarrow I}; \Theta_I) = \left\{ \tau + \Theta_I + \ln \left[ e^{-\tau} - \Gamma_{LIF}(\Theta_I, \varepsilon_{I \rightarrow I}) \right] \right\}^{-1}, \quad (2-A2)$$

where  $\Gamma_{LIF}$  is defined in Eq. 2-2, for the LIF-LIF model (model 1) and

$$f_{sine,ING}(\tau, \varepsilon_{I \rightarrow I}; \Theta_I) = \left\{ \tau + \Theta_I - \frac{\Theta_I}{\pi} \arctan \left[ \tan \left( \frac{\pi}{\Theta_I} \tau \right) e^{\frac{2\pi\varepsilon_{I \rightarrow I}}{\Theta_I}} \right] \right\}^{-1} \quad (2-A3)$$

for the LIF-sine model (model 2).

When we refer to the network oscillations for pure PING and for the full network, we refer to periodic firing of the E neuron. For pure PING we assume a rather “ideal” rhythm with (effectively) suprathreshold excitation of the I neuron. We note that in case of a LIF I neuron, we can have real suprathreshold excitation: When the membrane potential exceeds the threshold, the neuron is reset immediately (second line in Eq. 2-2). In case of a sine I neuron, the membrane potential can get arbitrarily near to the threshold in response to an input spike and can exceed it almost immediately after input due to external drive, such that we have effective

suprathreshold excitation. The firing frequency of the pure PING network (in particular of its E neuron) is given by

$$\left. \begin{aligned} f_{LIF,PING}(\tau, \varepsilon_{I \rightarrow E}; \Theta_E) \\ f_{sine,PING}(\tau, \varepsilon_{I \rightarrow E}; \Theta_E) \end{aligned} \right\} = \left[ 2\tau + \Theta_E - H_{LIF}(2\tau, \varepsilon_{I \rightarrow E}; \Theta_E) \right]^{-1}, \quad (2-A4)$$

$$= \left\{ 2\tau + \Theta_E + \ln \left[ e^{-2\tau} - \Gamma_{LIF}(\Theta_E, \varepsilon_{I \rightarrow E}) \right] \right\}^{-1},$$

both for the LIF-LIF model (model 1) and the LIF-sine model (model 2). In this expression  $2\tau$  corresponds to the time delay of neuronal activity of the E neuron in the loop from the E to the I neuron and from the I neuron back to the E neuron. The term  $H_{LIF}(2\tau, \varepsilon_{I \rightarrow E}; \Theta_E)$  in Eq. 2-A4 represents the transfer function of the E neuron (see Eq. 2-2) in response to the inhibition from the interneuron, which arrives at time  $2\tau$  after firing of the E neuron. The firing frequency only depends on the transfer function for the E neuron since the input to the I neuron is (practically) suprathreshold, which immediately initiates a spike in the I neuron.

In the full models, different modes of firing are possible for different parameter settings. Below we highlight those occurring for the parameter range covered by our figures.

For the LIF-LIF model, an ING rhythm occurs with frequency  $f_{LIF,Full}$  given by

$$f_{LIF,Full}(\Delta\varphi) = \left[ \tau + \Delta\varphi + \Theta_I - H_{LIF}(\tau + \Delta\varphi - \Delta\Theta, \varepsilon_{I \rightarrow E}; \Theta_E) \right]^{-1}, \quad (2-A5)$$

where  $\Delta\Theta$  is defined as  $\Theta_E - \Theta_I$ . The relevant phase difference  $\Delta\varphi$  between the E and I neurons for a periodic ING rhythm in Eq. 2-A5 is given by

$$\Delta\varphi = \ln \left\{ \frac{e^{-\tau} - e^{-H_{LIF}(\tau, \varepsilon_{I \rightarrow I}; \Theta_I) - \Delta\Theta}}{2e^{-\Delta\Theta} \Gamma(\Theta_E, \varepsilon_{I \rightarrow E})} \right. \\ \left. \pm \frac{\sqrt{\left[ e^{-H_{LIF}(\tau, \varepsilon_{I \rightarrow I}; \Theta_I) - \Delta\Theta} - e^{-\tau} \right]^2 + 4e^{-\Delta\Theta} \Gamma(\Theta_E, \varepsilon_{I \rightarrow E}) \Gamma(\Theta_I, \varepsilon_{E \rightarrow I})}}{2e^{-\Delta\Theta} \Gamma(\Theta_E, \varepsilon_{I \rightarrow E})} \right\}. \quad (2-A6)$$

The rhythm with this relative phase  $\Delta\varphi$  is found when  $\Delta\Theta - \tau \leq \Delta\varphi < \Delta\Theta$ . However, if the relative phase  $\Delta\varphi$  is such that  $\Delta\Theta \leq \Delta\varphi < \Delta\Theta + \tau$ , we get another ING rhythm with frequency  $f_{LIF,Full}$  given by also Eq. 2-A5 but the closed form of  $\Delta\varphi$  is given by

$$\Delta\varphi = \ln \left\{ \frac{\Gamma(\Theta_I, \varepsilon_{I \rightarrow I}) + e^{-\tau + \Delta\Theta} - e^{-\tau}}{2\Gamma(\Theta_E, \varepsilon_{I \rightarrow E})} \pm \frac{\sqrt{\left[ e^{-\tau} - \Gamma(\Theta_I, \varepsilon_{I \rightarrow I}) - e^{-\tau + \Delta\Theta} \right]^2 + 4\Gamma(\Theta_E, \varepsilon_{I \rightarrow E})\Gamma(\Theta_I, \varepsilon_{E \rightarrow I})e^{\Delta\Theta}}}{2\Gamma(\Theta_E, \varepsilon_{I \rightarrow E})} \right\}. \quad (2-A7)$$

Finally, for a PING rhythm where the excitatory input to the I neuron is suprathreshold, the firing frequency is described by  $f_{LIF,PING}$  (Eq. 2-A4), with  $\Delta\varphi$  given by

$$\Delta\varphi = \ln \left[ \frac{e^{-\tau} - \Gamma(\Theta_I, \varepsilon_{I \rightarrow I})}{e^{-2\tau} - \Gamma(\Theta_E, \varepsilon_{I \rightarrow E})} \right], \quad (2-A8)$$

where  $\Delta\varphi$  is in the range given by  $\Delta\Theta + \tau \leq \Delta\varphi \leq \Theta_E + \tau - H_{LIF}(\Theta_I, -\varepsilon_{E \rightarrow I}; \Theta_I)$ .

For the LIF-sine model, the firing frequency  $f_{\text{LIF-sine,Full}}$  of the occurring ING rhythm is given by

$$f_{\text{LIF-sine,Full}}(\Delta\varphi) = \left[ \tau + \Delta\varphi + \Theta_I - H_{LIF}(\tau + \Delta\varphi - \Delta\Theta, \varepsilon_{I \rightarrow E}; \Theta_E) \right]^{-1}, \quad (2-A9)$$

where  $\Delta\varphi$  is a solution of the equation

$$0 = \Delta\varphi - H_{LIF}(\tau + \Delta\varphi - \Delta\Theta, \varepsilon_{I \rightarrow E}; \Theta_E) + H_{\text{sine}} \left[ H_{\text{sine}}(\tau - \Delta\varphi + \Delta\Theta, \varepsilon_{E \rightarrow I}; \Theta_I) + \Delta\varphi - \Delta\Theta, \varepsilon_{I \rightarrow I}; \Theta_I \right], \quad (2-A10)$$

subject to the constraint  $\Delta\Theta \leq \Delta\varphi < \Delta\Theta + \tau$ . For the PING rhythm, the firing frequency of the LIF-sine model is given by



$$f_{\text{sync.Full}}(\Delta\varphi) = \left[ 2\tau + \Theta_E + \Theta_I - H_{\text{sync}}(\Theta_E - \Delta\varphi + \tau, \varepsilon_{E \rightarrow I}; \Theta_I) \right. \\ \left. - H_{\text{LIF}}(2\tau + \Theta_I - H_{\text{sync}}(\Theta_E - \Delta\varphi + \tau, \varepsilon_{E \rightarrow I}; \Theta_I), \varepsilon_{I \rightarrow E}; \Theta_E) \right]^{-1}, \quad (2-A11)$$

where  $\Delta\varphi$  is a solution of the equation

$$0 = \Delta\varphi + H_{\text{sync}}(\tau, \varepsilon_{I \rightarrow I}; \Theta_I) \\ - H_{\text{LIF}} \left[ 2\tau + \Theta_I - H_{\text{sync}}(\Theta_E - \Delta\varphi + \tau, \varepsilon_{E \rightarrow I}; \Theta_I), \varepsilon_{I \rightarrow E}; \Theta_E \right] \quad (2-A12)$$

and the phase difference  $\Delta\varphi$  must satisfy  $\Theta_E + \tau - H_{\text{sync}}(\Theta_I, -\varepsilon_{E \rightarrow I}; \Theta_I) < \Delta\varphi$  and  $2\tau - \Delta\Theta \leq H_{\text{sync}}(\Theta_E - \Delta\varphi + \tau, \varepsilon_{E \rightarrow I}; \Theta_I)$ .

# 3

## **Analyzing the competition of gamma rhythms with delayed pulse-coupled oscillators in phase representation**

Atthaphon Viriyopase

Raoul-Martin Memmesheimer

C.C.A.M. Gielen

Submitted to *Physical Review E*

### 3.1 Introduction

Many processes in biology, physics, chemistry, and engineering have an oscillatory character. Regular oscillations on a limit cycle can be described by a single variable, the phase, which characterizes the time needed to reach the current state due to free, unperturbed dynamics when starting from some specified “reset” point on the limit cycle (e.g. Winfree (1967); Izhikevich (2007)). If an oscillator receives inputs in form of pulses and an input-induced perturbation from the limit cycle relaxes back sufficiently quickly (i.e. before the next input arrives), the system's dynamics can be characterized by the phase together with a function telling how the phase changes in response to an input pulse: the phase response curve (PRC) or the phase transition curve/transfer function (Mirollo and Strogatz, 1990; Izhikevich, 2007; Smeal et al., 2010). This phase representation has been widely used to investigate network dynamics, synchronization and locking phenomena in areas of science as diverse as neural circuits (Goel and Ermentrout, 2002; Memmesheimer and Timme, 2006b; Jahnke et al., 2008; Viriyopase et al., 2012), technical networks (Nishimura and Friedman, 2011; Brandner et al., 2016) and insect behavior (Mirollo and Strogatz, 1990; Forrest et al., 1998).

A particularly simple type of oscillators are hybrid dynamical systems whose state variable follows some one-dimensional, possibly nonlinear continuous dynamics, periodically reaches a threshold and is then reset (Goebel et al., 2012). A rich source of such oscillators is the reduction of spiking neurons to integrate-and-fire type neuron models (Lapicque, 1907; Abbott and Kepler, 1990; Kistler et al., 1997): Biological neurons possess a complicated branched structure with protrusions of different function and many slow and fast degrees of freedom associated to the resulting compartments. In integrate-and-fire type neuron models, this spatial structure is reduced to a single compartment “point neuron” and the high-dimensional dynamics are reduced to one degree of freedom, interpreted as the membrane potential (Dayan and Abbott, 2001; Izhikevich, 2007). Integrate-and-fire-type neurons interact with pulses, mimicking spikes/action potentials; these are sent when the neuron is reset and are received by postsynaptic neurons often after some delay. In this chapter, we consider networks of two integrate-and-fire type neurons in phase representation to investigate the competition between mechanisms that are widely assumed to underlie oscillations in biological neural networks. Each

integrate-and-fire type neuron thereby represents a synchronized population of neurons.

Oscillations in biological neural networks may be important for information processing (Buzsáki, 2006; Thut et al., 2012). One hypothesis is that they may coordinate precise spike sending of neurons and in particular lead to synchronous spiking of neural populations (Buzsáki and Chrobak, 1995). Indeed, experiments have found examples of highly synchronous spiking associated with strong oscillations (Buzsáki et al., 1992), and the timing of individual spikes relative to a global oscillation's phase can carry important information (O'Keefe and Recce, 1993; Buzsáki and Chrobak, 1995; Arabzadeh et al., 2006; Wang et al., 2007; Luczak et al., 2015). Receiving neurons, in turn, can be highly sensitive to coincident input, in particular types of synaptic plasticity depend on the timing of spikes (Caporale and Dan, 2008). Under high-input conditions the spike-generating mechanism can adaptively enhance the sensitivity to synchronous input, while simultaneously decreasing the sensitivity to temporally uncorrelated inputs (Azouz and Gray, 2003). Furthermore, oscillatory modulation of the membrane potential, for example by input from a synchronously firing population of neurons, can provide a precise temporal window for the integration of synaptic inputs, favoring inputs arriving precisely at certain times (Volgushev et al., 1998; Jacobs et al., 2007). The “communication through coherence” hypothesis suggests that this promotes information transmission between coherently oscillating neuron populations in different brain areas and allows to focus on attended stimuli (Fries, 2005; Womelsdorf et al., 2007; Bastos et al., 2015; Fries, 2015). Higher frequency oscillations may support propagation and selection of information within areas (Jahnke et al., 2014a, b). Oscillation coordinated synchronous spiking across different neuron populations may also allow to bind different features of a stimulus into a coherent percept (Eckhorn, 1994; Singer and Gray, 1995; Singer, 1999; Tallon-Baudry and Bertrand, 1999; Palva et al., 2005) and generally parse and separate information into chunks of different length (Lisman and Idiart, 1995; Giraud and Poeppel, 2012; Luczak et al., 2015).

In the current chapter, we will focus on gamma (30 - 80 Hz) oscillations. These are prominent oscillations, which have been linked to input selectivity (Fries, 2005; Börgers and Kopell, 2008), spike-phase encoding (Buzsáki and Chrobak,

1995; Hopfield, 1995), feature binding (Singer, 1999), as well as to storage and retrieval of information (Lisman and Idiart, 1995; Giraud and Poeppel, 2012). Mainly two mechanisms have been proposed to underlie gamma oscillations (Colgin and Moser, 2010; Whittington et al., 2011; Buzsáki and Wang, 2012). Both involve populations of excitatory pyramidal cells (E cells) and inhibitory interneurons (I cells). Tonic excitation of the interneurons, e.g. due to averaging slow excitatory input, can give rise to interneuron network gamma (“ING”) (Lytton and Sejnowski, 1991; Cobb et al., 1995; Whittington et al., 1995; Traub et al., 1996a; Whittington et al., 2000b; Bartos et al., 2007): Imagine, by chance at some point more I cells spike and send the inhibition to the other I cells. This hinders the latter to spike before the spiking neurons have recovered, and recruits them into synchrony such that a rhythm emerges (Kopell and Ermentrout, 2004). The I cells undergo a cycle of enhanced spiking activity, resulting recurrent inhibition within the population and decreased network activity, subsequent recovery from inhibition and enhanced spiking. The resulting periodically increased inhibition generates rhythmic spiking in connected E cells. Pyramidal-interneuron network gamma (“PING”) is mediated by interacting populations of E cells and I cells (Whittington et al., 2000b; Tiesinga et al., 2001; Börgers and Kopell, 2003). Imagine, by chance at some point more E cells spike. The I cells respond to the increased excitatory input from the E cells by increased spiking. The resulting increased inhibitory input in turn hinders spiking in the E cells, such that their activity goes down. The lack of excitatory input leads to a decrease of I cell activity, such that the E cells can recover from inhibition and generate increased spiking, which completes the cycle. In model networks, there can be a sharp boundary in parameter space between the regime in which the I cells have weakly enough drive for PING, and the ING-regime in which the drive to the I cells is so large that they fire without being prompted by the E cells (Börgers and Kopell, 2005). However, recent studies have shown that this sharp transition may be a simplification (Börgers and Walker, 2013) and that there is a range in parameter space where ING and PING can co-exist (see **Chapter 2**.)

Using computer simulations, **Chapter 2** has shown that in the range of parameter space where ING and PING may in principle be expected to exist, both mechanisms compete such that the mechanism generating the higher oscillation frequency “wins”, i.e. the mechanism with the higher frequency determines the

frequency of the network oscillation and suppresses the other one. In the current chapter, we provide a theoretical analysis of the finding, using simplified networks of two oscillating integrate-and-fire type neurons. The simplified system allows to analytically study the interactions between ING and PING and to better understand their consequences for oscillations in networks of interacting E cells and I cells. The analytically tractable model consists of an E neuron, which belongs to the category of type I neurons, and an I neuron, which can be either type I or type II; for type I neurons an excitatory input always advances the next spike, the PRC is entirely positive. In contrast, an excitatory input arriving at a type II neuron can also delay the next spike, the PRC is partially negative (Hansel et al., 1995; Izhikevich, 2007). Indeed, there is experimental evidence that I cells involved in gamma oscillations may belong to the category of type II neurons (Erisir et al., 1999; Tateno et al., 2004; Tateno and Robinson, 2007).

We consider current-based integrate-and-fire neurons, where the currents have infinitesimally short temporal duration. The latter implies that the membrane potential responds in jump-like manner to the input, the former that the height of the jump is independent of the membrane potential. Note that also some conductance-based and more general models can be cast into this form by a transformation of variables (van Vreeswijk, 1996; Timme et al., 2003). For type I neurons, where an excitatory jump (towards the membrane potential threshold) always advances the phase, a phase representation has been derived in Mirollo and Strogatz (1990) as well as Memmesheimer and Timme (2006a). We adopt this phase representation for our type I neurons since the linearization of the free dynamics strongly simplifies the analytical study of the system and since the phase representation allows for simple and fast event based numerical simulations. To be able to study networks with type II interneurons likewise, we derive a generalized phase representation, which is applicable to neurons of this type. For this, we assume that an infinitesimal phase response curve (iPRC) of type II is given, and we derive the corresponding membrane potential dynamics as well as the PRC.

This chapter is structured as follows: Part two is dedicated to the standard phase representation of a one-dimensional oscillator, its derivation from the free dynamics and its application to the leaky integrate-and-fire (LIF) neuron, the type I neuron model that we use in the article. In part three, we derive the phase

representation of one-dimensional oscillators of type II, where the iPRC can change sign. We apply the scheme to derive the “sine-neuron”, the type II neuron model that we use throughout the article. Appendix 3.8.1 compares this neuron with the radial isochron clock, an oscillator model that has the same iPRC. In part four and Appendix 3.8.2, we consider delayed pulse-coupled networks of two model neurons and show the ways in which they interact depending on their phase difference. This yields a representation of the dynamics in terms of iterative maps whose fixed points yield the regular oscillations that we study in part five. Part six is dedicated to the competition and coexistence of the ING and PING oscillation mechanisms. We conclude with a discussion in part seven, which puts our findings in context to the existing literature and our previous larger scale simulation studies in **Chapter 2**.

## 3.2 Phase representation of type I one-dimensional oscillators

### 3.2.1 General theory

In the following, we review the standard phase representation of one-dimensional oscillators coupled by infinitesimally short pulsed interactions proposed in Mirollo and Strogatz (1990) as well as Memmesheimer and Timme (2006b), as needed for the purposes of the present article. For a more general derivation and discussion, see Memmesheimer and Timme (2006a).

A one-dimensional neural oscillator is generally characterized by a voltage-like state variable  $V$ . We assume that without arrival of fast inputs,  $V$  is strictly increasing up to a spike threshold  $\Theta_V > 0$ . When reaching the threshold at a time  $t$ ,  $V(t) = \Theta_V$ ,  $V$  is reset to zero, i.e.  $V(t^+) = 0$ , and starts increasing again. These free dynamics have period  $T$ . We note that when the dynamics  $V(t)$  are specified by an autonomous differential equation (the function specifying the rate of change of  $V$  does not depend on time) with unique solutions, trajectories cannot cross or overlap, and furthermore the oscillatory behavior forbids fixed points. This implies strict monotonicity of  $V$  except where  $V$  is being reset.

We now introduce a so-called phase variable  $\varphi(t)$ , which increases with slope one in absence of fast input,

$$\frac{d\varphi(t)}{dt} = 1, \quad (3-1)$$

and has a phase threshold  $\Theta$ . When reaching threshold at a time  $t$ ,  $\varphi(t) = \Theta$ , the phase is reset to zero,  $\varphi(t^+) = 0$ . Note that Eq. 3-1 implies that the free period of the phase is  $\Theta$ . Since we want to map  $\varphi(t)$  to  $V(t)$ , we choose the free periods identically,  $\Theta = T$ . The strict monotonicity of  $V(t)$  then implies that there is a strictly monotonic, bijective so-called rise function  $U$ , mapping phase  $\varphi$  to voltage  $V$ , i.e. at time  $t$

$$V(t) = U(\varphi(t)). \quad (3-2)$$

In particular,  $\Theta_V$  and  $\Theta$  are related by

$$\Theta_V = U(\Theta). \quad (3-3)$$

For the LIF neuron, the type I neuron we use in our study,  $U : ]-\infty, \Theta] \rightarrow ]-\infty, \Theta_V]$  (depending on the neuron model domain and codomain are different).  $U$  can be derived directly from free membrane potential dynamics: Consider free voltage dynamics  $\tilde{V}$  that start at the reset potential at  $t=0$ , i.e.  $\tilde{V}(0) = 0$ .  $\tilde{V}$  can be continued for negative times towards  $-\infty$  (or a possible lower bound) and for positive times to  $\Theta_V$ . The analogous dynamics of  $\varphi$  run from  $-\infty$  (or a possible lower bound) to  $\Theta = T$  with  $\varphi(0) = 0$ . We can then define  $U(\varphi) := \tilde{V}(\varphi)$ , since time equals phase for the considered piece of dynamics.

When  $\varphi$  reaches the phase threshold, it is reset and a spike is emitted. After a delay time  $\tau$ , the spike arrives at post-synaptic neurons at, say, time  $t_a$ . We assume that they respond with an instantaneous jump in their membrane potential. The strength  $\varepsilon$  of the coupling from the pre- to the postsynaptic neuron specifies the



height of the jump. The corresponding phase jump is computed using a transfer function  $H$ ,

$$\varphi(t_a^+) = H(\varphi(t_a), \varepsilon). \quad (3-4)$$

For convenience, we will omit  $t_a$  and use  $\varphi$  instead of  $\varphi(t_a)$ . If an input of strength  $\varepsilon$  is subthreshold, i.e.  $U(\varphi) + \varepsilon < \Theta_V$ , the transfer function is given by

$$H(\varphi, \varepsilon) = U^{-1}(U(\varphi) + \varepsilon). \quad (3-5)$$

We may understand this formula as follows: We take  $\varphi$  and change to the membrane potential domain using  $U$  given in Eq. 3-2. Here we know the impact of an input of strength  $\varepsilon$ , it additively changes the membrane potential  $U(\varphi)$  by  $\varepsilon$ . We compute the corresponding phase, i.e. the phase after the input, using  $U^{-1}$ . The composition of the steps,  $U^{-1}(U(\varphi) + \varepsilon)$ , maps the phase before the interaction to the phase after the interaction. We note that  $H(\varphi, \varepsilon)$  is strictly monotonically increasing, both as a function of  $\varepsilon$  and of  $\varphi$ , since  $U$  and thus  $U^{-1}$  are strictly monotonically increasing. Since suprathreshold input leads to immediate spiking and reset of the neuron, we need to extend the definition of the transfer function to

$$H(\varphi, \varepsilon) = \begin{cases} U^{-1}(U(\varphi) + \varepsilon) & \text{for } U(\varphi) + \varepsilon < \Theta_V, \\ 0 & \text{for } U(\varphi) + \varepsilon \geq \Theta_V. \end{cases} \quad (3-6)$$

$$(3-7)$$

$H(\varphi, \varepsilon)$  yields the new phase of a neuron when it receives an input  $\varepsilon$  at phase  $\varphi$  (cf. Eq. 3-4). It is thus closely related to the phase response curve  $PRC(\varphi, \varepsilon)$  (e.g. Smeal et al. (2010)) which yields the phase change induced by an input  $\varepsilon$  received at phase  $\varphi$ ,

$$PRC(\varphi, \varepsilon) = H(\varphi, \varepsilon) - \varphi. \quad (3-8)$$

The infinitesimal phase response curve  $iPRC(\varphi)$  characterizes the phase shift of a neuron around  $\varepsilon = 0$ , i.e. an infinitesimal input  $d\varepsilon$  generates an infinitesimal phase shift

$$d\varphi = iPRC(\varphi)d\varepsilon. \quad (3-9)$$

This is, for small  $\varepsilon$  around 0 we have  $\varepsilon \equiv d\varepsilon$  and  $PRC(\varphi, \varepsilon) \approx d\varphi = iPRC(\varphi)\varepsilon$ ;  $H(\varphi, \varepsilon) \approx \varphi + iPRC(\varphi)\varepsilon$ .  $iPRC(\varphi)$  and  $H(\varphi, \varepsilon)$  are thus related by

$$iPRC(\varphi) = \left. \frac{\partial H(\varphi, \varepsilon)}{\partial \varepsilon} \right|_{\varepsilon=0}. \quad (3-10)$$

As mentioned above,  $U^{-1}$  is strictly increasing in  $\varepsilon$ . Equations 3-6 and 3-8 then imply that so are  $H$  and  $PRC$ . Because  $PRC(\varphi, 0)$  equals 0,  $PRC(\varphi, \varepsilon) > 0$  for  $\varepsilon > 0$ : In other words, the PRC has to be of type I, the formalism is thus applicable to type I neurons only.

### 3.2.2 The LIF neuron in phase representation

We now derive the phase representation for the type I neuron model employed in our study, the LIF neuron (Lapicque, 1907), using the methods described in sec. 3.2.1 (cf. also Memmesheimer and Timme (2006a)). The dynamics of the membrane potential  $V_{LIF}(t)$  of the LIF neuron are given by

$$\frac{dV_{LIF}(t)}{dt} = -\gamma V_{LIF}(t) + I, \quad (3-11)$$

where  $\gamma$  represents the inverse of the membrane time constant and where  $I$  captures the external driving current. When the membrane potential reaches its threshold  $\Theta_V$ , the neuron spikes and the membrane potential is reset to zero. A spike arriving at time  $t$  at a synaptic connection with strength  $\varepsilon$  induces an instantaneous change in the membrane potential, i.e.  $V_{LIF}(t^+) = V_{LIF}(t) + \varepsilon$ . We assume that slow external inputs add up to a constant current, which drives the neurons continuously over the threshold, such that in absence of fast synaptic input the neurons oscillate. This

allows us to define the phase  $-\infty < \varphi \leq \Theta$ , which increases with slope 1 and is reset to zero when it reaches  $\Theta$ , where also a spike is emitted.

The rise function  $U$  linking the phase  $\varphi$  of the spiking cycle to the membrane potential description  $V$  can be determined as described in sec. 3.2.1 as

$$V_{LIF} = U_{LIF}(\varphi) = \frac{I}{\gamma} (1 - e^{-\gamma\varphi}), \quad (3-12)$$

(Mirolo and Strogatz, 1990; Memmesheimer and Timme, 2006a), yielding the inverse

$$U_{LIF}^{-1}(V_{LIF}) = \frac{1}{\gamma} \ln \left( \frac{I}{I - \gamma V_{LIF}} \right). \quad (3-13)$$

$U_{LIF}$  is a monotonically increasing function of  $\varphi$ . Figure 3-1, **B** and **C**, shows the rise function  $U_{LIF}$  and its inverse  $U_{LIF}^{-1}$ , respectively. The phase threshold is explicitly given in terms of the voltage threshold  $\Theta_V$  by

$$\Theta = U_{LIF}^{-1}(\Theta_V) = \frac{1}{\gamma} \ln \left( \frac{I}{I - \gamma \Theta_V} \right). \quad (3-14)$$

$U_{LIF}$  and  $U_{LIF}^{-1}$  yield the transfer function of the LIF neuron

$$H_{LIF}(\varphi, \varepsilon; \Theta_V) = \begin{cases} -\frac{1}{\gamma} \ln \left( e^{-\gamma\varphi} - \frac{\gamma\varepsilon}{I} \right) & \text{for } U_{LIF}(\varphi) + \varepsilon < \Theta_V, \\ 0 & \text{for } U_{LIF}(\varphi) + \varepsilon \geq \Theta_V, \end{cases} \quad (3-15)$$

$$(3-16)$$

cf. Eqs. 3-6 and 3-7. It is displayed in Fig. 3-2, **B** and **C**.

Note that the phase  $\varphi$  can assume all values within  $]-\infty, \Theta]$ , where negative phases correspond to the phase after inhibitory input, which causes hyperpolarization of the membrane potential. Since we use the convention that the phase  $\varphi$  is reset to zero when it reaches the threshold  $\Theta$ , at the time of spiking  $\varphi = \Theta$  rather than  $\varphi = 0$ . Since  $\gamma > 0$ , we can set  $\gamma = 1$  and  $\Theta_V = 1$  after appropriate scaling of time and

voltage, without loss of generality for a single neuron. For simplicity, we assume that in networks with two type I neurons the membrane time constants are the same,

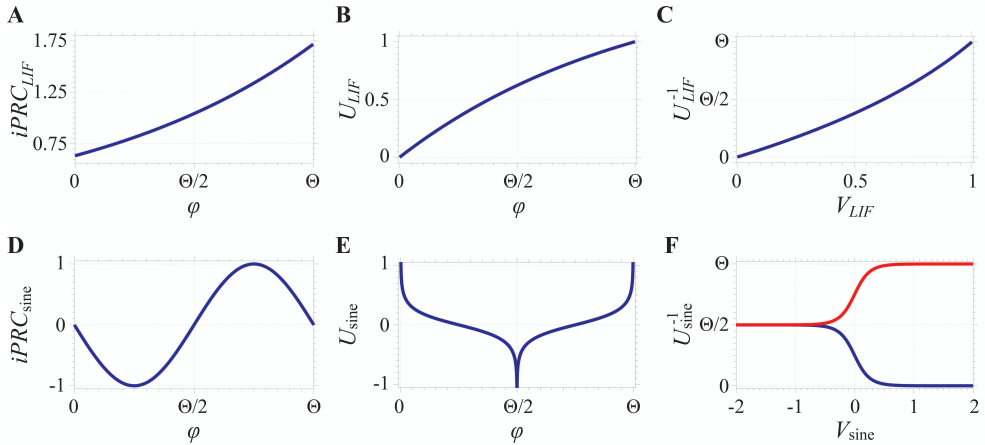


**Figure 3-1. Infinitesimal phase response curves ( $iPRC$ ), rise functions ( $U$ ), and inverse rise functions ( $U^{-1}$ ) for the type I leaky integrate-and-fire neuron and the type II sine neuron.** Upper panels show (A) the  $iPRC$ , (B) the rise function, and (C) the inverse rise function for the leaky integrate-and-fire neuron. Corresponding data are shown in the lower panels (D, E, and F, respectively) for the sine neuron (type II) with the two branches of the inverse rise function (blue:  $k = 1$ , red:  $k = 2$ ). Parameter setting:  $\gamma = 1$ ,  $\Theta_V = 1$ , and  $\Theta = 1$ .

such that the scaling is possible. The driving current  $I$  to the neuron, which gives  $U_{LIF}(\Theta) = 1$ , follows in a straightforward way from Eq. 3-12,

$$I = \frac{1}{1 - e^{-\Theta}}. \quad (3-17)$$

The rise function Eq. 3-12 and its inverse Eq. 3-13 are then given by

$$U_{LIF}(\varphi) = \frac{1 - e^{-\varphi}}{1 - e^{-\Theta}}, \quad (3-18)$$

$$U_{LIF}^{-1}(V_{LIF}) = -\ln\left[1 - (1 - e^{-\Theta})V_{LIF}\right]. \quad (3-19)$$

Equations 3-15 and 3-16 yield the transfer function

$$H_{LIF}(\varphi, \varepsilon; \Theta) = \begin{cases} -\ln[e^{-\varphi} - (1 - e^{-\Theta})\varepsilon] & \text{for } U_{LIF}(\varphi) + \varepsilon < 1, \\ 0 & \text{for } U_{LIF}(\varphi) + \varepsilon \geq 1, \end{cases} \quad (3-20)$$

$$(3-21)$$

and, according to Eq. 3-10, the iPRC is given by

$$iPRC_{LIF}(\varphi; \Theta) = (1 - e^{-\Theta})e^{\varphi}, \quad (3-22)$$

which is shown in Fig. 3-1A.

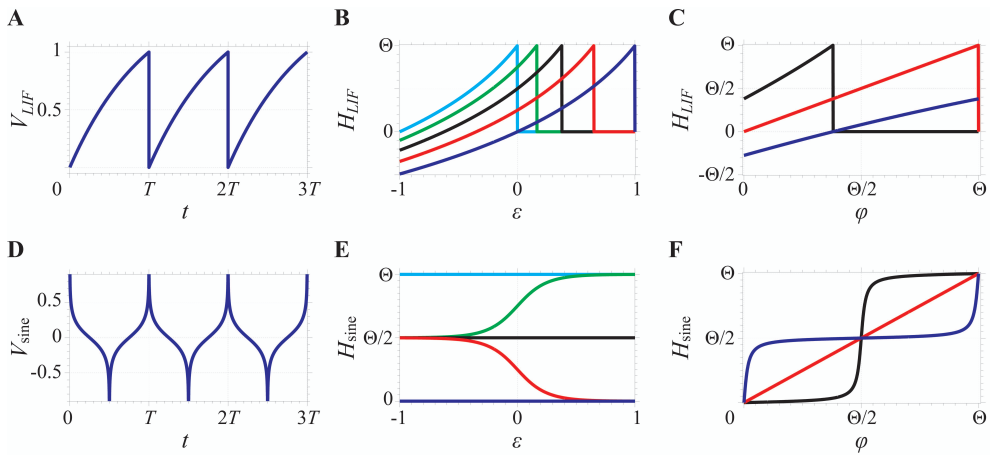


**Figure 3-2. Free dynamics ( $V$ ) and transfer functions ( $H$ ) for the type I leaky integrate-and-fire neuron and the type II sine neuron.** Upper panels show (A) the free membrane potential dynamics, (B) the transfer function as a function of the coupling strength  $\varepsilon$  for different constant values of the phase  $\varphi$  at input arrival (blue, red, black, green, cyan:  $\varphi = 0, 0.25, 0.5, 0.75$ , and  $1$ ), and (C) the transfer function as a function of  $\varphi$  for different constant  $\varepsilon$  (blue, red, and black:  $\varepsilon = -0.5, 0$ , and  $0.5$ ) for the type I LIF neuron. Lower panels (D-F) show the corresponding plots for the sine neuron (type II). Parameter setting:  $\gamma = 1$ ,  $\Theta_\nu = 1$ , and  $\Theta = 1$ .

### 3.3 Phase representation of type II one-dimensional oscillators

#### 3.3.1 General theory

The phase representation sec. 3.2 is only valid for one-dimensional neurons of type I, such as the LIF neuron. In the following we generalize it to neurons of type II, whose iPRC has negative and positive parts. We assume that our type II neuron is a current-based one-dimensional oscillator, which receives current inputs of infinitesimally small temporal extent. These generate jump-like responses in the membrane potential, the height of the jump is independent of the voltage. We further assume that the membrane dynamics are at first unknown, and the neuron dynamics are instead specified by an infinitesimal phase response curve, which specifies the phase response to input pulses of infinitesimally small strength. We then derive the free membrane dynamics as well as the full phase representation. They turn out to follow nearly uniquely from the iPRC for the considered class of oscillator models.

The domain of the iPRC can be divided into several intervals, in which the iPRC has the same sign, positive or negative. As an example, for a type I iPRC that is everywhere larger than zero, we have only one interval  $]-\infty, \Theta[$ , cf. the LIF neuron sec. 3.2.2. For a sine-like type II iPRC, cf. sec. 3.3.2 below, there are two subintervals  $]0, \Theta/2[$ ,  $]\Theta/2, \Theta[$  and the iPRC becomes zero at the ends of the intervals. We aim to construct rise functions for each subinterval and combine them to obtain the transfer function  $H$ .

Restricted to a single interval  $i$ , the iPRC is either completely positive or negative. A strictly increasing free voltage implies a positive iPRC: a small upward jump in the voltage maps the current state to a state, which would be reached in the future by free evolution, cf. sec. 3.2. A strictly decreasing free voltage implies a negative iPRC, as an upward jump in the voltage maps the current state to an earlier state. In turn, a positive/negative iPRC implies monotonically increasing/decreasing free voltage dynamics. We note that this implies that a differential equation specifying  $V$  must switch between intervals with different signs of the iPRC (cf. sec. 3.3.2 below). In interval  $i$  we can define a monotonically increasing/decreasing

transfer function  $U_i$ , which maps phase to voltage, cf. Eq. 3-2. For given  $\varphi$ , there are sufficiently small inputs  $\varepsilon$  such that the voltage and phase stay within the interval even if  $i$  is the interval neighboring the threshold. Then, the transfer function is given by Eq. 3-5 and

$$\frac{\partial H_i(\varphi, \varepsilon)}{\partial \varepsilon} = \frac{1}{U_i'(U_i^{-1}(U_i(\varphi) + \varepsilon))}. \quad (3-23)$$

By setting  $\varepsilon$  to 0 (see Eq. 3-10), we obtain for all  $\varphi$  in the interval the slope of  $U_i(\varphi)$

$$iPRC(\varphi) = \left. \frac{\partial H_i(\varphi, \varepsilon)}{\partial \varepsilon} \right|_{\varepsilon=0} = \frac{1}{U_i'(U_i^{-1}(U_i(\varphi)))} = \frac{1}{U_i'(\varphi)}. \quad (3-24)$$

Its slope specifies  $U_i(\varphi)$  up to a constant,  $U_i(\varphi)$  is basically the antiderivative  $F_i(\varphi)$  of  $1/iPRC(\varphi)$  in interval  $i$ ,

$$F_i(\varphi) = \int \frac{1}{iPRC(\varphi)} d\varphi. \quad (3-25)$$

We obtain  $U_i(\varphi)$  from  $F_i(\varphi)$  by specifying the voltage at some phase. When approaching an interval boundary where the iPRC has a zero,  $U_i(\varphi)$  and thus the voltage will usually tend to  $\pm\infty$ , which we then take as the value assumed by the rise function there. We note that the voltage can tend to  $+\infty$  even if the phase is not in the interval neighboring the threshold. Then the phase does not reach the phase threshold and the neuron does not spike. Models with this property may be interpreted as having a history dependent voltage spike threshold. We note that our formalism allows to construct oscillator models from the iPRC for which  $U_i(\varphi)$  does not have a reasonable biological interpretation in terms of a voltage. As an example, an iPRC that is negative in the interval adjacent to the phase threshold can give rise to a  $U_i(\varphi)$  that reaches  $-\infty$  as the phase approaches the phase threshold and the neuron spikes.

If  $\varepsilon$  does not lead the dynamics out of interval  $i$ , the transfer function is given by

$$H_i(\varphi, \varepsilon) = U_i^{-1}(U_i(\varphi) + \varepsilon). \quad (3-26)$$

It is uniquely determined by the iPRC, since adding a constant to  $U_i$ , i.e. using  $U_{i,c_i}(\varphi) = U_i(\varphi) + c_i$  to define  $H_i$ , does not change it,

$$H_i(\varphi, \varepsilon) = U_{i,c_i}^{-1}(U_{i,c_i}(\varphi) + \varepsilon) = U_i^{-1}(U_i(\varphi) + c_i + \varepsilon - c_i) = U_i^{-1}(U_i(\varphi) + \varepsilon). \quad (3-27)$$

We can derive the rise function also in more intuitive manner as follows: An input to our neuron models should have the same effect whether we apply it at once or in small pieces, which we may imagine to be separated by small temporal differences. Indeed, in the membrane potential representation, the input is simply additive, so this is certainly satisfied. In phase representation, it should be satisfied as well. An input  $d\tilde{\varepsilon}$  arriving at phase  $\varphi$  leads in linear approximation to a new phase  $\varphi^+ = \varphi + iPRC(\varphi)d\tilde{\varepsilon}$ . If the change due to an input piece  $d\tilde{\varepsilon}$  does not depend on the total input  $\varepsilon$ , we should get the same change, if the previous phase has been reached due to a previous piece  $\tilde{\varepsilon}$  of an input. Denoting the phase before the arrival of  $d\tilde{\varepsilon}$  by  $\varphi(\tilde{\varepsilon})$ , we find that the input  $\tilde{\varepsilon} + d\tilde{\varepsilon}$  leads to the phase  $\varphi(\tilde{\varepsilon} + d\tilde{\varepsilon}) = \varphi(\tilde{\varepsilon}) + iPRC(\varphi(\tilde{\varepsilon}))d\tilde{\varepsilon}$ . Note that  $\varphi(\tilde{\varepsilon})$  is the exact non-approximated phase after receiving  $\tilde{\varepsilon}$ , while the impact of  $d\tilde{\varepsilon}$  is covered up to first order. Knowing the impact of an additional input  $d\tilde{\varepsilon}$  up to first order (equivalently the impact of an infinitesimal input) allows to write the phase change in form of a differential equation,

$$\frac{d\varphi(\tilde{\varepsilon})}{d\tilde{\varepsilon}} = iPRC(\varphi(\tilde{\varepsilon})). \quad (3-28)$$

Since the impact of an input piece does not explicitly depend on the previously received input, the right-hand side does not explicitly depend on the independent variable  $\tilde{\varepsilon}$ , but only via  $\varphi(\tilde{\varepsilon})$ . In other words, the phase change  $\varphi(\tilde{\varepsilon})$  is characterized by an autonomous ordinary differential equation. In Appendix 3.8.1,



we highlight that general phase oscillators do not have this property, using the radial isochron clock. Note that Eq. 3-28 can also be derived by discretizing the time-like variable  $\varepsilon$  into many small steps of size  $d\tilde{\varepsilon}$ , expanding the PRC around zero coupling strength by its Taylor series, and taking the limit of  $d\tilde{\varepsilon} \rightarrow 0$ .

Solving Eq. 3-28 by separation of variables, we obtain

$$\int_{\varphi}^{\varphi^+} \frac{1}{iPRC(\varphi)} d\varphi = \int_0^{\varepsilon} d\tilde{\varepsilon} = \varepsilon, \quad (3-29)$$

where  $\varphi^+$  and  $\varphi$  are the phases before and after arrival of the total subthreshold input  $\varepsilon$ . By the first fundamental theorem of calculus, we have  $F_i(\varphi^+) - F_i(\varphi) = \varepsilon$ , where again  $F_i(\varphi) = \int 1/iPRC(\varphi) d\varphi$ . Since on the other hand

$$U_i(\varphi^+) - U_i(\varphi) = \varepsilon, \quad (3-30)$$

$F_i$  equals  $U_i$  up to an additive constant, and  $U_i$  is basically the antiderivative of  $1/iPRC(\varphi)$  in the interval  $i$ .

Equation 3-28 and its property of being autonomous can also be directly derived from the fact that  $dV_i$  (the change of the voltage due to  $d\tilde{\varepsilon}$ ) does not explicitly (not even implicitly) depend on already applied subthreshold input: While receiving an input,  $V_i$  may be seen as a function  $V_i(\tilde{\varepsilon})$  of the already applied piece of input  $\tilde{\varepsilon}$ , with initial value  $V_i(0) = V_i$  and  $\tilde{\varepsilon}$  running from 0 to  $\varepsilon$ .  $V_i(\tilde{\varepsilon})$  then satisfies the autonomous differential equation  $dV_i(\tilde{\varepsilon})/d\tilde{\varepsilon} = 1$ . This implies  $dU_i(\varphi(\tilde{\varepsilon}))/d\tilde{\varepsilon} = 1$  and, after application of the chain rule, the differential equation  $d\varphi(\tilde{\varepsilon})/d\tilde{\varepsilon} = 1/U_i'(\varphi(\tilde{\varepsilon}))$ . Since for  $\tilde{\varepsilon} = 0$  the left-hand side equals  $iPRC(\varphi)$  and the differential equation is autonomous, we have  $1/U_i'(\varphi) = iPRC(\varphi)$  for all phases. This implies that  $\varphi(\tilde{\varepsilon})$  satisfies Eq. 3-28 and it implies Eq. 3-30.

Equation 3-28 also allows to directly derive the transfer function and thus the complete phase representation from the iPRC. We note that  $\varphi(\tilde{\varepsilon}) = H_i(\varphi, \tilde{\varepsilon})$  and rewrite Eq. 3-28 as

$$\frac{\partial H_i(\varphi, \tilde{\varepsilon})}{\partial \tilde{\varepsilon}} = iPRC(H_i(\varphi, \tilde{\varepsilon})), \quad (3-31)$$

which reduces to Eq. 3-10 for  $\tilde{\varepsilon} = 0$ . Solving the differential equation yields the transfer function in interval  $i$ .

Phases  $\varphi$  where the iPRC is zero are fixed points of the dynamics Eqs. 3-28 and 3-31. Thus, under weak conditions on Eq. 3-28 (the iPRC is globally Lipschitz continuous such that the differential equation has a unique solution existing for all  $\varepsilon$ ), such a  $\varphi$  will not be changed by input,  $H_i(\varphi, \varepsilon) = \varphi = \text{const}$ ; furthermore, no finite input will lead beyond the borders of an interval  $i$  where the iPRC gets zero.

### 3.3.2 The sine neuron in phase representation

Typical type II neurons show a phase delay in response to excitatory input  $\varepsilon > 0$  arriving at small phases (early in the spiking cycle, shortly after a spike) and a phase advance when such input arrives at larger phases (Smeal et al., 2010; Börgers and Walker, 2013). With these characteristics in mind, we define our type II neurons as “sine-neurons” by an iPRC

$$iPRC_{\text{sine}}(\varphi) = -\sin\left(\frac{2\pi}{\Theta}\varphi\right), \quad (3-32)$$

where  $\varphi \in [0, \Theta]$  (see Fig. 3-1D) and  $\Theta \equiv T$  is the period and the phase threshold of the neuron. We use the sinusoidal function as iPRC of our type II neurons also because neuron models such as the Hodgkin-Huxley neuron can undergo Hopf bifurcations (Hodgkin and Huxley, 1952; Ermentrout, 1996). The normal form oscillator of Hopf bifurcating systems and thus general Hopf bifurcating systems with appropriate parameters have near the bifurcation for suitable inputs a sinusoidal iPRC Eq. 3-32 (Brown et al., 2004). To facilitate the analytical study of two-neuron networks that include type II neurons, we want to apply the phase oscillator

formalism to the sine neuron. Since the *iPRC* changes sign, we use the methodology derived in sec. 3.3.

We split the interval domain  $[0, \Theta]$  of  $iPRC_{\text{sine}}$  into two, i.e.  $]0, \Theta/2[$  and  $]\Theta/2, \Theta[$ , and treat  $U_{\text{sine}}(\varphi)$  at  $\varphi \in \{0, \Theta/2, \Theta\}$  separately. Using Eqs. 3-25 and 3-32, the rise functions for the first subinterval ( $U_{\text{sine},1}(\varphi), \varphi \in ]0, \Theta/2[$ ) and for the second subinterval ( $U_{\text{sine},2}(\varphi), \varphi \in ]\Theta/2, \Theta[$ ) are  $U_{\text{sine},k}(\varphi) = -\Theta \ln \left[ \left| \tan\left(\frac{\pi\varphi}{\Theta}\right) \right| \right] / 2\pi + c_k$ , where  $c_k \in \mathbb{R}$  and  $k \in \{1, 2\}$ . From the first subinterval, we compute the value of the rise function at  $\varphi = 0$  and  $\varphi = \Theta/2$ ,  $U_{\text{sine}}(0) = \lim_{\varphi \rightarrow 0^+} U_{\text{sine},1}(\varphi) = \infty$ ,  $U_{\text{sine}}(\Theta/2) = \lim_{\varphi \rightarrow \Theta^-/2} U_{\text{sine},1}(\varphi) = -\infty$ . Compatibly,  $\lim_{\varphi \rightarrow \Theta^+/2} U_{\text{sine},2}(\varphi) = -\infty$ . Finally, at  $\varphi = \Theta$ ,  $U_{\text{sine}}(\Theta) = \lim_{\varphi \rightarrow \Theta^-} U_{\text{sine},2}(\varphi) = \infty$ . In summary, the rise function of the sine neuron is given by

$$U_{\text{sine}}(\varphi) = \begin{cases} \infty & \text{for } \varphi \in \{0, \Theta\}, \\ -\infty & \text{for } \varphi = \Theta/2, \\ -\frac{\Theta}{2\pi} \ln \left[ \tan\left(\frac{\pi}{\Theta}\varphi\right) \right] + c_1 & \text{for } \varphi \in \left]0, \frac{\Theta}{2}\right[, \\ -\frac{\Theta}{2\pi} \ln \left[ \tan\left(-\frac{\pi}{\Theta}\varphi\right) \right] + c_2 & \text{for } \varphi \in \left]\frac{\Theta}{2}, \Theta\right[. \end{cases} \quad (3-33)$$

Figure 3-1, **E** and **F**, illustrates the rise function  $U_{\text{sine}}(\varphi)$  and its inverse  $U_{\text{sine}}^{-1}(V)$  for the sine neuron with  $c_1 = c_2 = 0$ .

Since the membrane potential of our sine neuron satisfies  $V_{\text{sine}}(t) = U_{\text{sine}}(\varphi(t))$ , it reaches  $+\infty$  in finite time (see Fig. 3-1**E**), so the spike threshold can be set to  $\infty$ . In this respect, the sine neuron resembles the theta or quadratic integrate-and-fire model (see, e.g., Izhikevich (2007)). However, the sine neuron is not reset to  $-\infty$ . When it reaches threshold, the membrane potential decreases from  $+\infty$  to  $-\infty$  half way through the cycle by its intrinsic dynamics. In this regime, excitatory input yields a phase delay. After switching to  $-\infty$ , the phase

progresses and the membrane potential increases gradually to  $+\infty$  in a regime where excitation yields a phase advance. The dynamical regime thus depends on the last “event”. If the last event was sending a spike ( $V_{\text{sine}} = \infty$ ), we are in regime  $k = 1$ , where excitation delays the phase. If the last event was reaching the reset potential ( $V_{\text{sine}} = -\infty$ ), we are in regime  $k = 2$ , where excitation advances the phase. Note that this is an extension to the dynamics of standard integrate-and-fire models, where neurons are only in one dynamical regime and reset in infinitesimally short time after they reach threshold. In contrast to the “spike response” extension (see Gerstner and Kistler (2002)), the dynamical regime in our extension does not only depend on the time after a spike that has been sent, but also on the full dynamics of the neuron. A stronger asymmetry between spiking and reset or a more rapid onset of spikes can be easily achieved by modifying the sinusoidal shape of  $iPRC_{\text{sine}}(\varphi)$  in Eq. 3-32.

Interestingly, the membrane potential of our sine neuron obeys the simple nonlinear differential equation

$$\frac{dV_{\text{sine}}(t)}{dt} = \frac{dU_{\text{sine}}(\varphi)}{d\varphi} \frac{d\varphi(t)}{dt} = -\cosh\left[\frac{2\pi}{\Theta} V_{\text{sine}}(t)\right] \tag{3-34}$$

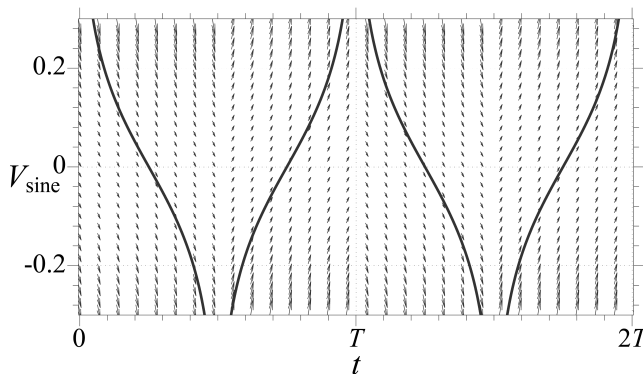


**Figure 3-3. Vector field of the sine neuron defined by Eqs. 3-34 and 3-35.** The solid curves represent  $V_{\text{sine}}(t) = U_{\text{sine}}(\varphi(t))$  for  $c_1 = c_2 = 0$ . The vector field switches when  $V_{\text{sine}}$  reaches  $+\infty$  or  $-\infty$ .

in the regime  $k = 1$ , i.e. if the previous event was a spike, and it obeys

$$\frac{dV_{\text{sine}}(t)}{dt} = \cosh \left[ \frac{2\pi}{\Theta} V_{\text{sine}}(t) \right] \quad (3-35)$$

in the regime  $k = 2$ , i.e. if the previous event was a reset, cf. Fig. 3-3.

Using Eq. 3-33, we can define an inverse function  $U_{\text{sine}}^{-1}$  with two branches. For the branch  $k = 1$  the inverse function  $U_{\text{sine}}^{-1}$  maps the state variable  $V_{\text{sine}} \in ]-\infty, \infty[$  to the phase  $\varphi \in ]0, \Theta / 2[$  by

$$U_{\text{sine}}^{-1}(V_{\text{sine}}) = \frac{\Theta}{\pi} \arctan \left( e^{\frac{2\pi}{\Theta}(V_{\text{sine}} - c_1)} \right). \quad (3-36)$$

For the branch  $k = 2$ , the inverse function  $U_{\text{sine}}^{-1}$  maps the membrane potential  $V_{\text{sine}}$  in the range  $]-\infty, \infty[$  to  $]\Theta / 2, \Theta[$ ,

$$U_{\text{sine}}^{-1}(V_{\text{sine}}) = -\frac{\Theta}{\pi} \arctan \left( e^{\frac{2\pi}{\Theta}(V_{\text{sine}} - c_2)} \right) + \Theta. \quad (3-37)$$

Using these branches, we can now construct the transfer function  $H_{\text{sine}}(\varphi)$ . For this, we first consider the membrane potential dynamics and note that an input  $\varepsilon$  cannot bring  $V_{\text{sine}}$  above  $+\infty$  or below  $-\infty$ . As a consequence, inputs do not alter the dynamical regime  $k$ . To compute the phase after an input we therefore have to use Eq. 3-36 if the original phase  $\varphi$  is within  $]0, \Theta / 2[$  (regime  $k = 1$ ) and Eq. 3-37 if  $\varphi \in ]\Theta / 2, \Theta[$  (regime 2). Further taking into account that the transfer function is the identity for any input at  $\varphi \in \{0, \Theta / 2, \Theta\}$  (the zeros of the PRC, see sec. 3.3), we arrive at  $H_{\text{sine}}(\varphi, \varepsilon)$

$$H_{\text{sine}}(\varphi, \varepsilon) = \begin{cases} U_{\text{sine},1}^{-1}(U_{\text{sine}}(\varphi) + \varepsilon) & \text{for } \varphi \in ]0, \Theta/2[, \\ U_{\text{sine},2}^{-1}(U_{\text{sine}}(\varphi) + \varepsilon) & \text{for } \varphi \in ]\Theta/2, \Theta[, \\ \varphi & \text{for } \varphi \in \{0, \Theta/2, \Theta\}, \end{cases} \quad (3-38)$$

$$= \begin{cases} \frac{\Theta}{\pi} \arctan \left[ \tan \left( \frac{\pi}{\Theta} \varphi \right) e^{-\frac{2\pi\varepsilon}{\Theta}} \right] & \text{for } \varphi \in ]0, \Theta/2[, \\ \frac{\Theta}{\pi} \arctan \left[ \tan \left( \frac{\pi}{\Theta} \varphi \right) e^{-\frac{2\pi\varepsilon}{\Theta}} \right] + \Theta & \text{for } \varphi \in ]\Theta/2, \Theta[, \\ \varphi & \text{for } \varphi \in \{0, \Theta/2, \Theta\}. \end{cases} \quad (3-39)$$

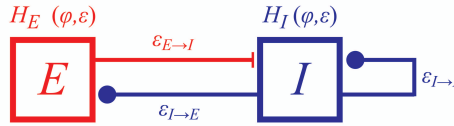
Figure 3-2, **E** and **F**, shows the transfer functions as a function of synaptic increment  $\varepsilon$  and as a function of phase  $\varphi$ , respectively. The panels illustrate in particular that  $\varphi$  can assume values in  $[0, \Theta]$ , that the neuron cannot be excited suprathresholdly and that inputs do not give rise to transitions between the regimes  $k=1$  and  $k=2$ . We note that in phase representation, we do not have to keep track of the type of the last event to execute the dynamical evolution since this information is contained in the current phase.

### 3.4 Interaction scenarios, iteration map and phase-locking equations

#### 3.4.1 Interaction scenarios

In this section, we start to consider networks of two neurons, an excitatory (henceforth E) and an inhibitory (henceforth I) neuron (cf. Fig. 3-4A). They represent two synchronized coupled neuron populations, an excitatory and an inhibitory population, by one representative neuron for each population. The couplings between the neuron populations are accounted for by couplings between the two representative neurons. We aim at setting up an event-based iteration map in the phase variables, which fully describes the network dynamics. Its fixed points and periodic orbits correspond to periodic oscillations in the phase dynamics (cf., e.g., Ermentrout and Kopell (1998)). To derive the map, we consider the phase difference

A



B

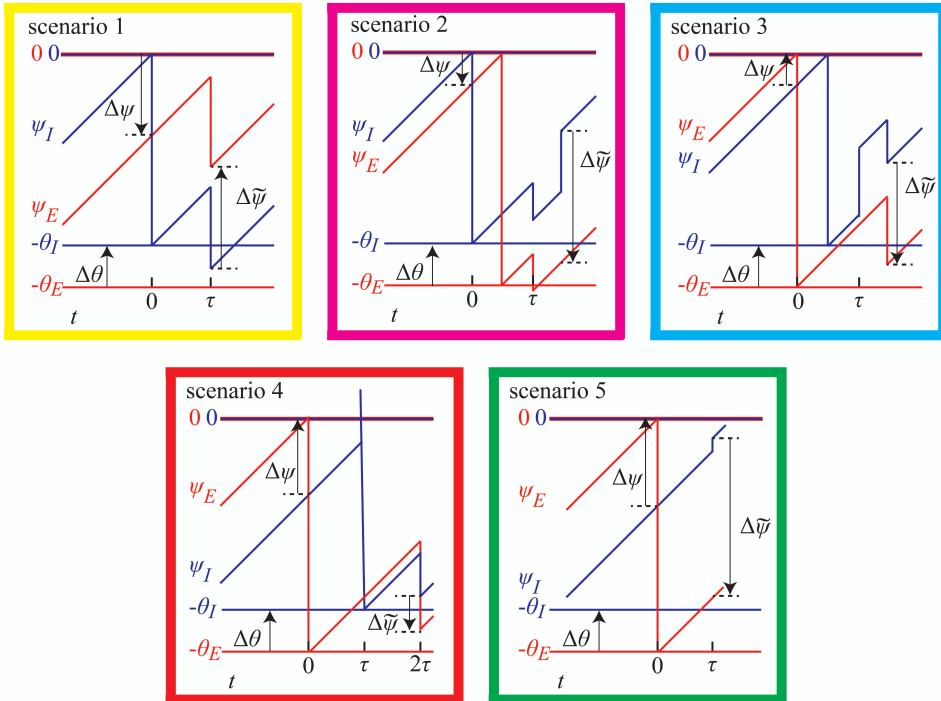


**Figure 3-4. Network of two neurons and illustrations of the five possible scenarios for interactions between them.** **A** displays the neurons (E: excitatory neuron, I: inhibitory neuron) and the couplings between them; their responses to inputs are governed by  $H_E(\varphi, \varepsilon)$  and  $H_I(\varphi, \varepsilon)$ , respectively. **B** shows the phase dynamics for  $\psi_E$  (red) and  $\psi_I$  (blue) in scenarios 1-5. The scenarios are arranged according to the initial value of the phase difference  $\Delta\psi$  (Eq. 3-42), starting from large magnitude negative values.

between the phases of the two neurons and describe how they change when the neurons send and receive spikes. We assume that the E and I neurons spike at most once per cycle in periodic oscillations and that the inhibition always induces a phase

delay in the E neuron. We will then argue which fixed points or periodic orbits in the dynamics correspond to ING and PING rhythms, and explore when they are generated and how they give way to each other.

We incorporate couplings from E to I (strength  $\varepsilon_{E \rightarrow I}$ ), from I to E ( $\varepsilon_{I \rightarrow E}$ ), and self-inhibition from I to itself ( $\varepsilon_{I \rightarrow I}$ ). For simplicity, we do not consider self-excitation from E to itself, as it is not critically involved in PING or ING rhythms. We choose the conduction delay between sending and receiving a spike to be  $\tau$  for all existing connections to reduce the number of free parameters. Furthermore, we assume that the neurons do not oscillate with too high frequencies (intrinsic period is  $2\tau$  or longer to ensure that a spike does not arrive in the next cycle). Due to the finite delay  $\tau$ , spikes of the two neurons can overlap in the sense that one neuron spikes, while a spike sent by the other neuron has not yet arrived. To deal with this, we setup our iteration map in terms of non-overlapping interaction scenarios where one or both neurons may send spikes, rather than in terms of single spike sending and receiving. This allows us to define pieces of an event-based iteration map  $G$ , which acts on a single variable  $\Delta\psi$ , a remaining phase difference of the two neurons taking into account the differences in intrinsic period.

Under the assumptions made, there are five oscillation-relevant interaction scenarios in which each neuron spikes at most once, cf. the five panels in Fig. 3-4B. Each interaction scenario gives rise to an iterative map  $G$ , which maps the remaining phase difference  $\Delta\psi$  before the scenario to the remaining phase difference  $\Delta\tilde{\psi}$  thereafter. In scenario 1, the I neuron spikes and the spike is received before any other event, in particular before the E neuron spikes. Similarly, in scenario 5 the E neuron spikes and the spike is received before any other event, in particular before the I neuron spikes. In regular rhythms, scenario 1 must be followed by scenario 5 and vice versa. We note that if scenario 1 follows shortly after scenario 5, the corresponding rhythm is PING, since the E input nearly generated the spiking of the I neuron. In scenario 2 the I neuron spikes, followed by the E neuron before the inhibitory input from the I neuron arrives and can hinder it. Since the I neuron spikes due to its own drive and the E input arrives shortly thereafter, this scenario gives rise to an ING rhythm. In scenario 3, the E neuron spikes, followed by the I neuron, which spikes before the spike from the E neuron arrives. Although the



sequence of spiking of the E and I neurons is reminiscent of PING, this scenario also gives rise to an ING rhythm, since the I neuron does not spike due to excitatory input from the E neuron, but again due to its own drive, while the E input arrives shortly thereafter. In scenario 4, again first the E neuron spikes, followed by the I neuron. However, the I neuron now spikes due to the excitatory input from the E neuron, which lets the I neuron exceed the spike threshold. This scenario is thus typical for PING. To explain the derivation of the equations that describe the dynamics of spiking of the pair of neurons in each of the scenarios, in the following we give a derivation for scenario 2 (ING) and scenario 4 (PING), while the other scenarios are explained in detail in Appendix 3.8.2.

### 3.4.2 Phase dynamics

We will now consider the interaction scenarios and their impact on the phases in detail. To identify quantities related to the E and I neurons, we endow them with an index  $E$  and  $I$ , in particular  $\varphi_E$  and  $\Theta_E$  are phase and phase threshold of the E neuron, and  $\varphi_I$  and  $\Theta_I$  are phase and phase threshold of the I neuron. To study neurons with different intrinsic periods ( $\Theta_E \neq \Theta_I$ ), we introduce new, shifted phase variables  $\psi_E$  and  $\psi_I$ , which describe the remaining phase of the E and I neurons to the threshold,

$$\psi_E := \varphi_E - \Theta_E, \quad (3-40)$$

$$\psi_I := \varphi_I - \Theta_I. \quad (3-41)$$

The neurons spike at phases  $\psi_E = 0$  and  $\psi_I = 0$ , they are reset to  $-\Theta_E$  and  $-\Theta_I$ . The remaining times to the next spiking generated by purely intrinsic dynamics (no synaptic inputs) are given by  $-\psi_E \geq 0$  and  $-\psi_I \geq 0$ . We denote the differences between the new phase variables, the standard phase variables, and the phase thresholds (periods) of the neurons by

$$\Delta\psi := \psi_E - \psi_I, \quad (3-42)$$

$$\Delta\varphi := \varphi_E - \varphi_I, \quad (3-43)$$

$$\Delta\Theta := \Theta_E - \Theta_I. \quad (3-44)$$

Equations 3-40 and 3-41 yield the relation

$$\Delta\psi = \Delta\varphi - \Delta\Theta. \quad (3-45)$$

We will now derive the transition from  $\Delta\psi$  before to  $\Delta\tilde{\psi}$  after the sequence of interactions for scenarios 2 and 4. For an analysis of the other scenarios, see Appendix 3.8.2. Without loss of generality, we assume  $t=0$  at the start of each scenario.

### 3.4.3 Scenario 2 (An example of ING)

In scenario 2 the I neuron spikes, followed by the E neuron within time interval  $\tau$ , cf. Fig. 3-4B. This happens if before the interaction

$$-\tau < \Delta\psi < 0. \quad (3-46)$$

The phase  $\psi_I$  of the I neuron (henceforth “I phase”) and the phase  $\psi_E$  of the E neuron (henceforth “E phase”) at the start of the interaction sequence at  $t=0$  are

$$\psi_I = 0, \quad (3-47)$$

$$\psi_E = \Delta\psi. \quad (3-48)$$

The interaction sequence consists of the sending and receiving of an I and an E spike. First, at  $t=0$ , the I neuron sends a spike and resets, then the E neuron spikes and resets, before the I spike arrives. The reset of the I neuron implies that  $\varphi_I$  equals  $\tau$  when it receives its own (self-inhibition) spike, cf. Eq. 3-1. Since the E spike has a conduction delay  $\tau$  as well, but was sent the time duration  $-\psi_E = -\Delta\psi$  after the I spike, the E spike arrives at the I neuron at  $\tau - \Delta\psi$ , i.e.  $-\Delta\psi$  after the self-inhibitory spike from the I neuron. The I phase thus proceeds for  $-\Delta\psi$  after the processing of the self-inhibitory I spike before the E spike arrives. This arrival also marks the end of the interaction sequence. Taken together, the phase  $\tilde{\varphi}_I$  directly after the interaction sequence (i.e. directly after receiving the E spike) reads with the interaction function  $H_I$  of the I neuron

$$\tilde{\varphi}_I = H_I\left(H_I\left(\tau, \varepsilon_{I \rightarrow I}\right) - \Delta\psi, \varepsilon_{E \rightarrow I}\right), \quad (3-49)$$

thus

$$\tilde{\psi}_I = \tilde{\varphi}_I - \Theta_I = H_I \left( H_I(\tau, \varepsilon_{I \rightarrow I}) - \Delta\psi, \varepsilon_{E \rightarrow I} \right) - \Theta_I. \quad (3-50)$$

We may assume  $H_I \left( H_I(\tau, \varepsilon_{I \rightarrow I}) - \Delta\psi, \varepsilon_{E \rightarrow I} \right) < \Theta_I$ , i.e. the I neuron does not spike upon arrival of the E spike, since a regular oscillation where scenario 2 begins again at its very end would require the E neuron to have intrinsic period smaller or equal to  $2\tau$ , which we excluded (the duration of scenario 2 is at most  $2\tau$  and the E neuron needs to reach its original phase again after its reset despite the inhibitory input). The E neuron is reset at  $t = -\Delta\psi$  after the time of the I neuron's spike at  $t = 0$ . It therefore has the phase  $\tau - (-\Delta\psi) = \tau + \Delta\psi$  when the input from the I neuron arrives. The I spike changes the phase of the E neuron to  $H_E(\tau + \Delta\psi, \varepsilon_{I \rightarrow E})$ , where  $H_E$  is the transfer function of the E neuron. Thereafter, the E neuron evolves freely (since  $\varepsilon_{E \rightarrow E} = 0$ ) for a duration  $-\Delta\psi$  until the end of the interaction sequence at  $t = (\tau - \Delta\psi)^+$ . The phase  $\tilde{\varphi}_E$  and the remaining phase  $\tilde{\psi}_E$  then read

$$\tilde{\varphi}_E = H_E(\tau + \Delta\psi, \varepsilon_{I \rightarrow E}) - \Delta\psi, \quad (3-51)$$

$$\tilde{\psi}_E = \tilde{\varphi}_E - \Theta_E = H_E(\tau + \Delta\psi, \varepsilon_{I \rightarrow E}) - \Delta\psi - \Theta_E. \quad (3-52)$$

Taken together,

$$\Delta\tilde{\psi} = \underbrace{H_E(\tau + \Delta\psi, \varepsilon_{I \rightarrow E}) - H_I \left( H_I(\tau, \varepsilon_{I \rightarrow I}) - \Delta\psi, \varepsilon_{E \rightarrow I} \right) - \Delta\psi - \Delta\Theta}_{=: G(\Delta\psi)}. \quad (3-53)$$

Our considerations resulted in an iteration map  $G$ , which maps the remaining phase difference before the interaction sequence to the remaining phase difference thereafter.

Scenario 2 can repeat to give rise to regular oscillations (synchronization between neurons of order 1:1 (Pikovsky et al., 2001)). The underlying phase dynamics then satisfy

$$G(\Delta\psi) = \Delta\psi. \quad (3-54)$$

Solving for  $\Delta\psi$  allows to determine the dynamics. If the E and I neurons are both LIF neurons, Eqs. 3-54 and 3-20 yield

$$\Delta\psi = \ln \left\{ \frac{e^{-\tau} - e^{-H_{LIF}(\tau, \varepsilon_{I \rightarrow I}; \Theta_I) - \Delta\Theta}}{2e^{-\Delta\Theta} \Gamma(\Theta_E, \varepsilon_{I \rightarrow E})} \pm \frac{\sqrt{\left[ e^{-H_{LIF}(\tau, \varepsilon_{I \rightarrow I}; \Theta_I) - \Delta\Theta} - e^{-\tau} \right]^2 + 4e^{-\Delta\Theta} \Gamma(\Theta_E, \varepsilon_{I \rightarrow E}) \Gamma(\Theta_I, \varepsilon_{E \rightarrow I})}}{2e^{-\Delta\Theta} \Gamma(\Theta_E, \varepsilon_{I \rightarrow E})} \right\} - \Delta\Theta, \quad (3-55)$$

where  $\Gamma(\Theta, \varepsilon)$  is defined as

$$\Gamma(\Theta, \varepsilon) := (1 - e^{-\Theta}) \varepsilon. \quad (3-56)$$

If the I neuron is the sine neuron, Eq. 3-39 has to be inserted for  $H_I$  in Eq. 3-54. We note that the I spike arrives at the I neuron at the phase  $\varphi = \tau$ , which is in the first branch ( $\varphi = \tau \in ]0, \Theta / 2[$ ), i.e. the input advances the phase and the first line of Eq. 3-39 will be used to write out  $H_I(\tau, \varepsilon_{I \rightarrow I})$ . However, the E spike can arrive at a phase of the I neuron either in the first branch  $]0, \Theta / 2[$  or in the second branch  $]\Theta / 2, \Theta[$ , so it either delays or advances the phase and the first or second line of Eq. 3-39 apply to the outer  $H_I$  in  $H_I(H_I(\tau, \varepsilon_{I \rightarrow I}) - \Delta\psi, \varepsilon_{E \rightarrow I})$ , depending on the value of  $H_I(\tau, \varepsilon_{I \rightarrow I}) - \Delta\psi$ .

If a (real-valued) solution  $\Delta\psi$  of Eq. 3-54 exists, the network can generate a regular oscillation characterized by repeated occurrence of scenario 2. The oscillation frequency can be determined directly from the dynamics of the E neuron in terms of  $\Delta\psi$ . We start at the time when the E neuron spikes and is reset. After a time duration  $\tau + \Delta\psi$  the inhibitory input from the I neuron arrives, cf. Eqs. 3-51 and 3-52 and the paragraph preceding them. The phase of the E neuron is changed to  $H_{LIF}(\tau + \Delta\psi, \varepsilon_{I \rightarrow E}; \Theta_E)$  and it takes the E neuron the time duration of  $\Theta_E - H_{LIF}(\tau + \Delta\psi, \varepsilon_{I \rightarrow E}; \Theta_E)$  to spike again and complete the period. Summing the two durations up yields the oscillation period and the frequency of scenario 2,

$$f(\Delta\psi) = \left[ \tau + \Delta\psi + \Theta_E - H_{LIF}(\tau + \Delta\psi, \varepsilon_{I \rightarrow E}; \Theta_E) \right]^{-1}. \quad (3-57)$$

### 3.4.4 Scenario 4 (An example of PING)

In scenario 4, the E neuron spikes first, followed by the I neuron, which spikes due to suprathreshold excitatory input from the E neuron (cf. Fig. 3-4B). We note that the scenario does not occur if the I neuron is a sine neuron because sine neurons cannot be suprathresholdly excited as the required input strength would be infinite (cf. derivation of Eqs. 3-38 and 3-39). In scenario 4 the E neuron spikes at  $t = 0$ , so the I and E phases at the start of the interaction sequence, at  $t = 0$ , read

$$\psi_I = -\Delta\psi, \quad (3-58)$$

$$\psi_E = 0. \quad (3-59)$$

For scenario 4,  $\Delta\psi$  must satisfy

$$\tau \leq \Delta\psi \leq \Theta_I + \tau - H_I(\Theta_I, -\varepsilon_{E \rightarrow I}). \quad (3-60)$$

The left-hand side inequality guarantees that the I neuron does not spike before the E spike arrives. The right-hand side inequality guarantees that  $\psi_I$  at the time of arrival of the excitatory input from the E neuron is sufficiently near the threshold to allow for suprathreshold excitation: The E spike arrives at time  $t = \tau$  where the I neuron has phase  $\psi_I = -\Delta\psi + \tau$  equivalent to  $\varphi_I = \Theta_I - \Delta\psi + \tau$ . The condition that the received input is suprathreshold is then

$$U_I(\Theta_I - \Delta\psi + \tau) + \varepsilon_{E \rightarrow I} \geq U_I(\Theta_I) = \Theta_{V,I}. \quad (3-61)$$

We assume that  $U_I(\varphi)$  is strictly increasing in the relevant range near the threshold, such that  $U_I^{-1}$  exists and is strictly increasing. We can then apply it to Eq. 3-61 maintaining the direction of the inequality:

$$\begin{aligned} \Theta_I - \Delta\psi + \tau &\geq U_I^{-1}(U_I(\Theta_I) - \varepsilon_{E \rightarrow I}), \\ &= H_I(\Theta_I, -\varepsilon_{E \rightarrow I}). \end{aligned} \quad (3-62)$$

Isolating  $\Delta\psi$  yields

$$\Delta\psi \leq \Theta_I + \tau - H_I(\Theta_I, -\varepsilon_{E \rightarrow I}), \quad (3-63)$$

which is the right-hand side inequality of Eq. 3-60.

The scenario now unfolds as follows: The E neuron sends its spike and resets and the I neuron receives the E spike at  $t = \tau$ . The excitatory input brings the I neuron suprathreshold, such that it spikes and resets subsequently. At  $t = 2\tau$  both neurons receive the I spike. Due to the suprathreshold excitation the precise value of the I phase when the E spike arrives is irrelevant for the final phase. The I phase when it receives the self-inhibitory I spike at the end of the interaction sequence is always  $\tau$ , so

$$\tilde{\varphi}_I = H_I(\tau, \varepsilon_{I \rightarrow I}), \quad (3-64)$$

$$\tilde{\psi}_I = H_I(\tau, \varepsilon_{I \rightarrow I}) - \Theta_I. \quad (3-65)$$

Since the E neuron was reset at  $t = 0^+$  and evolves freely until it receives the I spike at  $t = 2\tau$ ,

$$\tilde{\varphi}_E = H_E(2\tau, \varepsilon_{I \rightarrow E}), \quad (3-66)$$

$$\tilde{\psi}_E = H_E(2\tau, \varepsilon_{I \rightarrow E}) - \Theta_E. \quad (3-67)$$

The phase difference  $\Delta\tilde{\psi}$  after the interaction sequence thus reads

$$\Delta\tilde{\psi} = \underbrace{H_E(2\tau, \varepsilon_{I \rightarrow E}) - H_I(\tau, \varepsilon_{I \rightarrow I})}_{=: G(\Delta\psi)} - \Delta\Theta. \quad (3-68)$$

Scenario 4 can also repeat to give rise to regular oscillations. The underlying phase dynamics then satisfy

$$G(\Delta\psi) = \Delta\psi. \quad (3-69)$$

Solving for  $\Delta\psi$  allows to determine the dynamics. Equation 3-69 yields

$$\Delta\psi = \ln \left[ \frac{e^{-\tau} - \Gamma(\Theta_I, \varepsilon_{I \rightarrow I})}{e^{-2\tau} - \Gamma(\Theta_E, \varepsilon_{I \rightarrow E})} \right] - \Delta\Theta. \quad (3-70)$$

(both neurons are LIF neurons for the scenario to occur). If a real-valued solution  $\Delta\psi$  exists, the network can generate the oscillation. The oscillation period can be determined directly from the dynamics of the E neuron. At the beginning of the scenario, the E neuron sends a spike and is reset. The I spike arrives after a duration  $2\tau$  at the E neuron. The E phase at this point is  $2\tau$ , which changes to  $H_E(2\tau, \varepsilon_{I \rightarrow E})$ . The E neuron will thus spike next after a duration of  $\Theta_E - H_E(2\tau, \varepsilon_{I \rightarrow E})$ . Summing the two durations up yields the oscillation period and the frequency

$$f = [2\tau + \Theta_E - H_E(2\tau, \varepsilon_{I \rightarrow E})]^{-1}. \quad (3-71)$$

Inserting Eq. 3-20 yields

$$f = \left\{ 2\tau + \Theta_E + \ln \left[ e^{-2\tau} - \Gamma(\Theta_E, \varepsilon_{I \rightarrow E}) \right] \right\}^{-1}, \quad (3-72)$$

where  $\Gamma$  is defined in Eq. 3-56. We note that due to the suprathreshold excitation of the I neuron, the frequency is independent of  $\Delta\psi$  in contrast to oscillations generated by other scenarios.

### 3.5 Regular oscillations

In this section we consider the regular oscillations generated by the different scenarios. In a comparably straightforward ING condition, the constant drive to the I neuron largely exceeds the constant drive to the E neuron. This gives rise to a periodic spike sequence by the I neuron, which completely inhibits spiking of the E neuron. This type of ING rhythm has been described extensively in the literature (cf., e.g., Börgers and Kopell (2003); Kopell and Ermentrout (2004); Börgers and Kopell (2005)). Alternatively, we can consider networks without  $E \rightarrow I$  coupling, they generate the same I dynamics even if the E neuron continues to spike. Similarly well studied (cf., e.g., Börgers and Kopell (2003); Börgers et al. (2005); Börgers and Kopell (2005)) is the straightforward PING condition, where a relatively large drive to the E neuron causes it to spike periodically. These spikes generate spikes in the I neuron, which has small drive and would remain rather inactive without the input from the E neuron. In this chapter, we will focus on situations where ING and PING are in competition since both the E and I neurons have comparably strong drives and

all relevant couplings are present. However, we will consider the abovementioned straightforward “pure ING” and “pure PING” rhythms for comparison. As described in sec. 3.4 and Appendix 3.8.2, there are 5 possible scenarios for relative spiking of the E and I neurons. These can – alone or in combination – give rise to regular oscillations, more precisely to ING and PING rhythms. Scenarios 2 and 3, in which the I neuron spikes due to its intrinsic dynamics before the E input arrives, generate an ING rhythm. Scenario 4, in which the spike of the I neuron is generated by the input from the E neuron instantaneously upon its arrival, generates a PING rhythm. An oscillation generated by scenarios 5 and 1 in alternation should be interpreted as a PING rhythm, if the spike of the I neuron is generated shortly after the input of the E neuron, i.e. if the input from the E neuron basically generates the I spike. If the I spike occurs with larger distance from the E spike, the character of the oscillation is less clear. The I spike cannot shortly precede the E spike due to its inhibitory effect. We denote all scenario 5, 1-generated oscillations as PING in the following.

### 3.5.1 Global iteration map

To analytically identify regular oscillations, we gather the local iteration maps derived in sec. 3.4 and Appendix 3.8.2 into a global, piecewise defined iteration map  $G$ , which maps the remaining phase difference  $\Delta\psi$  to the remaining phase difference after the next occurring interaction scenario. The global iteration map consists of several sections, since the next interaction scenario and thus the applicable map depends on the current phase difference (Fig. 3-4B). Equations 3-A12, 3-46, 3-A24, 3-60, and 3-A35 specify the ranges in which the different scenarios occur and thus the domains of the individual map segments constituting  $G$ . Equations 3-A21, 3-53, 3-A31, 3-68 and 3-A43 give the corresponding maps. The regular oscillations are reflected by fixed points of  $G$  (scenarios 2,3, and 4) and  $G^2$  (scenarios 5,1 in alternation).

### 3.5.2 Phased locked oscillations in networks with type I E and I neurons

Figure 3-5A shows an example of an ING rhythm (scenario 2) in a network of two type I LIF neurons in standard phase representation (cf. sec. 3.2). In this scenario, the I neuron (blue trace) spikes just before spiking of the E neuron (red trace) such that the inhibition from the I neuron to the E neuron arrives after spiking of the E neuron. Figure 3-5C shows the global iteration map  $G$  for the same network



parameters. The panel displays the segments of the graph of  $G$  in different colors to highlight the five scenarios (see Fig. 3-4B for the color labels). The relative phases  $\Delta\psi$  that satisfy  $G(\Delta\psi) = \Delta\psi$  are fixed points, which may be stable (if the absolute value of the slope of the iteration map at the fixed point is less than 1) or unstable (if the absolute value of the slope is larger than 1). The only stable fixed point for  $G$  in Fig. 3-5C corresponds to the intersection of the magenta segment (scenario 2) with the diagonal (black, slope 1) near  $\Delta\psi = -0.2$ . Figure 3-5E shows the iteration map after two periods, i.e.  $G^2(\Delta\psi) := G(G(\Delta\psi))$ . The thick segment coloring of the curve indicates the scenarios occurring in the first iteration (same as in panel C), while the thin curves highlight the scenarios in the second iteration. In both maps Fig. 3-5, C and E, the fixed point near  $\Delta\psi = -0.2$  (repeated scenario 2) is the only one. It is stable and corresponds to the ING rhythm displayed in panel A. This fixed point is robust against variations in the drive to the E and I neurons and to changes in parameter values for synaptic connectivity.

Figure 3-5B shows an example of a PING rhythm (scenario 4) in a network with two type I LIF neurons in standard phase representation. The spike from the E neuron causes excitation of the I neuron above its spiking threshold, followed by a spike and reset of the I neuron. The global iteration map  $G$  is shown in Fig. 3-5D. There is a fixed point near  $\Delta\psi = 0.6$  where the red segment (scenario 4) crosses the diagonal. The segment is horizontal (slope zero). This means that the entire range of initial phase differences  $\Delta\psi$  between roughly 0.4 and 0.9 is mapped to the same value  $G(\Delta\psi)$  near 0.6. This can also be directly seen from Eq. 3-68: The right-hand side is independent of  $\Delta\psi$ , such that the piece of iteration map maps any initial relative phase in its domain to the same value. The double iteration map is shown in Fig. 3-5F. Both for the first and second iterations, we find the same stable fixed point.

### 3.5.3 Phased locked oscillations in networks with type I E and type II I neurons

We observe for the considered networks with an excitatory type I LIF neuron and an

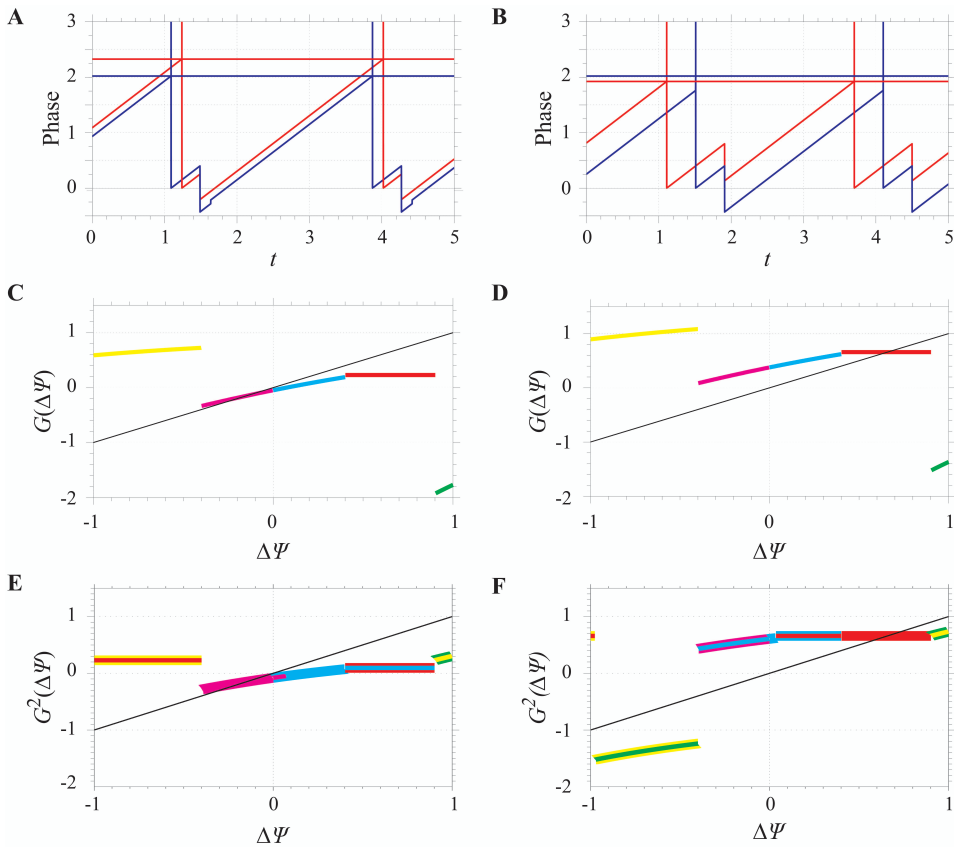


**Figure 3-5. ING and PING dynamics in a network of two type I (leaky integrate-and-fire) neurons.** **A**, ING dynamics (scenario 2) in phase representation. The panel shows  $\varphi_E$  (red) and  $\varphi_I$  (blue) versus time. **B**, PING dynamics (scenario 4) with suprathreshold excitation. **C**, Iteration map  $G$  with network parameters as in **A**. Pieces of the map originating from different scenarios are highlighted by different colors (scenario 1: yellow, 2: magenta, 3: cyan, 4: red, 5: green, cf. frame colors in Fig. 3-4B). There is a stable fixed point near  $\Delta\psi = -0.2$  corresponding to the ING rhythm in **A**. **D**, Iteration map  $G$  with network parameters as in **B**. The stable fixed point near  $\Delta\psi = 0.7$  corresponds to the PING rhythm in **B**. **E** and **F** show the double iteration maps  $G^2$ , where the thick coloring of the segments indicates the first iteration also appearing in **C** and **D** and the thin coloring indicates the second. Parameter settings:  $\varepsilon_{I \rightarrow E} = -0.5$ ,  $\varepsilon_{E \rightarrow I} = 0.1$ ,  $\varepsilon_{I \rightarrow I} = -1.0$ , and  $\tau = 0.4$ ; the

drive to the E and I neurons is  $1/\Theta_I = 0.495$  and  $1/\Theta_E = 0.43$  for **A** and  $1/\Theta_I = 0.495$  and  $1/\Theta_E = 0.52$  for **B**.

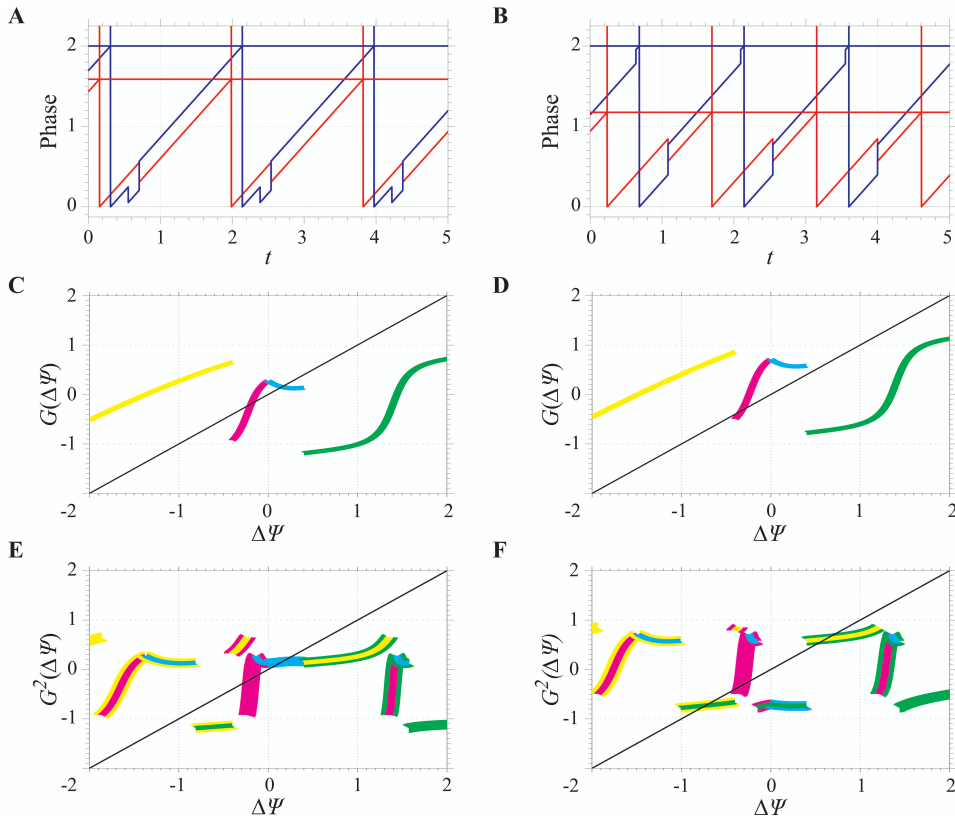
inhibitory type II sine neuron, scenario 2 does not give rise to stable oscillations; the absolute value of the slope of the iteration map at the fixed point is greater than 1, cf. Fig. 3-6C near  $\Delta\psi = -0.2$  and Fig. 3-6D near  $\Delta\psi = -0.3$ . This is a difference to our networks with two type I LIF neurons. Another difference is that for type II I neuron scenario 4 does not occur, cf. sec. 3.4.4. We therefore illustrate the dynamics of a network with an excitatory type I LIF neuron and an inhibitory type II sine neuron for other scenarios than for the network with two type I LIF neurons. We choose a scenario 3 ING rhythm and a scenario-5,1 PING rhythm.

Figure 3-6A shows the ING dynamics generated by scenario 3: the E neuron spikes just before spiking of the I spike. However, as argued above, this scenario does not belong to the class of PING, because spiking of the I neuron is not triggered by the E spike. The results for the iteration map are illustrated in Fig. 3-6C, which shows a stable fixed point near  $\Delta\psi = 0.3$  for scenario 3 (intersection of the cyan curve with the diagonal). The results for the double iteration map are shown in Fig. 3-6E with the same stable fixed point near  $\Delta\psi = 0.3$  (repeated scenario 3).

Figure 3-6B shows phase dynamics that are generated by alternation of scenarios 5 and 1. We can clearly classify this pattern as PING, since excitation from the E neuron brings the I neuron close to the spiking threshold, which results in spiking of the I neuron shortly thereafter. Figure 3-6D depicts the first iteration map  $G$ , which does not have a stable fixed point: The fixed point near  $\Delta\psi = -0.3$  is unstable. In contrast, the double iteration map  $G^2$  (Fig. 3-6F) has two stable fixed points, reflecting the period 2 orbit that generates the PING oscillation. They are located near  $\Delta\psi = 0.6$  and  $\Delta\psi = -0.7$  and correspond to alternating scenarios 5 and 1 and the phase dynamics Fig. 3-6B.

### 3.6 PING-ING interactions in networks of two oscillators

We saw in the previous section that for suitable parameter values, our networks can generate either ING or PING rhythms. In the following, we analyze how PING and



**Figure 3-6. ING and PING dynamics in a network of a type I (leaky integrate-and-fire) E neuron and a type II (sine) I neuron.** **A** and **B**, ING (scenario 3) and PING (combination of scenarios 5 and 1) dynamics in phase representation, respectively. **C** and **D**, Iteration maps  $G$  for the same network parameters as used in **A** and **B**, respectively. The stable fixed point near  $\Delta\psi = 0.3$  in **C** corresponds to the ING rhythm in **A**. The other fixed point near  $\Delta\psi = -0.2$  is unstable and corresponds to an unstable scenario 2 ING rhythm. (**D**) There is no fixed point of the first iteration map  $G$  corresponding to the PING dynamics shown in panel **B**, since they consist of a sequence of two scenarios and thus appear as a period 2 orbit in the iterations of  $G$ . The unstable fixed point near  $\Delta\psi = -0.3$  corresponds to an unstable scenario 2 ING rhythm. Pieces of the map generated by different scenarios are highlighted by different colors as in Fig. 3-5, **C** and **D**. **E** and **F**, The second iterates  $G^2$ . The period 2 orbit of the PING rhythm in **B** is reflected by two fixed points in the double iteration map **F**, in the domains of scenarios 1 and 5. Parameter settings:  $\varepsilon_{I \rightarrow E} = -0.2$ ,  $\varepsilon_{E \rightarrow I} = 0.5$ ,

$\varepsilon_{I \rightarrow I} = -0.42$ , and  $\tau = 0.4$ ; the drive to the I and E neurons is  $1/\Theta_I = 0.5$  and  $1/\Theta_E = 0.63$  for **A** and  $1/\Theta_I = 0.5$  and  $1/\Theta_E = 0.85$  for **B**.

ING rhythms compete to generate the network oscillation and how networks may switch from one rhythm to another when the values of the external drives change. We use “pure ING” and “pure PING” rhythms generated by reduced two-neuron networks, which do not allow for the generation of the other rhythm as reference. This allows to better understand the competition of PING and ING rhythms in the full network, which could in principle generate both rhythms. We express the external drive given to each neuron both for the LIF and sine neuron by the inverse of the period, i.e. by  $1/\Theta_E$  and  $1/\Theta_I$ , since – in contrast to the LIF neuron – the sine neuron does not have an explicit external driving current variable.

### 3.6.1 Pure PING and pure ING networks

In "pure ING" networks the only excitatory input to the I neuron is the external drive, the synaptic strength of the projection from the E to the I neurons is set to zero (cf. also **Chapter 2**). The frequency of the pure ING rhythm is determined by the I drive and the self-inhibitory input with strength  $\varepsilon_{I \rightarrow I}$  arriving a time duration  $\tau$  after reset of the I neuron; the frequency is explicitly given by Eq. 3-A23.

In "pure PING" networks, the I drive is sufficiently small such that the I neuron has a much lower intrinsic period than the E neuron. The circuit has a sufficiently strong projection from the E to the I neuron, such that each E spike brings the membrane potential of the I neuron above the threshold and elicits a spike just as in scenario 4. The frequency of the pure PING rhythm is determined by the E drive and the inhibitory input  $\varepsilon_{I \rightarrow E}$  that arrives after an interval  $2\tau$  after reset of the E neuron. The frequency is explicitly given by Eq. 3-72.

### 3.6.2 Analysis of PING-ING interactions in networks with type I E and I neurons

We will first study interactions between PING and ING rhythms for networks with two type I neurons. The drives to the I neuron (I drive expressed by  $1/\Theta_I$ ) and to the E neuron (E drive expressed by  $1/\Theta_E$ ) vary, see Fig. 3-7. The blue surface in

Fig. 3-7A shows the frequency of rhythmic spiking of the I neuron in pure ING networks. The red surface in Fig. 3-7A represents the frequency of rhythmic spiking of the E neuron in pure PING networks as a function of the E drive. The green surface in Fig. 3-7A shows the frequency of rhythmic spiking for the full network schematically drawn in Fig. 3-4A, as a function of the E and the I drives. The frequencies of the pure ING (blue surface) and of the full network (green surface) are not shown for some combinations of  $1/\Theta_I$  and  $1/\Theta_E$ ; these combinations do not elicit rhythmic spiking for any of the five scenarios, including alternation of scenarios 5 and 1 for the displayed network type. The intersection of the surfaces in Fig. 3-7A with a plane of constant E drive ( $1/\Theta_E = 0.495$ ) is shown in Fig. 3-7B and with a plane of constant I drive ( $1/\Theta_I = 0.495$ ) in Fig. 3-7C.

Figure 3-7B shows that for the range of smaller I drive  $1/\Theta_I$  the rhythm of the full network is PING (scenario 4, dark green curve in Fig. 3-7B). The spiking pattern of the rhythm is the same as the spiking pattern of the pure PING rhythm, cf. Fig. 3-5B for an example; the red curve (pure PING) and the green curve (PING for the full network) in Fig. 3-7B thus overlap. The rhythm of the full network is PING, because the E neuron recovers from the inhibition sooner than the I neuron does and the E spike elicits spiking of the I neuron at its arrival. This also implies that when the full network generates PING, its frequency is higher than the frequency of full network ING; otherwise the I neuron will spike by its own dynamics and consequently the full network generates ING. Equation 3-72 shows that the frequency of this PING rhythm (and the PING fixed point of the iteration map) does not depend on the I drive  $1/\Theta_I$  as long as it is sufficiently small. When the I drive increases, there is a bifurcation and a (stable) scenario-3 ING solution appears near  $1/\Theta_I = 0.52$  (light green curve): This ING solution lasts till near  $1/\Theta_I = 0.56$ , after which it switches to (stable) scenario-2 ING. The frequency of full-network ING increases with  $1/\Theta_I$ . It stays higher than the frequency of pure ING because the nonzero  $\varepsilon_{E \rightarrow I}$  provides an additional excitatory input to the I neuron and increases the frequency of the rhythm. Interestingly, we find coexistence of PING and ING and bistability, cf. the range  $0.52 \lesssim 1/\Theta_I \lesssim 0.53$  in Fig. 3-7B. As  $1/\Theta_I$  increases further, the PING rhythm (dark green curve) vanishes. If the network was oscillating

in PING mode before, it will change to ING rhythm and the oscillation frequency will increase in jump-like manner.

The reason for the vanishing of the PING mode is as follows: With increasing I drive,  $|\psi_I|$  (the phase distance to the threshold  $\Theta_I$ ) at arrival of the E spike becomes smaller until the I neuron reaches  $\Theta_I$  by its intrinsic dynamics at E spike arrival. Beyond this point, there is no PING rhythm, as the I neuron spikes before E spike arrival. The bifurcation point is at the crossing of the pure PING (red) and the pure ING curves (blue): Since the I neuron reaches threshold from its own drive simultaneously with the E spike arrival, the value of  $\varepsilon_{E \rightarrow I}$  becomes irrelevant. At this bifurcation point, any input will generate suprathreshold excitation and be completely canceled due to the I neuron's reset such that also the oscillation frequencies of pure PING (large  $\varepsilon_{E \rightarrow I}$ ) and pure ING ( $\varepsilon_{E \rightarrow I} = 0$ ) agree.

Taken together, we observe that the PING frequency is insensitive to changes in  $1/\Theta_I$ , while the ING frequency increases with the drive. The PING rhythm vanishes when its frequency drops below that of the pure ING rhythm and the ING rhythm vanishes when its frequency drops below that of the PING rhythm. Since the ING rhythm of the full network has higher frequency than the pure ING rhythm, we have a region of coexistence. When the full network generates ING, its frequency is always higher than the frequency of full network PING. This is due to the fact that, in ING, the inhibition arrives at the E phase less than  $2\tau$ . We note that the slope of the light green curve is larger than the slope of the dark green curve. In other words, the ING frequency is more sensitive to a change of the I drive  $1/\Theta_I$  than the insensitive PING frequency.

Figure 3-7C shows the frequency of rhythms as we fix  $1/\Theta_I$  and vary  $1/\Theta_E$ . For small E drive (e.g.  $0.42 \lesssim 1/\Theta_E \lesssim 0.46$  in Fig. 3-7C), the ING rhythm governs the dynamics of the full network: With our network parameters, it is the scenario-2 ING rhythm for  $0.42 \lesssim 1/\Theta_E \lesssim 0.44$  and the scenario-3 ING rhythm for  $0.44 \lesssim 1/\Theta_E \lesssim 0.47$ . As in Fig. 3-7B, in Fig. 3-7C the full network ING rhythm ( $\varepsilon_{E \rightarrow I} > 0$ , light green) has a higher frequency than the pure ING rhythm ( $\varepsilon_{E \rightarrow I} = 0$ , blue line) since the nonzero excitatory input from the E neuron advances the spiking

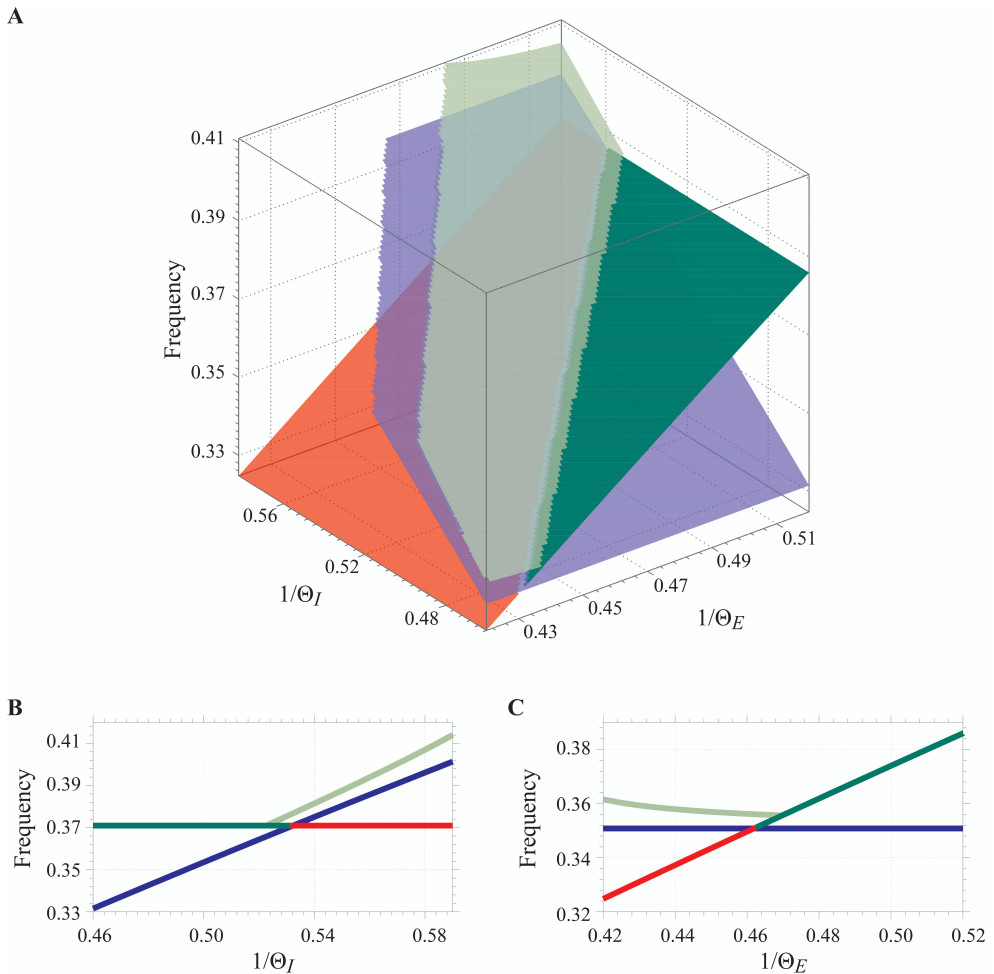


**Figure 3-7. Transitions between PING and ING in a network of two type I (leaky integrate-and-fire) neurons.** The blue and red surfaces or lines show the oscillation frequencies of pure ING and pure PING rhythms, respectively. The green surfaces or lines show the frequency of oscillations in the full two-neuron network. **A** displays the frequency of network oscillations versus the E and I drives (measured by intrinsic period<sup>-1</sup>). Termination of a surface in **A** occurs at parameters  $1/\Theta_E$  and  $1/\Theta_I$  where the highlighted network type does not yield any regular rhythm anymore. Panels **B** and **C** show cross sections of the surfaces given in **A**. The drive at the I neuron (**B**) or at the E neuron (**C**) increases from left to right, the other drive is kept fixed. Light green lines show the frequency of the full network ING rhythm, while dark green lines show the frequency of the full network PING rhythm.



Parameter settings:  $\varepsilon_{I \rightarrow E} = -0.5$ ,  $\varepsilon_{E \rightarrow I} = 0.1$ ,  $\varepsilon_{I \rightarrow I} = -1.0$ , and  $\tau = 0.4$ ; the drive to the I and E neurons is  $1/\Theta_E = 0.495$  for **B** and  $1/\Theta_I = 0.495$  for **C**.

of the I neuron. The higher the E drive, the earlier does the E spike arrive in the period of the I neuron and the smaller is its excitatory effect due to the I neuron's PRC and transfer function (Fig. 3-2C). The frequency of the ING rhythm thus slightly decreases with increasing E drive.

The absence of a PING rhythm for small E drive, where the pure ING frequency is higher than the pure PING frequency can be understood from Eqs. 3-72 and 3-A23, which specify the pure PING and pure ING frequencies, respectively. Equation 3-72 implies that the pure PING frequency is determined by the interval between spikes of the E neuron, which is subject to the inhibition  $\varepsilon_{I \rightarrow E}$  arriving at E phase  $2\tau$ . According to Eq. 3-A23, the pure ING frequency is determined by the interval between spikes of the I neuron subjected to the inhibition  $\varepsilon_{I \rightarrow I}$ . In a full network generating PING, the inhibition arrives at E phase  $2\tau$  or later, if the excitation of the I neuron is not suprathreshold. Since the delaying effect of the inhibition increases, the larger the E phase is at its arrival, the spiking interval of the full network E neuron is larger or equal to that in the pure PING network. For the full network to generate PING, the spiking interval of the E neuron subjected to inhibition  $\varepsilon_{I \rightarrow E}$  must at least to be shorter than the spiking interval of the I neuron subjected to inhibition  $\varepsilon_{I \rightarrow I}$  (the spiking interval in the pure ING network), since the additionally arriving excitation  $\varepsilon_{E \rightarrow I}$  further decreases the spike interval of the I neuron. When already the frequency of pure ING is higher than that of pure PING, this necessary condition is violated and the PING rhythm is excluded.

As the E drive increases, the pure PING frequency starts to exceed the pure ING frequency (in Fig. 3-7C near  $1/\Theta_E = 0.46$ ) and the full network becomes able to generate a PING rhythm. During the transition, the full network can generate either PING or ING depending on the initial state of the neurons. As the E drive increases further, the ING rhythm disappears (near  $1/\Theta_E = 0.47$  in Fig. 3-7C). This is because the phase advance of the I neuron due to the E spike becomes too small compared to the decreasing interval between spikes of the E neuron (Fig. 3-7C: the

light green curve meets the dark green one). We note that the (negative) slope of the light green curve is smaller in absolute value than the (positive) slope of the dark green curve. In other words, the PING frequency is more sensitive to a change of the E drive  $1/\Theta_E$  than the ING frequency.

### 3.6.3 Analysis of PING-ING interactions in networks with type I E and type II I neurons

We will now analyze interactions between PING and ING rhythms for networks with type I E and type II sine I neurons for varying I and E drives, see Fig. 3-8. Similar to Fig. 3-7, the blue surface or curves in Fig. 3-8 represent the frequency of the pure ING rhythm, red stands for pure PING rhythm, and green for full network rhythms. As before, the frequency of the pure ING rhythm is given by Eq. 3-A23. The pure PING rhythm assumes spiking of the I neuron at time  $\tau$  after spiking of the E neuron. The frequency of the pure PING rhythm is thus again given by Eq. 3-72. As mentioned above (sec. 3.3.2), the sine I neuron without an external constant drive cannot reach the threshold for finite value of  $\varepsilon_{E \rightarrow I}$ , it can nevertheless get close, such that the temporal distance between E and I spike is approximately  $\tau$ . We need to keep this point in mind when comparing pure PING and full network PING.

In contrast to the case of networks with type I E and I neurons, the full network with type I E and type II I neurons generates a stable oscillation with a frequency between those of pure ING and pure PING rhythms. Furthermore, our analysis reveals an unstable oscillation (scenario 2) generated by the full network, with a frequency that is much higher than the stable one for our parameters. For smaller I drive (lower  $1/\Theta_I$ , see Fig. 3-8B) the full network generates a PING rhythm (alternating scenarios 5 and 1, dark green curve in Fig. 3-8B). Its frequency is higher than the stable scenario-3 ING frequency; this is due to the fact that with scenario-3 ING the E spike has an inhibitory effect. Since the E spike brings the I neuron only close to its threshold  $\Theta_I$ , the next spike time still depends on the I drive: The larger the drive, the shorter the time that the I neuron needs to reach the threshold after the E spike arrival. Since this time is always at least slightly larger than zero, the full network PING frequency is lower than the pure PING frequency.

As we increase the I drive further, the full network switches from operating in PING mode to ING mode (scenario 3, light green curve) (near  $1/\Theta_I = 0.5$  in Fig. 3-8B). As for networks of two type I neurons (cf. Fig. 3-7B), the rate of change of ING frequency is higher than that of PING frequency; the ING frequency is more

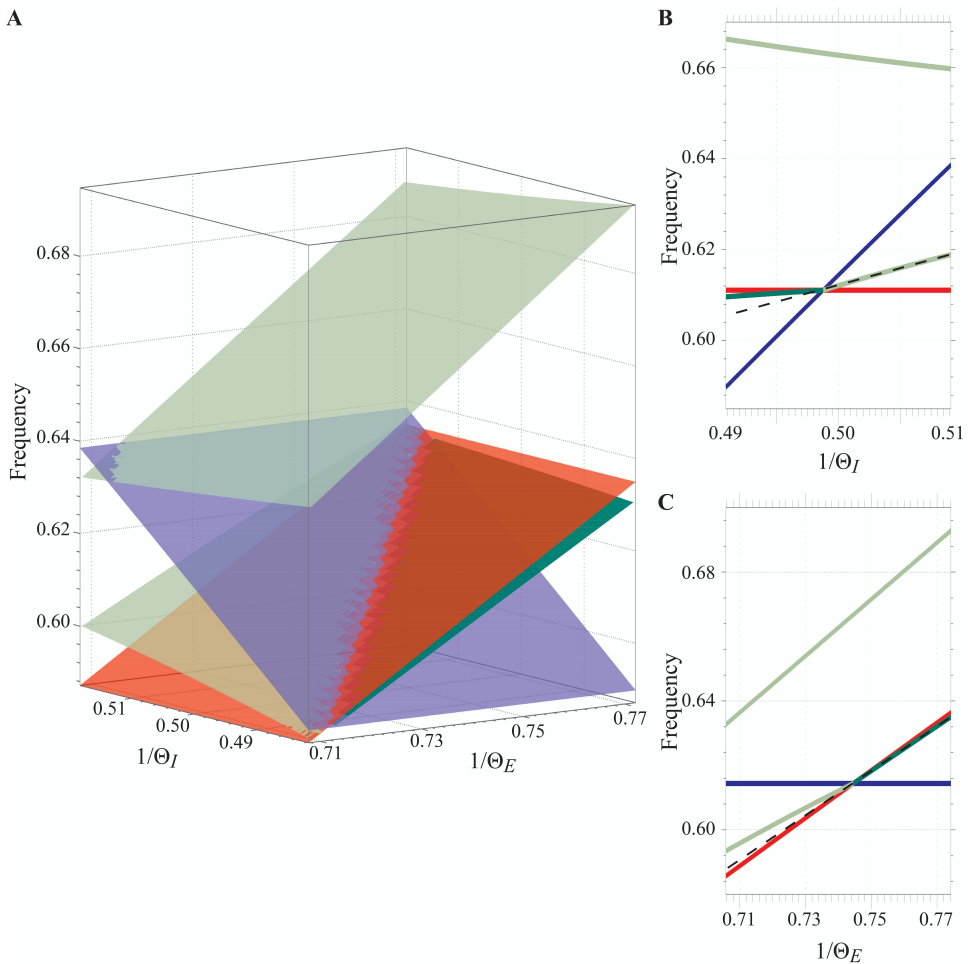


**Figure 3-8. Transitions between PING and ING in a network of a type I (leaky integrate-and-fire) E neuron and a type II (sine) I neuron.** The blue and red surfaces or lines show the oscillation frequencies of pure ING and pure PING rhythms, respectively. The green surfaces or lines show the frequency of oscillations in the full two-neuron network. **A** displays the frequency of network oscillations versus the E and I drives (measured by intrinsic period<sup>-1</sup>). Panels **B** and **C** show cross sections of the surfaces given in **A**: The drive

of the I neuron (**B**) or of the E neuron (**C**) increases from left to right, while the other drive is kept fixed. The light green (**B**) or the dark green (**C**) lines are continued by black dashed lines to allow a better comparison to the slope of the respective other line. The light green surface with comparably high frequencies in **A** and the related light green curves with high frequencies in **B** and **C** correspond to a scenario-2 unstable ING rhythm, while light green colored lower frequencies represent a scenario-3 stable ING rhythm. Dark green shows the frequency of the full network PING rhythm (scenarios 5,1 in alternation). Parameter settings:  $\varepsilon_{I \rightarrow E} = -0.2$ ,  $\varepsilon_{E \rightarrow I} = 0.5$ ,  $\varepsilon_{I \rightarrow I} = -0.42$ , and  $\tau = 0.4$ ; the drive to the I and E neurons is  $1/\Theta_E = 0.74$  for **B** and  $1/\Theta_I = 0.5$  for **C**.

sensitive to change of the I drive  $1/\Theta_I$  than the PING frequency (cf. the light green with the black dashed line in Fig. 3-8**B**). The ING rhythm (light green curve in Fig. 3-8**B**) appears in contrast to the case of two type-I neurons at the same point where the PING rhythm vanishes, when the frequency of the pure ING rhythm is higher than that of the pure PING rhythm. The latter can be understood as in case of two type I neurons, since the excitatory input in full network PING also advances the phase of the type II I neuron. The full network ING frequency is smaller than the pure ING frequency because in the full network there is an additional input from the E neuron. This causes a phase delay since the E spike arrives at an early phase in the spiking cycle of the type II sine neuron.

The frequency of the full network at the transition point where it switches from PING to ING is the same as the intersecting pure ING (blue curve) and pure PING (red curve) frequencies. This is because at the transition point, the I neuron spikes just before the E spike arrives and the E spike meets the I neuron at a phase near zero. It therefore has a negligible effect on the phase of the sine I neuron (cf. Fig. 3-1**D**) and the full network behaves like the reduced ING network. Furthermore, the I neuron's spiking and thus its effect on the E neuron is the same as in the pure PING network. So the frequencies of the full and the pure PING network are also the same.

For decreased E drive (see Fig. 3-8**C**), the I drive imposes an ING rhythm, which governs the dynamics of the full network, just as for networks of two type I neurons. However, as in the case of large I drive (Fig. 3-8**B**), for the network with

type II I neuron, we observe that the ING frequency is lower than the pure ING frequency, since the E spike has a phase delaying effect on the I neuron. The full network ING frequency is higher than the full network PING frequency, since the I spike always arrives at an E phase less than  $2\tau$ . When increasing the E drive, there is again a transition without a coexistence region. Beyond it, the full network assumes a PING rhythm (alternation of scenarios 5 and 1). The slope of the light green curve (ING frequency) is lower than that of the dark green curve (PING frequency) (cf. light green curve and black dashed line in Fig. 3-8C); that is, as for networks of two type-I neurons, the PING frequency is more sensitive to change of the E drive  $1/\Theta_E$  than the ING frequency. Near the right-hand side of the transition point, the E spike arrives when the I neuron is near threshold. The effect of the E spike on the phase of the I neuron is therefore small, which explains why the frequency of the PING rhythm is close to the frequency of the pure PING rhythm. It always lies below, since it takes some time for the I neuron to reach threshold after input from the E neuron. Thus, its inhibition does not arrive at the E neuron's phase  $2\tau$  but later and has a larger delaying impact.

### 3.7 Summary and discussion

In this study, we investigate the interaction between ING and PING oscillations using an analytical approach for a simple neuronal network. In this network, two neural oscillators, an excitatory (E) and an inhibitory (I) neuron, are reciprocally connected and, additionally, the I neuron has self-inhibition. The E neuron mimics a synchronized group of pyramidal cells, while the I neuron represents a synchronized group of interneurons. An important aspect of this model is the type of neurons (type I versus type II). Most results on the type of firing and on the PRC of pyramidal cells in the literature suggest that pyramidal cells in different brain areas belong to the category of type I neurons (Reyes and Fetz, 1993b; Netoff et al., 2005; Wang et al., 2013) (see, however, Galan et al. (2005); Lengyel et al. (2005); Stiefel et al. (2008)). We adopt this view and represent the E neuron by a (type I) leaky integrate-and-fire model. We review the derivation of the phase representation for this model, in particular the derivation of the transfer function  $H$ , which maps the phase of the neuronal oscillator before synaptic input to the phase after synaptic input. A full, general derivation of the phase representation for type I neurons was provided in a

previous study (see Memmesheimer and Timme (2006a)). The appropriate choice of interneuron phase response curve type is less clear. Oscillation-relevant interneurons can be either of type I (Mancilla et al., 2007) or type II (Tateno and Robinson, 2007) depending on the brain area. Therefore, we consider both options in our study: We model the I neuron as type-I leaky integrate-and-fire model or as type II sine neuron.

The interactions between the neurons are modeled by Dirac delta pulses, which induce a jump in the voltage of the receiving neuron by an amount that is described by the strength of the synaptic connection and independent of the voltage. In the present study, we provide the theoretical derivation of the phase dynamics for such neural oscillators if they have an iPRC of type II. In particular, for our type II sine I neuron, we derive the voltage dynamics and the full phase representation. The chosen infinitesimal phase response curve shows a change from negative to positive as typical for type II neurons. Concretely, we use the (inverted) sine iPRC of a normal form oscillator of the Hopf bifurcation (cf. Brown et al. (2004)). Using the phase description, we could provide a full theoretical analysis of the dynamics of a network model with an E neuron and an I neuron of arbitrary type.

Our results are also relevant for single oscillator studies, since they allow to investigate how different an oscillator model is from a model expressible by one-dimensional voltage dynamics with voltage-independent inputs. As an example, we consider the classical radial isochron clock (Glass and Mackey, 1988; Goel and Ermentrout, 2002; Izhikevich, 2007). In this model, a point circulates on its attractor cycle in the  $x,y$ -plane. Synaptic inputs cause deviations from the stable attractor cycle. Assuming that the radial deflection after an input quickly relaxes back while the change in the angular variable remains, this model reduces to a phase oscillator. For infinitesimal inputs, the resulting phase response is given by a sine iPRC. However, comparing the PRC with that in our study reveals a difference in the series expansion of the synaptic strength  $\varepsilon$  from second order on, see Appendix 3.8.1.

To theoretically investigate oscillations in our two-neuron networks, we first provide a basic framework by deriving the five relevant scenarios for the change of phase differences upon interactions of the E and I neurons (see Fig. 3-4). This allows to construct various modes of synchronization (Pikovsky et al., 2001) between the two oscillators by concatenating scenarios and determining whether the

concatenations result in fixed points. For example, scenarios 5 and 1 can be concatenated in alternation to have 1:1 synchronization between the E and I oscillators. For our study, we are only interested in such 1:1 synchronization because both the population of interneurons and the population of pyramidal cells display increased activity only once per gamma cycle (Hajos et al., 2004; Gloveli et al., 2005b). When our two-neuron network operates in the PING mode, an output of the E oscillator elicits spiking of the I oscillator, such as in scenario 4 and the alternating mode of scenarios 5 and 1. When the I oscillator controls the frequency of the network, the network operates in the ING mode (see scenario 2 for an example). We find that when the full network operates in PING-mode, its frequency is more sensitive to changes of the external drive to the E neuron than to changes of the external drive to the I neuron (see Fig. 3-7, **B** and **C**, and Fig. 3-6, **B** and **C**). When the full network operates in the ING-mode, the frequency more strongly depends on the external current given to the I neuron.

Our theoretical study also shows that the qualitative relation of the frequency of the full network and the frequencies of pure ING oscillations ( $\varepsilon_{E \rightarrow I} = 0$ ) and of pure PING oscillations (no/negligible I drive) depends on whether the I neuron belongs to the category of type I or type II. When the I neuron is of type I, the resulting frequency of the full network is above the pure ING frequency and the pure PING frequency. This can be understood from the fact that the excitatory output from the E neuron to the I neuron always advances the phase of a type I I neuron and therefore shortens the cycle and increases the frequency. However, when the I neuron is of type II, the frequency of the full network is between the frequencies of pure ING and pure PING. This can be understood from the fact that the excitatory input from the E neuron can delay the phase of the I neuron when the spike input from the E neuron arrives early in the phase of the I neuron. This increases the cycle duration and decreases the frequency.

When we compare the results of the two-neuron network with simulations in a large network of pyramidal cells and interneurons, the latter show the same tendency (Viriopase et al., 2016): The frequency of the full network with type I interneurons is slightly above the frequency of pure ING and of pure PING, while the frequency of the full network with type II interneurons could be in between. However, the full network PING frequency of the two-neuron network is

intermediate between the pure ING and pure PING frequencies (cf. Fig. 3-6, **B** and **C**), while it is slightly above for the large networks (cf. Fig. 2-7, **B** and **C**). The key to understand this discrepancy is the net value of the excitatory output from the E neuron (the population of the pyramidal cells) to the I neuron (the population of the interneurons). In the pure PING two-neuron network the coupling is assumed to be so strong that the E spike excites the I neuron to spike immediately, while in the full network the I neuron phase still needs to increase a bit up to the threshold. This causes the frequency of pure PING to be higher than that of the full network. However, the net value of the excitatory output in both large-network topologies (the pure PING network and the full network) is approximately the same. With additional drive to the interneurons in the full network, the frequency of the full network is thus higher than that of the purely PING network. Another discrepancy between the results for the two-neuron network and the results for the larger networks in **Chapter 2** concerns network bistability. The phase iteration map of two-neuron networks with type I I neuron has two stable fixed points (one corresponding to ING and another one corresponding to PING) for parameter values near the crossing of the pure ING and pure PING frequencies, giving rise to bistability between ING and PING, see Fig. 3-7, **B** and **C**. In contrast, the simulations of the large network reveal only one oscillation frequency near the crossing. Presumably, this is due to noise added to the input to the neurons in the large network. This gives rise to slightly different firing frequencies of the network's neurons, which together obscure the bistability into a gradual transition between ING and PING. A second fixed point also occurs for the phase iteration map of the two-neuron network with type II I neuron, cf. Figs. 3-6 and 3-8. It is unstable and corresponds to an unstable oscillation with higher frequency. In contrast, the large network simulations again reveal only one frequency. An obvious explanation is that the employed simulations cannot generate unstable oscillations due to noise. Although the results based on the two-neuron networks and the large networks given in **Chapter 2** yield differences in some details, the general picture is similar. In particular, the stable rhythm of the full network is usually realized by the one of ING or PING that generates the higher frequency. That is, the mechanism that generates the higher frequency "wins" in the sense that it determines the frequency of the full network. (In the two neuron network this is also the rhythm, which generates the higher frequency in the corresponding pure networks.) The rough explanation is that the higher frequency generating



mechanism absorbs the resources necessary to maintain a rhythm: A neuron will generally spike earlier due to recruitment into a higher frequency rhythm and is then not able to spike again to contribute to the lower frequency one. However, our analytical approaches in the present article allow for more detailed analyses, see sec. 3.6.

Most studies with a large impact on the field using two-neuron (oscillator) networks were conducted either for purely inhibitory networks (van Vreeswijk et al., 1994; Sato and Shiino, 2002; Ermentrout, 2003; Leibold, 2004; Nomura and Aoyagi, 2005; Di Garbo et al., 2007b; Oh and Matveev, 2009; Canavier et al., 2013) or purely excitatory networks (van Vreeswijk et al., 1994; Ernst et al., 1995; Neltner et al., 2000; Sato and Shiino, 2002; Ermentrout, 2003; Dhamala et al., 2004; WANG et al., 2008). Studies for two-neuron networks, in which one is excitatory and another is inhibitory, are less common and many of them are in different contexts (Jones et al., 2000; Netoff et al., 2005; Börgers and Kopell, 2008; Kramer et al., 2008; Lee et al., 2009). Börgers and Kopell (2005) presented a study related to ours, but without coupling delays and assuming that  $\varepsilon_{E \rightarrow I}$  is always suprathreshold. The article reports that when the intrinsic frequency of the I neuron is higher than the frequency of the PING network rhythm, the latter is destroyed via phase walkthrough that results in an irregular oscillation (I neuron spikes more than once per cycle).

Our study considers both type I and type II I oscillators as well as a finite conduction velocity. The consideration of the frequency aspect yields an intriguing dependence of the frequency changes when changing external drive, on the phase response curve of the oscillators as presented in sec. 3.6.

Unlike other methods for studying the two-neuron network, our method does not focus on determining the mode of the phase locking directly but based on fundamental interaction scenarios that can be used to construct different modes of locking under the assumption that the phase difference between the two oscillators changes only when an input arrives; the assumption is valid in our study because the connections are modeled by Dirac delta pulses. By this, we consider fast post-synaptic current (PSC) kinetics that ignores a PSCs rise and decay. van Vreeswijk et al. (1994) has shown that the duration of the PSCs relative to the interval of spiking is important. Since the time constant of the synapses relevant to gamma oscillations

is of the order of a few milliseconds (Geiger et al., 1997; Angulo et al., 1999; Bartos et al., 2002; Bartos et al., 2007), it may be reasonable to assume that their PSCs are short relative to the period of gamma oscillations, which is around 20 ms. Additionally, Bartos and collaborators (2002; 2007) analyzed ING and the impact of the inhibitory PSC kinetics on it. The studies indicate that probably inhibitory PSCs with fast kinetics underlie gamma oscillations. The assumption that the choice of Dirac delta pulses does not affect the central conclusions of our study is also corroborated by our comparisons with biologically more detailed, larger scale networks in **Chapter 2**.

The results of this study are relevant for in vitro and in vivo experimental studies, since they imply that a seemingly straightforward interpretation of an observed rhythm as ING or PING has to be done with care. As pointed out in the theoretical section of this manuscript, frequent firing of the pyramidal cells does not necessarily imply that the network is dominated by PING. Similar spike patterns can be generated both by ING (cf. scenario 3 and scenario 4) and by PING rhythms (alternation between scenarios 5 and 1 in Fig. 3-6B). In particular, the network can be dominated by ING in a situation where the pyramidal cell fires before inhibition from the interneurons sets in. If so, the interval between spiking of the pyramidal cell and the interneurons should be less than the time necessary for spikes from the interneurons to reach and effectively inhibit the pyramidal cell.

Various experiments show shifts of the frequency generated by cortical circuits when the influence of the excitatory input on the interneurons decreases via, for example, optogenetic silencing of the local pyramidal cells in vivo (Craig and McBain, 2015) or applying an antagonist of fast excitatory synaptic coupling in vitro (LeBeau et al., 2002). One might guess that if the cortical circuits produce oscillations whose frequency changes when one decreases the local excitatory input, the oscillations are likely to be PING because the oscillations depend on the excitation-inhibition loop. However, our studies in the two-neuron networks and in larger networks (**Chapter 2**) suggest that knowing only that the frequency changes when removing the local  $E \rightarrow I$  inputs  $\varepsilon_{E \rightarrow I}$  (by silencing pyramidal cells or disabling fast excitatory synaptic inputs) is not enough to determine whether the cortical circuits operate in either PING or ING mode. We also need to know the type

of the interneurons and the direction of change of the frequency to pinpoint whether the cortical circuits produce PING or ING oscillations.

Overall, we provide a mathematical framework to construct phase oscillators that can be described by a single voltage variable with voltage-independent input, based on basically any smooth infinitesimal phase response curve. Furthermore, we constructed iteration maps characterizing the dynamics of two-neuron networks. We used them to analyze how regular PING and ING oscillations in the two-neuron network interact. Our results show that the winning mechanism (either PING or ING) is the one with the higher frequency in the full and pure networks. Except for possible small coexistence regions, it will suppress the other one since it absorbs all “resources” (neurons ready to spike) available to maintain a rhythm.

## 3.8 Appendix

### 3.8.1 Comparison of our sine neuron with the radial isochron clock

The radial isochron clock or Andronov-Hopf oscillator (e.g. Glass and Mackey (1988); Goel and Ermentrout (2002); Izhikevich (2007)) is the normal form of systems near Hopf bifurcations. It is a two-dimensional dynamical system with the unit cycle as attractor. The dynamical equations for the radial and angular state variables are

$$\frac{dr}{dt} = \Lambda r(1-r)^2, \quad (3-A1)$$

$$\frac{d\varphi}{dt} = 1, \quad (3-A2)$$

with sufficiently large parameter  $\Lambda$  such that deflections in the radial direction are quickly eliminated and input pulses meet the system practically on the limit cycle. In contrast, Eq. 3-A2 implies that angular perturbations remain. The oscillator spikes and is reset when its angle reaches  $\Theta = 2\pi$  from below. One can now posit that inputs cause a deflection into the direction of the  $x$ -coordinate,

$$\begin{pmatrix} \cos(\varphi) \\ \sin(\varphi) \end{pmatrix} \rightarrow \begin{pmatrix} \cos(\varphi) + \varepsilon \\ \sin(\varphi) \end{pmatrix}, \quad (3-A3)$$

(Glass and Mackey, 1988; Goel and Ermentrout, 2002). Note that by this definition an input cannot cause the oscillator to cross threshold, as it changes the state parallel to it. Assuming that we are and stay in the first quadrant, the angle changes as

$\varphi \rightarrow \arctan\left(\frac{\sin(\varphi)}{\varepsilon + \cos(\varphi)}\right)$ . Since the angular deflection is conserved, while the radial

variable relaxes to one, the phase after the input is

$H_{\text{RIC}}(\varphi, \varepsilon) = \arctan\left(\frac{\sin(\varphi)}{\varepsilon + \cos(\varphi)}\right)$ . If we do not stay within the first quadrant, we

need to extend the definition,

$$H_{\text{RIC}}(\varphi, \varepsilon) = \begin{cases} \arctan\left(\frac{\sin(\varphi)}{\varepsilon + \cos(\varphi)}\right) & \text{for } \varphi \in ]0, \pi[ \text{ and } \cos(\varphi) + \varepsilon > 0, \\ \arctan\left(\frac{\sin(\varphi)}{\varepsilon + \cos(\varphi)}\right) + \pi & \text{for } \cos(\varphi) + \varepsilon < 0, \\ \arctan\left(\frac{\sin(\varphi)}{\varepsilon + \cos(\varphi)}\right) + 2\pi & \text{for } \varphi \in ]\pi, 2\pi[ \text{ and } \cos(\varphi) + \varepsilon > 0, \end{cases} \quad (3-A4)$$

with the appropriate continuations at the borders. The first derivative with respect to  $\varepsilon$  reads

$$\frac{\partial H_{\text{RIC}}(\varphi, \varepsilon)}{\partial \varepsilon} = -\frac{\sin(\varphi)}{1 + 2\varepsilon \cos(\varphi) + \varepsilon^2}. \quad (3-A5)$$

Equation 3-A5 specifies in linear approximation the change of the current phase  $H_{\text{RIC}}(\varphi, \varepsilon)$ , in terms of the already received input  $\varepsilon$  and the initial phase  $\varphi$ . This is in contrast to the differential equation Eq. 3-A5, which specifies the phase change in terms of the current phase. For  $\varepsilon = 0$  the initial phase equals the current phase, so Eq. 3-A5 yields the iPRC. Since

$$\left. \frac{\partial H_{\text{RIC}}(\varphi, \varepsilon)}{\partial \varepsilon} \right|_{\varepsilon=0} = -\sin(\varphi), \quad (3-A6)$$

the neuron is a sine neuron. It is, however, not the same sine-neuron as ours, see sec. 3.3.2. The transfer function of our sine-neuron can be obtained via the autonomous differential equation

$$\frac{\partial H_{\text{sine}}(\varphi, \varepsilon)}{\partial \varepsilon} = i\text{PRC}(H_{\text{sine}}(\varphi, \varepsilon)) = -\sin(H_{\text{sine}}(\varphi, \varepsilon)), \quad (3-A7)$$

cf. Eq. 3-31. The right-hand side of the equation does not depend on  $\varepsilon$  and is therefore uniquely specified by the iPRC. Solving Eq. 3-A7 using separation of variables yields for a neuron with period  $\Theta = 2\pi$

$$H_{\text{sine}}(\varphi, \varepsilon) = \begin{cases} 2 \arctan \left( \tan \left( \frac{\varphi}{2} \right) e^{-\varepsilon} \right) & \text{for } \varphi \in ]0, \pi[, \\ 2 \arctan \left( \tan \left( \frac{\varphi}{2} \right) e^{-\varepsilon} \right) + 2\pi & \text{for } \varphi \in ]\pi, 2\pi[, \end{cases} \quad (3-A8)$$

with appropriate continuations, cf. Eq. 3-39. The first derivative (e.g. computed from Eq. 3-A7) then explicitly reads

$$\begin{aligned} \frac{\partial H_{\text{sine}}(\varphi, \varepsilon)}{\partial \varepsilon} &= -\sin(H_{\text{sine}}(\varphi, \varepsilon)), \\ &= -\sin \left( 2 \arctan \left( \tan \left( \frac{\varphi}{2} \right) e^{-\varepsilon} \right) \right), \\ &= -\frac{2e^{\varepsilon} \tan \left( \frac{\varphi}{2} \right)}{e^{2\varepsilon} + \tan \left( \frac{\varphi}{2} \right)^2}, \end{aligned} \quad (3-A9)$$

which agrees only for  $\varepsilon = 0$  with Eq. 3-A5. We may conclude that  $H_{\text{RIC}}(\varphi, \varepsilon)$  does not obey the autonomous differential equation Eq. 3-31, but a non-autonomous one, where the right-hand side depends explicitly on the independent variable  $\varepsilon$  and which reduces to the iPRC at  $\varepsilon = 0$ . Graphically speaking: Consider a small input

piece  $d\tilde{\varepsilon}$  of a total input  $\varepsilon$ .  $d\tilde{\varepsilon}$  arrives after the input piece  $\tilde{\varepsilon}$  of  $\varepsilon$  has already been received. Then the impact of  $d\tilde{\varepsilon}$  does not only depend on the phase  $\varphi(\tilde{\varepsilon}) = H_{\text{RIC}}(\varphi, \tilde{\varepsilon})$  reached due to  $\tilde{\varepsilon}$  but also explicitly on  $\tilde{\varepsilon}$  itself.

The series expansions in  $\varepsilon$  of  $H_{\text{RIC}}(\varphi, \varepsilon)$  and  $H_{\text{sine}}(\varphi, \varepsilon)$  around zero differ from second order on (they agree by definition up to first order),

$$H_{\text{RIC}}(\varphi, \varepsilon) = \varphi - \sin(\varphi)\varepsilon + \frac{1}{2}\sin(2\varphi)\varepsilon^2 + O(\varepsilon^3), \quad (3\text{-A10})$$

$$H_{\text{sine}}(\varphi, \varepsilon) = \varphi - \sin(\varphi)\varepsilon + \frac{1}{4}\sin(2\varphi)\varepsilon^2 + O(\varepsilon^3). \quad (3\text{-A11})$$

Equations 3-31 and 3-A7 allow to compute expressions for the higher order derivatives and thus Taylor coefficients of its solution by differentiating both sides and replacing derivatives appearing on the right-hand side using the original equation. We note that as second derivative we obtain

$$\frac{\partial^2 H(\varphi, \varepsilon)}{\partial \varepsilon^2} = i\text{PRC}'(\varphi)i\text{PRC}(\varphi), \text{ which implies a second order Taylor coefficient}$$

$$\frac{1}{2}(\sin(\varphi)\cos(\varphi)) = \frac{1}{4}\sin(2\varphi) \text{ as present in Eq. 3-A11 but not in Eq. 3-A10. Figure}$$

3-A1 illustrates the increasing discrepancy of  $H_{\text{RIC}}(\varphi, \varepsilon)$  and  $H_{\text{sine}}(\varphi, \varepsilon)$  for increasing  $\varepsilon$ . For  $\varepsilon = 1$ ,  $H_{\text{RIC}}(\varphi, \varepsilon)$  has a singularity (at  $\varphi = \pi$ ) and beyond a discontinuity.

### 3.8.2 Additional scenarios

#### *Scenario 1*

Scenario 1, where only the I neuron spikes, occurs for

$$\Delta\psi \leq -\tau. \quad (3\text{-A12})$$

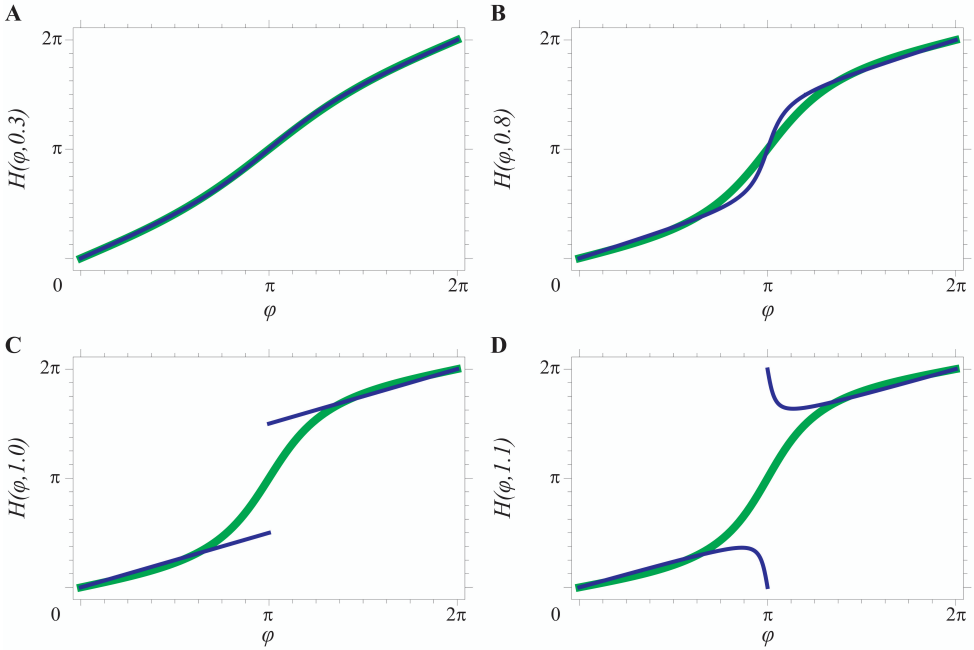


**Figure 3-A1.** Comparison of  $H_{\text{sine}}(\varphi, \varepsilon)$  (green) with  $H_{\text{RIC}}(\varphi, \varepsilon)$  (blue) for different values of  $\varepsilon$  ( $\varepsilon = 0.3, 0.8, 1$ , and  $1.1$  in panels *A*, *B*, *C*, and *D*).

The remaining I and E phases at the start of the interaction sequence are

$$\psi_I = 0, \quad (3\text{-A13})$$

$$\psi_E = \Delta\psi. \quad (3\text{-A14})$$

The interaction sequence in scenario 1 consists of sending and receiving of an I spike. The I neuron is reset after spiking. Thus, it receives its own spike while having the phase

$$\varphi_I(\tau) = \tau, \quad (3\text{-A15})$$

$$\psi_I(\tau) = \tau - \Theta_I. \quad (3\text{-A16})$$

After input processing and thus directly at the end of the interaction sequence, the phase is

$$\tilde{\varphi}_I = H_I(\tau, \varepsilon_{I \rightarrow I}), \quad (3-A17)$$

$$\tilde{\psi}_I = H_I(\tau, \varepsilon_{I \rightarrow I}) - \Theta_I. \quad (3-A18)$$

The E neuron receives the I spike while having a phase  $\varphi_E(0) + \tau = \Theta_E + \Delta\psi + \tau$ .

The E phase directly after the interaction sequence is thus

$$\tilde{\varphi}_E = H_E(\Theta_E + \Delta\psi + \tau, \varepsilon_{I \rightarrow E}), \quad (3-A19)$$

$$\tilde{\psi}_E = H_E(\Theta_E + \Delta\psi + \tau, \varepsilon_{I \rightarrow E}) - \Theta_E. \quad (3-A20)$$

Equations 3-A20 and 3-A18 yield the phase difference after the interaction,

$$\Delta\tilde{\psi} = \underbrace{H_E(\Theta_E + \Delta\psi + \tau, \varepsilon_{I \rightarrow E}) - H_I(\tau, \varepsilon_{I \rightarrow I})}_{=: G(\Delta\psi)} - \Delta\Theta. \quad (3-A21)$$

Scenario 1 can only generate regular oscillation with alternating firing of both neurons together with scenario 5 (see the related paragraph below). However, scenario 1 can repeat to give rise to a regular oscillation with suppressed E neuron. The I neuron has the same dynamics if the  $\varepsilon_{E \rightarrow I}$  connection is deleted, i.e. if we have a “pure ING” rhythm, even if the E neuron still spikes. We compute its frequency for comparison purposes.  $\Delta\psi$  at the beginning and end of the scenario is given by the solution of

$$G(\Delta\psi) = \Delta\psi. \quad (3-A22)$$

If a real-valued solution of Eq. 3-A22 exists, the system can generate the oscillation. The oscillation's period can be determined directly from dynamics of the I neuron in terms of  $\Delta\psi$ . The I neuron spikes at the beginning of the scenario. The generated spike arrives the I neuron after the duration  $\tau$  and induces an instantaneous change of the phase from  $\tau$  to  $H_I(\tau, \varepsilon_{I \rightarrow I})$ . To reach threshold and spike again, the I neuron needs the temporal duration of  $\Theta_I - H_I(\tau, \varepsilon_{I \rightarrow I})$ . The period of the oscillation is the sum of the two durations and the oscillation frequency is given by

$$f = [\tau + \Theta_I - H_I(\tau, \varepsilon_{I \rightarrow I})]^{-1}. \quad (3-A23)$$



*Scenario 3*

In scenario 3, first the E neuron spikes and then the I neuron, before the spike from the E neuron arrives. This scenario occurs for

$$0 \leq \Delta\psi < \tau. \quad (3-A24)$$

The E neuron is leading, so the I and E phases at the start of the interaction sequence read

$$\psi_I = -\Delta\psi, \quad (3-A25)$$

$$\psi_E = 0. \quad (3-A26)$$

The E neuron sends its spike and is reset at time  $t = 0^+$ , the I neuron is reset at time  $\Delta\psi^+$ , so the I neuron receives the E spike, while having a phase  $\tau - \Delta\psi$  at time  $\tau$ . Processing of the E spike by the I neuron yields  $H_I(\tau - \Delta\psi, \varepsilon_{E \rightarrow I})$  and subsequent time evolution until the receiving of the I spike by both the E and I neurons adds  $\Delta\psi$  to the phase. We may assume  $H_I(\tau - \Delta\psi, \varepsilon_{E \rightarrow I}) + \Delta\psi < \Theta_I$  and thus exclude direct generation of a spike of the I neuron because of the arrival of the spike from the E neurons, since such a spike would break a regular oscillation. Accounting for the I spike that arrives at the E and I neurons at time  $\tau + \Delta\psi$  we obtain at the end of the scenario

$$\tilde{\varphi}_I = H_I(H_I(\tau - \Delta\psi, \varepsilon_{E \rightarrow I}) + \Delta\psi, \varepsilon_{I \rightarrow I}), \quad (3-A27)$$

$$\tilde{\psi}_I = H_I(H_I(\tau - \Delta\psi, \varepsilon_{E \rightarrow I}) + \Delta\psi, \varepsilon_{I \rightarrow I}) - \Theta_I, \quad (3-A28)$$

and

$$\tilde{\varphi}_E = H_E(\tau + \Delta\psi, \varepsilon_{I \rightarrow E}), \quad (3-A29)$$

$$\tilde{\psi}_E = H_E(\tau + \Delta\psi, \varepsilon_{I \rightarrow E}) - \Theta_E. \quad (3-A30)$$

We conclude

$$\Delta\tilde{\psi} = \underbrace{H_E(\tau + \Delta\psi, \varepsilon_{I \rightarrow E}) - H_I(H_I(\tau - \Delta\psi, \varepsilon_{E \rightarrow I}) + \Delta\psi, \varepsilon_{I \rightarrow I})}_{=: G(\Delta\psi)} - \Delta\Theta. \quad (3-A31)$$

Scenario 3 can repeat to give rise to regular oscillations. As before, if a real-valued solution of

$$G(\Delta\psi) = \Delta\psi \quad (3-A32)$$

exists, the network can generate the oscillations and the solution  $\Delta\psi$  specifies the underlying phase dynamics. The oscillation's frequency can be determined directly from dynamics of the E neuron in terms of  $\Delta\psi$ . At the beginning of the scenario, the E neuron spikes, and at the end the E neuron's phase is given by Eq. 3-A29. It thus spikes again after a time duration of  $\Theta_E - H_{LIF}(\tau + \Delta\psi, \varepsilon_{I \rightarrow E}; \Theta_E)$  to complete the oscillation cycle. The period of the oscillation is the sum of the durations  $\tau + \Delta\psi$  of the interaction sequence and the time to complete the cycle, such that the oscillation frequency is given by

$$f(\Delta\psi) = \left[ \tau + \Delta\psi + \Theta_E - H_{LIF}(\tau + \Delta\psi, \varepsilon_{I \rightarrow E}; \Theta_E) \right]^{-1}. \quad (3-A33)$$

When the E and I neurons are LIF neurons, Eq. 3-A32 yields

$$\Delta\psi = \ln \left\{ \frac{\Gamma(\Theta_I, \varepsilon_{I \rightarrow I}) + e^{-\tau + \Delta\Theta} - e^{-\tau}}{2\Gamma(\Theta_E, \varepsilon_{I \rightarrow E})} \pm \frac{\sqrt{\left[ e^{-\tau} - \Gamma(\Theta_I, \varepsilon_{I \rightarrow I}) - e^{-\tau + \Delta\Theta} \right]^2 + 4\Gamma(\Theta_E, \varepsilon_{I \rightarrow E})\Gamma(\Theta_I, \varepsilon_{E \rightarrow I})e^{\Delta\Theta}}}{2\Gamma(\Theta_E, \varepsilon_{I \rightarrow E})} \right\} \quad (3-A34)$$

$$- \Delta\Theta,$$

where  $\Gamma(\Theta, \varepsilon)$  is given by Eq. 3-56. Placing  $\Delta\psi$  given in Eq. 3-A34 into Eq. 3-A33 yields the frequency of the oscillation.

If the I neuron is the sine neuron, the E spike arrives at the I neuron at a phase that is always within the first branch, i.e. within  $]0, \Theta / 2[$ , because we assume that the intrinsic period of the neurons should be longer than  $2\tau$ .  $H_I(\tau - \Delta\psi, \varepsilon_{E \rightarrow I})$  in Eq. 3-A31 is then explicitly defined by the first line of Eq. 3-39 and the excitatory

input delays the phase of the I neuron. The I spike thus also always arrives at the I neuron at a phase within the first branch and advances the phase.

### Scenario 5

Scenario 5 (cf. Fig. 3-4) is similar to scenario 1, with only the E neuron spiking. It occurs for

$$\Theta_I + \tau - H_I(\Theta_I, -\varepsilon_{E \rightarrow I}) < \Delta\psi, \quad (3-A35)$$

the phases of the I and E neurons at the start of the interaction sequence are

$$\psi_I = -\Delta\psi, \quad (3-A36)$$

$$\psi_E = 0. \quad (3-A37)$$

The E neuron sends a spike at the beginning of the sequence, which is received by the I neuron at  $t = \tau$ . Since the I neuron does not spike, this marks the end of the scenario. The phase  $\varphi_I$  of the I neuron at receiving is

$$\varphi_I = \Theta_I - \Delta\psi + \tau. \quad (3-A38)$$

After the receiving, at the end of the scenario it reads

$$\tilde{\varphi}_I = H_I(\Theta_I - \Delta\psi + \tau, \varepsilon_{E \rightarrow I}), \quad (3-A39)$$

$$\tilde{\psi}_I = H_I(\Theta_I - \Delta\psi + \tau, \varepsilon_{E \rightarrow I}) - \Theta_I. \quad (3-A40)$$

The condition  $\Theta_I + \tau - H_I(\Theta_I, -\varepsilon_{E \rightarrow I}) < \Delta\psi$  implies  $H_I(\Theta_I - \Delta\psi + \tau, \varepsilon_{E \rightarrow I}) < \Theta_I$ , such that the I neuron does not spike. The E neuron evolves freely after its reset at  $t = 0^+$ , so

$$\tilde{\varphi}_E = \tau, \quad (3-A41)$$

$$\tilde{\psi}_E = \tau - \Theta_E, \quad (3-A42)$$

which yields

$$\Delta\tilde{\psi} = \tau - \underbrace{H_I(\Theta_I + \tau - \Delta\psi, \varepsilon_{E \rightarrow I})}_{=: G(\Delta\psi)} - \Delta\Theta. \quad (3-A43)$$

*Alternation between scenarios 5 and 1*

In scenarios 2, 3, and 4 both neurons spike such that regular oscillations with alternating firing must be generated by repeating a single scenario. In contrast, scenarios 1 and 5 have to alternate to generate a regular oscillation. Without loss of generality, we assume that the spiking pattern begins with scenario 5 and scenario 1 follows.  $\Delta\psi$  at  $t=0$  has to satisfy Eq. 3-A35 for scenario 5 to occur.  $\Delta\tilde{\psi}$  after scenario 5 given in Eq. 3-A43 has to satisfy Eq. 3-A12 for scenario 1 to occur. Thus, alternation between scenarios 5 and 1 occurs for

$$\Theta_I + \tau - H_I(\Theta_I, -\varepsilon_{E \rightarrow I}) < \Delta\psi, \quad (3-A44)$$

$$2\tau - \Delta\Theta \leq H_I(\Theta_I + \tau - \Delta\psi, \varepsilon_{E \rightarrow I}). \quad (3-A45)$$

Composing the maps Eqs. 3-A43 and 3-A21, we obtain

$$\Delta\tilde{\psi} = H_E\left(\Theta_I + 2\tau - H_I(\Theta_I + \tau - \Delta\psi, \varepsilon_{E \rightarrow I}), \varepsilon_{I \rightarrow E}\right) - \underbrace{H_I(\tau, \varepsilon_{I \rightarrow I}) - \Delta\Theta}_{=: G^2(\Delta\psi)} \quad (3-A46)$$

Note that now we have two iterations of the map  $G$ , which maps the remaining phase difference before scenario 5 to the remaining phase difference after scenario 1. To determine the phase underlying the oscillation, we need to solve

$$\Delta\psi = G^2(\Delta\psi)$$

for  $\Delta\psi$ . If a real-valued solution  $\Delta\psi$  exists, the network can generate the oscillations. Its frequency can then be derived in terms of  $\Delta\psi$ : In the initial scenario 5 (cf. Fig. 3-4B), the E neuron spikes at time  $t=0$ . The E and I phases at the scenario's end are given by Eqs. 3-A39 and 3-A41. The duration of the scenario is  $\tau$ . Initializing scenario 1, the I neuron spikes after the duration of  $\Theta_I - H_I(\Theta_I + \tau - \Delta\psi, \varepsilon_{E \rightarrow I})$ . The output from the I neuron arrives at the E neuron at the phase  $2\tau + \Theta_I - H_I(\Theta_I + \tau - \Delta\psi, \varepsilon_{E \rightarrow I})$  of the E neuron and causes its phase to jump to  $H_E(2\tau + \Theta_I - H_I(\Theta_I + \tau - \Delta\psi, \varepsilon_{E \rightarrow I}), \varepsilon_{I \rightarrow E})$ . The duration of scenario 1 is  $\tau$  as well. The E neuron needs a temporal duration of

$\Theta_E - H_E(2\tau + \Theta_I - H_I(\Theta_I + \tau - \Delta\psi, \varepsilon_{E \rightarrow I}), \varepsilon_{I \rightarrow E})$  until it spikes again and completes the oscillation cycle. The period of the spiking pattern of alternation between scenarios 5 and 1 thus equals  $2\tau + \Theta_E + \Theta_I - H_I(\Theta_I + \tau - \Delta\psi, \varepsilon_{E \rightarrow I}) - H_E(2\tau + \Theta_I - H_I(\Theta_I + \tau - \Delta\psi, \varepsilon_{E \rightarrow I}), \varepsilon_{I \rightarrow E})$  and the frequency is

$$f(\Delta\psi) = \left[ 2\tau + \Theta_E + \Theta_I - H_I(\Theta_I + \tau - \Delta\psi, \varepsilon_{E \rightarrow I}) - H_E(2\tau + \Theta_I - H_I(\Theta_I + \tau - \Delta\psi, \varepsilon_{E \rightarrow I}), \varepsilon_{I \rightarrow E}) \right]^{-1}. \quad (3-A47)$$

# 4

## **When long-range zero-lag synchronization is feasible**

Atthaphon Viriyopase

Ingo Bojak

Magteld Zeitler-Geurds

C.C.A.M. Gielen

Published in *Frontiers in Computational Neuroscience* 6 (2012): 49

## 4.1 Introduction

Coupling between different oscillators and pacemakers can generate a large range of different behaviors and has been a topic of study in many different conditions, for example in cardiac pacemaking and chemical oscillations (see also e.g. Goldbeter (1997); Koch and Segev (1998); Roxin et al. (2005)). A special case is the interaction between neurons that gives rise to neuronal oscillations in particular frequency bands. Neuronal gamma band synchronization has been reported in many species and in a large number of brain structures for a variety of sensory and motor tasks (Gray et al., 1989; Fries et al., 2001; Pesaran et al., 2002; Schoffelen et al., 2005; Fries et al., 2008). This large-scale synchronization of multiple cortical areas has been postulated as a potential mechanism for integration and coordination of neuronal activity in cognitive tasks (Engel et al., 1992; Singer and Gray, 1995; Fries, 2005).

The first studies on this topic presented experimental evidence that the relative phase of gamma oscillations in widely separated brain areas is near zero (Frien et al., 1994; Roelfsema et al., 1997; Castelo-Branco et al., 1998; Rodriguez et al., 1999; Gross et al., 2004). This result was remarkable since synchronization requires interactions between distant brain areas that come with considerable delays due to axonal conduction and synaptic transmission. Many further studies hence investigated how distant oscillatory brain regions can synchronize at zero-lag in spite of non-negligible delays. Several theoretical studies have argued that direct mutual pulse-coupling between two dynamical systems with delays and excitatory synapses cannot easily lead to zero-lag synchrony (Ernst et al., 1995, 1998; Goel and Ermentrout, 2002; Zeitler et al., 2009). Therefore, Fischer et al. (2006) and Vicente et al. (2008) suggested that zero-lag synchronization between brain areas might be mediated by a third (relay) oscillator. A potential candidate for this neuronal relay oscillator is the thalamus (Gollo et al., 2010; Theyel et al., 2010).

To obtain a better understanding of the possibilities for zero-lag synchronization of distant brain areas, we have investigated the proposed network of neuronal oscillators coupled indirectly by a relay oscillator (Fischer et al., 2006; Vicente et al., 2008). We have investigated the model with both

type I Mirolo-Strogatz neurons as well as with type II Hodgkin-Huxley neurons. We focused in particular on the robustness of zero phase synchronization as a function of both the delay time between oscillators and the strength of synaptic coupling. Various types of synaptic coupling were investigated, including spike-timing dependent plasticity (STDP), since STDP has been suggested to contribute to efficient information transmission (Buonomano and Maass, 2009; Lindner et al., 2009; Hennequin et al., 2010). Our results show that zero-lag synchrony can occur, especially for models with Hodgkin-Huxley type II neurons. STDP facilitates zero-lag synchrony as STDP modifies synaptic strengths and thereby allows a larger range of initial synaptic strengths that may lead at zero-lag synchronization.

## 4.2 Materials and methods

The model consists of three coupled neuronal oscillators (see Fig. 4-1A). Each oscillator can be considered as a single neuron or as a population of neurons, where the activity of the neurons within each population is assumed to be homogeneous and highly synchronized. As illustrated in Fig. 4-1A, the “relay” or “inner” oscillator (oscillator 2) is coupled bi-directionally with two “outer” oscillators (oscillators 1 and 3). The outer oscillators are only coupled with the relay oscillator but not directly to each other. As starting point we assume that all three oscillators are identical with the same intrinsic firing period  $T_0$ .

We have used the Mirolo-Strogatz (MS) phase oscillator (Mirolo and Strogatz, 1990) and the classical Hodgkin-Huxley (HH) neuron (Hodgkin and Huxley, 1952) with parameters given in Vicente et al. (2008). For the MS phase oscillator,  $T_0$  is chosen to be 25 ms and  $T_0$  of the HH neuron is 14.66 ms with the parameters given in Vicente et al. (2008). In Fig. 4-1A  $\varepsilon_{ij}$  represents the coupling strength from presynaptic oscillator  $j$  to postsynaptic oscillator  $i$ . All synaptic couplings in the model are excitatory. The delay time  $\tau_k$  represents the conduction time for spikes along axons that connect oscillator  $k$  with the relay oscillator. Here we make the simplifying assumption that delay times are constant and symmetric (i.e., the delay time from oscillator  $i$  to  $j$  is equal to that from oscillator  $j$  to  $i$ ). These delay times are typically considerably shorter than the period of neuronal



oscillations (Fries, 2005). Therefore, in the following we will only consider conduction delays shorter than  $T_0/2$ , with  $\tau_k$  expressed as a fraction of the intrinsic period  $T_0$  and thus in the range between 0 and 0.5.

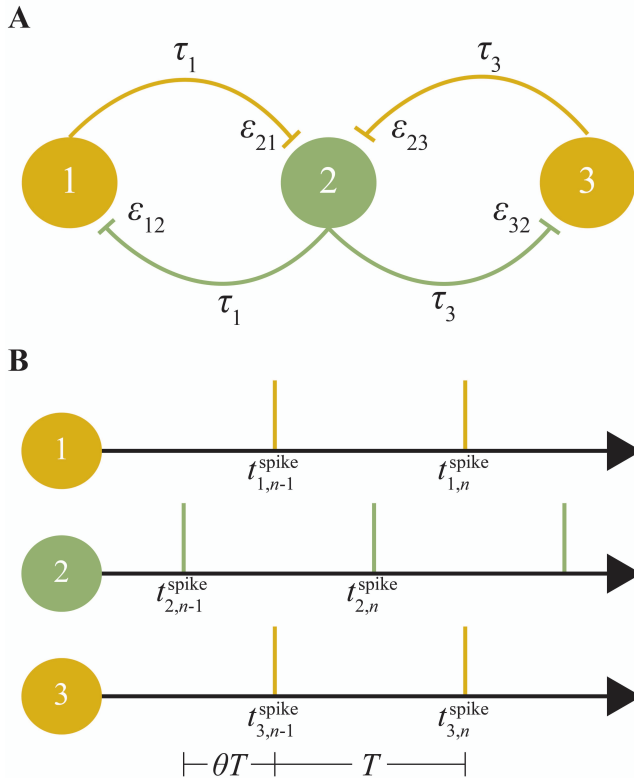


**Figure 4-1. Schematic of the model and its 1:1 phase-locked zero-lag synchrony mode.** *A*, Sketch of oscillators 1 and 3 with bi-directional pulse coupling via relay oscillator 2.  $\epsilon_{ij}$  represents the excitatory synaptic weight from oscillator  $j$  to oscillator  $i$ ,  $\tau_k$  the conduction delay between relay oscillator 2 and oscillator  $k$ . *B*, An example of 1:1 phase-locked zero-lag synchrony mode. Vertical bars represent the spike times of the oscillators.  $T_0$  is the intrinsic period of the oscillators,  $T < T_0$  the common period of the oscillators in the phase-locked mode, and  $\theta T$  the delay between the firing of the relay and the outer oscillators.  $t_{1,n}^{\text{spike}}$ ,  $t_{2,n}^{\text{spike}}$ , and  $t_{3,n}^{\text{spike}}$  are the  $n$ -th spike times of oscillators 1, 2, and 3, respectively.

The MS phase oscillator (Mirollo and Strogatz, 1990) is characterized by a voltage-like state variable  $f \in [0,1]$ , which increases monotonically from 0 towards the threshold value  $f = 1$ . Within a cycle, the state of the uncoupled neuronal oscillator is defined by a monotonically increasing concave function  $f(\varphi): [0,1] \rightarrow [0,1]$ :

$$f(\varphi) = \frac{1}{b} \ln \left[ 1 + (e^b - 1) \varphi \right], \quad (4-1)$$

$$\frac{d\varphi}{dt} = \frac{1}{T_0}, \quad (4-2)$$

with a phase variable  $\varphi \in [0,1]$  and a dissipation parameter  $b$ .  $T_0$  is the intrinsic firing period of the oscillator. When the threshold is reached, the oscillator fires, the state variable  $f$  is reset to zero, and the cycle repeats. As in Ernst et al. (1995) and Zeitler et al. (2009), the setting  $b = 3$  is used throughout this study. The MS neuron is a so-called type I neuron (Izhikevich, 2007), where excitatory input always gives a phase advance of the neuronal oscillator.

For the classical HH neuron the membrane potential  $V$  is governed by the differential equation:

$$C \frac{dV}{dt} = -g_{Na} m^3 h (V - E_{Na}) - g_K n^4 (V - E_K) - g_L (V - E_L) + I_{ext} + I_{syn}, \quad (4-3)$$

with the membrane capacitance  $C$  and the maximal conductance of sodium  $g_{Na}$ , potassium  $g_K$ , and leakage  $g_L$ . The corresponding reversal potentials  $(E_{Na}, E_K, E_L)$  and the external current  $I_{ext}$  are as given in Vicente et al. (2008). The voltage-gated ion channels  $m, h$ , and  $n$  are described by first order differential equations. Note that the expression for  $\alpha_n$  in Vicente et al. (2008) was not correct and should be read as  $\alpha_n(V) = [(V + 55)/100] / \{1 - \exp[-0.1(V + 55)]\}$ . The excitatory synaptic current  $I_{syn}$  is  $-\varepsilon_{ij} S(t) V$ , where  $\varepsilon_{ij}$  is the maximum synaptic conductance and  $S(t)$  is the Dirac delta function (in case of an “instantaneous

synapse”) or an alpha function (in case of an “alpha synapse”). This classical HH neuron is a so-called type II neuron (Izhikevich, 2007), where excitatory input in early phases of the firing cycle causes a phase delay but a phase advance in later phases of the firing cycle.

#### 4.2.1 Synaptic coupling

We investigate two models for pulse-coupling between the oscillators. For an instantaneous synapse with coupling strength  $\varepsilon_{ij}$ , the neuronal state  $f_i$  of the MS phase oscillator after arrival of a spike from oscillator  $j$  is incremented instantaneously

$$f_i^{\text{new}}(\varphi_i) = \min[f_i(\varphi_i) + \varepsilon_{ij}, 1], \quad (4-4)$$

with  $\varphi_i$  the phase of the postsynaptic oscillator  $i$  at the time of the spike arrival. The phase  $\varphi_i$  for which the oscillator reaches the threshold after spike input (i.e.  $f_i(\varphi_i) + \varepsilon_{ij} = 1$ ) is called the critical phase  $\varphi_c$  (Zeitler et al., 2009) and is given by

$$\varphi_c(\varepsilon_{ij}) = \frac{e^{b(1-\varepsilon_{ij})} - 1}{e^b - 1}. \quad (4-5)$$

If a spike arrives at  $\varphi_i < \varphi_c$ ,  $f_i$  will increase instantaneously by  $\varepsilon_{ij}$ . The instantaneous change of the state  $f_i$  by  $\varepsilon_{ij}$  corresponds to a phase shift  $\Delta\varphi_i = f_i^{-1}[f_i(\varphi_i) + \varepsilon_{ij}] - \varphi_i$ , which yields

$$\Delta\varphi_i(\varphi_i; \varepsilon_{ij}) = \begin{cases} \chi_b(\varepsilon_{ij}) + \beta_b(\varepsilon_{ij})\varphi_i & \text{for } 0 \leq \varphi_i < \varphi_c, \\ 1 - \varphi_i & \text{for } \varphi_c \leq \varphi_i < 1, \end{cases} \quad (4-6)$$

with

$$\chi_b(x) := \frac{\beta_b(x)}{\beta_b(1)}, \beta_b(x) := e^{bx} - 1, \quad (4-7)$$

where  $\varphi_i$  is the phase of the postsynaptic oscillator just before arrival of the input spike. Note that  $\varphi_c(\varepsilon_{ij}) = \left[1 - \chi_b(\varepsilon_{ij})\right] / \left[1 + \beta_b(\varepsilon_{ij})\right]$ .

Tsubo et al. (2007) measured the phase shifts of layer-5 and layer-2/3 pyramidal neurons in rat motor cortex. The maxima of the averaged phase shifts were found to be in the second half of the oscillatory period for these neurons at all frequencies (including the gamma band; see their Fig. 4). Hence, we require here that the maximum of the phase shift  $\Delta\varphi_i$  is in the second part of the intrinsic cycle of the oscillator, and therefore  $\varphi_c > 0.5$ . This restriction imposes an upper bound of  $\varepsilon_{ij} < 1 - \ln\left[\left(1 + e^b\right)/2\right]/b = 0.21$  for  $b = 3$  on the synaptic strength through Eq. 4-5. In case of  $\varepsilon_{ij} = 0.21$ , a spike can cause an increase in the state variable  $f$  of about 21% of the difference between rest state  $f = 0$  and the threshold value  $f = 1$ . For the HH neuron, the upper bound for the maximum synaptic conductance is  $3.15 \text{ mS/cm}^2$ , which corresponds to an increase of 21% of  $(V_{onset} - V_{rest})$ , since the resting potential  $V_{rest}$  and the onset of the action potential  $V_{onset}$  are near -65 and -50 mV, respectively.

A more realistic synaptic coupling model is provided by the so-called alpha function. For an ‘‘alpha synapse’’, the postsynaptic potential after arrival of a spike at time  $t_0$  at the synapse with strength  $\varepsilon_{ij}$  is described by

$$\alpha(t; \varepsilon_{ij}, \tau_{syn}) = \begin{cases} 0 & \text{for } t < t_0, \\ \varepsilon_{ij} \frac{t - t_0}{\tau_{syn}^2} \exp\left(-\frac{t - t_0}{\tau_{syn}}\right) & \text{for } t \geq t_0, \end{cases} \quad (4-8)$$

where  $\tau_{syn} > 0$  is the synaptic rise time of the input. Unless stated otherwise,  $\tau_{syn} = 2 \text{ ms}$  in this study. The numerical simulations are implemented using an Euler scheme with a time step size equal to  $2.5 \mu\text{s}$  ( $\approx 10^{-4} T_0$ ). In our implementation, there is no current reset after spiking of the postsynaptic neuron, i.e. the ‘‘tail’’ of the alpha function is carried over into the next cycle.

### 4.2.2 Spike-timing dependent plasticity (STDP)

In general, the synaptic coupling strength is not constant but varies depending on pre- and postsynaptic activity due to STDP (Hebb, 1949; Bi and Poo, 1998). We have implemented the additive STDP rule (Froemke et al., 2006) for both instantaneous and alpha synapses. For a presynaptic spike at arrival time  $t_k^{\text{arr}}$  and a postsynaptic spike at  $t_l^{\text{spike}}$ , the fractional synaptic modification  $W(\Delta t)$  is given by

$$W(\Delta t) := \begin{cases} A_- \exp\left(\frac{\Delta t}{\tau_-}\right) & \text{for } \Delta t < 0, \\ 0 & \text{for } \Delta t = 0, \\ A_+ \exp\left(-\frac{\Delta t}{\tau_+}\right) & \text{for } \Delta t > 0, \end{cases} \quad (4-9)$$

with  $\Delta t := t_l^{\text{spike}} - t_k^{\text{arr}}$ .

The spike arrival time  $t_k^{\text{arr}}$  is defined as the time of the onset of the postsynaptic potential, as in the experimental protocol by Bi and Poo (1998). Unless stated otherwise, the time constants for potentiation  $\tau_+$  and depression  $\tau_-$  are  $\tau_{+,0} := 16.8$  ms and  $\tau_{-,0} := 33.7$  ms, respectively. In this study the standard values for the maximum amplitude of potentiation  $A_+$  and depression  $A_-$  are  $A_{+,0} := 0.78$  and  $A_{-,0} := -0.27$ , respectively. These standard parameter values for STDP were fitted to the data from Bi and Poo (1998), who determined the fractional synaptic modification  $W$  as the relative change in synaptic strength after evoking an input and output spike pair 60 times. We assume that the change of the synaptic weight  $\Delta\varepsilon$  caused by each input spike is constant and defined by  $\Delta\varepsilon = \varepsilon_0 W(\Delta t)/60$  (Song et al., 2000; van Rossum et al., 2000) with initial synaptic weight  $\varepsilon_0$  and  $W(\Delta t)$  as in Eq. 4-9. Therefore, the learning rule used here for a particular pair of pre- and postsynaptic spikes is given by  $\varepsilon_0 \rightarrow \varepsilon_0 + \varepsilon_0 W(\Delta t)/60$ , in agreement with Lee et al. (2009).

The simulation procedure of the network for STDP is as follows: The evolution of the state of the network is studied over 60 consecutive sessions. At the

start of each session, the initial phases of the three oscillators are chosen arbitrarily from a uniform random distribution. The first session starts with equal coupling strengths for all synapses, which then change due to STDP. All succeeding sessions start with the coupling strengths that resulted at the end of the previous session but with re-randomized phases of the oscillators to prevent that the system converges into a locally rather than a globally stable state.

In order to be physiologically relevant for synchronization, convergence should not take too much time. Therefore, we assume that convergence to a stable relative phase between oscillators 1 and 3 in the model takes place within a session consisting of  $n_{\text{sess}} = 15$  cycles. Thus, with STDP we typically run 60 sessions of 15 cycles each to investigate convergence of the network into a stable synchronization state. Without STDP the couplings do not change, and a single session of 15 cycles is used. To avoid any spurious dependence on the random initial phases, we repeat each calculation  $35^3 = 42,875$  times. Thus, in the STDP case almost 40 million cycles are computed for every chosen setting of coupling strengths and delay times.

### 4.2.3 Phase-locking equation and stability analysis

Phase-locking equations are useful to determine the new period of a network and the relative phases of coupled oscillators (van Vreeswijk et al., 1994; Bressloff and Coombes, 1998). For the simple MS phase oscillator, the phase-locking equation can be derived analytically. A full analysis for our model is provided in Appendix 4.5, where we derive the relationships between synaptic weight, conduction delay, and the new period of the oscillators for zero-lag 1:1 phase-locked firing of the outer oscillators. Here we will just consider a simple example (see Fig. 4-1B).

Without loss of generality, we set the time of the  $(n-1)$ -th firing of the relay oscillator  $t_{2,n-1}^{\text{spike}} = 0$  and call the period of the 1:1 phase-locked oscillators  $T$ . For zero-lag synchrony there is a  $\theta \in [0, 1[$  such that the outer oscillators fire at  $t_{1,n-1}^{\text{spike}} = t_{3,n-1}^{\text{spike}} = \theta T$ ,  $t_{1,n}^{\text{spike}} = t_{3,n}^{\text{spike}} = \theta T + T$ , etc. For equal delays  $\tau_1 = \tau_3 = \tau$ , both spikes from the outer oscillators arrive at the relay oscillator at the phase  $\tau + \theta T/T_0$  (if  $\tau + \theta T/T_0 \leq T/T_0$ ) with excitatory coupling strength  $\varepsilon$ . The two synaptic inputs reduce the period of the relay oscillator from the intrinsic period  $T_0$  to

$$T = T_0 \left[ 1 - \Delta\varphi(\tau + \theta T/T_0; 2\varepsilon) \right], \quad (4-10)$$

with  $\Delta\varphi$  as defined in Eq. 4-6. Since the relay oscillator fires at  $T$ , the outer oscillators will each receive a spike at  $T + \tau T_0$ . The outer oscillators spiked at  $\theta T$  and hence their phase will be  $\tau + (1-\theta)T/T_0$  (if  $\tau + (1-\theta)T/T_0 \leq T/T_0$ ) at the arrival of the spike from the relay oscillator. Therefore, the period of the outer oscillators is given by

$$T = T_0 \left[ 1 - \Delta\varphi(\tau + (1-\theta)T/T_0; \varepsilon) \right]. \quad (4-11)$$

Equations 4-10 and 4-11 are the 1:1 phase-locking equations for the mentioned conditions.

Assume now that both arrival phases exceed the critical phases  $\varphi_c(2\varepsilon)$  and  $\varphi_c(\varepsilon)$ , respectively. Then rewriting Eqs. 4-10 and 4-11 using Eq. 4-6 yields

$$T = \tau T_0 + \theta T \quad \text{and} \quad T = \tau T_0 + (1-\theta)T \Rightarrow T = 2\tau T_0, \quad \theta = 1/2. \quad (4-12)$$

Thus the period of all oscillators is twice the conduction delay and activity switches between inner and outer oscillators every half period. All oscillators immediately spike upon spike input. We will call this mode the “driven synchrony” (DS) mode (see Fig. 4-2B). Two other typical modes are also illustrated in Fig. 4-2: “slave synchrony”, where only the relay oscillator spikes directly after input, and “pacemaker synchrony”, where only the outer oscillators do so.

To investigate the stability of DS, we assume small perturbations. Since we use the relay oscillator spikes as reference time, the perturbation affects the phase of the outer oscillators to  $[\tau + \delta\varphi_1, \tau + \delta\varphi_3]$  at  $t_{2,n-1}^{\text{spike}}$ . DS is asymptotically stable, if there is a  $\delta > 0$  such that the phases of outer oscillators 1 and 3 will be closer to  $\tau$  at the next spike at  $t_{2,n}^{\text{spike}}$  for  $\sqrt{\delta\varphi_1^2 + \delta\varphi_3^2} < \delta$ . Since  $\varphi_c(\varepsilon) < 2\tau$ , we can define a value  $\delta := 2\tau - \varphi_c(\varepsilon) > 0$ , and thus  $\varphi_c(\varepsilon) = 2\tau - \delta$ . The spike from the relay arrives when the phase of oscillator 1 is in the range  $2\tau - \delta < \varphi_1 < 2\tau + \delta$  that exceeds this critical phase  $\varphi_c(\varepsilon)$ . Therefore, oscillator 1 will spike immediately after receiving

input from the relay oscillator, and the same is true for oscillator 3. Thus perfect synchronization is re-established as long as the perturbation was sufficiently small, proving that the DS mode is an asymptotically stable mode. To determine the stability of other synchrony modes, it is necessary to calculate the eigenvalues  $\lambda$  of the Jacobian of the (phase) return map (Zeitler et al., 2009), see Appendix 4.5 for details.

We now briefly consider the effect of STDP on slave synchrony. The coupling strengths from the outer oscillators to the relay oscillator remain unchanged for slave synchrony, since the relay oscillator immediately spikes upon input from the outer oscillators. In Appendix 4.5 we show that the coupling strengths from the relay oscillator to the outer oscillators increase with  $\varepsilon_n > \varepsilon_{n-1}$  for  $\tau \geq 0.25$  using the STDP window  $W(\Delta t)$  of Eq. 4-9, since the spike from the relay oscillator arrives well before the outer oscillators spike. Hence synaptic weights increase to  $\varphi_c^{-1}(2\tau) = 1 - \ln[2\tau(e^b - 1) + 1]/b$ , at which point the outer oscillators also spike immediately after input and STDP stops. Thus, STDP turns slave synchrony into DS.

In the driven, pacemaker, and slave synchrony modes oscillators 1 and 3 spike simultaneously. There are other, asynchronous stable modes where this is not the case. Figure 4-3, **C** and **D**, shows the dynamics of the oscillators for a typical asynchronous case. This mode will be referred to as a “pacemaker-slave” because the relay drives oscillator 1 and is driven by oscillator 3.

#### 4.2.4 Synchronization measures

For a proper analysis of synchronized firing, a quantitative definition of synchrony is required. In experiments perfect synchrony will never be observed as noise causes small variations in the timing of action potentials. Instead we will define synchrony as firing of two oscillators within a small time window, where the time window should be sufficiently large to eliminate the effect of noise and sufficiently small to provide an accurate estimate of synchrony. While we could measure synchrony here to the limits of the numerical accuracy of our simulations, we define synchrony as the condition when the spikes of the outer oscillators occur within  $|t_{1,n}^{\text{spike}} - t_{3,n}^{\text{spike}}| \leq 0.02T_0$  (Engel and Singer, 2001), which is 0.5 ms for simulations of



the model with MS phase oscillators and 0.2932 ms for the model with the classical HH neurons.

Synchronized firing of the outer oscillators does not only depend on the synaptic weights and delay times, but also on the initial phase of the three oscillators. Hence we have to consider the robustness of convergence to synchronous firing for variations in the initial relative phase of the neuronal oscillators. Therefore, we define “*synchronization quality*” (SQ) as the fraction of the number of initial phase combinations that leads to stable synchronous firing of the outer oscillators. SQ has a value between 0% and 100%, where 100% means that the outer oscillators will always converge to synchronous spiking within the simulation period, independent of their initial phases. This provides a measure of the attraction domain of the initial phases for reaching synchronization of the outer oscillators. To determine SQ, we repeat our simulations  $35^3 = 42,875$  times with randomly chosen initial phases.

To investigate the impact of the various parameters of the STDP learning window, we wish to derive a single value for the SQ, rather than one value for each combination of synaptic weights and conduction delay. For this purpose we consider various synaptic weights in 100 evenly spaced steps in the range from 0.01 to 0.21 and conduction delays in 100 evenly spaced steps in the range from 0.01 to 0.49. Then we average the SQ over these 10,000 pairs to obtain an “average SQ” for each parameter set of the learning window. Note that for an STDP run with 60 sessions, this means that we compute almost 400 billion cycles of the model for each change of the STDP parameters.

For some combinations of the synaptic weights, delay times, and initial phases the state of zero-lag synchronization is reached faster than for other combinations. Therefore, we define a “*convergence promptness*” (CP) for the network to achieve zero-lag synchronization of the outer oscillators. This is calculated as  $CP = SQ \times \left(1 - \frac{\langle n_{\text{sync}} \rangle}{n_{\text{sess}}}\right)$ , where  $\langle n_{\text{sync}} \rangle$  is the average number of intrinsic periods  $T_0$  needed to achieve zero-lag synchrony. When there is no zero-lag synchrony established within  $n_{\text{sess}} = 15$  cycles, CP equals to 0. Note that  $\langle n_{\text{sync}} \rangle \leq n_{\text{sess}}$  with  $n_{\text{sess}} = 15$  for the simulations in this study, and that the measure

is multiplied with the SQ to account for the readiness of the system to achieve zero-lag synchrony at all.

Finally, not only are we interested in synchrony of the outer oscillators, but also in the relative phase  $\varphi_r$  for stable modes in which oscillators 1 and 3 are not in synchrony. The relative phase between the outer oscillators is defined by  $\varphi_r := (t_{3,n}^{\text{spike}} - t_{1,n}^{\text{spike}}) / T_0$  with a value between -1 and 1. Since values for  $\varphi_r$  of -1, 0, and 1 all refer to the same state, we report  $\varphi_r$  rescaled to the range  $-1/2$  to  $1/2$  by periodically mapping  $[-1, -0.5]$  to  $[0, 0.5]$  and  $[0.5, 1]$  to  $[-0.5, 0]$ , respectively.

## 4.3 Results

### 4.3.1 Equal delay times and coupling strengths

Figure 4-2, **A** and **C**, shows simulation results for the SQ and the CP, respectively, as a function of the conduction delay  $\tau$  and the synaptic weight  $\varepsilon$  for the MS model with instantaneous synapses, identical delay times ( $\tau_1 = \tau_3 = \tau$ ), and identical coupling strengths ( $\varepsilon_{12} = \varepsilon_{21} = \varepsilon_{23} = \varepsilon_{32} = \varepsilon$ ). The three solid black curves show the analytically calculated boundaries between different modes of synchrony using the phase-locking equations, for details see sec. “Synchrony modes derived from the phase-locking equation” in Appendix 4.5.1. The upper right area, indicated by IV, is bounded by the curve

$$\tau = \frac{1 - \chi_b(\varepsilon)}{2}, \quad (4-13)$$

where  $\chi_b$  is defined in Eq. 4-7. For a detailed derivation see the discussion below Eq. 4-A12 in Appendix 4.5. Our simulations show that in region IV zero-lag synchronization occurs mainly when the relay oscillator spikes immediately upon arrival of synaptic input from the outer oscillators, but the outer ones do not after input from the relay one (Fig. 4-2**B**, **middle**). The period  $T_{\text{IV}}$  of this “slave synchrony” mode is given by Eq. 4-A12 “SS2” in Appendix 4.5.

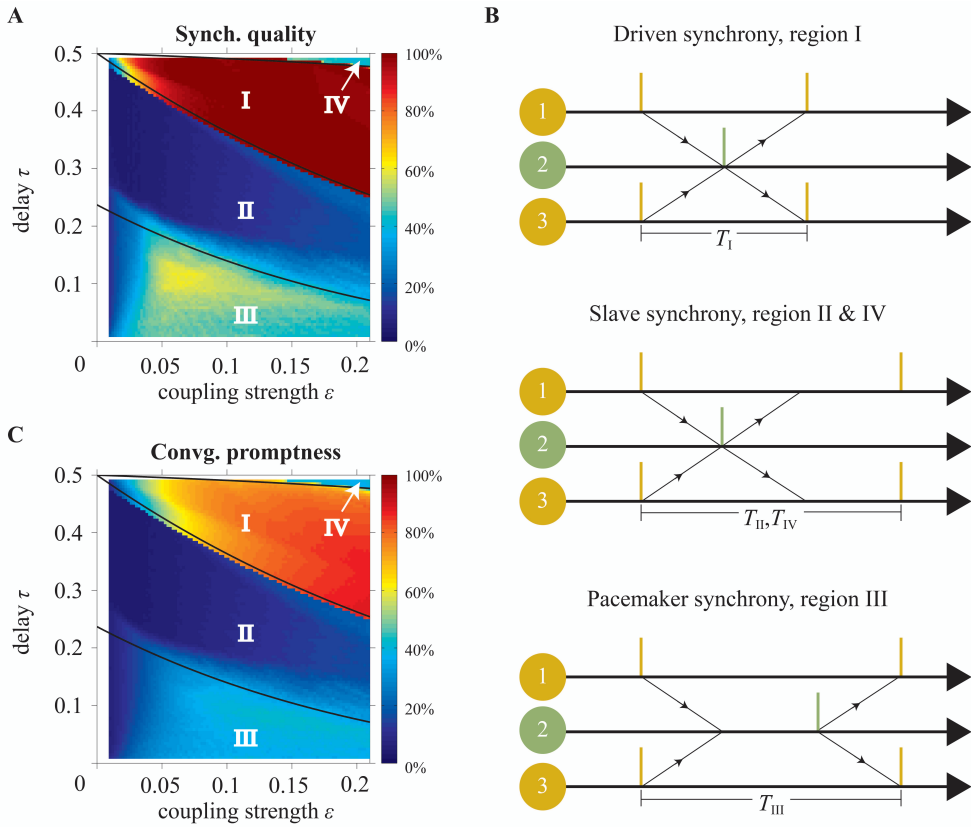


**Figure 4-2. Features of synchronization depending on delay time and coupling strength.** *A* and *C*, Synchronization quality (SQ) and convergence promptness (CP) for model with instantaneous synapses respectively. Thick black curves in *A* and *C* indicate boundaries of dynamics calculated analytically using the phase-locking equation. *B*, Illustration of synchrony modes dominant in regions indicated by roman numerals in *A* and *C*. SQ is high in region I, low in regions II and IV, and intermediate in region III. Slave synchrony (regions II and IV) is not stable, whereas driven (region I) and pacemaker (region III) synchrony are asymptotically stable. CP is highest in region I, indicating synchronization within about 4 cycles.

The curve separating regions I and II is given by  $\tau = \varphi_c(\varepsilon)/2$ . In region I, zero-lag synchronization occurs mainly when both the relay and outer oscillators spike immediately when synaptic input arrives (Fig. 4-2B, upper). This represents

“DS” with period  $T_I$  for all neurons: see Eq. 4-A7 in Appendix 4.5. The curve separating regions II and III is given by

$$\tau = \frac{1 - \chi_b(2\varepsilon) - \varphi_c(\varepsilon)}{2\beta_b(2\varepsilon)}, \quad (4-14)$$

where  $\varphi_c$ ,  $\chi_b$ , and  $\beta_b$  defined in Eqs. 4-5 and 4-7, respectively. For a detailed derivation see the discussion below Eq. 4-A10 in Appendix 4.5. Region II shows mainly slave synchrony like region IV but with a different period  $T_{II}$ : see Eq. 4-A12 “SS1”. In region III, zero-lag synchronization occurs mainly when the outer oscillators spike immediately upon arrival of synaptic input, while the relay oscillator does not. This “pacemaker synchrony” (Fig. 4-2B, **lower**) has period  $T_{III}$  according to Eq. 4-A10 “PS1” in Appendix 4.5.

Figure 4-2A shows that the SQ changes from high (region I) to low (region II) and back to intermediate values (region III) when the conduction delay decreases from 0.5 to 0. Stability analysis indicates that regions II and IV show poor SQ because slave synchrony that dominates in these regions is unstable, whereas driven and pacemaker synchrony that dominate in regions I and III are asymptotically stable and robust against changes in the initial phases. Most combinations of delay and synaptic weight yield a SQ that is below 50%. Figure 4-2C shows that the delay and the synaptic weight in region I yield fast convergence to synchronization within about 4 cycles. In the other regions, zero-lag synchrony is established much more slowly or not at all.

Figure 4-3A shows a histogram of the relative phase  $\varphi_r$  for the stable pacemaker-slave ( $\varphi_r \neq 0$ ) and unstable slave synchrony ( $\varphi_r = 0$ ) modes of the model with a conduction delay  $\tau = 0.25$  and a synaptic weight  $\varepsilon = 0.1$  (parameters in region II, see Fig. 4-2A). Two nonzero relative phases, corresponding to the stable pacemaker-slave mode, and one zero-lag phase, corresponding to the unstable slave synchrony mode, occur. The nonzero relative phases have the same absolute value

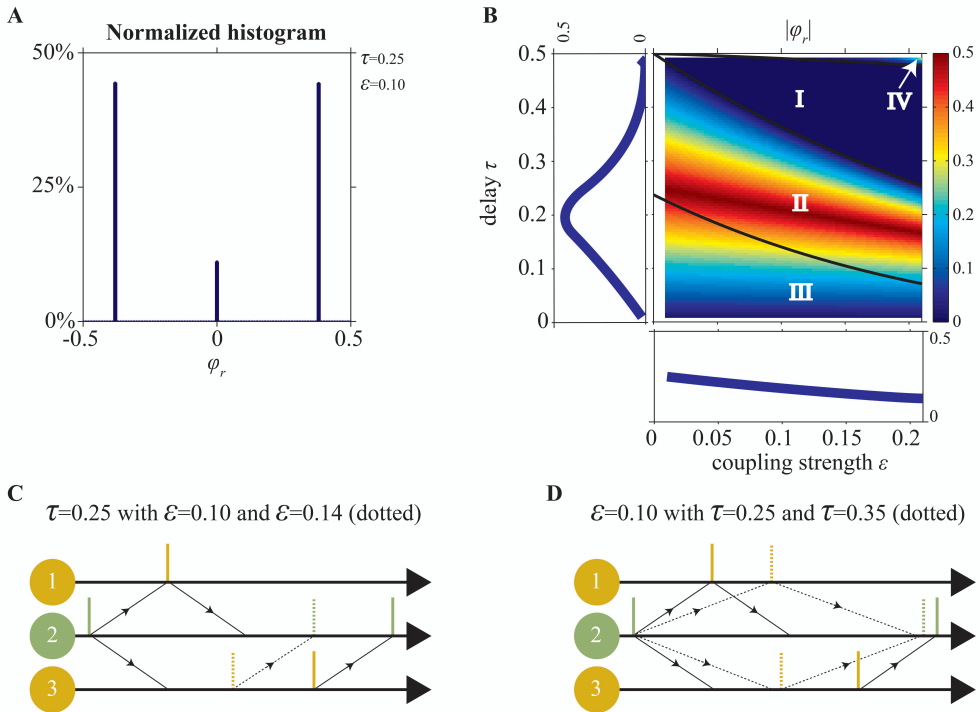


**Figure 4-3. Dominance of nonzero relative phases.** *A*, Normalized histogram of the relative phase  $\varphi_r$  for stable states with  $\tau = 0.25$  and  $\varepsilon = 0.1$ . For about 90% of possible initial phases, the system converges to a nonzero relative phase. *B*,  $|\varphi_r|$  as a function of the conduction delay  $\tau$  and the synaptic weight  $\varepsilon$  with averages projected into side panels.  $|\varphi_r|$  decreases when  $\varepsilon$  increases and has a maximum for  $\tau$  near 0.2. *C* and *D*, dynamics of “pacemaker-slave” synchrony corresponding to nonzero relative phase. Solid lines represent spike times for parameter values  $\tau = 0.25$  and  $\varepsilon = 0.1$ , dotted lines for a stronger synaptic weight  $\varepsilon = 0.14$  in *C* and longer delay time  $\tau = 0.35$  in *D*, respectively.

because of the symmetry of the network. For about 90% of the initial phases of the oscillators, the system converges to the two nonzero relative phases and for 10% to a state with zero-lag synchrony. For other values of the delay and the weight in region II, III, and IV, the histograms are qualitatively similar to that shown in Fig. 4-3A, i.e., two nonzero and one zero-lag relative phases. Thus in general zero-lag

synchrony only occurs for a very limited set of initial phases in parameter regions II, III, and IV.

To illustrate how the nonzero relative phase varies for different parameter values in the network, Fig. 4-3B shows the absolute value  $|\varphi_r|$  as a function of the conduction delay  $\tau$  and the synaptic weight  $\varepsilon$ . The three black curves in Fig. 4-3B indicate the boundaries between regions I, II, III, and IV as in Fig. 4-2 calculated analytically using the phase-locking equation. To understand the results in Fig. 4-3B, we consider the “pacemaker-slave” mode that corresponds to the positive relative phase illustrated in Fig. 4-3, C and D. Vertical solid lines represent the spiking times for  $\varepsilon = 0.1$  and  $\tau = 0.25$ , and the dotted lines correspond to a stronger weight  $\varepsilon = 0.14$  in Fig. 4-3C and a longer delay  $\tau = 0.35$  in Fig. 4-3D. When the synaptic weight increases in Fig. 4-3C, oscillators 2 and 3 will spike sooner after input from oscillator 1, whereas oscillator 1 always spikes immediately after input from oscillator 2. Hence the relative phase between oscillators 3 and 1 decreases when the coupling strength increases. At longer delay times in Fig. 4-3D, the synaptic inputs from oscillator 2 arrive later in time at oscillators 1 and 3 as indicated by the dotted arrows. The input causes oscillator 1 to spike immediately but not so for oscillator 3. For the longer delay time, oscillator 3 will be further in its natural cycle, and therefore it will spike sooner after the input. Thus oscillators 1 and 3 will both spike later, but their relative phase difference is reduced for longer delays. Fig. 4-3B, left, shows the relative phase as a function of the delay, averaged over all values of synaptic coupling. The lower panel shows the relative phase as a function of coupling strength, averaged over all delays.

Next, we study synchronization for a model with HH neurons. Figure 4-4, A and E, shows simulation results for the model with HH neurons for the SQ and the CP, respectively, as a function of the conduction delay  $\tau$  and the synaptic weight  $\varepsilon$  for instantaneous synapses. Comparing Fig. 4-4, A and E, with the same results for the MS oscillator in Fig. 4-2, A and C, shows that the model with HH neurons yields a high SQ and large CP for a larger range of  $\tau$  and  $\varepsilon$  values than the MS neuron.

Figure 4-4A also shows that perfect SQ is not possible when the delay time is shorter than approximately 0.05 of the intrinsic period, which roughly corresponds to half the refractory period of the HH neuron. If the time delay is  $0.05T_0$  or less, the

time interval from spiking of the outer oscillators and spike input from the relay oscillator to the outer oscillators is less or equal to the refractory period. In that case,

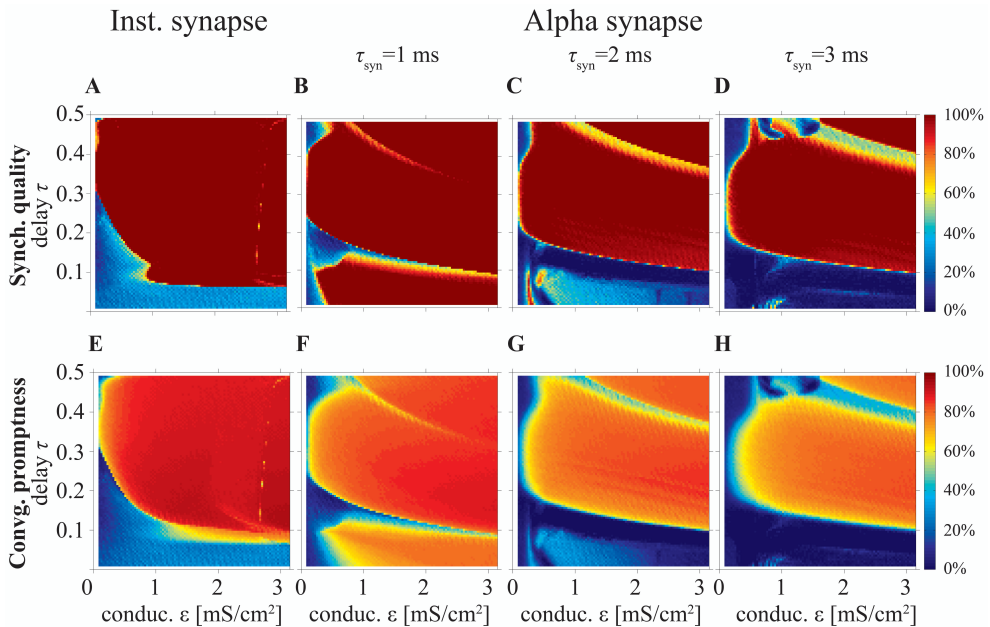


**Figure 4-4. Excellent synchronization for alpha synapses with short rise times.** (Top row) Synchronization quality (SQ) and (bottom row) convergence promptness (CP) for a Hodgkin-Huxley based model with instantaneous synapses (*A* and *E*) and alpha synapses for various rise times (*B-D*, *F-H*). Comparing *A* and *E* with the results for the MS neurons (see Fig. 4-2, *A* and *C*) shows that SQ and CP clearly improve for HH neurons. Moreover, SQ and CP for short rise times of the alpha synapses (*B* and *F*) are better than for instantaneous synapses (*A* and *E*) but decrease for longer rise times.

input from the relay oscillator to the outer oscillators arrives in the refractory period, which effectively reduces the coupling strength when the outer oscillators tend to synchronize and thereby disables the zero-lag DS mode when the delay time is short.

Figure 4-4, *B-D* and *F-H*, shows the SQ and the CP, respectively, as a function of the conduction delay  $\tau$  and the synaptic weight  $\epsilon$  for the HH neuron model with alpha synapses of various synaptic rise times (left, middle, and right columns for  $\tau_{\text{syn}} = 1, 2, \text{ and } 3$  ms, respectively). Quite surprisingly, in the context

of the results in Fig. 4-4, **A** and **E**, the SQ is high for very small time delays for  $\tau_{\text{syn}} = 1$  ms (Fig. 4-4**B**). This can be understood from the fact that the alpha synapse adds an effective delay such that spike input from the relay neuron to the outer neurons arrives after the refractory period when the outer oscillators fire in perfect synchrony. When the synaptic rise time increases, the range of time delays and synaptic strengths with high SQ decreases (Fig. 4-4, **B-D**). To understand this, assume that synaptic inputs from the relay oscillator arrive when the phase of oscillators 1 and 3 is  $\varphi_1$  and  $\varphi_1 + \delta$ , respectively. If  $\delta$  differs from zero, then oscillators 1 and 3 will spike at different times, unless the input is strong enough to

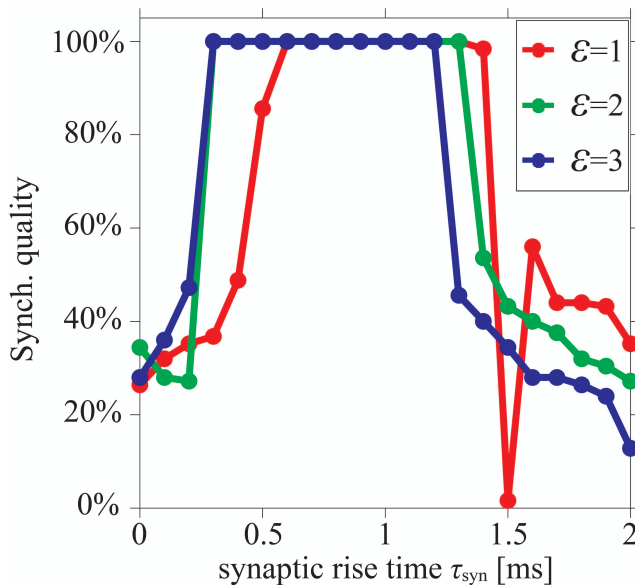


**Figure 4-5. Optimal synchronization for moderately fast synaptic rise time.** SQ at  $\tau = 0.02$  for three synaptic strengths  $\epsilon = 1$  (red), 2 (green), and 3 (blue) mS/cm<sup>2</sup> in a model with alpha synapses and Hodgkin-Huxley neurons, shown as a function of the synaptic rise time  $\tau_{\text{syn}}$ . Almost perfect SQ can be obtained when the synaptic rise time is moderately fast, i.e., approximately between 0.5 and 1 ms.

immediately initiate a spike in both oscillators. For larger rise times and the same synaptic strength  $\epsilon$ , less input per unit of time is received since the synaptic input



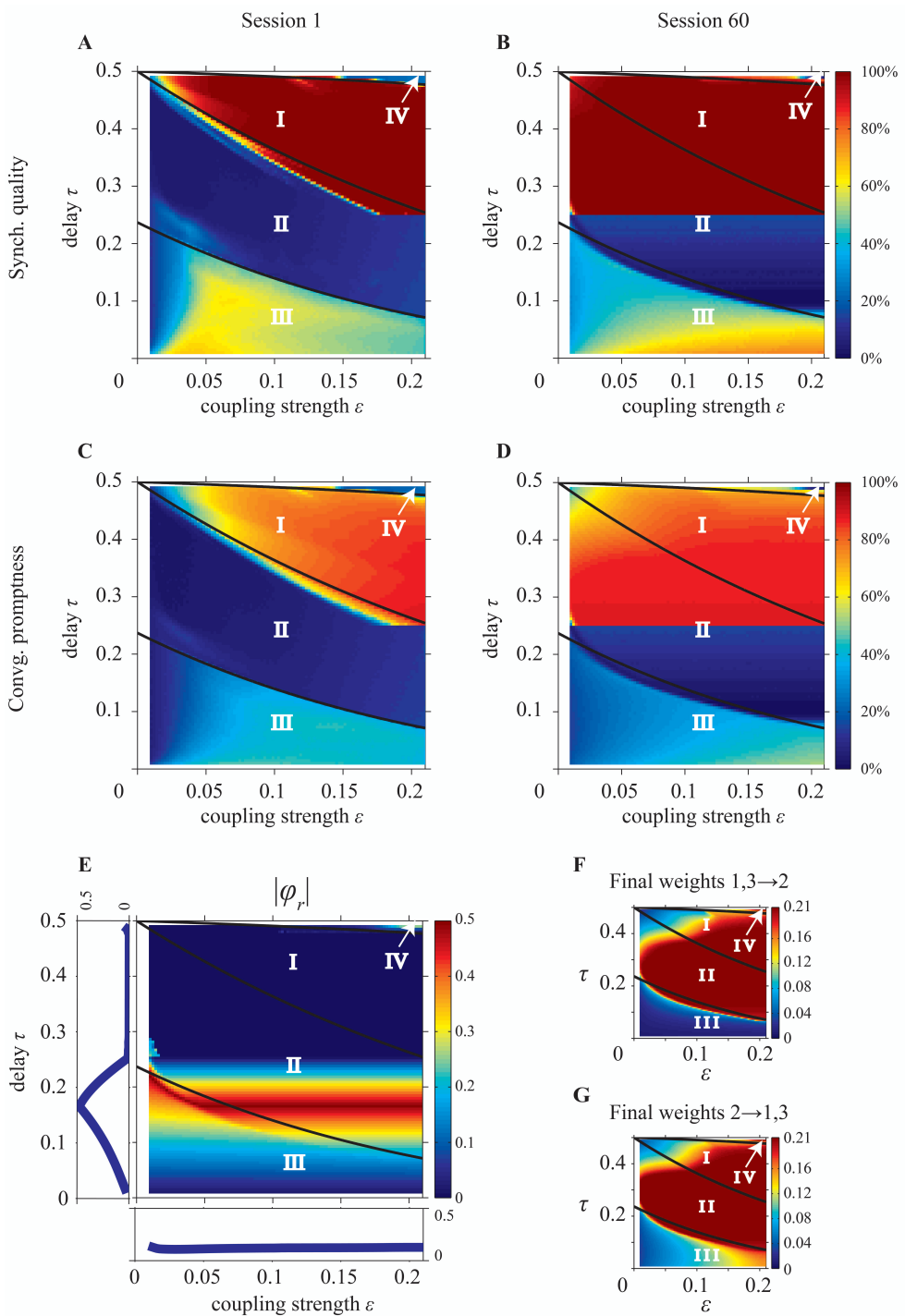


**Figure 4-6. STDP improves long-range synchronization for instantaneous synapses and decreases the fraction of nonzero relative phases.** *A* and *B*, SQ after the first and the 60-th session, respectively. *C* and *D*, Corresponding CP. For conduction delays  $\tau \geq 0.25$ , synchrony improves due to an increase of initial weights  $\varepsilon$  by STDP. *E*,  $|\varphi_r|$  as in Fig. 4-3B but after 60 learning sessions. *F*, Synaptic weights from the outer oscillators to the relay oscillator; *G*, Synaptic weights from the relay oscillator to the outer oscillators. Changes in  $|\varphi_r|$  relative to that in Fig. 4-3B are largely caused by an increase of the synaptic weights by STDP. To compare with the results without STDP, we show the solid black curves that separate regions with different dynamics in Fig. 4-2.

is spread out over a longer time. Therefore, input from an instantaneous synapse (equivalent to “ $\tau_{\text{syn}} = 0$ ”) or fast alpha synapse (small  $\tau_{\text{syn}}$ ) can more readily synchronize the outer oscillators than a slow alpha synapse (large  $\tau_{\text{syn}}$ ).

High SQ is possible for short delay times ( $\tau < 0.05$ ), if the synaptic rise time is short (Fig. 4-4B), but less so when the synaptic rise time increases (Fig. 4-4, C and D). This suggests that there is a range of synaptic rise times that favor a high SQ for short time delays. Figure 4-5 shows the SQ, as a function of the synaptic rise time  $\tau_{\text{syn}}$ , evaluated at  $\tau = 0.02$  for  $\varepsilon = 1$  (red), 2 (green), and 3 (blue) mS/cm<sup>2</sup>. Perfect SQ is obtained when the synaptic rise time is moderately fast, i.e., approximately between 0.5 and 1 ms, for a large range of synaptic coupling strengths. Therefore, moderately fast synaptic rise times favor zero-lag synchrony.

#### *STDP facilitates zero-lag synchronization*

We now investigate the effect of STDP on synchronization of the MS neuron, starting with the simple instantaneous synapses. Figure 4-6 shows the SQ and the CP with short (left column) and long STDP adaptation (right column), i.e., after the first and sixtieth session, respectively. To allow an easy comparison to the results without STDP in Fig. 4-2, we have drawn the same thick black curves in Fig. 4-6 that separate regions with different dynamics as in Fig. 4-2. Note that the synaptic strength  $\varepsilon$  along the horizontal axes in Fig. 4-6 represents the *initial* synaptic weight, not the final values after adaptation by STDP. The results in Fig. 4-6, A and

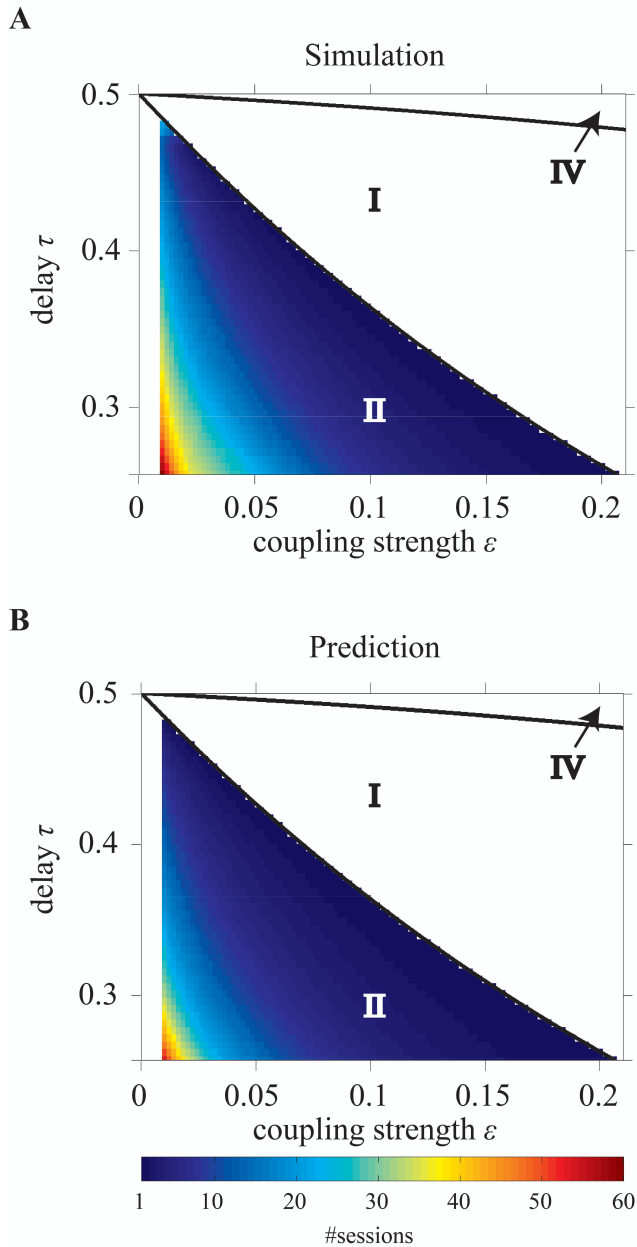


**Figure 4-7. Time required to reach 100% SQ by STDP.** *A*, Number of sessions to achieve 100% SQ according to direct simulations; *B* same but according to analytical calculations for converting slave into driven synchrony for the relevant part  $\tau_c^+ \leq \tau < \varphi_c(\varepsilon)/2$  of region II. Solid black curves in *A* and *B* separate regions with different dynamics as shown in Fig. 4-2.

*B*, show that the effect of STDP is a gradual expansion of the range of coupling strengths that give rise to synchronization. With STDP, the weak coupling gradually increases to larger synaptic strengths that allow synchronous firing, corresponding to DS. Likewise, the CP increases, as shown in Fig. 4-6, *C* and *D*.

The higher SQ and the faster CP in region II for large delay times in Fig. 4-6, *A-D*, can be understood as follows: by increasing coupling strengths, STDP converts slave synchrony that is unstable and a dominant zero-lag synchronization mode in region II into DS that is asymptotically stable. For slave synchrony STDP increases the coupling strength from the relay oscillator to the outer oscillator. The sharp border is related to the maximum coupling strength  $\varepsilon_{\max} = 0.21$ : the slave to drive synchrony conversion can only occur if  $\tau$  exceeds  $\tau_c^+ := \varphi_c(\varepsilon_{\max})/2 \approx 0.25$ . Notice that the fully improved domain of attraction for zero-lag synchrony is reached only after 60 sessions with STDP. This suggests that STDP can contribute to zero-lag synchrony but generally only after many cycles of weight adaptation (here up to 900 oscillations).

Figure 4-7 shows the number of sessions for STDP required to obtain 100% SQ when the network begins with four equally strong coupling strengths in the range between  $0 < \varepsilon \leq 0.21$  and delay times  $\tau_c^+ \leq \tau < \varphi_c(\varepsilon)/2$ , i.e., where STDP changes slave synchrony into DS as just discussed. The solid black curves in Fig. 4-7 separate the regions with different dynamics as in Fig. 4-2 (without STDP). Figure 4-7, *A* and *B*, is obtained from direct simulations and from analytical calculations, respectively. The analytical results are obtained using Eqs. 4-A26 and 4-A27 in Appendix 4.5 iteratively. The simulated and analytical results are in good agreement. The network requires a slightly smaller number of sessions to reach a high SQ value in the analytical calculations because these start from the condition of slave synchrony, whereas the direct simulations start from random initial phases and reach the driven

state after achieving slave synchrony first. For smaller initial coupling strengths, it takes more time to converge to stable zero-lag synchronization with STDP: 20 cycles (about 0.5 seconds) or more.

Figure 4-6E shows the absolute value of the nonzero relative phase  $|\varphi_r|$  as a function of the delay time  $\tau$  and the synaptic weight  $\varepsilon$  after convergence of the network to a stable state by STDP. This result should be compared to the case without STDP in Fig. 4-3B. Note that the synaptic strength  $\varepsilon$  along the horizontal axes in Fig. 4-6 represents the initial synaptic weight at the start of the simulations that is assumed to be equally strong for the four connections (cf. Fig. 4-1A) and will change during the simulations by STDP. The average values of final synaptic weights are shown as a function of the delay and the weight in Fig. 4-6F (connections from the outer to the relay oscillator) and Fig. 4-6G (connections from the relay to the outer oscillators). After training for 60 sessions, the values of  $|\varphi_r|$  for the stable states of the network, shown in Fig. 4-6E, significantly decrease in region II, while  $|\varphi_r|$  changes slightly in regions I, III, and IV as compared to the values before adaptation of the synapses by STDP (Fig. 4-3B). This is largely caused by STDP-induced increase of the coupling strength in region II, as shown in Fig. 4-6, F and G. The final weights overall are quite similar in both directions in region II. In region III they differ because pacemaker synchrony is dominant, which implies different timing of pre- and postsynaptic firing for the relay and outer oscillators and therefore different effects of STDP. The final weights in regions I, II, and IV in Fig. 4-6, F and G, are similar because, after many learning sessions, DS is dominant here. In DS, the firing behavior of the relay and outer oscillators is the same, i.e., a synaptic input arrives at phase  $2\tau$  and makes the neuron spike instantaneously. Since all connections start with the same initial weight, the same weight adaptation is applied to the connections from the relay to the outer oscillators and vice versa.

To investigate the robustness of our results for variations of the STDP parameter values, we return to the instantaneous synapses. We have varied the amplitudes  $A_+$  and  $A_-$  of the fractional synaptic modification  $W$  (Eq. 4-9 and Fig.

4-8A). Figure 4-8, **B** and **C**, shows the SQ and the CP, respectively, for various values of  $A_+$  and  $A_-$  as a function of the number of learning sessions. The black curves in Fig. 4-8 show the results for the asymmetric learning window with our standard parameters of STDP obtained from the Bi and Poo data (Bi and Poo, 1998), while the red curves show results for smaller ( $0.5A_{+,0}$ : dashed curve) and larger ( $1.5A_{+,0}$ : thick curve) values of potentiation amplitude  $A_+$ . The blue curves are for smaller ( $0.5A_{-,0}$ : dashed curve) and larger ( $1.5A_{-,0}$ : thick curve) values of depression amplitude  $A_-$ .

When depression dominates over potentiation (dashed red and solid blue curves), the SQ is poor even after many sessions (Fig. 4-8**B**). Larger values for potentiation relative to depression give rise to faster and better synchrony (dashed blue and solid red curves). However, after about 25-40 learning sessions, the standard set of parameters (Bi and Poo, 1998) yields better results, i.e., higher values of average SQ and faster convergence to synchronization, as shown in Fig. 4-8, **B** and **C**. To explain this, we will consider why the average SQ in region III becomes higher for the standard set of STDP parameters than for the potentiation-dominated parameter sets (dashed blue and solid red curves in Fig. 4-8A). For the other regions (I, II, and IV), both parameter sets yield similar values of average SQ because there the system converges to the DS mode after several learning sessions.

We first consider the effects of STDP on the coupling strengths of the network starting with initial coupling strength  $\varepsilon$  and delay time  $\tau$  in region III just below the curve that separates regions II and III. STDP will increase the weights  $\varepsilon$  to larger values due to larger potentiation relative to depression. This moves  $(\varepsilon, \tau)$  from region III to region II, where the zero-lag synchronization modes “SS1” of Eq. 4-A12 in Appendix 4.5 and “NDS2” of Eq. 4-A13 in Appendix 4.5 are unstable. Hence the average SQ in region III decreases because the initial weights  $\varepsilon$  will be increased to values that correspond to unstable zero-lag synchronization modes in

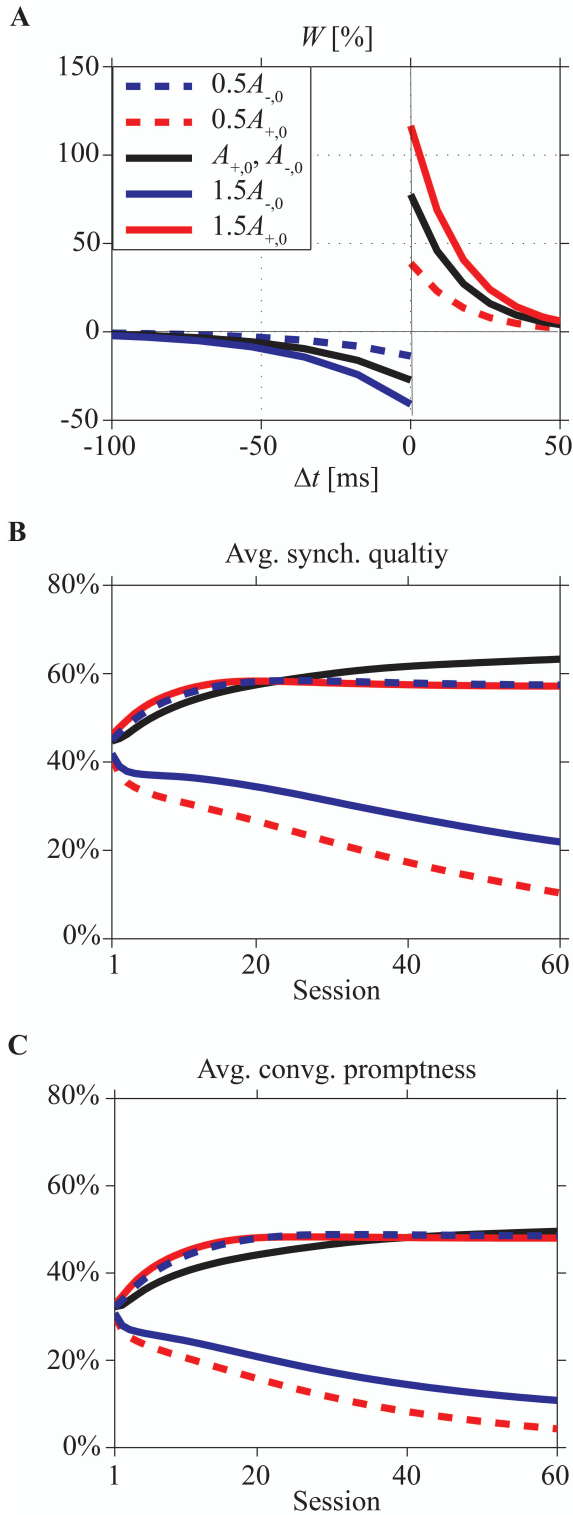


**Figure 4-8. Effects of changing the STDP learning window.** *A*, Shapes of the learning windows for various amplitudes of  $A_+$  and  $A_-$ . Black curves represent the standard parameter set (Bi and Poo, 1998), while red and blue curves indicate changing values of potentiation  $A_+$  and depression  $A_-$ , respectively, by a factor 0.5 (dashed curves) or 1.5 (thick curves). *B* and *C*, Dependence of average SQ and CP, respectively, on the number of learning sessions. After about 25-40 sessions, the standard learning window (black curves) becomes optimal.

region II. However, when the initial weights and the delay times are farther away from the curve separating regions II and III, the effects of STDP on the weights are different. To understand this, we focus on pacemaker synchrony, a stable synchronization mode in region III. The period of oscillations for pacemaker synchrony in region III becomes longer when the weights  $\varepsilon$  become smaller since the delay between the arrival of spike input and firing increases, cf. formula “PS1” in Eq. 4-A10 in Appendix 4.5. Since the time window for depression is much larger than that for potentiation, longer delays suppress potentiation more, leaving depression dominant. Close to pacemaker synchrony, this concerns mainly the synapses from the outer oscillators onto the relay oscillator since the outer oscillators fire quickly after receiving input. A weakening of these synapses reinforces pacemaker synchrony. Overall then, increasing the strength of potentiation beyond the standard rule will shift more  $(\varepsilon, \tau)$  to region II without stable synchronization, leaving fewer  $(\varepsilon, \tau)$  that will achieve stable pacemaker synchrony. Hence the SQ and CP in region III eventually becomes higher for the standard STDP set than for the potentiation-dominated one; and the average over all regions follows this trend (Fig. 4-8, **B** and **C**).

Results for different time constants for potentiation  $\tau_+$  and depression  $\tau_-$  (not shown) are qualitatively similar to the results for changing the amplitudes  $A_+$  and  $A_-$ , i.e., a larger value of  $\tau_+$  relative to  $\tau_-$  gives rise to faster and better synchrony and the standard values for  $\tau_+$  and  $\tau_-$  yield better results for zero-lag synchrony when the number of the learning sessions is large. Our results are robust for decreases of depression (dashed blue curve) or increases in potentiation (solid red curve) but not vice versa (dashed red and solid blue curves). Figure 4-9 shows



the SQ and the CP for the model with STDP with HH neurons with instantaneous synapses (Fig. 4-9, **A** and **C**, respectively) and with alpha synapses (Fig. 4-9, **B** and **D**, respectively). Comparing Fig. 4-9**A** with Fig. 4-4**A** reveals hardly any improvement of the SQ by STDP. However, for alpha synapses STDP significantly improves the average SQ by increasing the synaptic coupling  $\varepsilon$  (compare Figs. 4-9**B** and 4-4**C**).

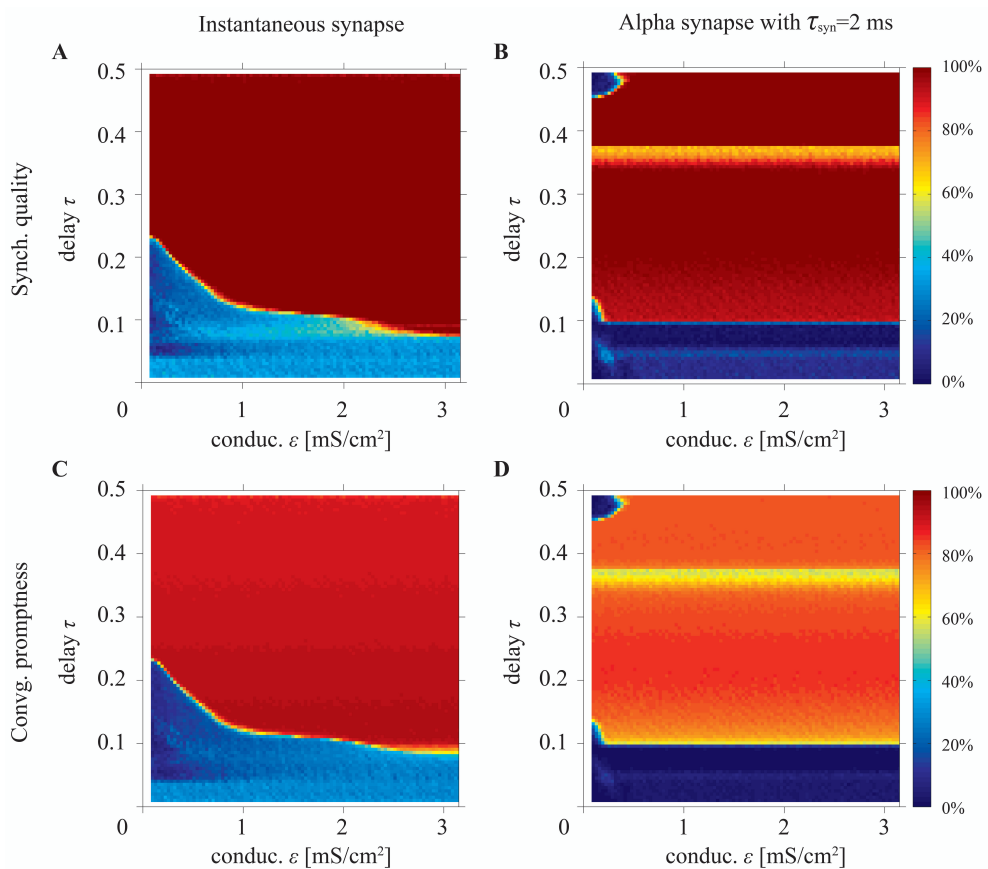


**Figure 4-9. STDP improves long-range synchronization for the model with HH neurons.** *A* and *B*, SQ after the 60-th session for instantaneous synapses and the 2-ms- $\tau_{\text{syn}}$  alpha synapse, respectively. *C* and *D*, Corresponding CP. For conduction delays, approximately  $\tau \geq 0.1$ , synchrony improves due to STDP-mediated increase of synaptic strength  $\varepsilon$ .

In summary, the conditions that contribute to zero-lag long range synchronization are as follows. First, the delay times relative to the intrinsic frequency  $T_0$  should be long enough, i.e., more than about 0.35 (8.75 ms for  $T_0 = 25$  ms ) for the model with MS phase oscillators with the instantaneous synapse (cf. Fig. 4-2, **A** and **C**) and 0.15 (2.2 ms for  $T_0 = 14.66$ ms) for the model with HH neurons with the alpha synapse (cf. Fig. 4-4). Moreover, alpha synapses with short synaptic rise times are required for zero-lag synchronization for short delay times (cf. Fig. 4-5). Third, STDP facilitates the synchronization but generally only after many cycles of weight adaptation (cf. Figs. 4-6 - 4-9).

### 4.3.2 When delay times from the relay oscillator to outer oscillators are not identical

We now investigate the dynamics of the model in Fig. 4-1A when the delay times  $\tau_1$  and  $\tau_3$  are different. Simulation results (not shown) show that zero-lag synchrony then is lost, in agreement with Fischer et al. (2006) and Vicente et al. (2008). Similar results (not shown) were found for the model with HH neurons. To understand why zero-lag synchronization disappears when the delay times are different, we consider the MS network with instantaneous synapses. Let us assume that oscillators 1 and 3 fire simultaneously. When oscillator 2 generates an action potential, the spikes arrive at oscillators 1 and 3 after delays  $\tau_1$  and  $\tau_3$ , respectively. When the spikes arrive at oscillators 1 and 3 at a phase exceeding the critical phase, oscillators 1 and 3 will spike immediately after arrival of the spike. This implies that oscillators 1 and 3 spike with a time difference  $|t_{1,n+1}^{\text{spike}} - t_{3,n+1}^{\text{spike}}| = |\tau_1 - \tau_3|T_0$ . This illustrates that zero-lag synchrony is lost when the delay times  $\tau_1$  and  $\tau_3$  are different. Qualitatively similar results (not shown) are obtained for asymmetric coupling strengths.

Figure 4-10 shows a histogram of the relative phase  $\varphi_r$  for various stable modes for the synaptic weight  $\varepsilon = 0.1$  for five pairs of conduction delays:  $(\tau_1, \tau_3) = (0.35, 0.25)$  in Fig. 4-10A,  $(0.25, 0.15)$  in 4-10B,  $(0.25, 0.25)$  in 4-10C,  $(0.25, 0.35)$  in 4-10D, and  $(0.15, 0.25)$  in 4-10E. Figure 4-10A shows two peaks of

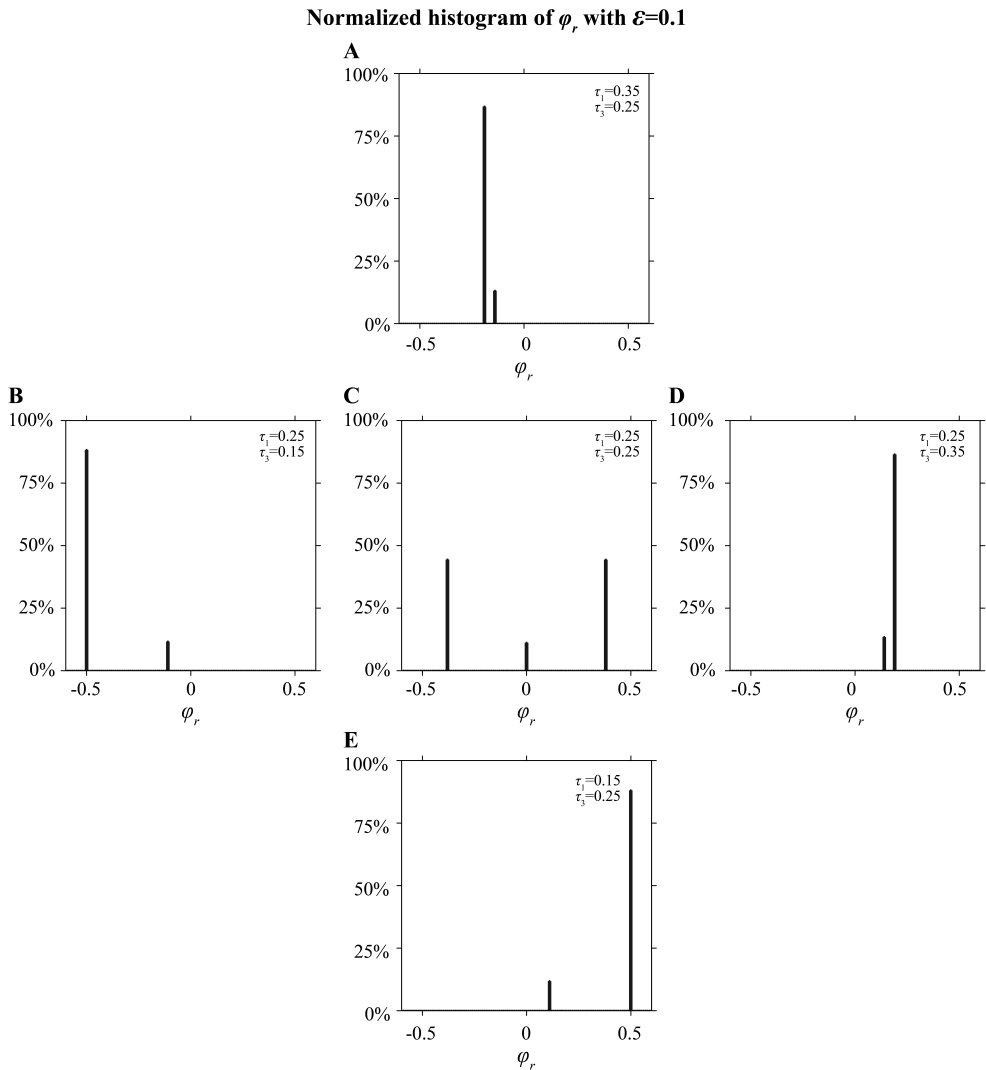


**Figure 4-10. Effect of unequal delays on relative phase.** *A-E*, Histograms showing the fraction of initial phases that converge to a particular relative phase  $\varepsilon = 0.1$  for different pairs  $(\tau_1, \tau_3) = (0.35, 0.25)$ ,  $(0.25, 0.15)$ ,  $(0.25, 0.25)$ ,  $(0.25, 0.35)$ , and  $(0.15, 0.25)$ . When delays between the outer oscillator and the relay neuron become asymmetric, one of the nonzero relative phases disappears and the zero relative phase shifts to nonzero values, corresponding to a state where the outer oscillator with the shorter delay spikes earlier.

relative phases near -0.19 and -0.14, instead of the three peaks appearing in Fig. 4-10C, which include one at zero. Figure 4-10, **B**, **D**, and **E**, also yields two nonzero peaks instead of three. Figure 4-10, **A** and **B**, are mirror images of **D** and **E**, respectively, because the delay times are exchanged and the outer oscillator with the shorter delay time spikes first. Essentially, the symmetric nonzero peaks in Fig. 4-10C collapse into one for asymmetric delays, and the zero-lag peak shifts to a nonzero value, which is equal to the value of the zero-lag peak. Other combinations of the synaptic weight  $\varepsilon$  and non-equal conduction delays  $\tau_1$  and  $\tau_3$  yield qualitatively similar results.

#### 4.4 Discussion

In this study we have investigated the conditions for zero-lag synchrony between two neuronal oscillators that interact via a relay oscillator. The main result of our study is that for the model with type II Hodgkin-Huxley neurons, synchronization is easier to achieve than for type I Mirollo-Strogatz neurons. Synapses with short rise times (typically less than 2 ms) are more suitable to achieve zero-lag synchronization than synapses with longer rise times. With STDP the network converges to zero-lag synchronization at a faster rate and for a larger range of synaptic strengths and time delays than without STDP. However, when the delay times between the two synchronizing oscillators and the relay oscillator are different, zero phase lag may easily get lost.

The network used in this study is a simplified model for interacting neuronal populations. This obviously raises the question whether our results about zero-lag synchrony may be biased by the simplifications inherent in our model. We will argue in the next paragraphs below that this is not the case. Our choice of indirect interactions between oscillating neuronal populations, i.e., via a relay oscillator, was inspired by previous studies, which showed that pulse-coupled neuronal oscillators with direct excitatory coupling and signal delays in general do not oscillate at zero phase lag (van Vreeswijk et al., 1994; Ernst et al., 1995, 1998; Knoblauch and Sommer, 2003; Zeitler et al., 2009), unless the neurons are of type II with biphasic PRC's (Goel and Ermentrout, 2002; Woodman and Canavier, 2011). Inhibitory coupling between directly interacting oscillators can cause near zero-lag synchrony (van Vreeswijk et al., 1994; Zeitler et al., 2009). However, the dominant connectivity

between cortical areas, such as V1, V2, V4, and FEF, is excitatory rather than inhibitory. These considerations led Fischer et al. (2006) and Vicente et al. (2008) to postulate a network model of oscillators interacting via a relay oscillator that supports zero-lag synchrony. Subcortical structures like the thalamus are good physiological candidates for such a mediating relay (Theyel et al., 2010). Our study elaborates on this relay network model.

The most simplified version of our model assumes that the oscillators used to represent neuronal population activity are of the Mirollo-Strogatz type. The Mirollo-Strogatz oscillator corresponds to the type I neuron class (Izhikevich, 2007). Although there is evidence that cortical pyramidal cells can switch between type I and type II by means of cholinergic modulation (Ermentrout et al., 2001; Jeong and Gutkin, 2007; Prescott et al., 2008; Stiefel et al., 2008, 2009), the majority of pyramidal cells in neocortex seems to be type I neurons (Reyes and Fetz, 1993b, a; Kawaguchi, 1995; Erisir et al., 1999; Tateno et al., 2004). Our results show that synchronization is hard to achieve for the model with type I MS neurons for weak and strong synaptic coupling strengths, unless the delays are relatively long. To appreciate this result, one should realize that the literature on this topic is divided in studies assuming weak coupling using infinitesimal phase response curves and others assuming strong synaptic coupling. Our results are in agreement with the results of Ermentrout (1996), who used a perturbation method, which is equivalent to assuming weak coupling, for networks of type I neurons with excitatory coupling. However, Mirollo and Strogatz (1990) reported that for almost all initial conditions, a network with strongly coupled type I neurons (without delays!) evolves to a state with synchronous firing. When delays are involved, zero-lag synchrony is lost (Ernst et al., 1995, 1998). Recently, Wang et al. (2012) showed that synchrony in a network with strongly coupled type I oscillators is possible in the absence of delays or with delays greater than half of the network period. Although we did not study the model with delays exceeding 0.5, our results reveal the largest amount of synchrony for long delays, which is in agreement with the results by Wang et al. (2012).

Replacing the Mirollo-Strogatz neurons by more realistic type II Hodgkin-Huxley neurons allows for a broader range of synaptic strengths and time delays that is compatible with zero-lag synchronization. This result suggests a functional role for changes in neuronal properties from type I to type II, in agreement with

suggestions by Prescott et al. (2008). However, there are no experimental data available yet that can be used to test the hypothesis that the properties of pyramidal cells change from type I to type II when synchrony arises in neuronal populations, as far as we know. Another possibility might be that properties of pyramidal cells do not change from type I to type II, but that the activity of interneurons causes strong inhibition after firing of the pyramidal cells (see Börgers et al. (2010) for a more extended description of the effect of inhibition). In that case, the inhibition by the interneurons after firing causes effectively a biphasic PRC with phase delays early in the firing cycle and phase advances later in the cycle for the pyramidal cell/interneuron couple that contributes to synchrony both for direct coupling between two pyramidal cells as well as for a pyramidal cells interacting via a relay neuron.

Delays in networks of interacting neurons can give a variety of complex behaviors with a wealth of bifurcations and a rich phase diagram, which includes oscillatory bumps, traveling waves, lurching waves, standing waves arising via a period-doubling bifurcation, aperiodic regimes, and regimes of multistability (Roxin et al., 2005). Synchronous firing is just one of these modes, which only occurs for a limited range of model parameters. A neuronal property that greatly contributes to synchrony is that the phase response curve of the neurons is biphasic with phase delays early in the firing cycle and phase advances later in the cycle, like for type II Hodgkin-Huxley neurons. This applies both to weakly coupled oscillators (see e.g. Hansel and Mato (1993); Hansel et al. (1993b, 1993a)) as well as for strongly coupled coupled ones (Bressloff and Coombes, 2000; Izhikevich, 2007). Their results are in agreement with the results in our study, which show that the model with type II Hodgkin-Huxley neurons more easily leads to zero-lag synchronisation than with type I MS neurons.

Another assumption of this study, which requires some more discussion, is that all oscillators in the model have identical intrinsic properties with the same oscillation period. If the intrinsic periods of the outer oscillators differ, zero-lag synchrony may get lost. Whether synchrony will be lost depends on the neuron type. If the synaptic input to the outer oscillators that have different natural frequencies resets their oscillation periods to the same value, zero-lag synchronization is easily obtained. Synchronization of non-linear oscillators with different oscillatory

properties is feasible if the interactions between the oscillators (the synaptic strengths in our study) are sufficiently strong (Pikovsky et al., 2001). A special condition is the situation where the intrinsic period of the relay oscillator is different from that of the outer oscillators. This might not be unusual if the relay oscillators are thalamic cells and the outer oscillators cortical cells. In this case, the synchronization properties change quantitatively but not qualitatively. These results have been confirmed by simulations (not shown) but can be understood from the following: If we make the period of the relay oscillator different from that of the outer oscillators, the combinations of synaptic strength and delay where input can elicit spikes immediately after arrival change only slightly with adjustments of the period. Hence the boundaries of regions with driven, pacemaker, and slave synchrony will change quantitatively, but not qualitatively, unless the differences in the period become too large.

If the periods of the two outer oscillators are different from each other and if input from the relay oscillator does not make the period of the outer oscillators the same, input from the relay oscillator to the outer oscillators will elicit spikes at different times. In that case, the spike input from the outer oscillators to the relay oscillator also arrives at different times. This is essentially equivalent to the situation with different delay times, which we have studied (see sec. 4.3.2), where we have shown that zero-lag synchrony is easily lost if the delay times become different (see also Fig. 4-10). Therefore, synaptic coupling strengths should be sufficiently strong to ensure zero-lag synchrony when the oscillation periods of the outer oscillators differ.

In our study we have introduced “SQ” as a measure for the robustness of synchrony against variations in the initial phases of the oscillators. SQ was used together with the “CP” to assess zero-lag synchrony between the two outer oscillators in our relay network. The time interval for “synchrony” was chosen as spike coincidence within 0.5 ms (Engel and Singer, 2001), which in experimental settings is long enough to take into account typical noise on spike timings but short enough to speak about “zero-lag”. Increasing the time interval to 1 ms did not affect the results qualitatively though quantitatively some minor differences were observed.

In agreement with Knoblauch and Sommer (2003), we found that if spike-timing dependent plasticity (STDP) adapts synaptic coupling, the network state converges more easily to a stable state with zero-lag synchrony (see Figs. 4-6 and 4-9). However, adaptation of the synapses by STDP often took quite some time (in general more than 500 cycles (one session corresponds to 60 cycles), see Fig. 4-7), which implies that STDP may not always play a dominant role for the rapid development of zero-lag synchronization. Vicente et al. (2008) reported that the mechanism of synchronization rests on the ability of an excitatory postsynaptic potential to modify the firing latencies of a postsynaptic neuron in a consistent manner. We agree with this conclusion, but our results show that the mechanism of STDP may take too much time (considerably more than the observed time range of 200-250 ms in visual perception, see Rodriguez et al. (1999)) to generate zero-lag synchrony for oscillations in the gamma frequency range.

Overall, our results demonstrate that gamma oscillations in various cortical areas can be synchronized at zero-lag in a network model where neuronal oscillators are coupled via a relay oscillator, in agreement with previous studies (Fischer et al., 2006; Vicente et al., 2008). In addition, we show that STDP expands the range of parameter values that allow zero-lag synchrony.

## 4.5 Appendix

### 4.5.1 Detailed analysis of phase-locking and stability

Analytical derivations of the various synchrony modes and their stability are provided. An overview of these results is provided by Fig. 4-A1.

#### *Synchrony modes derived from the phase-locking equation*

To investigate the existence of zero-lag synchrony as a function of  $\tau$  and  $\varepsilon$ , we will derive the 1:1 synchronized phase-locking equation of the oscillators, cf. Fig. 4-1B. The firing of the relay oscillator  $t_{2,n-1}^{\text{spike}}$  is chosen as reference time, i.e.,  $t_{2,n-1}^{\text{spike}} = 0$ . For zero-lag synchrony there exists some value  $\theta \in [0, 1[$  such that the firing times  $t_{1,n-1}^{\text{spike}}$



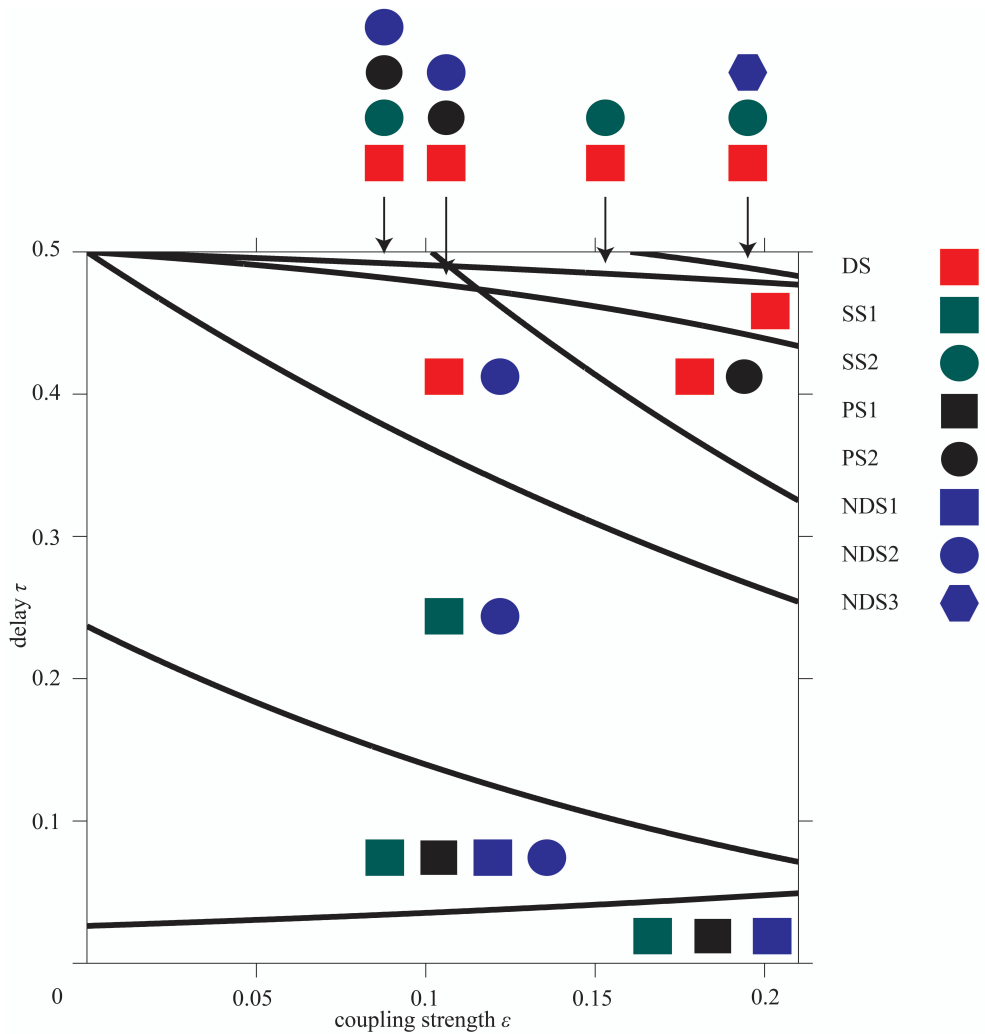


**Figure 4-A1. Synchronization regions in the parameter plane of delay time and coupling strength.** Different combinations of possible synchrony modes divide the parameter plane of delay time  $\tau$  and synaptic weight  $\varepsilon$  into ten distinct regions. These are shown separated by black curves and the corresponding synchrony modes are indicated by symbols referring to results listed in Appendix 4.5: driven synchrony – Eq. 4-A7 “DS” in Appendix 4.5; pacemaker synchrony – Eq. 4-A10 “PS1” and “PS2” in Appendix 4.5; slave synchrony – Eq. 4-A12 “SS1” and “SS2” in Appendix 4.5; and non-driven synchrony – Eq. 4-A13 “NDS1”, “NDS2”, and “NDS3” in Appendix 4.5.

and  $t_{3,n-1}^{\text{spike}}$  of both oscillators 1 and 3 are equal to  $\theta T$ , and  $t_{1,n}^{\text{spike}}$  and  $t_{3,n}^{\text{spike}}$  are equal to  $\theta T + T$ , with  $T$  the period of the oscillations in the network. The spikes from the outer oscillators arrive at the relay oscillator at phase  $\tau + \theta T/T_0$ , if  $\tau \leq (1-\theta)T/T_0$  or at  $\tau - (1-\theta)T/T_0$ , if  $\tau > (1-\theta)T/T_0$ . The new period of relay oscillator 2 is hence given by

$$T = \begin{cases} T_0 - T_0 \Delta\varphi\left(\tau + \theta \frac{T}{T_0}; 2\varepsilon\right) & \text{for } \tau \leq (1-\theta) \frac{T}{T_0}, \\ T_0 - T_0 \Delta\varphi\left(\tau - (1-\theta) \frac{T}{T_0}; 2\varepsilon\right) & \text{for } \tau > (1-\theta) \frac{T}{T_0}, \end{cases} \quad (4-A1)$$

where  $\Delta\varphi$  is defined in Eqs. 4-6 and 4-7 of the main text, repeated here for convenience:

$$\Delta\varphi_i(\varphi_i; \varepsilon_{ij}) = \begin{cases} \chi_b(\varepsilon_{ij}) + \beta_b(\varepsilon_{ij})\varphi_i & \text{for } 0 \leq \varphi_i < \varphi_c, \\ 1 - \varphi_i & \text{for } \varphi_c \leq \varphi_i < 1, \end{cases} \quad (4-A2)$$

$$\chi_b(x) := \frac{\beta_b(x)}{\beta_b(1)}, \beta_b(x) := e^{bx} - 1. \quad (4-A3)$$

The spike from oscillator 2 will arrive at oscillators 1 and 3 at phase  $\tau + (1-\theta)T/T_0$ , if  $\tau \leq \theta T/T_0$ , or  $\tau - \theta T/T_0$ , if  $\tau > \theta T/T_0$ . The new period of outer oscillators 1 and 3 is hence given by

$$T = \begin{cases} T_0 - T_0 \Delta\varphi\left(\tau + (1-\theta) \frac{T}{T_0}; \varepsilon\right) & \text{for } \tau \leq \theta \frac{T}{T_0}, \\ T_0 - T_0 \Delta\varphi\left(\tau - \theta \frac{T}{T_0}; \varepsilon\right) & \text{for } \tau > \theta \frac{T}{T_0}. \end{cases} \quad (4-A4)$$

Equations 4-A1 and 4-A4 are the 1:1 phase-locking equations, which give a relation between the synaptic weight  $\varepsilon$ , the conduction delay  $\tau$ , and the new period of the oscillators  $T$ .

Using Eqs. 4-A1 and 4-A4, we will derive four synchronization modes: driven, pacemaker, slave, and non-driven synchrony. In driven synchrony spikes from the outer oscillators immediately initiate a spike of the relay oscillator, and vice versa, cf. Fig. 4-2B, **top**. In pacemaker synchrony arrival of a spike from the relay oscillator at the outer oscillators immediately elicits a spike, but not vice versa, cf. Fig. 4-2B, **bottom**. When the relay oscillator spikes immediately after spikes from the outer oscillators, but not vice versa, we call this slave synchrony, cf. Fig. 4-2B, **middle**. Finally, non-driven synchrony occurs when neither the relay oscillator nor the outer oscillators spike immediately after input.

First, we consider driven synchrony. In order for all input spikes to elicit a spike in the receiving oscillators, we must have the following: for the relay oscillator  $\varphi_c(2\varepsilon) \leq \tau + \theta T/T_0$  if  $\tau \leq (1-\theta)T/T_0$ , and  $\varphi_c(2\varepsilon) \leq \tau - (1-\theta)T/T_0$  if  $\tau > (1-\theta)T/T_0$ ; and for the outer oscillators  $\varphi_c(\varepsilon) \leq \tau + (1-\theta)T/T_0$  if  $\tau \leq \theta T/T_0$ , and  $\varphi_c(\varepsilon) \leq \tau - \theta T/T_0$  if  $\tau > \theta T/T_0$ . Using Eqs. 4-A1, 4-A2, and 4-A4, we can then rewrite the new period of the relay oscillator as

$$T = \begin{cases} \tau T_0 + \theta T & \text{for } \tau \leq (1-\theta)\frac{T}{T_0} \text{ and } \varphi_c(2\varepsilon) \leq \tau + \theta\frac{T}{T_0}, \\ \tau T_0 - (1-\theta)T & \text{for } \tau > (1-\theta)\frac{T}{T_0} \text{ and } \varphi_c(2\varepsilon) \leq \tau - (1-\theta)\frac{T}{T_0}, \end{cases} \quad (4-A5)$$

and the new period of the outer oscillators as

$$T = \begin{cases} \tau T_0 + (1-\theta)T & \text{for } \tau \leq \theta\frac{T}{T_0} \text{ and } \varphi_c(\varepsilon) \leq \tau + (1-\theta)\frac{T}{T_0}, \\ \tau T_0 - \theta T & \text{for } \tau > \theta\frac{T}{T_0} \text{ and } \varphi_c(\varepsilon) \leq \tau - \theta\frac{T}{T_0}. \end{cases} \quad (4-A6)$$

We can now solve for  $\theta$  and  $T$  by using one part of Eqs. 4-A5 and 4-A6 each, and combining them under the condition that the new periods  $T$  of the relay and outer oscillators, respectively, must be identical to achieve synchrony. This yields four possible combinations:

$$\left(\theta, \frac{T}{T_0}\right) = \begin{cases} \left(\frac{1}{2}, 2\tau\right) & \text{for } \varphi_c(\varepsilon) \leq 2\tau \text{ and } \varphi_c(2\varepsilon) \leq 2\tau \quad \text{DS,} \\ (0, \tau) & \text{for } \varphi_c(\varepsilon) \leq \tau \text{ and } \varphi_c(2\varepsilon) \leq \tau, \\ (1, \tau) & \text{for } \varphi_c(\varepsilon) \leq \tau \text{ and } \varphi_c(2\varepsilon) \leq \tau, \\ \left(\frac{1}{2}, \frac{2}{3}\tau\right) & \text{for } \varphi_c(\varepsilon) \leq \frac{2}{3}\tau \text{ and } \varphi_c(2\varepsilon) \leq \frac{2}{3}\tau. \end{cases} \quad (4-A7)$$

For biologically realistic conditions  $\tau \in [0, 0.5]$  and  $\varepsilon \in [0, 0.21]$  and our choice  $b = 3$ , only the driven synchrony mode labeled “DS” turns out to be valid. The firing dynamics of “DS” is illustrated in Fig. 4-2B, **top**. For the other cases, the  $\varphi_c$  conditions are not fulfilled and therefore these solutions are rejected. Moreover, the third solution also has a  $\theta$  value out of range for 1:1 phase-locking. We will similarly identify the valid modes of other solutions below. Since  $\varphi_c(2\varepsilon) \leq \varphi_c(\varepsilon)$ ,  $\varphi_c(\varepsilon) \leq 2\tau$  implies  $\varphi_c(2\varepsilon) \leq 2\tau$  and the  $\varphi_c(\varepsilon) \leq 2\tau$  constraint is sufficient. This constraint divides the  $\varepsilon$  and  $\tau$  parameter space into two regions: driven synchrony is possible in the region where  $\varphi_c(\varepsilon) \leq 2\tau$  but not in the region where  $\varphi_c(\varepsilon) > 2\tau$ . These two regions are separated by the curve  $\varphi_c(\varepsilon) = 2\tau$  illustrated as the curve separating regions I and II in Fig. 4-2, **A** and **C**.

Second, we investigate pacemaker synchrony. For pacemaker synchrony only the outer oscillators spike directly upon input but not the relay one. Thus for the relay oscillator, we must have  $\varphi_c(2\varepsilon) > \tau + \theta T/T_0$  if  $\tau \leq (1-\theta)T/T_0$ , and  $\varphi_c(2\varepsilon) > \tau - (1-\theta)T/T_0$  if  $\tau > (1-\theta)T/T_0$ . For the outer oscillators, we must have  $\varphi_c(\varepsilon) \leq \tau + (1-\theta)T/T_0$  if  $\tau \leq \theta T/T_0$ , and  $\varphi_c(\varepsilon) \leq \tau - \theta T/T_0$  if  $\tau > \theta T/T_0$ . Using Eq. 4-A2 in Appendix 4.5, we can rewrite the new period of the relay oscillator given by Eq. 4-A1 as

$$T = \begin{cases} T_0\gamma_b(2\varepsilon) - \theta T\beta_b(2\varepsilon) & \text{for } \tau \leq (1-\theta)\frac{T}{T_0} \text{ and } \varphi_c(2\varepsilon) > \tau + \theta\frac{T}{T_0}, \\ T_0\gamma_b(2\varepsilon) + (1-\theta)T\beta_b(2\varepsilon) & \text{for } \tau > (1-\theta)\frac{T}{T_0} \text{ and } \varphi_c(2\varepsilon) > \tau - (1-\theta)\frac{T}{T_0}, \end{cases} \quad (4-A8)$$

$$\gamma_b(x) := 1 - \chi_b(x) - \beta_b(x)\tau, \quad (4-A9)$$

whereas the new period of the outer oscillators is given by Eq. 4-A6 in Appendix 4.5. Solving for  $\theta$  and  $T$  as before, we find the following four possibilities:

$$\left(\theta, \frac{T}{T_0}\right) = \begin{cases} \left(\tau \frac{T_0}{T}, \gamma_b(2\varepsilon) - \beta_b(2\varepsilon)\tau\right) & \text{for } \varphi_c(\varepsilon) \leq \frac{T}{T_0} \text{ and } \varphi_c(2\varepsilon) > 2\tau & \text{PS1,} \\ \left(\tau \frac{T_0}{T} - 1, \frac{\gamma_b(2\varepsilon) - \beta_b(2\varepsilon)\tau}{1 - \beta_b(2\varepsilon)}\right) & \text{for } \varphi_c(\varepsilon) \leq \frac{T}{T_0} \text{ and } \varphi_c(2\varepsilon) > 2\tau - \frac{T}{T_0}, \\ \left(\tau \frac{T_0}{T}, \frac{\gamma_b(2\varepsilon) - \beta_b(2\varepsilon)\tau}{1 - \beta_b(2\varepsilon)}\right) & \text{for } \varphi_c(\varepsilon) \leq \frac{T}{T_0} \text{ and } \varphi_c(2\varepsilon) > 2\tau - \frac{T}{T_0} & \text{PS2,} \\ \left(\tau \frac{T_0}{T} - 1, \frac{\gamma_b(2\varepsilon) - \beta_b(2\varepsilon)\tau}{1 - 2\beta_b(2\varepsilon)}\right) & \text{for } \varphi_c(\varepsilon) \leq \frac{T}{T_0} \text{ and } \varphi_c(2\varepsilon) > 2\tau - 2\frac{T}{T_0}. \end{cases} \quad (4-A10)$$

The two valid modes for pacemaker synchrony given our constraints are labeled “PS1” and “PS2” in Eq. 4-A10 in Appendix 4.5, respectively. Within our ranges of interest for  $\varepsilon$  and  $\tau$ , one can check numerically for the “PS1” and “PS2” pacemaker synchrony that  $\varphi_c(\varepsilon) \leq T/T_0$  implies  $\varphi_c(2\varepsilon) > 2\tau$  and  $\varphi_c(2\varepsilon) > 2\tau - T/T_0$ , respectively. Hence, only the  $\varphi_c(\varepsilon) \leq T/T_0$  constraint is required. “PS1” pacemaker synchrony is possible in the region  $\{(\varepsilon, \tau) \in [0, 0.21] \times [0, 0.5] \mid \varphi_c(\varepsilon) \leq T/T_0\}$ , while “PS2” is possible in the region  $\{(\varepsilon, \tau) \in [0, 0.21] \times [0, 0.5] \mid \varphi_c(\varepsilon) \leq T/T_0 \text{ and } (1-\theta)T/T_0 < \tau\}$ , where  $(1-\theta)T/T_0 < \tau$  refers to the condition given in Eq. 4-A1 in Appendix 4.5. The equality  $\varphi_c(\varepsilon) = T/T_0$  of “PS1” gives the curve separating regions II and III in Fig. 4-2, **A** and **C**. The firing dynamics for “PS1” pacemaker synchrony is illustrated in Fig. 4-2**B**.

Third, in slave synchrony only the relay oscillator spikes upon input, i.e., in case of the relay oscillator, we must have  $\varphi_c(2\varepsilon) \leq \tau + \theta T/T_0$  if  $\tau \leq (1-\theta)T/T_0$ , and  $\varphi_c(2\varepsilon) \leq \tau - (1-\theta)T/T_0$  if  $\tau > (1-\theta)T/T_0$ . For the outer oscillators, we must have  $\varphi_c(\varepsilon) > \tau + (1-\theta)T/T_0$  if  $\tau \leq \theta T/T_0$ , and  $\varphi_c(\varepsilon) > \tau - \theta T/T_0$  if  $\tau > \theta T/T_0$ . The new

period of the relay oscillator is given by Eq. 4-A5, and from Eqs. 4-A2 and 4-A4 we obtain the following expression for the new period of the outer oscillators

$$T = \begin{cases} T_0\gamma_b(\varepsilon) - (1-\theta)T\beta_b(\varepsilon) & \text{for } \tau \leq \theta\frac{T}{T_0} \text{ and } \varphi_c(\varepsilon) > \tau + (1-\theta)\frac{T}{T_0}, \\ T_0\gamma_b(\varepsilon) + \theta T\beta_b(\varepsilon) & \text{for } \tau > \theta\frac{T}{T_0} \text{ and } \varphi_c(\varepsilon) > \tau - \theta\frac{T}{T_0}. \end{cases} \quad (4-A11)$$

The four combinations are then:

$$\left(\theta, \frac{T}{T_0}\right) = \begin{cases} \left(1 - \tau\frac{T_0}{T}, \gamma_b(\varepsilon) - \beta_b(\varepsilon)\tau\right) & \text{for } \varphi_c(\varepsilon) > 2\tau & \text{and } \varphi_c(2\varepsilon) \leq \frac{T}{T_0} & \text{SS1,} \\ \left(1 - \tau\frac{T_0}{T}, \frac{\gamma_b(\varepsilon) - \beta_b(\varepsilon)\tau}{1 - \beta_b(\varepsilon)}\right) & \text{for } \varphi_c(\varepsilon) > 2\tau - \frac{T}{T_0} & \text{and } \varphi_c(2\varepsilon) \leq \frac{T}{T_0} & \text{SS2,} \\ \left(2 - \tau\frac{T_0}{T}, \frac{\gamma_b(\varepsilon) - \beta_b(\varepsilon)\tau}{1 - \beta_b(\varepsilon)}\right) & \text{for } \varphi_c(\varepsilon) > 2\tau - \frac{T}{T_0} & \text{and } \varphi_c(2\varepsilon) \leq \frac{T}{T_0}, \\ \left(2 - \tau\frac{T_0}{T}, \frac{\gamma_b(\varepsilon) - \beta_b(\varepsilon)\tau}{1 - 2\beta_b(\varepsilon)}\right) & \text{for } \varphi_c(\varepsilon) > 2\tau - 2\frac{T}{T_0} & \text{and } \varphi_c(2\varepsilon) \leq \frac{T}{T_0}. \end{cases} \quad (4-A12)$$

The two valid slave synchronization modes will be called “SS1” and “SS2”, respectively. Within our ranges of interest for  $\varepsilon$  and  $\tau$ , one can check numerically for the “SS1” slave synchrony mode that  $\varphi_c(\varepsilon) > 2\tau$  implies  $\varphi_c(2\varepsilon) \leq T/T_0$ ; whereas the constraints for “SS2” are always fulfilled in our ranges for  $\varepsilon$  and  $\tau$ . Hence “SS1” slave synchrony, of which the firing dynamic is illustrated in Fig. 4-2B, is possible in the region  $\{(\varepsilon, \tau) \in [0, 0.21] \times [0, 0.5] \mid \varphi_c(\varepsilon) > 2\tau\}$ , while “SS2” is possible in the region  $\{(\varepsilon, \tau) \in [0, 0.21] \times [0, 0.5] \mid \tau > \theta T/T_0\}$ , where  $\tau > \theta T/T_0$  refers to the condition given in Eq. 4-A4 in Appendix 4.5. The equality  $\tau = \theta T/T_0$  of “SS2” gives the curve separating regions I and IV in Fig. 4-2, A and C.

Finally, for non-driven synchrony none of oscillators fires immediately after receiving a spike. This implies that for the relay oscillator  $\varphi_c(2\varepsilon) > \tau + \theta T/T_0$  if  $\tau \leq (1-\theta)T/T_0$ , and  $\varphi_c(2\varepsilon) > \tau - (1-\theta)T/T_0$  if  $\tau > (1-\theta)T/T_0$ . For the outer

oscillators  $\varphi_c(\varepsilon) > \tau + (1-\theta)T/T_0$  if  $\tau \leq \theta T/T_0$ , and  $\varphi_c(\varepsilon) > \tau - \theta T/T_0$  if  $\tau > \theta T/T_0$ . The new period is then given by Eqs. 4-A8 and 4-A11 in Appendix 4.5 for the relay and outer oscillators, respectively. The resulting combinations are:

$$\left(\theta, \frac{T}{T_0}\right) = \begin{cases} \left(\frac{\rho_{++0}, \rho_{0+0+}}{\rho_{0+0+}, \zeta_+}\right) & \text{for } \varphi_c(\varepsilon) > \tau - \frac{\rho_{+0-}}{\zeta_+} \text{ and } \varphi_c(2\varepsilon) > \tau + \frac{\rho_{++0}}{\zeta_+} & \text{NDS1,} \\ \left(\frac{\rho_{+0-0}, \rho_{0+0+}}{\rho_{0+0+}, \zeta_0}\right) & \text{for } \varphi_c(\varepsilon) > \tau - \frac{\rho_{+0-0}}{\zeta_0} \text{ and } \varphi_c(2\varepsilon) > \tau + \frac{\rho_{+0-0}}{\zeta_0}, \\ \left(\frac{\rho_{++++}, \rho_{0+0+}}{\rho_{0+0+}, \zeta_0}\right) & \text{for } \varphi_c(\varepsilon) > \tau - \frac{\rho_{+0-0}}{\zeta_0} \text{ and } \varphi_c(2\varepsilon) > \tau + \frac{\rho_{+0-0}}{\zeta_0} & \text{NDS2,} \\ \left(\frac{\rho_{+0+}, \rho_{0+0+}}{\rho_{0+0+}, \zeta_-}\right) & \text{for } \varphi_c(\varepsilon) > \tau - \frac{\rho_{+0+}}{\zeta_-} \text{ and } \varphi_c(2\varepsilon) > \tau + \frac{\rho_{+0-0}}{\zeta_-} & \text{NDS3,} \end{cases} \quad (4-A13)$$

with  $\rho_{mnop} = [m + n\beta_b(\varepsilon)]\gamma_b(2\varepsilon) + [o + p\beta_b(2\varepsilon)]\gamma_b(\varepsilon)$ , where indices can take on the values +1, 0, -1 as represented by the signs, and likewise  $\zeta_m := \beta_b(\varepsilon) + \beta_b(2\varepsilon) + m\beta_b(\varepsilon)\beta_b(2\varepsilon)$ . The three valid non-driven synchronization modes will be called NDS1, NDS2, and NDS3, respectively. From the constraints of  $\varepsilon$  and  $\tau$  for “NDS1” slave synchrony,  $\varphi_c(\varepsilon) > \tau - \rho_{+0-}/\zeta_+$  implies  $\varphi_c(2\varepsilon) > \tau + \rho_{++0}/\zeta_+$ . For the “NDS2” slave synchrony,  $\varphi_c(\varepsilon) > \tau - \rho_{+0-0}/\zeta_0$  implies  $\varphi_c(2\varepsilon) > \tau + \rho_{+0-0}/\zeta_0$ . But the constraints of “NDS3” fulfill automatically in our range of  $\varepsilon$  and  $\tau$ . Hence the “NDS1” slave synchrony is possible in the region  $\{(\varepsilon, \tau) \in [0, 0.21] \times [0, 0.5] \mid \varphi_c(\varepsilon) > \tau - \rho_{+0-}/\zeta_+\}$ , while “NDS2” is possible in the region  $\{(\varepsilon, \tau) \in [0, 0.21] \times [0, 0.5] \mid \varphi_c(\varepsilon) > \tau - \rho_{+0-0}/\zeta_0$  and  $\tau > (1-\theta)T/T_0\}$  and “NDS3” in the region  $\{(\varepsilon, \tau) \in [0, 0.21] \times [0, 0.5] \mid \tau > (1-\theta)T/T_0\}$ , where  $\tau > (1-\theta)T/T_0$  refers to the condition given in Eq. 4-A1 in Appendix 4.5.

Based on different combinations of the synchronization modes DS from Eq. 4-A7 in Appendix 4.5, PS1 and PS2 from Eq. 4-A10 in Appendix 4.5, SS1 and SS2

from Eq. 4-A12 in Appendix 4.5, and NDS1, NDS2, and NDS3 from Eq. 4-A13 in Appendix 4.5, we can separate the parameter plane of time delay  $\tau$  and synaptic weight  $\varepsilon$  into ten regions, see Fig. 4-A1. In summary, the regions in the  $\varepsilon$  and  $\tau$  parameter space, where the modes are possible, are given by

$$\begin{aligned}
 & \{(\varepsilon, \tau) \in [0, 0.21] \times [0, 0.5] \mid \varphi_c(\varepsilon) \leq 2\tau\} && \text{for DS,} \\
 & \{(\varepsilon, \tau) \in [0, 0.21] \times [0, 0.5] \mid \varphi_c(\varepsilon) \leq T/T_0\} && \text{for PS1,} \\
 & \{(\varepsilon, \tau) \in [0, 0.21] \times [0, 0.5] \mid \varphi_c(\varepsilon) \leq T/T_0 \text{ and } (1-\theta)T/T_0 < \tau\} && \text{for PS2,} \\
 & \{(\varepsilon, \tau) \in [0, 0.21] \times [0, 0.5] \mid \varphi_c(\varepsilon) > 2\tau\} && \text{for SS1,} \\
 & \{(\varepsilon, \tau) \in [0, 0.21] \times [0, 0.5] \mid \tau > \theta T/T_0\} && \text{for SS2,} \\
 & \{(\varepsilon, \tau) \in [0, 0.21] \times [0, 0.5] \mid \varphi_c(\varepsilon) > \tau - \rho_{+0-}/\zeta_+\} && \text{for NDS1,} \\
 & \{(\varepsilon, \tau) \in [0, 0.21] \times [0, 0.5] \mid \varphi_c(\varepsilon) > \tau - \rho_{+0-}/\zeta_0 \text{ and } \tau > (1-\theta)T/T_0\} && \text{for NDS2,} \\
 & \{(\varepsilon, \tau) \in [0, 0.21] \times [0, 0.5] \mid \tau > (1-\theta)T/T_0\} && \text{for NDS3.}
 \end{aligned} \tag{4-A14}$$

### *Stability analysis of synchrony modes*

To investigate the stability of driven synchrony, we assume that the fixed point Eq. 4-A7 “DS” in Appendix 4.5 suffers from small phase perturbations  $(\varphi_1, \varphi_3) = (\tau + \delta\varphi_1, \tau + \delta\varphi_3)$  at time  $t_{2,n-1}^{\text{spike}}$ . Driven synchrony is asymptotically stable, if there is a  $\delta > 0$  such that the phases of the outer oscillators will be closer to  $\tau$  at the next spike time  $t_{2,n}^{\text{spike}}$  for  $\sqrt{\delta\varphi_1^2 + \delta\varphi_3^2} < \delta$ . Since  $\varphi_c(\varepsilon) < 2\tau$ , we can define  $\delta := 2\tau - \varphi_c(\varepsilon) > 0$ , and by this definition  $\varphi_c(\varepsilon) = 2\tau - \delta$ . The spike from the relay arrives when oscillator 1 has phase  $2\tau - \delta < \varphi_1 < 2\tau + \delta$  that exceeds the critical phase  $\varphi_c(\varepsilon)$ . Therefore, oscillator 1 will spike immediately after input. Since the same argument applies to oscillator 3, the outer oscillators will again spike in synchrony, proving asymptotic stability for small perturbations. Similar arguments can be made to show that the pacemaker synchrony of Eq. 4-A10 “PS1” and “PS2” in Appendix 4.5 is asymptotically stable.



Next we investigate the stability of the slave synchronization mode Eq. 4-A12 “SS1” in Appendix 4.5. Here one has to calculate the eigenvalues  $\lambda$  of the Jacobian of the return map near the fixed point of the outer oscillator phases (Zeitler et al., 2009). If all eigenvalues are within the unit circle ( $|\lambda| < 1$ ), then the fixed point is asymptotically stable, otherwise it is unstable ( $\exists \lambda \in \mathbb{C}; |\lambda| > 1$ ). Assume at time  $t_{2,n-1}^{\text{spike}}$  that phases are perturbed away from the fixed point of Eq. 4-A12 “SS1” in Appendix 4.5:  $(\varphi_1, \varphi_3) = (\tau + \delta\varphi_1, \tau + \delta\varphi_3)$ . Thus synaptic inputs from oscillators 1 and 3 will arrive at oscillator 2 at slightly different times. Without loss of generality, we assume that the synaptic input from oscillator 1 arrives earlier. This first synaptic input can make the relay oscillator spike immediately if  $\varphi_c(\varepsilon) < \tau + \theta T/T_0$ . Assuming that the perturbation is small enough for the solution in Eq. 4-A12 “SS1” in Appendix 4.5 to remain applicable, we find  $\varphi_c(\varepsilon) < \tau + \theta T/T_0 = 1 - \chi_b(\varepsilon) - 2\beta_b(\varepsilon)\tau = [1 + \beta_b(\varepsilon)]\varphi_c(\varepsilon) - 2\beta_b(\varepsilon)\tau$ . For nonzero coupling this is equivalent to  $2\tau < \varphi_c(\varepsilon)$ , which is biologically reasonable (Tsubo et al., 2007). Therefore, we assume  $\varphi_c(\varepsilon) < \tau + \theta T/T_0$ , and the spike from oscillator 1 will make the relay oscillator spike instantaneously when it arrives. Define  $\tilde{\varphi}_1$  as the phase of oscillator 1 at this relay spike time  $t_{2,n}^{\text{spike}}$ , then obviously  $\tilde{\varphi}_1 = \tau$ , the conduction delay.

To find the phase  $\tilde{\varphi}_3$  of oscillator 3 when oscillator 2 spikes at  $t_{2,n}^{\text{spike}}$ , we first derive the previous spike times of the outer oscillators  $t_{1,n-1}^{\text{spike}}$  and  $t_{3,n-1}^{\text{spike}}$ . The phase of oscillator 1 is  $\tau + \delta\varphi_1$  when the relay oscillator fires at  $t_{2,n-1}^{\text{spike}} = 0$ . After a delay  $\tau T_0$ , the spike from the relay oscillator arrives at oscillator 1, thus at its phase  $\varphi_1^{\text{old}} = 2\tau + \delta\varphi_1$ . If  $\delta\varphi_1$  is small enough we can still assume  $2\tau + \delta\varphi_1 < \varphi_c(\varepsilon)$ , i.e., this input from the relay will not make oscillator 1 spike instantaneously. Instead its phase will jump to  $\varphi_1^{\text{new}} = \varphi_1^{\text{old}} + \chi_b(\varepsilon) + \beta_b(\varepsilon)\varphi_1^{\text{old}}$ , cf. Eq. 4-A2 in Appendix 4.5. After receiving the spike, it takes an amount of time  $T_0(1 - \varphi_1^{\text{new}})$  until oscillator 1 spikes at  $t_{1,n-1}^{\text{spike}}$ . Hence  $t_{1,n-1}^{\text{spike}}$  is obtained by adding the conduction delay  $\tau T_0$  between

oscillators 2 and 1 to the time  $T_0(1 - \varphi_1^{\text{new}})$  that oscillator 1 still needs to evolve before spiking. Spike time  $t_{3,n-1}^{\text{spike}}$  can be obtained in a similar way, and thus one finds:

$$t_{1,n-1}^{\text{spike}} = T_0 \left\{ 1 - \chi_b(\varepsilon) - \beta_b(\varepsilon)\tau - [1 + \beta_b(\varepsilon)](\tau + \delta\varphi_1) \right\}, \quad (4-A15)$$

$$t_{3,n-1}^{\text{spike}} = T_0 \left\{ 1 - \chi_b(\varepsilon) - \beta_b(\varepsilon)\tau - [1 + \beta_b(\varepsilon)](\tau + \delta\varphi_3) \right\}. \quad (4-A16)$$

The next spike of the relay oscillator occurs at  $t_{2,n}^{\text{spike}} = t_{1,n-1}^{\text{spike}} + \tau T_0$ , as explained above. Since  $\tilde{\varphi}_3 = (t_{2,n}^{\text{spike}} - t_{3,n-1}^{\text{spike}})/T_0 = \tau + (t_{1,n-1}^{\text{spike}} - t_{3,n-1}^{\text{spike}})/T_0$ , we find the following return map for our local stability analysis

$$\tilde{\varphi}_1 = \tau, \quad (4-A17)$$

$$\tilde{\varphi}_3 = \tau - [1 + \beta_b(\varepsilon)]\varphi_1 + [1 + \beta_b(\varepsilon)]\varphi_3. \quad (4-A18)$$

The corresponding Jacobian matrix is

$$\begin{pmatrix} 0 & 0 \\ -[1 + \beta_b(\varepsilon)] & 1 + \beta_b(\varepsilon) \end{pmatrix}. \quad (4-A19)$$

The eigenvalues of this matrix are 0 and  $1 + \beta_b(\varepsilon) > 1$ . Consequently, this fixed point is not stable. Equation 4-A12 ‘‘SS2’’ in Appendix 4.5 can be shown to be unstable in a similar manner.

Finally, we investigate the stability of non-driven synchronization Eq. 4-A13 ‘‘NDS1’’ in Appendix 4.5. We will discuss the return map near the fixed point  $(\varphi_1^*, \varphi_3^*) = ((1 - \theta)T, (1 - \theta)T)$ . At time  $t_{2,n-1}^{\text{spike}}$ , we assume a small perturbation  $(\varphi_1, \varphi_3) = (\varphi_1^* + \delta\varphi_1, \varphi_3^* + \delta\varphi_3)$ . The arguments used to derive Eqs. 4-A15 and 4-A16 in Appendix 4.5 hold here, except that the perturbed fixed point is  $\tau + \delta\varphi_1 \rightarrow \varphi_1^* + \delta\varphi_1$  and  $\tau + \delta\varphi_3 \rightarrow \varphi_3^* + \delta\varphi_3$ , respectively. Without loss of generality, we assume that the synaptic input from oscillator 1 arrives at oscillator 2 before that from oscillator 3. Thus when oscillator 1 spikes at  $t_{1,n-1}^{\text{spike}}$ , the spike input

from oscillator 1 arrives at oscillator 2 at phase  $t_{1,n-1}^{\text{spike}}/T_0 + \tau$  and causes the phase of oscillator 2 to change to  $\chi_b(\varepsilon) + [1 + \beta_b(\varepsilon)][t_{1,n-1}^{\text{spike}}/T_0 + \tau]$ . Then the spike generated at  $t_{3,n-1}^{\text{spike}}$  by oscillator 3 will arrive when oscillator 2 has phase  $\chi_b(\varepsilon) + [1 + \beta_b(\varepsilon)][t_{1,n-1}^{\text{spike}}/T_0 + \tau] + (t_{3,n-1}^{\text{spike}} - t_{1,n-1}^{\text{spike}})/T_0$  and this causes a change in phase of oscillator 2 to

$$\varphi_2^{\text{new}} := [1 + \beta_b(\varepsilon)] \left\{ \chi_b(\varepsilon) + [1 + \beta_b(\varepsilon)][t_{1,n-1}^{\text{spike}}/T_0 + \tau] + (t_{3,n-1}^{\text{spike}} - t_{1,n-1}^{\text{spike}})/T_0 \right\} + \chi_b(\varepsilon), \quad (4-A20)$$

$$\Delta t := (1 - \varphi_2^{\text{new}})T_0, \quad (4-A21)$$

with oscillator 2 spiking after this additional time  $\Delta t$  has passed. Hence, when oscillator 2 spikes, the phases of the outer oscillators at the time  $t_{2,n}^{\text{spike}}$  are

$$\tilde{\varphi}_1 = \tau + \frac{\Delta t}{T_0} + \frac{t_{3,n-1}^{\text{spike}} - t_{1,n-1}^{\text{spike}}}{T_0}, \quad (4-A22)$$

$$\tilde{\varphi}_1 = \tau + \frac{\Delta t}{T_0}. \quad (4-A23)$$

The corresponding Jacobian matrix is

$$\begin{pmatrix} [1 + \beta_b(\varepsilon)] \{1 + \beta_b(\varepsilon)[1 + \beta_b(\varepsilon)]\} & [1 + \beta_b(\varepsilon)]\beta_b(\varepsilon) \\ \beta_b(\varepsilon)[1 + \beta_b(\varepsilon)]^2 & [1 + \beta_b(\varepsilon)]^2 \end{pmatrix}, \quad (4-A24)$$

with resulting eigenvalues

$$\lambda_1 = 1 + \beta_b(\varepsilon), \quad \lambda_2 = [1 + \beta_b(\varepsilon)]^3. \quad (4-A25)$$

This fixed point is not stable because these eigenvalues exceed the value one for  $\varepsilon \in ]0, 0.21]$ . In a similar manner one can show that Eq. 4-A13 “NDS2” and “NDS3” in Appendix 4.5 are unstable.

*Impact of STDP on coupling in slave synchrony*

In slave synchrony, the coupling strengths from the outer oscillators to the relay oscillator remain unchanged by STDP since the relay oscillator instantly spikes upon input from the outer oscillators. How about the coupling from the relay oscillator to the outer oscillators? Say their strengths are  $\varepsilon_{n-1}$  just after the outer oscillators spike at  $t_{1,n-1}^{\text{spike}} = t_{3,n-1}^{\text{spike}}$ . The relay spike arrives when the outer oscillators have phase  $2\tau$  since the relay oscillator fired at their phase  $\tau$ . Considering all prior spikes of the outer oscillators at times  $t_{1,l}^{\text{spike}}$ , this new relay spike arriving at time  $t_{1,n-1}^{\text{spike}} + 2\tau T_0$  changes the coupling strength by

$$\tilde{\varepsilon}_{n-1} = \varepsilon_{n-1} + \varepsilon_{n-1} \sum_{l=0}^{n-1} W \left[ t_{1,l}^{\text{spike}} - (t_{1,n-1}^{\text{spike}} + 2\tau T_0) \right] / 60 < \varepsilon_{n-1}. \quad (4-A26)$$

Note that this change is a decrease in coupling strength because  $t_{1,l}^{\text{spike}} < t_{1,n-1}^{\text{spike}} + 2\tau T_0$  for  $l = 0, 1, \dots, n-1$  and therefore  $W \left[ t_{1,l}^{\text{spike}} - (t_{1,n-1}^{\text{spike}} + 2\tau T_0) \right] < 0$ . The input from the relay oscillator also causes a phase shift  $\Delta\varphi(2\tau; \varepsilon_{n-1})$  of the outer oscillators such that their next spike occurs at  $t_{1,n}^{\text{spike}} = t_{1,n-1}^{\text{spike}} + T_0 - T_0 \Delta\varphi(2\tau; \varepsilon_{n-1})$ . Hence the new relay spike arrival at the outer oscillators precedes the next outer oscillator spike by  $(1-2\tau)T_0 - T_0 \Delta\varphi(2\tau; \varepsilon_{n-1})$ , and the previous relay spikes arrive at the outer oscillators at  $t_{1,n-1}^{\text{spike}} - t_{1,k}^{\text{spike}}$  for  $k = 0, 1, \dots, n-2$  earlier than the new relay spike arrival. Therefore, all previous synaptic inputs considered as a whole lead to an increase of the synaptic weight by

$$\begin{aligned} \varepsilon_n &= \tilde{\varepsilon}_{n-1} + \tilde{\varepsilon}_{n-1} \sum_{k=0}^{n-1} W \left[ (1-2\tau)T_0 - T_0 \Delta\varphi(2\tau; \varepsilon_{n-1}) + t_{1,n-1}^{\text{spike}} - t_{1,k}^{\text{spike}} \right] / 60, \\ &> \tilde{\varepsilon}_{n-1}. \end{aligned} \quad (4-A27)$$

Under certain conditions, see main text, this leads to STDP turning slave synchrony into driven synchrony, and the transition time can be determined by numerically iterating the formulas for  $\tilde{\varepsilon}_{n-1}$  and  $\varepsilon_n$ .



# 5

## **Robustness of long-range zero-lag synchronization**

## 5.1 Introduction

Neuronal gamma-band synchronization has been reported in many species and in a large number of brain structures in sensory and motor tasks (Gray et al., 1989; Fries et al., 2001; Pesaran et al., 2002; Schoffelen et al., 2005; Fries et al., 2008). Although the first studies on this topic presented experimental evidence that the relative phase of gamma oscillations in widely separated brain areas is near zero (Frien et al., 1994; Roelfsema et al., 1997; Castelo-Branco et al., 1998; Rodriguez et al., 1999; Gross et al., 2004), later studies focusing on a more careful consideration of phase differences suggested that phase differences might not be zero. In particular, Gregoriou et al. (2009a) showed that neuronal oscillations in the frontal eye fields (FEF) and area V4 in visual cortex are tightly coupled but not at zero-lag. These authors reported that attention to a visual stimulus in receptive fields of cells in FEF and V4 leads to enhanced oscillatory coupling between the two areas in the gamma frequency range, but the oscillations are shifted in time by 8 to 13 ms. Uhlhaas et al. (2009) reported that the activity of neurons in different parts of neocortex is rarely synchronized with exact zero lag. Instead, cross-correlation histograms usually reveal small but highly stable and significant delays (Konig et al., 1995b; Roelfsema et al., 1997; Schneider and Nikolic, 2006; Nikolic, 2007; Havenith et al., 2009). These new findings raise the question whether previously measured lags in synchrony of distal brain areas were really zero. They also raise the question whether zero-lag coupling between distal brain areas with considerable time delays in the connections is possible at all. To address this question, we have investigated whether zero-lag synchrony is possible and if so, which conditions regarding synaptic coupling strength and time delay may allow zero-lag synchrony.

In Viriyopase et al. (2012) we have shown that a neural network with two neuronal oscillators coupled by a relay oscillator can reveal zero-lag synchronous activity. In that study we have explained several modes of synchronous firing, where some of the modes are stable and others are unstable. The results showed that synchrony can be achieved much easier with type II Hodgkin–Huxley neurons, which have a biphasic phase response curve, than with type I neurons in the network. Input from an instantaneous synapse or from a fast alpha synapse with short rise and decay time constants can more readily synchronize the outer oscillators than input from a slow alpha synapse with longer rise and decay time constants. Spike-timing

dependent plasticity (STDP) allows a larger range of coupling strengths to produce synchronization. This can be understood from the fact that by STDP a weak coupling, which is not strong enough to cause synchronous firing, gradually increases to larger synaptic strengths that allow synchronous firing.

In this chapter, we will explore these results in more detail for a similar network architecture with neuronal oscillators coupled indirectly by a relay oscillator. First, we will investigate the role of the phase response curve on synchronization. In **Chapter 4** (see also Viriyopase et al. (2012)), we have shown that a network with Hodgkin-Huxley neurons, which have type II phase response curves, is more suitable to obtain zero-lag synchrony than a network with Mirollo-Strogatz (MS) neurons, which have type I phase response curves. The MS neuron has a peculiar phase response curve. Therefore, we will explore zero-lag synchrony for several variations of more realistic type I phase response curves, including a refractory period.

Secondly, elaborating on our results in **Chapter 4** (see also Viriyopase et al. (2012)), where we showed that STDP significantly contributes to zero-lag synchrony, we will explore the effect of changes in the potentiation and depression parts of STDP. The intuitive idea is that STDP requires a careful balance between potentiation, which strengthens synaptic connections, and depression, which has the opposite effect. We will investigate this both for instantaneous synapses and for alpha synapses. Finally, we will investigate the robustness of zero-lag synchrony when the time delays between various oscillators are not identical. Our results show that even small differences in the time delay between various oscillators is sufficient to eliminate zero-lag synchrony.

## 5.2 Materials and methods

### 5.2.1 Network model

As in **Chapter 4** (see also Viriyopase et al. (2012)), the model consists of three coupled neuronal oscillators, where each oscillator can be considered as a single neuron or as a population of neurons. A “relay” or “inner” oscillator is coupled bidirectionally with two “outer” oscillators. The outer oscillators are only coupled with the relay oscillator but not with each other. Unless stated otherwise, all three



oscillators are identical with the same intrinsic firing period  $T_0 = 25$  ms, corresponding to oscillations in the gamma frequency range. The coupling strength  $\varepsilon_{ij}$  refers to the coupling strength from presynaptic oscillator  $j$  to postsynaptic oscillator  $i$ . All synaptic couplings in the model are excitatory. The delay times between inner and outer oscillators are constant and symmetric: that is, the delay time from oscillator  $i$  to  $j$  is equal to that from oscillator  $j$  to  $i$ . These delay times  $\tau_k$  are typically considerably shorter than the oscillation period (Fries, 2005). Therefore, in the following we will consider conduction delays shorter than  $T_0/2$  with  $\tau_k$  that is expressed as a fraction of the intrinsic period  $T_0$  and thus in the range between 0 and 0.5.

### 5.2.2 Neuronal model

In this study we have investigated the dynamics of the network with neurons of the type I Mirollo-Strogatz (MS) phase oscillator (Mirollo and Strogatz, 1990), characterized by a voltage-like state variable  $f \in [0,1]$ , increasing monotonically from 0 towards the threshold value  $f = 1$ . Within a cycle the state of the uncoupled neuronal oscillator is defined by a monotonically increasing concave function  $f(\varphi): [0,1] \rightarrow [0,1]$ :

$$f(\varphi) = \frac{1}{b} \ln \left[ 1 + (e^b - 1) \varphi \right], \quad (5-1)$$

$$\frac{d\varphi}{dt} = \frac{1}{T_0}, \quad (5-2)$$

with a phase variable  $\varphi \in [0,1]$  and a dissipation parameter  $b$ .  $T_0$  in Eq. 5-2 is the intrinsic firing period of the oscillator. When the threshold is reached, the oscillator fires, the state variable  $f$  is reset to zero, and the cycle repeats. The value  $b = 3$  is used throughout this study.

### 5.2.3 Instantaneous synaptic coupling

We have used two types of synaptic coupling in the network. The first type of coupling is with instantaneous synapses. For an instantaneous synapse with coupling

strength  $\varepsilon_{ij}$ , the neuronal state  $f_i$  after arrival of a spike from oscillator  $j$  is incremented instantaneously to

$$f_i^{\text{new}}(\varphi_i) = \min[f_i(\varphi_i) + \varepsilon_{ij}, 1] \quad (5-3)$$

with  $\varphi_i$  the phase of postsynaptic oscillator  $i$  at the time of the spike arrival. The phase  $\varphi_i$  for which the oscillator reaches the threshold after spike input ( $f_i(\varphi_i) + \varepsilon_{ij} = 1$ ) is called the critical phase  $\varphi_c$  (Zeitler et al., 2009) and is given by

$$\varphi_c(\varepsilon_{ij}) = \frac{e^{b(1-\varepsilon_{ij})} - 1}{e^b - 1}. \quad (5-4)$$

If a spike arrives at  $\varphi_i < \varphi_c$ ,  $f_i$  will increase instantaneously by  $\varepsilon_{ij}$ . The instantaneous change of the state  $f_i$  by  $\varepsilon_{ij}$  corresponds to a phase shift  $\Delta\varphi_i$  given by  $\Delta\varphi_i = f_i^{-1}[f_i(\varphi_i) + \varepsilon_{ij}] - \varphi_i$ , which yields

$$\Delta\varphi_i(\varphi_i; \varepsilon_{ij}) = \begin{cases} \chi_b(\varepsilon_{ij}) + \beta_b(\varepsilon_{ij})\varphi_i & \text{for } 0 \leq \varphi_i < \varphi_c, \\ 1 - \varphi_i & \text{for } \varphi_c \leq \varphi_i < 1, \end{cases} \quad (5-5)$$

$$\chi_b(x) := \frac{\beta_b(x)}{\beta_b(1)}, \beta_b(x) := e^{bx} - 1, \quad (5-6)$$

where  $\varphi_i$  is the phase of the postsynaptic oscillator just before arrival of the input spike.

The phase shift  $\Delta\varphi_i$  depends on the phase  $\varphi_i$  when the spike input arrives. The maximum of the phase shift  $\Delta\varphi_i$  should be in the second part of the intrinsic cycle of the oscillator (Tsubo et al., 2007), and therefore  $\varphi_c > 0.5$ . This restriction imposes an upper bound on the value of  $\varepsilon_{ij} < 0.21$  through Eq. 5-4.

### 5.2.4 Phase response curve

The phase response curve (PRC) gives the phase change of the postsynaptic oscillator due to an excitatory input pulse as a function of the phase of input. The PRC is defined by

$$PRC(\varphi_i; \varepsilon_{ij}) := 1 - \frac{T(\varphi_i; \varepsilon_{ij})}{T_0} \quad (5-7)$$

with  $T(\varphi_i; \varepsilon_{ij})$  representing the new period of postsynaptic oscillator  $i$  after receiving input with strength  $\varepsilon_{ij}$  at phase  $\varphi_i$ . By Taylor expansion of the expression for  $PRC$  for infinitesimal inputs, the following expression for the PRC of the MS neuron is obtained

$$PRC1(\varphi_i; \varepsilon_{ij}) := \begin{cases} \frac{e^{b\varepsilon_{ij}} - 1}{e^b - 1} + [e^{b\varepsilon_{ij}} - 1]\varphi_i & \text{for } 0 \leq \varphi_i \leq \varphi_c, \\ 1 - \varphi_i & \text{for } \varphi_c \leq \varphi_i \leq 1. \end{cases} \quad (5-8)$$

The shape of the PRC of the MS neuron (indicated by  $PRC1$  in Eq. 5-8) for  $\varepsilon_{ij} = 0.1$  (circles) and  $\varepsilon_{ij} = 0.05$  (“+” symbols) is shown in Fig. 5-1.  $PRC1$  can be distinguished in two sections. When excitatory input arrives at the postsynaptic oscillator at a phase  $\varphi_i$  in the first part ( $0 \leq \varphi_i < \varphi_c$ ), the state of the postsynaptic oscillator is incremented by  $\varepsilon_{ij}$  causing a phase advance. When excitatory input arrives in the second part ( $\varphi_c \leq \varphi_i < 1$ ), where the value of the slope of  $PRC1$  is -1, the postsynaptic oscillator spikes immediately.

Note that the phase increment for a synaptic input arriving at  $\varphi_i = 0$  for  $PRC1$  is not zero that is physiologically not plausible. Therefore, we have modified  $PRC1$  by changing its slope between  $\varphi_i = 0$  and  $\varphi_i = \varphi_c$  such that the value of  $PRC1$  for phase  $\varphi_i = 0$  is zero. Moreover, we have implemented an absolute refractory period with a duration  $\varphi_r \geq 0$ . This gives the following  $PRC2$

$$PRC2(\varphi_i; \varepsilon_{ij}, \varphi_r) := \begin{cases} 0 & \text{for } 0 \leq \varphi_i < \varphi_r, \\ \left[ \frac{1 - \varphi_c(\varepsilon_{ij})}{\varphi_c(\varepsilon_{ij}) - \varphi_r} \right] (\varphi_i - \varphi_r) & \text{for } \varphi_r \leq \varphi_i < \varphi_c, \\ 1 - \varphi_i & \text{for } \varphi_c \leq \varphi_i < 1. \end{cases} \quad (5-9)$$

Figure 5-1 shows an example of  $PRC2$  for  $\varphi_r = 0.1$  and  $\varepsilon_{ij} = 0.1$ .

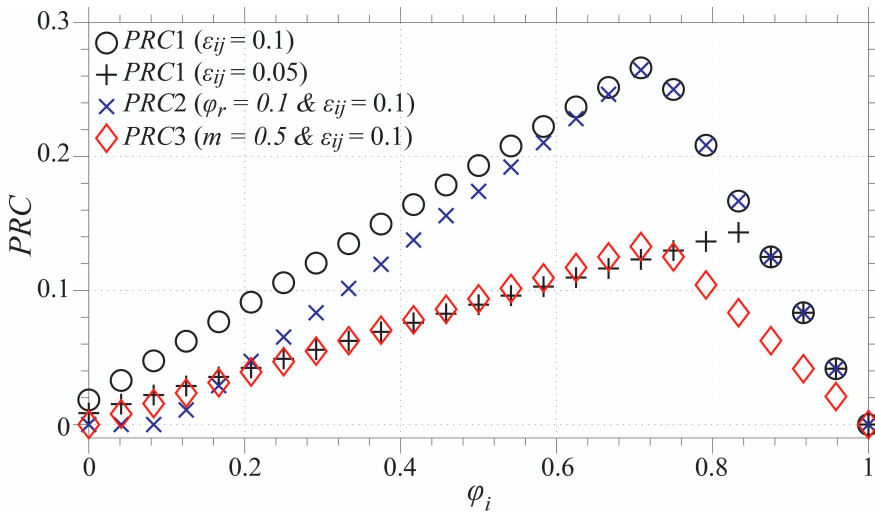


**Figure 5-1. Examples of various phase response curves.**  $PRC1$ , defined by Eq. 5-8, is shown for coupling strengths  $\varepsilon_{ij} = 0.1$  (black circles) and  $0.05$  (black “+” symbols). Blue crosses show an example of  $PRC2$  with the absolute refractory period of length  $0.1$ , while red diamonds show an example of  $PRC3$  with the slope of the second part of PRC  $m = -0.5$ .

$PRC1$  and  $PRC2$  give rise to instantaneous spiking when the synaptic input arrives in the last part of the oscillatory cycle ( $\varphi_c \leq \varphi_i < 1$ ). In most physiological conditions, a single synaptic input will not immediately elicit an action potential (Tsubo et al., 2007). Therefore, we have modified the slope of  $PRC2$  without the absolute refractory period to prevent instantaneous spiking. We define this new PRC as  $PRC3$  by

$$PRC3(\varphi_i; \varepsilon_{ij}) := \begin{cases} m \left[ \frac{1 - \varphi_c(\varepsilon_{ij})}{\varphi_c(\varepsilon_{ij})} \right] \varphi_i & \text{for } 0 \leq \varphi_i < \varphi_c, \\ m(1 - \varphi_i) & \text{for } \varphi_c \leq \varphi_i \leq 1. \end{cases} \quad (5-10)$$

An example of  $PRC3$  with  $\varepsilon_{ij} = 0.1$  and  $m = 0.5$  is shown in Fig. 5-1. Note that  $PRC1$ ,  $PRC2$ , and  $PRC3$  all belong to the category of type I PRCs.

### 5.2.5 Temporally extended synaptic coupling

In addition to instantaneous input, we will evaluate the dynamics of the network with a more realistic synaptic coupling model provided by the so-called alpha function. For an ‘‘alpha synapse’’, the postsynaptic potential after arrival of a spike at time  $t_0$  at a synapse with strength  $\varepsilon_{ij}$  is described by

$$\alpha(t; \varepsilon_{ij}, \tau_{\text{syn}}) = \begin{cases} 0 & \text{for } t < t_0, \\ \varepsilon_{ij} \frac{t - t_0}{\tau_{\text{syn}}^2} \exp\left(-\frac{t - t_0}{\tau_{\text{syn}}}\right) & \text{for } t \geq t_0, \end{cases} \quad (5-11)$$

where  $\tau_{\text{syn}} > 0$  is the synaptic rise time of the input. Unless stated otherwise,  $\tau_{\text{syn}} = 2$  ms in this study. For the simulations with the alpha synapse, the numerical simulation is implemented using an Euler scheme with a time step size equal to 2.5  $\mu\text{sec}$ . ( $\approx 10^{-4} T_0$ ).

### 5.2.6 Spike-timing dependent plasticity (STDP)

We have implemented the usual additive STDP rule that depends on the relative spike times for each pair of pre- and postsynaptic spikes (Froemke et al., 2006) for both instantaneous and alpha synapses. For a presynaptic spike at arrival time  $t_k^{\text{arr}}$  and a postsynaptic spike at  $t_l^{\text{spike}}$ , the fractional synaptic modification  $W(\Delta t)$  is given by

$$W(\Delta t) := \begin{cases} A_- \exp\left(\frac{\Delta t}{\tau_-}\right) & \text{for } \Delta t < 0, \\ 0 & \text{for } \Delta t = 0, \\ A_+ \exp\left(-\frac{\Delta t}{\tau_+}\right) & \text{for } \Delta t > 0, \end{cases} \quad (5-12)$$

with  $\Delta t := t_i^{\text{spike}} - t_k^{\text{arr}}$ .

The spike arrival time  $t_k^{\text{arr}}$  is defined as the time of the onset of the postsynaptic potential, just as in the experimental protocol by Bi and Poo (1998). Unless stated otherwise, the time constant for potentiation  $\tau_+$  and depression  $\tau_-$  is  $\tau_{+,0} := 16.8 \text{ ms}$  ( $\approx 0.67T_0$ ) and  $\tau_{-,0} := 33.7 \text{ ms}$  ( $\approx 1.35T_0$ ), respectively. In this study the standard value for the maximum amplitude of potentiation  $A_+$  and depression  $A_-$  is  $A_{+,0} := 0.78$  and  $A_{-,0} := -0.27$ , respectively. These standard parameter values for STDP were fitted to the data from Bi and Poo (1998), who determined the fractional synaptic modification  $W$  as the relative change in synaptic strength after evoking an input and output spike pair 60 times. We assume that the change of the synaptic weight  $\Delta\varepsilon$  caused by each input spike is constant and defined by  $\Delta\varepsilon = \varepsilon_0 W(\Delta t)/60$  (Song et al., 2000; van Rossum et al., 2000) with initial synaptic weight  $\varepsilon_0$  and  $W(\Delta t)$  as in Eq. 5-12. Therefore, the learning rule used for a particular pair of pre- and postsynaptic spikes is given by  $\varepsilon_0 \rightarrow \varepsilon_0 + \varepsilon_0 W(\Delta t)/60$ , in agreement with Lee et al. (2009). The simulation procedure for modification of synaptic strengths by STDP has been described in detail in sec. 4.2.2 of **Chapter 4** (see also Viriyopase et al. (2012)).

### 5.2.7 Synchronization measures

The synchronization and convergence to synchronization were calculated using the phase-locking equations described in **Chapter 4** (see also Viriyopase et al. (2012)). These phase-locking equations determine the oscillation period of a network and the relative phase of the oscillators for the stable state where the oscillators are phase-locked to each other (van Vreeswijk et al., 1994; Bressloff and Coombes, 1998). The

phase-locking equations can be used to determine whether synchrony exists for a particular set of parameter values.

Synchronous firing is defined as firing of two oscillators within a small time window, where the time window should be sufficiently large to eliminate the effect of small amounts of noise and sufficiently small to provide an accurate estimate of synchrony. We define synchrony or synchronous firing as the condition when the spikes of the outer oscillators occur within a time interval of  $|t_{1,n}^{\text{spike}} - t_{3,n}^{\text{spike}}| \leq 0.02T_0 \approx 0.5 \text{ ms}$  (Engel and Singer, 2001). “Synchronization quality” (SQ) is defined as the fraction of the number of initial phase combinations that leads to stable synchronous firing of the outer oscillators. SQ has a value between 0% and 100%, where 100% means that the outer oscillators always converge to synchronous spiking, independent of their initial relative phases. This provides a measure of the attraction domain of the initial phases for reaching synchronization of the outer oscillators.

To investigate the impact of the various parameters of the STDP learning window, we wish to derive a single value for the SQ, rather than one value for each combination of synaptic weights and conduction delays. For this purpose we consider various synaptic weights in 100 equally spaced steps in the range from 0.01 to 0.21 and conduction delays in 100 equally spaced steps in the range from 0.01 to 0.49. Then we average the SQ over these 10,000 results to obtain an “average synchronization quality” (average SQ) for each parameter set of the learning window.

For some combinations of the synaptic weights, delay times, and initial phases, the state of zero-lag synchronization is reached faster than for other combinations. Therefore, we define a “convergence promptness” (CP) for the network to achieve zero-lag synchronization of the outer oscillators. This is calculated as  $CP = SQ \times \left(1 - \frac{\langle n_{\text{sync}} \rangle}{n_{\text{sess}}}\right)$ , where  $\langle n_{\text{sync}} \rangle$  is the average number of intrinsic periods  $T_0$  needed to achieve zero-lag synchrony. Only simulations actually resulting in zero-lag synchrony are counted in that average. When there is no zero-lag synchrony established within  $n_{\text{sess}} = 15$  cycles, CP equals to 0. Note that

$\langle n_{\text{sync}} \rangle \leq n_{\text{sess}}$  with  $n_{\text{sess}} = 15$  here, and that the measure is multiplied with the SQ to account for the readiness of the system to achieve zero-lag synchrony at all.

Finally, not only are we interested in synchrony of the outer oscillators, but also in the relative phase  $\varphi_r$  for stable modes in which the outer oscillators oscillate in a stable state that does not correspond to synchrony. The relative phase between the outer oscillators is defined by  $\varphi_r := (t_{3,n}^{\text{spike}} - t_{1,n}^{\text{spike}}) / T_0$  with a value between -1 and 1. Since values for  $\varphi_r$  of -1, 0, and 1 all refer to the same state, we rescaled  $\varphi_r$  to the range  $-1/2$  to  $1/2$  by periodically mapping  $[-1, -0.5]$  to  $[0, 0.5]$  and  $[0.5, 1]$  to  $[-0.5, 0]$ .

### 5.3 Results

We will start with a short summary of the synchronization properties of the network with the MS neurons, of which the PRC is explicitly given by  $PRC1$  (Eq. 5-8), as reported in **Chapter 4** (see also Viriyopase et al. (2012)). Figure 5-2A shows the simulation results after 15 cycles for the SQ as a function of the conduction delay  $\tau$  and the synaptic weight  $\varepsilon$  for the MS model with instantaneous synapses, identical delay times ( $\tau_1 = \tau_3 = \tau$ ), and identical coupling strengths ( $\varepsilon_{12} = \varepsilon_{21} = \varepsilon_{23} = \varepsilon_{32} = \varepsilon$ ). The three solid black curves show the analytically calculated boundaries between different modes of synchrony. In the upper right area, indicated by IV, the dynamics is dominated by “slave synchrony”, which implies that the relay oscillator spikes immediately upon arrival of synaptic input from the outer oscillators, but the outer ones do not so after input from the relay one (Fig. 5-2B, **right**). In region I, zero-lag synchronization occurs mainly when both the relay and outer oscillators spike immediately upon arrival of synaptic input. This “driven synchrony” mode (DS) with period  $T_I$  for all neurons (Fig. 5-2B, **left**) is stable. Region II shows mainly slave synchrony like in region IV but with a different period  $T_{II}$ . In region III, zero-lag synchronization occurs mainly when the outer oscillators spike immediately upon arrival of synaptic input while the relay oscillator does not (“pacemaker synchrony”). Since pacemaker synchrony is a stable mode with a slow convergence



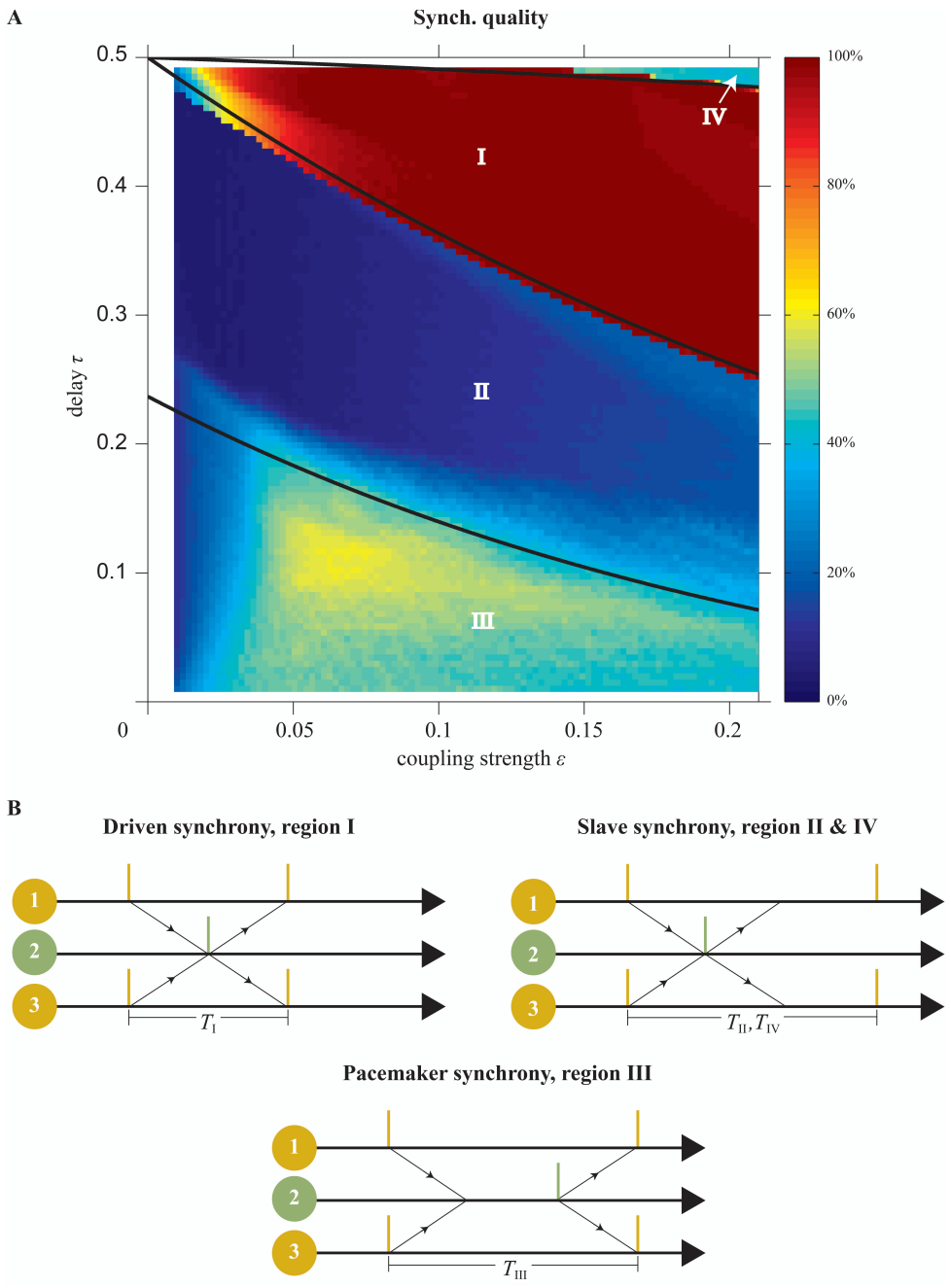


**Figure 5-2. Features of synchronization depending on delay time and coupling strength.** *A*, Synchronization quality (SQ) for model with instantaneous synapses. Black curves

indicate boundaries of dynamics calculated analytically using the phase-locking equation. **B**, Illustration of synchrony modes dominant in regions indicated by roman numerals in **A**. SQ is high in region I, low in regions II and IV, and intermediate in region III. Slave synchrony (regions II and IV) is not stable, whereas driven (region I) and pacemaker (region III) synchrony are asymptotically stable.

rate, zero-lag synchrony exists but is reached only after many cycles. For more details see Viriyopase et al. (2012).

In summary, the SQ changes from high (region I) to low (region II) and back to intermediate values (region III) when the conduction delay decreases from 0.5 to 0. A stability analysis indicates that regions II and IV show poor SQ because slave synchrony that dominates in these regions is unstable, whereas driven and pacemaker synchrony that dominate in regions I and III are asymptotically stable and robust against changes in the initial phases. Most combinations of delay and synaptic weight yield a SQ that is below 50%. The physiological interpretation of this result is that if zero-lag synchrony exists for a particular set of parameter values for the delay and the synaptic strength, the model only converges to zero-lag synchrony for a limited set of initial relative phases of the neuronal oscillators. For other initial relative phases, the system converges to a stable rhythm where the relative phase between the outer oscillators is different from zero (see Fig. 4-3 in **Chapter 4**).

The results in Fig. 5-2 were obtained using *PRC1*. In order to explore the effect of other PRCs, Fig. 5-3, **A** and **B**, show the results for *PRC2* ( $\varphi_r = 0.1$ ) and *PRC3* ( $m = -0.5$ ), respectively. Qualitatively, these results are very similar to the results in Fig. 5-2A. However, some quantitative differences exist.

Figure 5-3A shows a lower SQ for small time delays (range from  $\tau = 0$  to 0.05) for *PRC2* than for *PRC1* in Fig. 5-2A. This is a consequence of the refractory period  $\varphi_r$  of *PRC2* phase oscillators in region III where pacemaker synchrony dominates. For pacemaker synchrony the synaptic inputs from the outer phase oscillators trigger a spike in the relay phase oscillator that arrives the outer ones when their phase is  $2\tau$ . If the time delay is small such that  $2\tau \leq \varphi_r$ , the input from

the relay phase oscillator arrives in the refractory period of the outer phase oscillators. This eliminates the effective coupling between the relay phase oscillator and the outer phase oscillators and thereby eliminates synchrony.

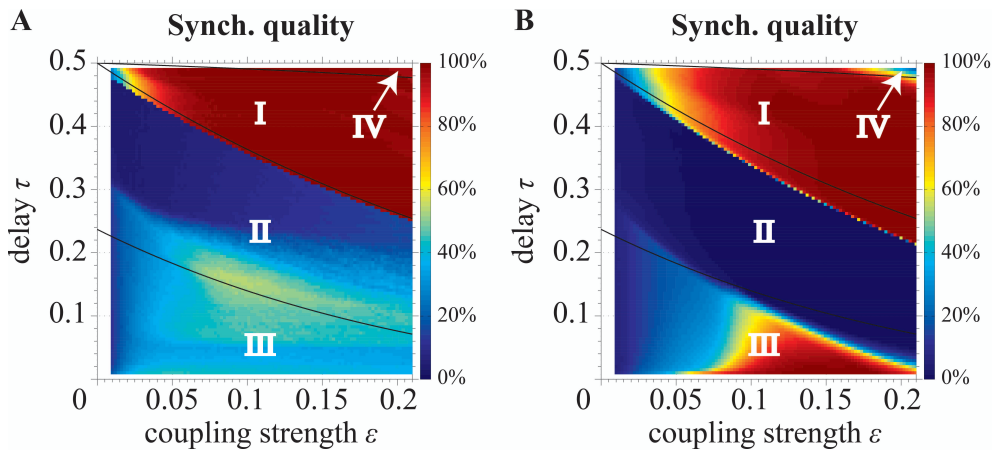


**Figure 5-3. Synchronization quality (SQ) for the model in Fig. 5-2 with PRC2 and PRC3.** *A* shows SQ with PRC2 with an absolute refractory period  $\varphi_r = 0.1$ , i.e. 2.5 ms for 40 Hz. *B* shows SQ for PRC3 with a slope  $-0.5$  in the last part of the PRC.

Another quantitative difference with the results in Fig. 5-2A is found in region IV. Figure 5-3A shows almost perfect synchrony in region IV, whereas Fig. 5-2A shows a SQ near 50% in region IV. The reason that Fig. 5-3A shows excellent synchronization in region IV is that slave synchrony (Fig. 5-2B, right) appearing in region IV with PRC1 changes to driven synchrony with PRC2 (Fig. 5-2B, left). The explanation for the change is as follows. In region IV the time delays are relatively long. For PRC1 the main synchronization mode in region IV is slave synchrony where the relay oscillator spikes immediately upon arrival of synaptic input from the outer oscillators and spikes from the relay oscillator arrive at the outer ones early in the oscillation phase of their next cycle. It is important to realize that the outer oscillators have completed a full cycle before arrival of the spikes from the relay oscillator because  $2\tau$  exceeds the oscillation period due to the relatively large value of the delay  $\tau$ . Therefore, the spikes from the relay oscillator arrive at the outer oscillators during their refractory period, and the outer oscillators will not

respond to the outputs from the relay oscillator. Because the outer oscillators lack the excitatory input from the relay oscillator, the outer oscillators have a longer interspike interval than the interval of the outer oscillators when they receive the excitatory inputs with *PRC1*. Hence, the slave synchrony in region IV is not possible with *PRC2* and the slave synchrony mode will eventually be converted to the driven synchrony mode. This explains the excellent SQ for region IV in Fig. 5-3A.

Figure 5-3B shows that the range of  $\tau$  and  $\varepsilon$  values that give a high SQ for *PRC3* increases compared to that for *PRC1* and *PRC2*. This increased domain with high SQ values for *PRC3* in region III is a consequence of the lack of instantaneous spiking after synaptic input due to the larger slope (-0.5 instead of -1) at the end of *PRC3*. The lack of instantaneous spiking will eliminate the pacemaker-slave mode, which is a stable mode of asynchronous firing for *PRC1* (see Fig. 4-3, C and D, in **Chapter 4** for the relative firing behavior of the oscillators in this mode), because the outer oscillators will no longer spike immediately upon arrival of the input from the relay oscillator nor does the relay oscillator upon arrival of the input from the outer oscillators. When we switch the PRC from *PRC1* to *PRC3*, spikes from the relay oscillator arrive in the second part of *PRC3* of the outer oscillators, while outputs from the outer oscillators arrive in the first part of the relay oscillator. This gives rise to a new stable mode of synchrony, which will be explained below.

Let us assume that the PRC is *PRC1* and that the network oscillates in the pacemaker-slave mode. When we switch the PRC from *PRC1* to *PRC3*, oscillators 1 and 2 in the pacemaker-slave mode (see Fig. 4-3, C and D, in **Chapter 4**) will not spike immediately upon arrival of the spike inputs because the phase increments are smaller for *PRC3* than for *PRC1*. Therefore, the spiking interval of oscillators 1 and 3 increases and so does the spiking interval of oscillator 2. Because oscillator 2 receives two input spikes, the phase advance of oscillator 2 will be larger than that of oscillators 1 and 3. As a consequence, the next spike from oscillator 2 arrives at oscillators 1 and 3 earlier in the cycle. This process repeats itself until a new stable phase is reached where output from oscillator 2 arrives at oscillators 1 and 3 at a phase in the second part of *PRC3*. Because, with *PRC1*, about 50% of the initial phases of the oscillators in region III leads to the pacemaker-slave mode (see Fig. 4-2A in **Chapter 4**), these 50% of the initial phases lead to the new stable synchrony

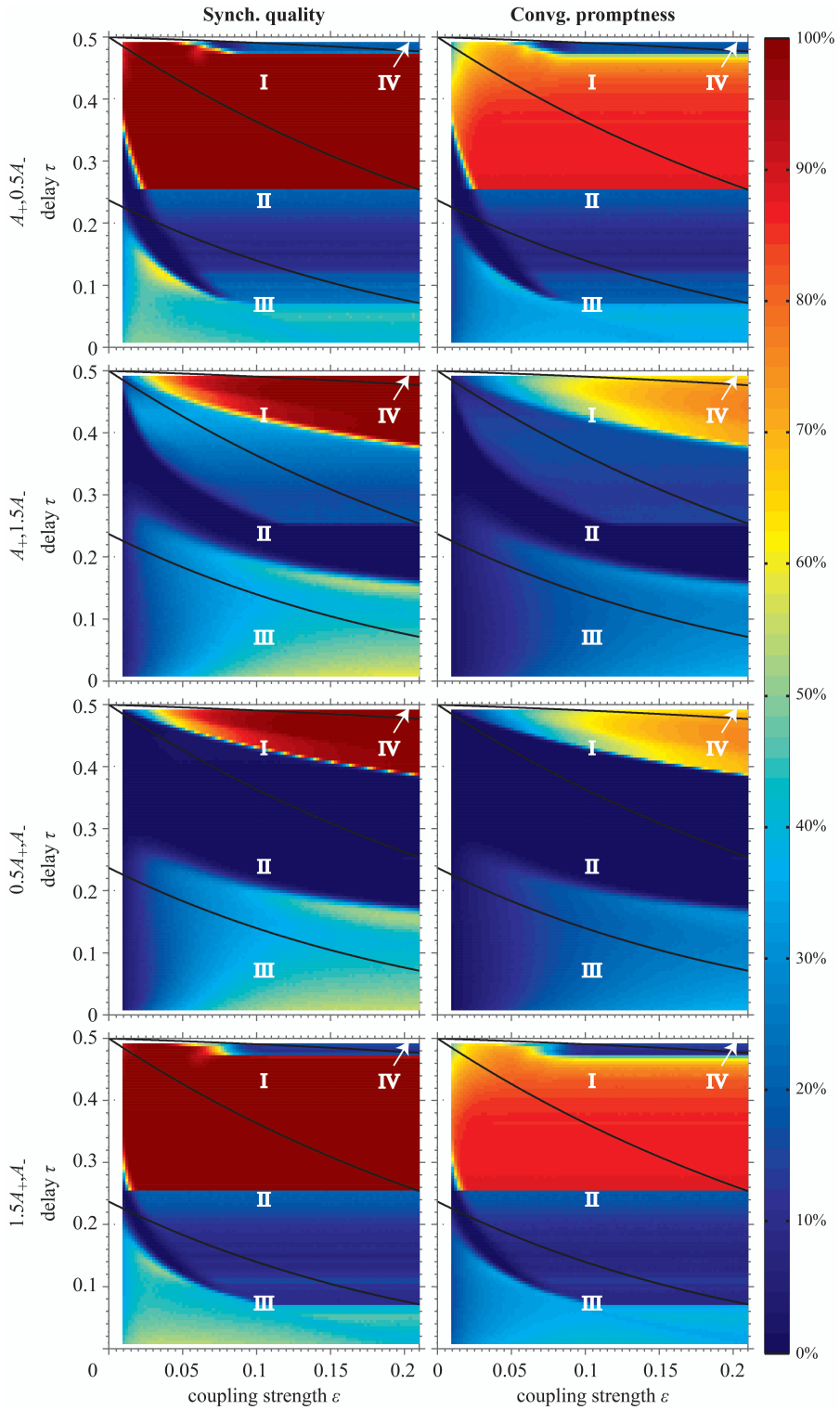


**Figure 5-4. Increasing potentiation leads to better synchronization quality and convergence promptness for delay times  $\tau \geq 0.25$ .** Left (right) column shows synchronization quality (convergence promptness) for various values for potentiation and depression. Panels in the first and second row show the results for decreased and increased depression, respectively. Panels in the third and fourth row show results for decreased and increased potentiation, respectively. When the ratio between potentiation and depression increases relative to the ratio for the standard STDP parameter values, both the synchronization quality and convergence promptness increase for delay times  $\tau \geq 0.25$ . This is because the synaptic weights are increased by STDP, when potentiation dominates depression. When depression dominates, the synchronization quality and convergence promptness deteriorate. Note that the synaptic strength  $\varepsilon$  along the horizontal axes represents the *initial* synaptic weight, not the final values of the synaptic strength after modification by STDP.

mode for *PRC3*. Hence, the SQ in region III with *PRC3* is higher than the SQ with *PRC1* for the same parameters provided that the number of cycles is large enough for convergence to the stable state. Similar arguments can be applied to the case of *PRC2* to explain the higher SQ for *PRC3* in region III compared to that for *PRC2*.

The results in Figs. 5-2 and 5-3 demonstrate that variations in the type I PRC give rise to quantitative differences in synchronization, but qualitatively the results are similar. For some combinations of synaptic coupling strength and time delay, the network may converge to zero-lag synchrony, but for many other parameter values, zero-lag synchrony is not possible. In this context it is important to notice that if the type I PRC is replaced by a type II PRC, the synchronization performance increases. As shown in Fig. 4-4 in **Chapter 4**, the same model with Hodgkin-Huxley neurons with type II PRCs gives a much larger range of parameter values that allow zero-lag synchronization.

In sec. “STDP facilitates zero-lag synchronization” of **Chapter 4** (see also Viriyopase et al. (2012)), we have shown that STDP may enlarge the range of parameter values that give rise to a high SQ. Without STDP synchronous firing is observed for delay times  $\tau \geq 0.25$  and synaptic coupling strengths that are sufficiently large (see Fig. 5-2A). Viriyopase et al. (2012) found a higher SQ and a faster convergence promptness (CP) in region II for large delay times with STDP. This result can be understood as follows. Initially, the dominant mode in region II is

slave synchrony, which is unstable. For slave synchrony the spikes from the inner oscillator arrive at the outer oscillators before the outer oscillators spike. Hence STDP (i.e. the potentiation part of STDP) leads to increase of the synaptic weights for the connections from the relay to the outer oscillator. If the value of the synaptic coupling strength has increased sufficiently, the increased coupling strength turns slave synchrony into driven synchrony, which is asymptotically stable.

We now investigate the effect of the amount of potentiation and depression in STDP on zero-lag synchronization, beginning with the simple model with instantaneous synapses. Figure 4-8 and the corresponding text in **Chapter 4** explained how variations in relative strength of potentiation and depression affect the convergence to zero-lag synchrony. The results in Fig. 4-8 were averaged over all time delays and relative phases. This result is illustrated in more detail in Fig. 5-4, which shows the SQ and the CP after the 60<sup>th</sup> simulation session in the left and right column, respectively, as a function of time delay and synaptic strength (same format as in Figs. 5-2A and 5-3) for various values of potentiation and depression. Panels in the first and second row show the results for decreased ( $0.5A_-$ ) and increased ( $1.5A_-$ ) depression, respectively. Panels in the third and fourth row show results for decreased ( $0.5A_+$ ) and increased ( $1.5A_+$ ) potentiation. When the ratio between potentiation and depression increases relative to the ratio for the standard STDP parameter values, both the SQ and the CP for delay times  $\tau \geq 0.25$  increase (see Fig. 5-4, **the first and fourth rows**). This is because the synaptic weights are increased by STDP when potentiation dominates over depression. When depression dominates, the SQ and the CP deteriorate (see Fig. 5-4, **the second and third rows**).

These results add a caveat to the results in Viriyopase et al. (2012) where it was shown that STDP contributes to a better SQ. This conclusion is correct, but the result critically depends on the relative strength of potentiation and depression of STDP. The parameters characterizing potentiation and depression that have been measured in in vitro studies (see Bi and Poo (1998)) seem to be close to optimal to achieve zero-lag synchronization.

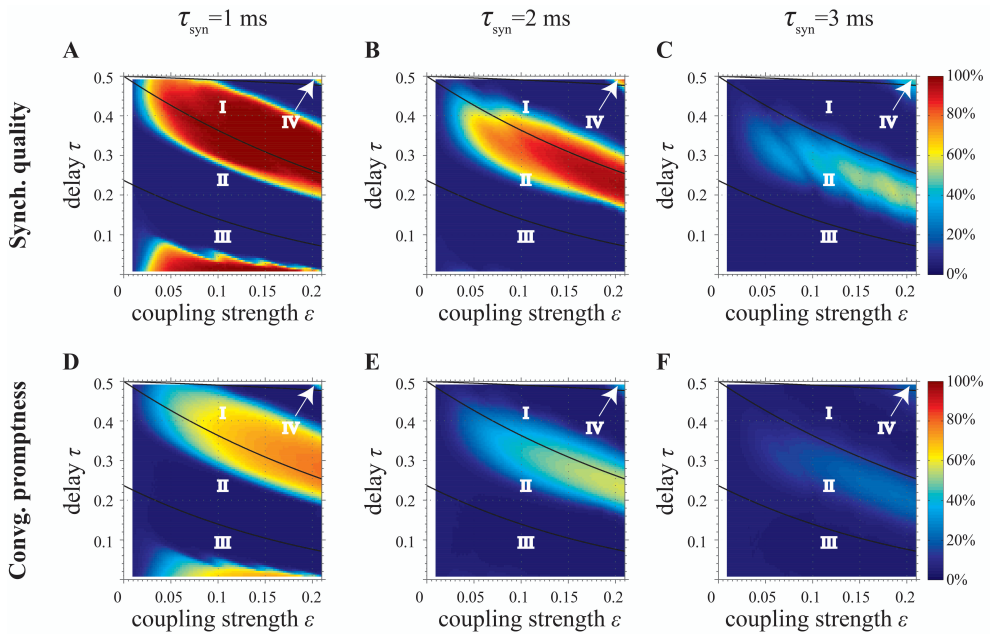


**Figure 5-5. Influence of rise time of alpha synapses.** *A-C*, SQ and *D-F*, CP for the network with alpha synapses. The rise times  $\tau_{\text{syn}}$  of the alpha synapse is set to 1 ms in *A* and *D*, 2 ms in *B* and *E*, and 3 ms in *C* and *F*. For longer rise times, the SQ decreases and the CP deteriorates.

Since time delays are important to achieve zero-lag synchronization, it is a legitimate question to ask whether synchronization is affected when instantaneous synapses are replaced by alpha synapses because the shape of the alpha synapse causes a frequency-dependent phase shift. Figure 5-5 shows the SQ and the CP as a function of the conduction delay  $\tau$  and the synaptic weight  $\varepsilon$  for the same simple model without STDP but with alpha synapses for various synaptic rise times (left, middle, and right columns for  $\tau_{\text{syn}} = 1, 2,$  and  $3$  ms, respectively). Comparing Fig. 5-2A with Fig. 5-5, *A - C*, shows that high SQ values are found near smaller delay times when alpha synapses are introduced. This shift can be attributed to the synaptic rise time of the alpha synapse: the longer the rise time, the longer the effective delay by the synapse. More importantly, longer synaptic rise times decrease the ability of the system to synchronize with zero lag, as shown in Fig. 5-5, *A - C*. This is also illustrated by Fig. 5-5, *D - F*, which shows that it takes longer time to synchronize



for longer synaptic rise times. To understand this, assume that synaptic inputs from the relay oscillator arrive when the phases of oscillators 1 and 3 are  $\varphi_1$  and  $\varphi_1 + \delta$ , respectively. If  $\delta$  is not 0, then oscillators 1 and 3 will spike at different times, unless the input is strong enough to make both oscillators spike immediately. For increased rise times (but such that the integral over the post-synaptic potential remains constant, i.e. the peak of the PSP decreases for longer rise times), less input per unit of time is received. Therefore, input from an instantaneous synapse (equivalent to “ $\tau_{\text{syn}} = 0$ ”) or fast alpha synapse (small  $\tau_{\text{syn}}$ ) provides more input per unit of time and therefore more easily synchronizes the outer oscillators than a slow alpha synapse (large  $\tau_{\text{syn}}$ ) by triggering an immediate response and thereby enforcing synchrony. We indeed find that larger synaptic rise times  $\tau_{\text{syn}}$  result in larger average spike time differences for the outer oscillators and hence less synchronization. In general, SQ is reduced for alpha synapses compared to instantaneous synapses, indicating that zero-lag synchrony is more difficult to obtain with realistic alpha-type synapse models for a model with type I MS neurons.

We will now address the question to what extent the improved SQ by STDP is affected by alpha synapses. Figure 5-6, **A** and **B**, shows the SQ and the CP, respectively, after 60 learning sessions for the model with STDP and alpha synapses with synaptic rise time  $\tau_{\text{syn}} = 2$  ms. Comparing the results in Figs. 5-6**A** and 5-6**B** shows that STDP improves the average SQ and the CP, like for instantaneous synapses. The main difference between the synchronization for instantaneous synapses and alpha-synapses is that rather long time delays (range 0.25 - 0.5) are required to achieve zero-lag synchronization, whereas alpha synapses reduce this range to smaller delay values (0.15 - 0.3).

#### *When delay times are not identical*

We now investigate the dynamics of the model when the delay times  $\tau_1$  and  $\tau_3$  are different with the initial coupling strengths all identical ( $\varepsilon_{12} = \varepsilon_{21} = \varepsilon_{23} = \varepsilon_{32} = \varepsilon$ ). Figure 5-7**A** shows the SQ for the model with instantaneous synapses, and Fig. 5-7**B** with alpha synapses ( $\tau_{\text{syn}} = 2$  ms). When the delay times are almost identical

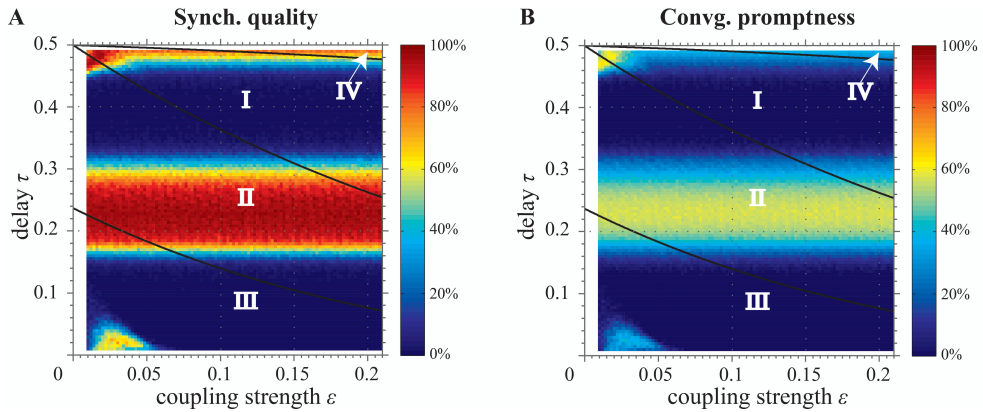


**Figure 5-6. Long-range synchronization improves with STDP for alpha synapses.** *A* and *B*, SQ and CP, respectively, after 60 sessions with a synaptic rise time  $\tau_{\text{syn}} = 2$  ms. Comparison with Fig. 5-5, *B* and *E*, shows that the range of parameter values that allows zero-lag synchrony is increased. However, CP remains poor with 6 cycles or more to achieve synchrony.

(close to the diagonal), strong synchrony is found in a limited range of delay times from 0.37 to 0.5 for instantaneous synapses and from 0.3 to 0.4 for alpha synapses. When the delay times are different, synchronous firing disappears.

To understand why zero-lag synchronization disappears when the delay times are different, we consider the network with instantaneous synapses. Let us assume that oscillators 1 and 3 fire simultaneously. When oscillator 2 generates an action potential, the spikes arrive at oscillators 1 and 3 after delays  $\tau_1$  and  $\tau_3$ , respectively. Because the spikes arrive at oscillators 1 and 3 when the phase exceeds the critical phase, oscillators 1 and 3 will spike immediately after arrival of the spike, which implies that oscillators 1 and 3 will spike with a time difference  $|t_{1,n+1}^{\text{spike}} - t_{3,n+1}^{\text{spike}}| = |\tau_1 - \tau_3|T_0$ . This illustrates that zero-lag synchrony is lost when the delay times  $\tau_1$  and  $\tau_3$  are different. By our definition, oscillators 1 and 3 are in synchrony if  $|\tau_1 - \tau_3|T_0 \leq 0.5$  ms, hence synchronous firing is found for a limited range of delay times close to the diagonal. Qualitatively similar results (not shown) are obtained for asymmetric coupling strengths.

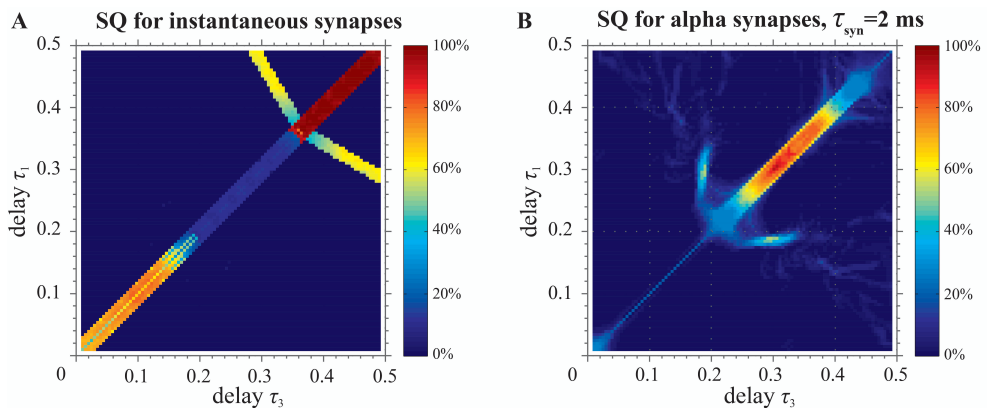


**Figure 5-7. Zero-lag synchronization only for identical delay times.** *A* and *B*, SQ for instantaneous synapses and alpha synapses ( $\tau_{\text{syn}} = 2$  ms), respectively. The coupling strengths of all connections are  $\varepsilon = 0.1$ . When  $\tau_1$  and  $\tau_3$  differ, i.e. off the diagonal, SQ is poor.

In Fig. 4-10 in **Chapter 4**, we have shown that the network may converge to stable modes where the outer neurons fire with a relative phase different from zero. In general, there are two stable modes with a small and large relative phase. These nonzero relative phases are shown in Fig. 5-8.

Figure 5-8 shows typical patterns for stable modes of asynchronous firing of the outer oscillators. Figure 5-8, **A** and **B**, shows stable firing for a small relative phase of the outer oscillators (corresponding to Fig. 4-10, **D** and **E**, in **Chapter 4**, respectively), while Fig. 5-8**C** shows a stable mode for a larger relative phase. The relative phases  $\varphi_r$  for the dynamics of the three oscillators shown in Fig. 5-8, **A**, **B**, and **C**, are determined using methods similar to that for deriving the phase-locking equations Eqs. 4-10 and 4-11 in **Chapter 4**. The relative phases that correspond to the stable modes of firing are given by

$$\varphi_r = (\tau_3 - \tau_1) \frac{T_0}{T(\tau_3, \varepsilon)}, \quad (5-13)$$

$$\varphi_r = (\tau_3 - \tau_1) \frac{T_0}{T(\tau_1, \varepsilon)}, \quad (5-14)$$

$$\varphi_r = \left[ 1 - \chi_b(\varepsilon) - 2\beta_b(1)\chi_b(\varepsilon)\tau_3 - \tau_3 - \tau_1 \right] \frac{T_0}{T(\tau_3, \varepsilon)}, \quad (5-15)$$

where Eqs. 5-13 and 5-14 give the relative phase values that are relatively small, whereas the relative phase in Eq. 5-15 corresponds to a larger value.  $T(\tau_1, \varepsilon)$  and  $T(\tau_3, \varepsilon)$  in Eqs. 5-13 - 5-15 are the new period of the phase-locked oscillators defined by

$$T(\tau, \varepsilon) = \left[ 1 - \chi_b(\varepsilon) - 2\beta_b(1)\chi_b(\varepsilon)\tau \right] T_0. \quad (5-16)$$

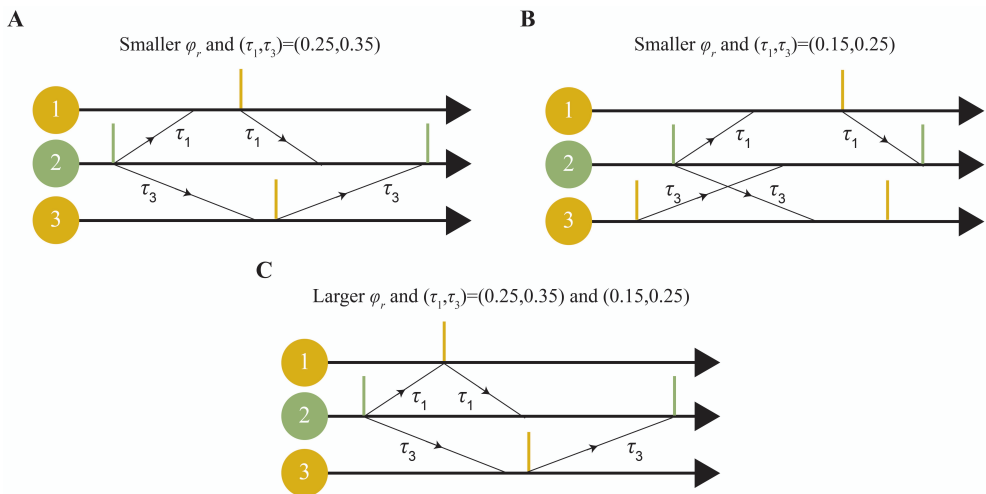


**Figure 5-8. Typical stable modes of nonzero relative phase of the outer oscillators.** *A* and *B* show stable modes corresponding to small relative phases (as in Fig. 4-10, *D* and *E*, in **Chapter 4**, respectively), while *C* shows a stable mode corresponding to a larger relative phase.

Inserting the values for  $\tau_1$  and  $\tau_3$  in Eqs. 5-13 - 5-14, which were used to obtain Fig. 4-10, *D* and *E*, in **Chapter 4**, gives relative phases near 0.14 and 0.11, respectively, exactly the same as in Fig. 4-10, *D* and *E*, in **Chapter 4**. The larger relative phases determined by Eq. 5-15 with  $(\tau_1, \tau_3) = (0.25, 0.35)$  and  $(\tau_1, \tau_3) = (0.15, 0.25)$  are approximately equal to 0.19 and 0.50 in agreement with

the simulation results in Fig. 4-10, **D** and **E**, in **Chapter 4**, respectively. When the delay times  $\tau_1$  and  $\tau_3$  are equal, the relative phase  $\varphi_r$  becomes zero according to Eqs. 5-13 and 5-14. In addition, there is a stable relative phase according to Eq. 5-15, which gives a stable firing mode at a relative phase of 0.38 for  $\varepsilon = 0.1$ . When  $\tau_1$  and  $\tau_3$  are not equal,  $\varphi_r$  deviates from zero proportionally to the difference of  $\tau_1$  and  $\tau_3$ . This shows that zero-lag synchronization is not robust for differences in time delays between the relay oscillator and the outer oscillators.

## 5.4 Discussion

Several studies in the past have provided evidence for zero-lag synchrony between different brain areas that were well separated (Frien et al., 1994; Roelfsema et al., 1997; Castelo-Branco et al., 1998; Rodriguez et al., 1999; Gross et al., 2004). This finding was quite remarkable considering the synaptic and conduction delays involved in their interactions. The phenomenon of zero-lag gamma synchronization has attracted much attention and has led to speculations about its possible functional role, such as a mechanism for feature binding (Engel et al., 1992; Singer and Gray, 1995), efficient neuronal communication (Fries, 2005), and learning (Pare et al., 2009). Recently two studies (Gregoriou et al., 2009a; Uhlhaas et al., 2009) have demonstrated that oscillations in the gamma frequency range (40-80 Hz) in different cortical regions synchronize, but with phase differences significantly different from zero. This has led to a discussion whether precise zero-lag synchronization occurs in the brain, and if so, under which conditions.

In the present study we have investigated the conditions for zero-lag synchrony between distal cortical areas using a network model. The main result of our study is that two pulse-coupled oscillators that interact via a relay oscillator can easily synchronize their activity but in general not at zero phase lag. Zero-lag synchrony is observed only for a restricted set of synaptic coupling strengths and delay times. Furthermore, as soon as the delay times between the synchronizing oscillators and the relay oscillator differ, zero phase lag is lost. Since conduction delays between various cortical areas and/or subcortical structures generally will not be perfectly identical, and since connectivity properties are highly variable across

the brain, we conclude that zero-lag synchrony can only be the exception and not the rule.

The network used in this study is a simplified model for interacting neuronal populations. This obviously raises the question whether our negative findings about zero-lag synchrony may be due to the simplifications inherent in our model. We will argue that this is not the case. Our choice of indirect interactions between oscillating neuronal populations, i.e., via a relay oscillator, was inspired by previous studies. They showed that pulse-coupled neuronal oscillators with direct excitatory coupling and signal delays never oscillate with zero phase lag (van Vreeswijk et al., 1994; Ernst et al., 1995, 1998; Knoblauch and Sommer, 2003; Zeitler et al., 2009). Inhibitory coupling between directly interacting oscillators can cause near zero-lag synchrony (van Vreeswijk et al., 1994; Zeitler et al., 2009). However, the dominant connectivity between cortical areas, such as V1, V2, V4, and FEF, is excitatory, rather than inhibitory. These considerations led Fischer et al. (2006) and Vicente et al. (2008) to postulate a network model of oscillators interacting via a relay oscillator, which supports zero-lag synchrony. Subcortical structures like the thalamus are good physiological candidates for such a mediating relay (Theyel et al., 2010). Our study elaborates on this proposed relay network model since it appears to be the only viable candidate to obtain zero-lag synchronization.

A further simplification in our model is that the oscillators used to represent neuronal population activity are of the Mirollo-Strogatz kind. The Mirollo-Strogatz oscillator corresponds to the type I neuron class (Izhikevich, 2007). Although there is evidence that cortical pyramidal cells can switch between type I and type II by means of cholinergic modulation (Ermentrout et al., 2001; Jeong and Gutkin, 2007; Stiefel et al., 2008, 2009), the majority of pyramidal cells in neocortex are type I neurons (Reyes and Fetz, 1993b, a; Kawaguchi, 1995; Erisir et al., 1999; Tateno et al., 2004). Furthermore, replacing the Mirollo-Strogatz neurons by more realistic Hodgkin-Huxley ones does not change the qualitative nature of our conclusions regarding zero-lag synchrony of this study. This result was verified by computer simulations (not shown) but also follows theoretically from the fact that our analytical results are based on the assumption of periodically oscillating neurons with type I phase response curves (i.e. only phase advance, no phase delay), which applies to both the Mirollo-Strogatz and most Hodgkin-Huxley-type neurons. Using

the much simpler Mirollo-Strogatz oscillator has allowed us to perform a comprehensive analytical and computational study of synchronization properties without sacrificing the applicability of our results.

A final assumption of this study, which requires some more discussion, is that all oscillators in the model have identical intrinsic properties with the same oscillation period. If the intrinsic periods of the outer oscillators differ, zero-lag synchrony is lost quickly, whereas if the intrinsic period of the relay oscillator differs from those of the outer oscillators, synchronization properties change quantitatively but not qualitatively. These results have been confirmed by simulation (not shown) but can be understood in a straightforward way. Firstly, if we make the period of the relay oscillator different from that of the outer oscillators, the combinations of synaptic strength and delay where input can elicit spikes immediately after arrival change only slightly with adjustments of the period. Hence the boundaries of regions with driven, pacemaker, and slave synchrony will change quantitatively but not qualitatively, unless the differences in the period become very large. These boundaries (Fig. 5-2) in turn determine the overall synchronization properties that hence also remain qualitatively similar.

Secondly, if the periods of the outer oscillators are different from each other, input from the relay oscillator may elicit a spike in one outer oscillator, followed by a spike in the other outer oscillator later in time. In that case, the spike inputs from the outer oscillators to the relay oscillator arrive at different times. This is essentially equivalent to the situation with different delay times that we have studied above (see sec. “When delay times are not identical” in sec. 5.3). We have shown that zero-lag synchrony is lost when the delay times are different. So likewise, any differences in the periods of the outer oscillators quickly abolish zero-lag synchrony. Therefore, our network model in Fig. 4-1A in **Chapter 4** with equal properties of the oscillators is optimal for obtaining zero-lag synchrony. If this homogeneous model cannot produce zero-lag synchrony, neither can models with unequal oscillator properties.

In agreement with Knoblauch and Sommer (2003), we found that STDP adapts the synaptic coupling strengths such that the network converges to a stable state with zero-lag synchrony for a larger range parameter values (see Fig. 5-4). However, adaptation of the synapses by STDP often took a long time (up to 500

cycles in our simulations, see Fig. 4-7 in **Chapter 4**), which implies that STDP cannot play a dominant role for the rapid development of zero-lag synchronization in novel visual perception tasks. Vicente et al. (2008) reported that the mechanism of synchronization rests on the ability of an excitatory postsynaptic potential to modify the firing latencies of a postsynaptic neuron in a consistent manner. We agree with this conclusion, but our results show that STDP takes too much time (considerably more than 200 to 250 ms that is generally considered as the range for build-up of gamma oscillations to novel visual stimuli) to generate zero-lag synchrony in the gamma frequency range.

Figure 4-8 in **Chapter 4** suggests that the parameters for STDP, as reported by Bi and Poo (1998), are close to optimal to achieve zero-lag synchronization in the sense that a large range of short delays ( $\tau \leq 0.15$ ) and long delays ( $\tau \geq 0.25$ ) may yield relatively good zero-lag synchronization (see Fig. 4-6B in **Chapter 4**). For long delays ( $\tau \geq 0.25$ ) synchronization can be improved by increasing the relative amount of potentiation of the learning window by increasing potentiation or by decreasing depression. Thus, the more the contribution of potentiation, the smaller the number of learning sessions needed to achieve zero-lag synchronization (see Fig. 5-4 with  $(A_+, 0.5A_-)$  and  $(1.5A_+, A_-)$  as examples). In contrast, increasing the relative amount of depression favours zero-lag synchronization for short delays ( $\tau \leq 0.15$ ), as shown in Fig. 5-4 with  $(0.5A_+, A_-)$  and  $(A_+, 1.5A_-)$ . In summary, when the time delays are restricted to either the short delays or the long delays, the parameters of the learning window for STDP as reported by Bi and Poo are not optimal to achieve zero-lag synchronization. That is, zero-lag synchronization at long delays is enhanced by a larger amount of potentiation, while a relatively larger amount of depression facilitates zero-lag synchrony for short delays.

Can STDP lead to changes in the synaptic weights such that zero-lag synchronization becomes possible when the delays are different? Eqs. 5-13 and 5-14 show that zero-lag synchronization ( $\phi_r = 0$ ) is possible only if  $\tau_1$  equals  $\tau_3$ . Hence, changes in the synaptic weights by STDP will not lead to zero-lag synchronization. Next we address the question whether STDP can perhaps change the phase in Eq. 5-15 to zero. In simulations with initial weight  $\varepsilon = 0.1$ , we find that



the synaptic weights of the connections from the relay to the outer oscillators gradually increase to their maximum value by STDP. We observe the same symmetric increase of coupling from the relay to the outer oscillators for most other values of the initial weight. Zero-lag synchronization then is not possible because unequal values of the synaptic weights from the relay to the outer oscillators would be needed to compensate for unequal time delays, but STDP symmetrically increases the synaptic weights. Hence, STDP cannot restore zero-lag synchronization for asymmetric delays. This claim has also been confirmed for alpha synapses by simulation.

Overall, our results demonstrate that it is unlikely that gamma oscillations in various cortical areas are synchronized at zero-lag for neuronal architectures used in this study. Rather our studies support recent experimental data (Gregoriou et al., 2009a) that neuronal oscillations in various cortical areas can be synchronized, but not at zero-lag.

# Summary

Neuronal oscillations play an important role in neuronal information processing. These oscillations have been reported at various frequency bands in the range between 2 and 200 Hz. This thesis focused on neuronal oscillations in the gamma band (frequency range between 30-80 Hz). In the thesis we have investigated the properties of the gamma oscillations with different networks: a simplified network with two neurons, a biologically plausible network with thousands of neurons (corresponding to a brain region of about hundreds of microns), as well as interactions between interacting brain areas at a distance of centimeters or more. We conducted our studies by means of mathematical modeling and extensive computer simulations. In the thesis the mathematical description for the dynamics of the biologically plausible neurons can range from a very simple one (one state variable) to a very complex one (more than ten state variables).

At a microscopic scale, the generation of brain rhythms in the gamma band involves two major classes of neurons; pyramidal cells and interneurons. In vivo and in vitro studies have suggested that two major mechanisms (interneuron network gamma, ING, and pyramidal interneuron network gamma, PING) underlie the generation of brain rhythms in the gamma band. For the first mechanism (ING), the gamma band rhythm is generated by a network of interneurons, while for the second mechanism (PING), it is the result of interactions between the interneurons and pyramidal cells. In **Chapter 2**, we investigated how the two major mechanisms interact using extensive computer simulations of a biologically plausible neuronal network, consisting of thousands of neurons. **Chapter 3** addresses the same question using a fully analytical approach for a simple network. The results obtained from the computer simulations for a biologically plausible network and the analytical approach for a simplified network in general agree well. Both approaches demonstrated that the two mechanisms ING and PING compete: The mechanism

generating the higher oscillation frequency "wins". The winning mechanism determines the frequency of the network oscillation and suppresses the other mechanism.

Both neurophysiological as well as neuro-imaging studies have reported that neuronal activity between distant parts of the brain synchronizes with zero phase lag. This is a remarkable result because of time delays between the interacting brain areas: it takes a significant amount of time for action potentials to travel from one area to the other. In **Chapter 4**, we investigated under what conditions zero-lag synchrony between distant brain regions is possible using an analytical approach supported by computer simulations. In **Chapter 5**, we extended the model of the oscillators by including additional features of the biologically plausible neurons. From the results in both chapters, we conclude that zero-lag synchrony is indeed possible, but not likely for the actual conditions in the brain. This suggests a cautious re-evaluation of the existence and proposed role of zero-lag synchrony in neuronal communication.

## **Chapter 2 - Cooperation and competition of gamma oscillation mechanisms**

Brain rhythms appearing in various frequency ranges are one of the hallmarks of the brain. One of the most important frequency ranges is the gamma band (30-80 Hz), which is assumed to be relevant during sensory, motor, and cognitive tasks. There are two different mechanisms (ING and PING) that have been suggested to underlie the generation of the gamma band rhythms. Because these mechanisms have a very different origin, several studies in the literature have proposed a different biological function for these mechanisms. In this chapter, we highlighted our research on how the two oscillation-generating mechanisms interact using mathematical modeling and extensive computer simulations.

We found that the two cortical mechanisms compete: The mechanism generating the higher oscillation frequency "wins". The winning mechanism determines the frequency of the network oscillation and suppresses the other mechanism. Furthermore, our computational study suggests approaches to decide in experimental studies to what extent oscillatory gamma activity is dominated by ING or PING by simply investigating the response frequency of the network when the

input to either the pyramidal cells or to the interneurons is varied. The theoretical predictions of this study are in line with the results of various experimental studies.

### **Chapter 3 - Analyzing the competition of gamma rhythms with delayed pulse-coupled oscillators in phase representation**

In this chapter, we extended our study conducted in **Chapter 2** by analytically investigating the competition between the two major mechanisms that have been suggested to underlie the generation of the brain rhythms in the gamma frequency band (30-80 Hz). We used a network of two coupled oscillators to allow for a detailed theoretical analysis. Based on the network of two coupled oscillators, we derived all possible stable interaction modes between the two oscillators and their relative phase of spiking.

In general, the results based on our analysis of two coupled oscillators agree well with the main results obtained by the computer simulations of the dynamics of large networks conducted in **Chapter 2**. According to the theoretical analysis of the two coupled oscillators, we can switch between ING and PING by simply adjusting the current to one of the oscillators. Our two-neuron study further suggests that we can easily find out whether ING or PING dominates the gamma oscillations since the frequency of gamma oscillations increases with a different slope as a function of the input to the interneurons or pyramidal cells for ING and PING. At the intersection point of the two lines with different slope, ING (PING) takes over from PING (ING).

### **Chapter 4 - When long-range zero-lag synchronization is feasible in cortical networks**

Several experimental studies using neurophysiological techniques and brain imaging have reported that neuronal activity in different brain regions synchronizes at zero phase lag. This is a remarkable result, since neuronal populations in different parts of the brain, sometimes more than 20 cm apart, have to synchronize at zero phase lag despite considerable time delays of 3 ms or more along the axons connecting these brain areas. The occurrence of zero-lag synchrony has led to many speculations about its functional role in neuronal communication, e.g., for attention, memory and feature binding. However, some recent studies have reported synchrony with a

nonzero phase lag, where activity in one brain area consistently leads the activity in the other area, in contradiction with previous reports.

Therefore, the aim of this study was to investigate under what conditions zero-lag synchrony could potentially occur. We adopted a very simple network configuration, which has been postulated before in the literature as a potential candidate for coupling between distant brain areas. In this model two brain areas are connected via a neuronal relay population. We then showed that zero-lag synchrony is indeed possible, but not likely for biologically plausible conditions. Therefore, our study supports the more recent experimental results, which suggest that the reports on zero-lag synchrony may not be valid. This suggests a cautious re-evaluation of the proposed role of zero-lag synchrony in neuronal communication.

### **Chapter 5 - Robustness of long-range zero-lag synchronization for changes in cortical connectivity**

The simple oscillators used to conduct the theoretical analyses in **Chapter 4** lack some important properties of realistic neurons. First, neurons hardly respond to synaptic input arriving shortly after spiking of the neurons because of the refractory period of neurons. Second, neurons do not spike exactly at the arrival time of a pulse input. In this chapter, we thus extended our study presented in **Chapter 4** by investigating the effect of these two features on zero-lag synchrony: We did so by additionally constructing two different phase oscillators, each of which exhibits each feature.

Our study shows that the refractory period of neurons and the temporal dynamics of neurons do affect the zero-lag synchrony. In fact, adding these properties reduces the conditions where zero-lag synchrony is feasible. Therefore, we conclude that zero-lag synchrony between distal brain areas is highly unlikely, supporting the results in **Chapter 4**.

## References

- Abbott L, Kepler TB (1990) Model neurons: From Hodgkin-Huxley to hopfield. In: *Statistical Mechanics of Neural Networks*, pp 5-18. Berlin: Springer-Verlag.
- Abbott LF, van Vreeswijk C (1993) Asynchronous states in networks of pulse-coupled oscillators. *Phys Rev E* 48:1483-1490.
- Achuthan S, Canavier CC (2009) Phase-Resetting Curves Determine Synchronization, Phase Locking, and Clustering in Networks of Neural Oscillators. *J Neurosci* 29:5218-5233.
- Aladjalova NA (1957) Infra-slow rhythmic oscillations of the steady potential of the cerebral cortex. *Nature* 179:957-959.
- Amzica F, Nunez A, Steriade M (1992) Delta frequency (1-4 Hz) oscillations of perigeniculate thalamic neurons and their modulation by light. *Neuroscience* 51:285-294.
- Angulo MC, Rossier J, Audinat E (1999) Postsynaptic glutamate receptors and integrative properties of fast-spiking interneurons in the rat neocortex. *J Neurophysiol* 82:1295-1302.
- Aoki F, Fetz EE, Shupe L, Lettich E, Ojemann GA (1999) Increased gamma-range activity in human sensorimotor cortex during performance of visuomotor tasks. *Clin Neurophysiol* 110:524-537.
- Arabzadeh E, Panzeri S, Diamond ME (2006) Deciphering the spike train of a sensory neuron: counts and temporal patterns in the rat whisker pathway. *J Neurosci* 26:9216-9226.
- Ascoli GA, Atkeson JC (2005) Incorporating anatomically realistic cellular-level connectivity in neural network models of the rat hippocampus. *Biosystems* 79:173-181.
- Azevedo FA, Carvalho LR, Grinberg LT, Farfel JM, Ferretti RE, Leite RE, Jacob Filho W, Lent R, Herculano-Houzel S (2009) Equal numbers of neuronal and nonneuronal cells make the human brain an isometrically scaled-up primate brain. *J Comp Neurol* 513:532-541.
- Azouz R, Gray CM (2003) Adaptive coincidence detection and dynamic gain control in visual cortical neurons in vivo. *Neuron* 37:513-523.
- Barry RJ, Clarke AR, Johnstone SJ, Magee CA, Rushby JA (2007) EEG differences between eyes-closed and eyes-open resting conditions. *Clin Neurophysiol* 118:2765-2773.

- Bartos M, Vida I, Jonas P (2007) Synaptic mechanisms of synchronized gamma oscillations in inhibitory interneuron networks. *Nat Rev Neurosci* 8:45-56.
- Bartos M, Vida I, Frotscher M, Geiger J, Jonas P (2001) Rapid signaling at inhibitory synapses in a dentate gyrus interneuron network. *J Neurosci* 21:2687-2698.
- Bartos M, Vida I, Frotscher M, Meyer A, Monyer H, Geiger JRP, Jonas P (2002) Fast synaptic inhibition promotes synchronized gamma oscillations in hippocampal interneuron networks. *Proc Natl Acad Sci U S A* 99:13222-13227.
- Bastos AM, Vezoli J, Fries P (2015) Communication through coherence with inter-areal delays. *Curr Opin Neurobiol* 31:173-180.
- Bem T, Rinzel J (2004) Short duty cycle destabilizes a half-center oscillator, but gap junctions can restabilize the anti-phase pattern. *J Neurophysiol* 91:693-703.
- Bem T, Le Feuvre Y, Rinzel J, Meyrand P (2005) Electrical coupling induces bistability of rhythms in networks of inhibitory spiking neurons. *Eur J Neurosci* 22:2661-2668.
- Berger H (1929) Electroencephalogram in humans. *Arch Psychiatr Nervenkr* 87:527-570.
- Bi G-Q, Poo M-M (1998) Synaptic Modifications in Cultured Hippocampal Neurons: Dependence on Spike Timing, Synaptic Strength, and Postsynaptic Cell Type. *J Neurosci* 18:10464-10472.
- Bland BH (1986) The physiology and pharmacology of hippocampal formation theta rhythms. *Prog Neurobiol* 26:1-54.
- Börgers C, Kopell N (2003) Synchronization in networks of excitatory and inhibitory neurons with sparse, random connectivity. *Neural Comput* 15:509-538.
- Börgers C, Kopell N (2005) Effects of noisy drive on rhythms in networks of excitatory and inhibitory neurons. *Neural Comput* 17:557-608.
- Börgers C, Kopell NJ (2008) Gamma oscillations and stimulus selection. *Neural Comput* 20:383-414.
- Börgers C, Walker B (2013) Toggling between gamma-frequency activity and suppression of cell assemblies. *Front Comput Neurosci* 7:33.
- Börgers C, Epstein S, Kopell NJ (2005) Background gamma rhythmicity and attention in cortical local circuits: A computational study. *Proc Natl Acad Sci U S A* 102:7002-7007.
- Börgers C, Krupa M, Gielen S (2010) The response of a classical Hodgkin-Huxley neuron to an inhibitory input pulse. *J Comput Neurosci* 28:509-526.

- Bou-Flores C, Berger AJ (2001) Gap junctions and inhibitory synapses modulate inspiratory motoneuron synchronization. *J Neurophysiol* 85:1543-1551.
- Bouyer JJ, Montaron MF, Rougeul A (1981) Fast fronto-parietal rhythms during combined focused attentive behaviour and immobility in cat: cortical and thalamic localizations. *Electroen Clin Neuro* 51:244-252.
- Bragin A, Jando G, Nadasdy Z, Hetke J, Wise K, Buzsáki G (1995) Gamma (40-100 Hz) oscillation in the hippocampus of the behaving rat. *J Neurosci* 15:47-60.
- Brandner G, Schilcher U, Bettstetter C (2016) Firefly synchronization with phase rate equalization and its experimental analysis in wireless systems. *Com Net* 97:74-87.
- Bressler SL (1995) Large-scale cortical networks and cognition. *Brain Res Rev* 20:288-304.
- Bressler SL, Freeman WJ (1980) Frequency analysis of olfactory system EEG in cat, rabbit, and rat. *Electroen Clin Neuro* 50:19-24.
- Bressloff PC, Coombes S (1998) Desynchronization, Mode Locking, and Bursting in Strongly Coupled Integrate-and-Fire Oscillators. *Phys Rev Lett* 81:2168.
- Bressloff PC, Coombes S (2000) Dynamics of strongly coupled spiking neurons. *Neural Comput* 12:91-129.
- Brown E, Moehlis J, Holmes P (2004) On the phase reduction and response dynamics of neural oscillator populations. *Neural Comput* 16:673-715.
- Brunel N (2000) Dynamics of sparsely connected networks of excitatory and inhibitory spiking neurons. *J Comput Neurosci* 8:183-208.
- Brunel N, Hakim V (1999) Fast global oscillations in networks of integrate-and-fire neurons with low firing rates. *Neural Comput* 11:1621-1671.
- Brunel N, Wang XJ (2003) What determines the frequency of fast network oscillations with irregular neural discharges? I. Synaptic dynamics and excitation-inhibition balance. *J Neurophysiol* 90:415-430.
- Buhl EH, Tamás G, Fisahn A (1998) Cholinergic activation and tonic excitation induce persistent gamma oscillations in mouse somatosensory cortex in vitro. *J Physiol* 513:117-126.
- Buia C, Tiesinga P (2006) Attentional modulation of firing rate and synchrony in a model cortical network. *J Comput Neurosci* 20:247-264.
- Buonomano DV, Maass W (2009) State-dependent computations: spatiotemporal processing in cortical networks. *Nat Rev Neurosci* 10:113-125.
- Buzsáki G (1991) The thalamic clock: emergent network properties. *Neuroscience* 41:351-364.
- Buzsáki G (1996) The hippocampo-neocortical dialogue. *Cereb Cortex* 6:81-92.



- Buzsáki G (2002) Theta oscillations in the hippocampus. *Neuron* 33:325-340.
- Buzsáki G, Chrobak JJ (1995) Temporal structure in spatially organized neuronal ensembles: A role for interneuronal networks. *Curr Opin Neurobiol* 5:504-510.
- Buzsáki G, Draguhn A (2004) Neuronal oscillations in cortical networks. *Science* 304:1926-1929.
- Buzsáki G, Wang XJ (2012) Mechanisms of gamma oscillations. *Annu Rev Neurosci* 35:203-225.
- Buzsáki G, Leung LW, Vanderwolf CH (1983) Cellular bases of hippocampal EEG in the behaving rat. *Brain Res* 287:139-171.
- Buzsáki G, Geisler C, Henze DA, Wang XJ (2004) Interneuron Diversity series: Circuit complexity and axon wiring economy of cortical interneurons. *TINS* 27:186-193.
- Buzsáki G, Horvath Z, Urioste R, Hetke J, Wise K (1992) High-frequency network oscillation in the hippocampus. *Science* 256:1025-1027.
- Buzsáki G, Buhl DL, Harris KD, Csicsvari J, Czeh B, Morozov A (2003) Hippocampal network patterns of activity in the mouse. *Neuroscience* 116:201-211.
- Buzsáki G (2006) *Rhythms of the brain*. Oxford: Oxford University Press.
- Canavier CC, Wang S, Chandrasekaran L (2013) Effect of phase response curve skew on synchronization with and without conduction delays. *Front Neural Circuits* 7:194.
- Caporale N, Dan Y (2008) Spike timing-dependent plasticity: a Hebbian learning rule. *Annu Rev Neurosci* 31:25-46.
- Cardin JA, Carlen M, Meletis K, Knoblich U, Zhang F, Deisseroth K, Tsai LH, Moore CI (2009) Driving fast-spiking cells induces gamma rhythm and controls sensory responses. *Nature* 459:663-U663.
- Castelo-Branco M, Neuenschwander S, Singer W (1998) Synchronization of visual responses between the cortex, lateral geniculate nucleus, and retina in the anesthetized cat. *J Neurosci* 18:6395-6410.
- Chapman CA, Xu Y, Haykin S, Racine RJ (1998) Beta-frequency (15-35 Hz) electroencephalogram activities elicited by toluene and electrical stimulation in the behaving rat. *Neuroscience* 86:1307-1319.
- Chow CC, Kopell N (2000) Dynamics of spiking neurons with electrical coupling. *Neural Comput* 12:1643-1678.
- Chow CC, White JA, Ritt J, Kopell N (1998) Frequency control in synchronized networks of inhibitory neurons. *J Comput Neurosci* 5:407-420.
- Clark BD, Goldberg EM, Rudy B (2009) Electrogenic tuning of the axon initial segment. *Neuroscientist* 15:651-668.
- Cobb SR, Buhl EH, Halasy K, Paulsen O, Somogyi P (1995) Synchronization of neuronal activity in hippocampus by individual GABAergic interneurons. *Nature* 378:75-78.

- Colgin LL, Moser EI (2010) Gamma Oscillations in the Hippocampus. *Physiology* 25:319-329.
- Compte A, Sanchez-Vives MV, McCormick DA, Wang XJ (2003) Cellular and network mechanisms of slow oscillatory activity (<1 Hz) and wave propagations in a cortical network model. *J Neurophysiol* 89:2707-2725.
- Contreras D, Llinas R (2001) Voltage-sensitive dye imaging of neocortical spatiotemporal dynamics to afferent activation frequency. *J Neurosci* 21:9403-9413.
- Cooper R, Winter AL, Crow HJ, Walter WG (1965) Comparison of subcortical, cortical and scalp activity using chronically indwelling electrodes in man. *Electroen Clin Neuro* 18:217-&.
- Craig MT, McBain CJ (2015) Fast gamma oscillations are generated intrinsically in CA1 without the involvement of fast-spiking basket cells. *J Neurosci* 35:3616-3624.
- Csicsvari J, Jamieson B, Wise KD, Buzsáki G (2003) Mechanisms of gamma oscillations in the hippocampus of the behaving rat. *Neuron* 37:311-322.
- Cunningham MO, Whittington MA, Bibbig A, Roopun A, LeBeau FEN, Vogt A, Monyer H, Buhl EH, Traub RD (2004) A role for fast rhythmic bursting neurons in cortical gamma oscillations in vitro. *Proc Natl Acad Sci U S A* 101:7152-7157.
- Cutsuridis V, Graham B, Cobb S, Vida I (2010) *Hippocampal microcircuits: A computational modeler's resource book*. New York: Springer.
- Dayan P, Abbott LF (2001) *Theoretical neuroscience: computational and mathematical modeling of neural systems*. Cambridge, Mass: Massachusetts Institute of Technology Press.
- Deans MR, Gibson JR, Sellitto C, Connors BW, Paul DL (2001) Synchronous activity of inhibitory networks in neocortex requires electrical synapses containing connexin36. *Neuron* 31:477-485.
- Debanne D, Guerineau NC, Gahwiler BH, Thompson SM (1995) Physiology and pharmacology of unitary synaptic connections between pairs of cells in areas CA3 and CA1 of rat hippocampal slice cultures. *J Neurophysiol* 73:1282-1294.
- Debanne D, Campanac E, Bialowas A, Carlier E, Alcaraz G (2011) Axon physiology. *Physiol Rev* 91:555-602.
- Dhamala M, Jirsa VK, Ding M (2004) Enhancement of Neural Synchrony by Time Delay. *Phys Rev Lett* 92:074104.
- Di Garbo A, Barbi M, Chillemi S (2002) Synchronization in a network of fast-spiking interneurons. *Biosystems* 67:45-53.

- Di Garbo A, Barbi M, Chillemi S (2007a) The synchronization properties of a network of inhibitory interneurons depend on the biophysical model. *Biosystems* 88:216-227.
- Di Garbo A, Panarese A, Barbi M, Chillemi S (2007b) The kinetics of the IPSC, the heterogeneity and the noise affect the firing coherence of a population of inhibitory interneurons. *Neurocomputing* 70:2705-2715.
- Eckhorn R (1994) Oscillatory and non-oscillatory synchronizations in the visual cortex and their possible roles in associations of visual features. *Prog Brain Res* 102:405-426.
- Economou MN, White JA (2012) Membrane properties and the balance between excitation and inhibition control gamma-frequency oscillations arising from feedback inhibition. *PLoS Comput Biol* 8:e1002354.
- Eeckman FH, Freeman WJ (1990) Correlations between unit firing and EEG in the rat olfactory system. *Brain Res* 528:238-244.
- Engel AK, Singer W (2001) Temporal binding and the neural correlates of sensory awareness. *Trends Cogn Sci* 5:16-25.
- Engel AK, Fries P (2010) Beta-band oscillations - signalling the status quo? *Curr Opin Neurobiol* 20:156-165.
- Engel AK, Fries P, Singer W (2001) Dynamic predictions: Oscillations and synchrony in top-down processing. *Nat Rev Neurosci* 2:704-716.
- Engel AK, Konig P, Kreiter AK, Singer W (1991) Interhemispheric synchronization of oscillatory neuronal responses in cat visual cortex. *Science* 252:1177-1179.
- Engel AK, Konig P, Kreiter AK, Schillen TB, Singer W (1992) Temporal Coding in the Visual-Cortex - New Vistas on Integration in the Nervous-System. *TINS* 15:218-226.
- Erisir A, Lau D, Rudy B, Leonard CS (1999) Function of specific K<sup>+</sup> channels in sustained high-frequency firing of fast-spiking neocortical interneurons. *J Neurophysiol* 82:2476-2489.
- Ermentrout B (1996) Type I membranes, phase resetting curves, and synchrony. *Neural Comput* 8:979-1001.
- Ermentrout B (2003) Dynamical Consequences of Fast-Rising, Slow-Decaying Synapses in Neuronal Networks. *Neural Comput* 15:2483-2522.
- Ermentrout B, Pascal M, Gutkin B (2001) The effects of spike frequency adaptation and negative feedback on the synchronization of neural oscillators. *Neural Comput* 13:1285-1310.
- Ermentrout GB, Kopell N (1998) Fine structure of neural spiking and synchronization in the presence of conduction delays. *Proc Natl Acad Sci U S A* 95:1259-1264.
- Ernst U, Pawelzik K, Geisel T (1995) Synchronization induced by temporal delays in pulse-coupled oscillators. *Phys Rev Lett* 74:1570-1573.

- Ernst U, Pawelzik K, Geisel T (1998) Delay-induced multistable synchronization of biological oscillators. *Phys Rev E* 57:2150-2162.
- Famiglietti EV, Jr. (1970) Dendro-dendritic synapses in the lateral geniculate nucleus of the cat. *Brain Res* 20:181-191.
- Fellous JM, Sejnowski TJ (2000) Cholinergic induction of oscillations in the hippocampal slice in the slow (0.5-2 Hz), theta (5-12 Hz), and gamma (35-70 Hz) bands. *Hippocampus* 10:187-197.
- Fisahn A, Pike FG, Buhl EH, Paulsen O (1998) Cholinergic induction of network oscillations at 40 Hz in the hippocampus in vitro. *Nature* 394:186-189.
- Fisahn A, Contractor A, Traub R, Buhl E, Heinemann S, McBain C (2004) Distinct roles for the kainate receptor subunits GluR5 and GluR6 in kainate-induced hippocampal gamma oscillations. *J Neurosci* 24:9658-9668.
- Fischer I, Vicente R, Buldú JM, Peil M, Mirasso CR, Torrent MC, García-Ojalvo J (2006) Zero-lag long-range synchronization via dynamical relaying. *Phys Rev Lett* 97:123901.
- Forrest T, Ariaratnam J, Strogatz S (1998) Synchrony in cricket calling songs: Models of coupled biological oscillators. *J Acoust Soc Am* 103:2827-2827.
- Forster E, Zhao ST, Frotscher M (2006) Laminating the hippocampus. *Nat Rev Neurosci* 7:259-U212.
- Frien A, Eckhorn R, Bauer R, Woelbern T, Kehr H (1994) Stimulus-Specific Fast Oscillations at Zero Phase between Visual Areas V1 and V2 of Awake Monkey. *Neuroreport* 5:2273-2277.
- Fries P (2005) A mechanism for cognitive dynamics: neuronal communication through neuronal coherence. *Trends Cogn Sci* 9:474-480.
- Fries P (2009) Neuronal gamma-band synchronization as a fundamental process in cortical computation. *Annu Rev Neurosci* 32:209-224.
- Fries P (2015) Rhythms for Cognition: Communication through Coherence. *Neuron* 88:220-235.
- Fries P, Scheeringa R, Oostenveld R (2008) Finding gamma. *Neuron* 58:303-305.
- Fries P, Reynolds JH, Rorie AE, Desimone R (2001) Modulation of oscillatory neuronal synchronization by selective visual attention. *Science* 291:1560-1563.
- Friesen WO (1994) Reciprocal inhibition: A mechanism underlying oscillatory animal movements. *Neurosci Biobehav Rev* 18:547-553.
- Froemke RC, Tsay IA, Raad M, Long JD, Dan Y (2006) Contribution of individual spikes in burst-induced long-term synaptic modification. *J Neurophysiol* 95:1620-1629.

- Fukuda T, Kosaka T (2000) Gap junctions linking the dendritic network of GABAergic interneurons in the hippocampus. *J Neurosci* 20:1519-1528.
- Gais S, Plihal W, Wagner U, Born J (2000) Early sleep triggers memory for early visual discrimination skills. *Nat Neurosci* 3:1335-1339.
- Galan RF, Ermentrout GB, Urban NN (2005) Efficient estimation of phase-resetting curves in real neurons and its significance for neural-network modeling. *Phys Rev Lett* 94:158101.
- Galarreta M, Hestrin S (1999) A network of fast-spiking cells in the neocortex connected by electrical synapses. *Nature* 402:72-75.
- Galarreta M, Hestrin S (2001a) Electrical synapses between GABA-releasing interneurons. *Nat Rev Neurosci* 2:425-433.
- Galarreta M, Hestrin S (2001b) Spike transmission and synchrony detection in networks of GABAergic interneurons. *Science* 292:2295-2299.
- Galarreta M, Hestrin S (2002) Electrical and chemical synapses among parvalbumin fast-spiking GABAergic interneurons in adult mouse neocortex. *Proc Natl Acad Sci U S A* 99:12438-12443.
- Gall FJ (1835) On the functions of the brain and of each of its parts : with observations on the possibility of determining the instincts, propensities, and talents, or the moral and intellectual dispositions of men and animals, by the configuration of the brain and head. Boston: Marsh, Capen & Lyon.
- Geiger J, Lübke J, Roth A, Frotscher M, Jonas P (1997) Submillisecond AMPA receptor-mediated signaling at a principal neuron-interneuron synapse. *Neuron* 18:1009-1023.
- Gerstner W, Kistler WM (2002) Spiking neuron models: Single neurons, populations, plasticity. Cambridge, U.K.: Cambridge University Press.
- Gibson J, Beierlein M, Connors B (1999) Two networks of electrically coupled inhibitory neurons in neocortex. *Nature* 402:75-79.
- Gibson JR, Beierlein M, Connors BW (2005) Functional properties of electrical synapses between inhibitory interneurons of neocortical layer 4. *J Neurophysiol* 93:467-480.
- Girard P, Hupe JM, Bullier J (2001) Feedforward and feedback connections between areas V1 and V2 of the monkey have similar rapid conduction velocities. *J Neurophysiol* 85:1328-1331.
- Giraud A-L, Poeppel D (2012) Cortical oscillations and speech processing: emerging computational principles and operations. *Nat Neurosci* 15:511-517.
- Glass L, Mackey MC (1988) From clocks to chaos: the rhythms of life. Princeton, N.J.: Princeton University Press.
- Gloveli T, Dugladze T, Rotstein H, Traub R, Monyer H, Heinemann U, Whittington M, Kopell N (2005a) Orthogonal arrangement of rhythm-

- generating microcircuits in the hippocampus. *Proc Natl Acad Sci U S A* 102:13295-13300.
- Gloveli T, Dugladze T, Saha S, Monyer H, Heinemann U, Traub R, Whittington M, Buhl E (2005b) Differential involvement of oriens/pyramidal interneurons in hippocampal network oscillations in vitro. *J Physiol-London* 562:131-147.
- Goebel R, Sanfelice RG, Teel AR (2012) *Hybrid Dynamical Systems: modeling, stability, and robustness*. Princeton: Princeton University Press.
- Goel P, Ermentrout B (2002) Synchrony, stability, and firing patterns in pulse-coupled oscillators. *Physica D* 163:191-216.
- Goldbeter A (1997) *Biochemical Oscillations and Cellular Rhythms: The Molecular Bases of Periodic and Chaotic Behaviour*. Cambridge: Cambridge University Press.
- Goldwyn J, Shea-Brown E (2011) The what and where of adding channel noise to the Hodgkin-Huxley equations. *PLoS Comput Biol* 7.
- Gollo LL, Mirasso C, Villa AEP (2010) Dynamic control for synchronization of separated cortical areas through thalamic relay. *Neuroimage* 52:947-955.
- Golomb D, Hansel D (2000) The Number of Synaptic Inputs and the Synchrony of Large, Sparse Neuronal Networks. *Neural Comput* 12:1095-1139.
- Gray CM (1994) Synchronous oscillations in neuronal systems: mechanisms and functions. *J Comput Neurosci* 1:11-38.
- Gray CM, Singer W (1989) Stimulus-specific neuronal oscillations in orientation columns of cat visual cortex. *Proc Natl Acad Sci U S A* 86:1698-1702.
- Gray CM, McCormick DA (1996) Chattering cells: Superficial pyramidal neurons contributing to the generation of synchronous oscillations in the visual cortex. *Science* 274:109-113.
- Gray CM, König P, Engel AK, Singer W (1989) Oscillatory Responses in Cat Visual-Cortex Exhibit Inter-Columnar Synchronization Which Reflects Global Stimulus Properties. *Nature* 338:334-337.
- Gray EG (1959) Axo-somatic and axo-dendritic synapses of the cerebral cortex: an electron microscope study. *J Anat* 93:420-433.
- Gregoriou GG, Gotts SJ, Zhou HH, Desimone R (2009a) High-Frequency, Long-Range Coupling Between Prefrontal and Visual Cortex During Attention. *Science* 324:1207-1210.
- Gregoriou GG, Gotts SJ, Zhou H, Desimone R (2009b) Long-range neural coupling through synchronization with attention. *Prog Brain Res* 176:35-45.

- Griesmayr B, Gruber WR, Klimesch W, Sauseng P (2010) Human frontal midline theta and its synchronization to gamma during a verbal delayed match to sample task. *Neurobiol Learn Mem* 93:208-215.
- Gross J, Schmitz F, Schnitzler I, Kessler K, Shapiro K, Hommel B, Schnitzler A (2004) Modulation of long-range neural synchrony reflects temporal limitations of visual attention in humans. *Proc Natl Acad Sci U S A* 101:13050-13055.
- Gulyas AI, Megias M, Emri Z, Freund TF (1999) Total number and ratio of excitatory and inhibitory synapses converging onto single interneurons of different types in the CA1 area of the rat hippocampus. *J Neurosci* 19:10082-10097.
- Haegens S, Nacher V, Luna R, Romo R, Jensen O (2011) Alpha-oscillations in the monkey sensorimotor network influence discrimination performance by rhythmical inhibition of neuronal spiking. *Proc Natl Acad Sci U S A* 108:19377-19382.
- Hajos N, Palhalmi J, Mann EO, Nemeth B, Paulsen O, Freund TF (2004) Spike timing of distinct types of GABAergic interneuron during hippocampal gamma oscillations in vitro. *J Neurosci* 24:9127-9137.
- Hajos N, Katona I, Naiem SS, MacKie K, Ledent C, Mody I, Freund TF (2000) Cannabinoids inhibit hippocampal GABAergic transmission and network oscillations. *Eur J Neurosci* 12:3239-3249.
- Hájos N, Paulsen O (2009) Network mechanisms of gamma oscillations in the CA3 region of the hippocampus. *Neural Netw* 22:1113-1119.
- Hansel D, Mato G (1993) Patterns of synchrony in a heterogeneous Hodgkin-Huxley neural network with weak coupling. *Physica A* 200:662-669.
- Hansel D, Mato G, Meunier C (1993a) Phase Dynamics for Weakly Coupled Hodgkin-Huxley Neurons. *Europhys Lett* 23:367.
- Hansel D, Mato G, Meunier C (1993b) Clustering and slow switching in globally coupled phase oscillators. *Phys Rev E* 48:3470-3477.
- Hansel D, Mato G, Meunier C (1995) Synchrony in excitatory neural networks. *Neural Comput* 7:307-337.
- Hardin J, Bertoni G, Kleinsmith LJ, Becker WM (2012) *Becker's world of the cell*. Boston: Benjamin Cummings.
- Hartline DK (2008) What is myelin? *Neuron Glia Biol* 4:153-163.
- Hasenstaub A, Shu Y, Haider B, Kraushaar U, Duque A, McCormick DA (2005) Inhibitory postsynaptic potentials carry synchronized frequency information in active cortical networks. *Neuron* 47:423-435.
- Hasselmo ME (2005) What is the function of hippocampal theta rhythm?-- Linking behavioral data to phasic properties of field potential and unit recording data. *Hippocampus* 15:936-949.

- Havenith MN, Zemmar A, Yu S, Baudrexel SM, Singer W, Nikolic D (2009) Measuring sub-millisecond delays in spiking activity with millisecond time-bins. *Neurosci Lett* 450:296-300.
- He BJ, Raichle ME (2009) The fMRI signal, slow cortical potential and consciousness. *Trends Cogn Sci* 13:302-309.
- Hebb DO (1949) *The organization of behaviour: A neuropsychological theory*. New York: Wiley.
- Hennequin G, Gerstner W, Pfister JP (2010) STDP in Adaptive Neurons Gives Close-To-Optimal Information Transmission. *Front Comput Neurosc* 4:143.
- Hiltunen T, Kantola J, Abou Elseoud A, Lepola P, Suominen K, Starck T, Nikkinen J, Remes J, Tervonen O, Palva S, Kiviniemi V, Palva JM (2014) Infra-slow EEG fluctuations are correlated with resting-state network dynamics in fMRI. *J Neurosci* 34:356-362.
- Hodgkin AL, Huxley AF (1952) A Quantitative Description of Membrane Current and Its Application to Conduction and Excitation in Nerve. *J Physiol* 117:500-544.
- Hopfield JJ (1995) Pattern-Recognition Computation Using Action-Potential Timing for Stimulus Representation. *Nature* 376:33-36.
- Hormuzdi SG, Pais I, LeBeau FEN, Towers SK, Rozov A, Buhl EH, Whittington MA, Monyer H (2001) Impaired electrical signaling disrupts gamma frequency oscillations in connexin 36-deficient mice. *Neuron* 31:487-495.
- Huber R, Ghilardi MF, Massimini M, Tononi G (2004) Local sleep and learning. *Nature* 430:78-81.
- Izhikevich EM (2007) *Dynamical systems in neuroscience: The geometry of excitability and bursting*. Cambridge, Mass: MIT Press.
- Jacobs J, Kahana MJ, Ekstrom AD, Fried I (2007) Brain oscillations control timing of single-neuron activity in humans. *J Neurosci* 27:3839-3844.
- Jahnke S, Memmesheimer R-M, Timme M (2008) Stable Irregular Dynamics in Complex Neural Networks. *Phys Rev Lett* 100:048102.
- Jahnke S, Memmesheimer RM, Timme M (2014a) Hub-activated signal transmission in complex networks. *Phys Rev E* 89:5.
- Jahnke S, Memmesheimer RM, Timme M (2014b) Oscillation-induced signal transmission and gating in neural circuits. *PLoS Comput Biol* 10:e1003940.
- Jan YN, Jan LY (2010) Branching out: mechanisms of dendritic arborization. *Nat Rev Neurosci* 11:316-328.
- Jefferys JGR, Traub RD, Whittington MA (1996) Neuronal networks for induced '40 Hz' rhythms. *TINS* 19:202-208.
- Jeong HY, Gutkin B (2005) Study on the role of GABAergic synapses in synchronization. *Neurocomputing* 65:859-868.



- Jeong HY, Gutkin B (2007) Synchrony of neuronal oscillations controlled by GABAergic reversal potentials. *Neural Comput* 19:706-729.
- Jia X, Tanabe S, Kohn A (2013) Gamma and the coordination of spiking activity in early visual cortex. *Neuron* 77:762-774.
- Joliot M, Ribary U, Llinas R (1994) Human oscillatory brain activity near 40 Hz coexists with cognitive temporal binding. *Proc Natl Acad Sci U S A* 91:11748-11751.
- Jones MS, Barth DS (1997) Sensory-evoked high-frequency (gamma-band) oscillating potentials in somatosensory cortex of the unanesthetized rat. *Brain Res* 768:167-176.
- Jones SR, Pinto DJ, Kaper TJ, Kopell N (2000) Alpha-Frequency Rhythms Desynchronize over Long Cortical Distances: A Modeling Study. *J Comput Neurosci* 9:271-291.
- Kandel A, Buzsáki G (1997) Cellular-synaptic generation of sleep spindles, spike-and-wave discharges, and evoked thalamocortical responses in the neocortex of the rat. *J Neurosci* 17:6783-6797.
- Kandel ER (2013) *Principles of neural science*. New York: McGraw-Hill Medical.
- Kawaguchi Y (1995) Physiological Subgroups of Nonpyramidal Cells with Specific Morphological-Characteristics in Layer II/III of Rat Frontal-Cortex. *J Neurosci* 15:2638-2655.
- Kilpatrick ZP, Ermentrout B (2011) Sparse gamma rhythms arising through clustering in adapting neuronal networks. *PLoS Comput Biol* 7:e1002281.
- Kistler WM, Gerstner W, vanHemmen JL (1997) Reduction of the Hodgkin-Huxley equations to a single-variable threshold model. *Neural Comput* 9:1015-1045.
- Klimesch W (1999) EEG alpha and theta oscillations reflect cognitive and memory performance: a review and analysis. *Brain Res Rev* 29:169-195.
- Klimesch W (2012) Alpha-band oscillations, attention, and controlled access to stored information. *Trends Cogn Sci* 16:606-617.
- Knoblauch A, Sommer FT (2003) Synaptic plasticity, conduction delays, and inter-areal phase relations of spike activity in a model of reciprocally connected areas. *Neurocomputing* 52-4:301-306.
- Koch C, Segev I (1998) *Methods in neuronal modeling : from ions to networks*, 2nd Edition. Cambridge, Mass: MIT Press.
- Konig P, Engel AK, Singer W (1995a) Relation between oscillatory activity and long-range synchronization in cat visual cortex. *Proc Natl Acad Sci U S A* 92:290-294.
- Konig P, Engel AK, Roelfsema PR, Singer W (1995b) How Precise Is Neuronal Synchronization. *Neural Comput* 7:469-485.

- Kopell N, LeMasson G (1994) Rhythmogenesis, amplitude modulation, and multiplexing in a cortical architecture. *Proc Natl Acad Sci U S A* 91:10586-10590.
- Kopell N, Ermentrout B (2004) Chemical and electrical synapses perform complementary roles in the synchronization of interneuronal networks. *Proc Natl Acad Sci U S A* 101:15482-15487.
- Kopell N, Ermentrout GB, Whittington MA, Traub RD (2000) Gamma rhythms and beta rhythms have different synchronization properties. *Proc Natl Acad Sci U S A* 97:1867-1872.
- Kramer MA, Roopun AK, Carracedo LM, Traub RD, Whittington MA, Kopell NJ (2008) Rhythm generation through period concatenation in rat somatosensory cortex. *PLoS Comput Biol* 4:e1000169.
- Krogh-Madsen T, Butera R, Ermentrout GB, Glass L (2012) Phase resetting neural oscillators: Topological theory versus the real world. In: *Phase response curves in neuroscience: theory, experiment, and analysis*, pp 33-51. New York, NY: Springer.
- Krupa M, Gielen S, Gutkin B (2014) Adaptation and shunting inhibition leads to pyramidal/interneuron gamma with sparse firing of pyramidal cells. *J Comput Neurosci* 37:357-376.
- Lachaux JP, Rodriguez E, Martinerie J, Varela FJ (1999) Measuring phase synchrony in brain signals. *Hum Brain Mapp* 8:194-208.
- Lachaux JP, Rodriguez E, Martinerie J, Adam C, Hasboun D, Varela FJ (2000) A quantitative study of gamma-band activity in human intracranial recordings triggered by visual stimuli. *Eur J Neurosci* 12:2608-2622.
- Lamsa KP, Heeroma JH, Somogyi P, Rusakov DA, Kullmann DM (2007) Anti-Hebbian long-term potentiation in the hippocampal feedback inhibitory circuit. *Science* 315:1262-1266.
- Lapicque L (1907) Recherches quantitatives sur l'excitation électrique des nerfs traitée comme une polarisation. *J Physiol Pathol Gen* 9:620-635.
- Laurent G (2002) Olfactory network dynamics and the coding of multidimensional signals. *Nat Rev Neurosci* 3:884-895.
- LeBeau FEN, Towers SK, Traub RD, Whittington MA, Buhl EH (2002) Fast network oscillations induced by potassium transients in the rat hippocampus in vitro. *J Physiol-London* 542:167-179.
- Lee S, Sen K, Kopell N (2009) Cortical gamma rhythms modulate NMDAR-mediated spike timing dependent plasticity in a biophysical model. *PLoS Comput Biol* 5:e1000602.
- Leibold C (2004) Stability Analysis of Asynchronous States in Neuronal Networks with Conductance-Based Inhibition. *Phys Rev Lett* 93:208104.

- Lengyel M, Kwag J, Paulsen O, Dayan P (2005) Matching storage and recall: hippocampal spike timing-dependent plasticity and phase response curves. *Nat Neurosci* 8:1677-1683.
- Lent R, Azevedo FAC, Andrade-Moraes CH, Pinto AVO (2012) How many neurons do you have? Some dogmas of quantitative neuroscience under revision. *Eur J Neurosci* 35:1-9.
- Lewis DA, Hashimoto T, Volk DW (2005) Cortical inhibitory neurons and schizophrenia. *Nat Rev Neurosci* 6:312-324.
- Lewis TJ, Rinzel J (2003) Dynamics of spiking neurons connected by both inhibitory and electrical coupling. *J Comput Neurosci* 14:283-309.
- Lindner B, Gangloff D, Longtin A, Lewis JE (2009) Broadband Coding with Dynamic Synapses. *J Neurosci* 29:2076-2088.
- Lisman JE (1999) Relating hippocampal circuitry to function: Recall of memory sequences by reciprocal dentate-CA3 interactions. *Neuron* 22:233-242.
- Lisman JE, Idiart MAP (1995) Storage of  $7 \pm 2$  short-term memories in oscillatory subcycles. *Science* 267:1512-1515.
- Llinas R, Ribary U, Contreras D, Pedroarena C (1998) The neuronal basis for consciousness. *Philos T Roy Soc B* 353:1841-1849.
- Llinas RR, Ribary U, Jeanmonod D, Kronberg E, Mitra PP (1999) Thalamocortical dysrhythmia: A neurological and neuropsychiatric syndrome characterized by magnetoencephalography. *Proc Natl Acad Sci U S A* 96:15222-15227.
- Long MA, Deans MR, Paul DL, Connors BW (2002) Rhythmicity without synchrony in the electrically uncoupled inferior olive. *J Neurosci* 22:10898-10905.
- Luczak A, McNaughton BL, Harris KD (2015) Packet-based communication in the cortex. *Nat Rev Neurosci* 16:745-755.
- Lytton WW, Sejnowski TJ (1991) Simulations of cortical pyramidal neurons synchronized by inhibitory interneurons. *J Neurophysiol* 66:1059-1079.
- MacIver MB, Tanelian DL, Mody I (1991) Two mechanisms for anesthetic-induced enhancement of GABAA-mediated neuronal inhibition. *Ann N Y Acad Sci* 625:91-96.
- Maier N, Draguhn A, Schmitz D, Both M (2013) Fast network oscillations in the hippocampus. *eNeuroforum* 4:1-10.
- Maloney KJ, Cape EG, Gotman J, Jones BE (1997) High-frequency gamma electroencephalogram activity in association with sleep-wake states and spontaneous behaviors in the rat. *Neuroscience* 76:541-555.
- Mancilla JG, Lewis TJ, Pinto DJ, Rinzel J, Connors BW (2007) Synchronization of electrically coupled pairs of inhibitory interneurons in neocortex. *J Neurosci* 27:2058-2073.

- Mann-Metzer P, Yarom Y (1999) Electrotonic coupling interacts with intrinsic properties to generate synchronized activity in cerebellar networks of inhibitory interneurons. *J Neurosci* 19:3298-3306.
- Mann EO, Radcliffe CA, Paulsen O (2005a) Hippocampal gamma-frequency oscillations: From interneurons to pyramidal cells, and back. *J Physiol* 562:55-63.
- Mann EO, Suckling JM, Hajos N, Greenfield SA, Paulsen O (2005b) Perisomatic feedback inhibition underlies cholinergically induced fast network oscillations in the rat hippocampus in vitro. *Neuron* 45:105-117.
- Maquet P (2001) The role of sleep in learning and memory. *Science* 294:1048-1052.
- McBain CJ, Fisahn A (2001) Interneurons unbound. *Nat Rev Neurosci* 2:11-23.
- McBain CJ, Kauer JA (2009) Presynaptic plasticity: targeted control of inhibitory networks. *Curr Opin Neurobiol* 19:254-262.
- Memmesheimer R-M (2010) Quantitative prediction of intermittent high-frequency oscillations in neural networks with supralinear dendritic interactions. *Proc Natl Acad Sci U S A* 107:11092-11097.
- Memmesheimer RM, Timme M (2006a) Designing complex networks. *Physica D* 224:182-201.
- Memmesheimer RM, Timme M (2006b) Designing the dynamics of spiking neural networks. *Phys Rev Lett* 97.
- Merriam EB, Netoff TI, Banks MI (2005) Bistable network behavior of layer I interneurons in auditory cortex. *J Neurosci* 25:6175-6186.
- Meyrand P, Cattaert D, Ostaszewski H, Bem T (2009) Inhibitory network of spiking neurons may express a sharp peak of synchrony at low frequency band. *Biol Cybern* 101:325-338.
- Miltner WH, Braun C, Arnold M, Witte H, Taub E (1999) Coherence of gamma-band EEG activity as a basis for associative learning. *Nature* 397:434-436.
- Minlebaev M, Colonnese M, Tsintsadze T, Sirota A, Khazipov R (2011) Early gamma oscillations synchronize developing thalamus and cortex. *Science* 334:226-229.
- Mirollo RE, Strogatz SH (1990) Synchronization of Pulse-Coupled Biological Oscillators. *Siam J Appl Math* 50:1645-1662.
- Misulis KE, Abou-Khalil B (2014) Atlas of EEG and seizure semiology and management. Oxford: Oxford University Press.
- Moiseeva NI, Aleksanian ZA (1986) Slow-wave oscillations of the multi-unit activity average frequency in the human brain during drowsiness and sleep. *Electroen Clin Neuro* 63:431-437.

- Nacher V, Ledberg A, Deco G, Romo R (2013) Coherent delta-band oscillations between cortical areas correlate with decision making. *Proc Natl Acad Sci U S A* 110:15085-15090.
- Neltner L, Hansel D, Mato G, Meunier C (2000) Synchrony in heterogeneous networks of spiking neurons. *Neural Comput* 12:1607-1641.
- Netoff TL, Banks MI, Dorval AD, Acker CD, Haas JS, Kopell N, White JA (2005) Synchronization in hybrid neuronal networks of the hippocampal formation. *J Neurophysiol* 93:1197-1208.
- Niedermeyer E (1997) Alpha rhythms as physiological and abnormal phenomena. *Int J Psychophysiol* 26:31-49.
- Nikolic D (2007) Non-parametric detection of temporal order across pairwise measurements of time delays. *J Comput Neurosci* 22:5-19.
- Nishimura J, Friedman EJ (2011) Robust Convergence in Pulse-Coupled Oscillators with Delays. *Phys Rev Lett* 106:194101.
- Noachtar S, Binnie C, Ebersole J, Mauquiére F, Sakamoto A, Westmoreland B (2004) A glossary of terms most commonly used by clinical electroencephalographers and proposal for the report form for the EEG findings. *Klin Neurophysiol* 35:5-21.
- Nomura M, Aoyagi T (2005) Stability of synchronous solutions in weakly coupled neuron networks. *Prog Theor Phys* 113:911-925.
- Nomura M, Fukai T, Aoyagi T (2003) Synchrony of fast-spiking interneurons interconnected by GABAergic and electrical synapses. *Neural Comput* 15:2179-2198.
- Norton S, Jewett RE (1965) Frequencies of slow potential oscillations in the cortex of cats. *Electroen Clin Neuro* 19:377-386.
- Nowacki J, Osinga HM, Brown JT, Randall AD, Tsaneva-Atanasova K (2011) A unified model of CA1/3 pyramidal cells: An investigation into excitability. *Prog Biophys Mol Bio* 105:34-48.
- Nunez A, Amzica F, Steriade M (1992) Intrinsic and synaptically generated delta (1-4 Hz) rhythms in dorsal lateral geniculate neurons and their modulation by light-induced fast (30-70 Hz) events. *Neuroscience* 51:269-284.
- Nunez PL (2002) Electroencephalography (EEG). In: *Encyclopedia of the Human Brain*, pp 169-179. New York, NY: Academic Press.
- Nunez PL, Srinivasan R (2006) *Electric fields of the brain : the neurophysics of EEG*. Oxford: Oxford University Press.
- O'Keefe J, Nadel L (1978) *The hippocampus as a cognitive map*. Oxford: Oxford University Press.
- O'Keefe J, Recce ML (1993) Phase relationship between hippocampal place units and the EEG theta rhythm. *Hippocampus* 3:317-330.

- Oh M, Matveev V (2009) Loss of phase-locking in non-weakly coupled inhibitory networks of type-I model neurons. *J Comput Neurosci* 26:303-320.
- Oren I, Mann EO, Paulsen O, Hajos N (2006) Synaptic currents in anatomically identified CA3 neurons during hippocampal gamma oscillations in vitro. *J Neurosci* 26:9923-9934.
- Otto T, Eichenbaum H, Wiener SI, Wible CG (1991) Learning-related patterns of CA1 spike trains parallel stimulation parameters optimal for inducing hippocampal long-term potentiation. *Hippocampus* 1:181-192.
- Palhalmi J, Paulsen O, Freund TF, Hajos N (2004) Distinct properties of carbachol- and DHPG-induced network oscillations in hippocampal slices. *Neuropharmacology* 47:381-389.
- Palva JM, Palva S, Kaila K (2005) Phase synchrony among neuronal oscillations in the human cortex. *J Neurosci* 25:3962-3972.
- Palva S, Palva JM (2007) New vistas for alpha-frequency band oscillations. *TINS* 30:150-158.
- Pare D, Popescu AT, Popa D (2009) Coherent gamma oscillations couple the amygdala and striatum during learning. *Nat Neurosci* 12:801-U161.
- Patel J, Schomburg EW, Berenyi A, Fujisawa S, Buzsáki G (2013) Local generation and propagation of ripples along the septotemporal axis of the hippocampus. *J Neurosci* 33:17029-17041.
- Penttonen M, Buzsáki G (2003) Natural logarithmic relationship between brain oscillators. *Thalamus Relat Syst* 2:145-152.
- Pesaran B, Pezaris JS, Sahani M, Mitra PP, Andersen RA (2002) Temporal structure in neuronal activity during working memory in macaque parietal cortex. *Nat Neurosci* 5:805-811.
- Pfeuty B, Mato G, Golomb D, Hansel D (2003) Electrical synapses and synchrony: The role of intrinsic currents. *J Neurosci* 23:6280-6294.
- Pfeuty B, Mato G, Golomb D, Hansel D (2005) The combined effects of inhibitory and electrical synapses in synchrony. *Neural Comput* 17:633-670.
- Pikovsky A, Rosenblum M, Kurths J (2001) *Synchronization : a universal concept in nonlinear sciences*. Cambridge: Cambridge University Press.
- Prakash R, Yizhar O, Grewe B, Ramakrishnan C, Wang N, Goshen I, Packer AM, Peterka DS, Yuste R, Schnitzer MJ, Deisseroth K (2012) Two-photon optogenetic toolbox for fast inhibition, excitation and bistable modulation. *Nat Methods* 9:1171-U1132.
- Prescott SA, Ratté S, De Koninck Y, Sejnowski TJ (2008) Pyramidal neurons switch from integrators in vitro to resonators under in vivo-like conditions. *J Neurophysiol* 100:3030-3042.
- Purves D (2004) *Neuroscience*. Sunderland, Mass: Sinauer Associates.

- Purves D (2012) Neuroscience. Sunderland, Mass: Sinauer Associates.
- Rappelsberger P, Pockberger H, Petsche H (1982) The contribution of the cortical layers to the generation of the EEG: field potential and current source density analyses in the rabbit's visual cortex. *Electroen Clin Neuro* 53:254-269.
- Reyes AD, Fetz EE (1993a) Effects of transient depolarizing potentials on the firing rate of cat neocortical neurons. *J Neurophysiol* 69:1673-1683.
- Reyes AD, Fetz EE (1993b) Two modes of interspike interval shortening by brief transient depolarizations in cat neocortical neurons. *J Neurophysiol* 69:1661-1672.
- Rodriguez E, George N, Lachaux JP, Martinerie J, Renault B, Varela FJ (1999) Perception's shadow: long-distance synchronization of human brain activity. *Nature* 397:430-433.
- Roelfsema PR, Engel AK, Konig P, Singer W (1997) Visuomotor integration is associated with zero time-lag synchronization among cortical areas. *Nature* 385:157-161.
- Rougeul-Buser A, Buser P (1997) Rhythms in the alpha band in cats and their behavioural correlates. *Int J Psychophysiol* 26:191-203.
- Routh BN, Johnston D, Harris K, Chitwood RA (2009) Anatomical and electrophysiological comparison of CA1 pyramidal neurons of the rat and mouse. *J Neurophysiol* 102:2288-2302.
- Roxin A, Brunel N, Hansel D (2005) Role of delays in shaping spatiotemporal dynamics of neuronal activity in large networks. *Phys Rev Lett* 94:1-4.
- Salami M, Itami C, Tsumoto T, Kimura F (2003) Change of conduction velocity by regional myelination yields constant latency irrespective of distance between thalamus and cortex. *Proc Natl Acad Sci U S A* 100:6174-6179.
- Saleh M, Reimer J, Penn R, Ojakangas CL, Hatsopoulos NG (2010) Fast and slow oscillations in human primary motor cortex predict oncoming behaviorally relevant cues. *Neuron* 65:461-471.
- Sato YD, Shiino M (2002) Spiking neuron models with excitatory or inhibitory synaptic couplings and synchronization phenomena. *Phys Rev E* 66:041903.
- Schneider G, Nikolic D (2006) Detection and assessment of near-zero delays in neuronal spiking activity. *J Neurosci Meth* 152:97-106.
- Schoffelen JM, Oostenveld R, Fries P (2005) Neuronal coherence as a mechanism of effective corticospinal interaction. *Science* 308:111-113.
- Sherman SM, Guillery RW (2002) The role of the thalamus in the flow of information to the cortex. *Philos T Roy Soc B* 357:1695-1708.
- Siapas AG, Wilson MA (1998) Coordinated interactions between hippocampal ripples and cortical spindles during slow-wave sleep. *Neuron* 21:1123-1128.

- Siarey RJ, Andreasen M, Lambert JD (1995) Serotonergic modulation of excitability in area CA1 of the in vitro rat hippocampus. *Neurosci Lett* 199:211-214.
- Siegel JM (2005) Clues to the functions of mammalian sleep. *Nature* 437:1264-1271.
- Sik A, Penttonen M, Ylinen A, Buzsáki G (1995) Hippocampal CA1 interneurons: an in vivo intracellular labeling study. *J Neurosci* 15:6651-6665.
- Singer W (1999) Neuronal synchrony: a versatile code for the definition of relations? *Neuron* 24:49-65, 111-125.
- Singer W, Gray CM (1995) Visual Feature Integration and the Temporal Correlation Hypothesis. *Annu Rev Neurosci* 18:555-586.
- Smeal RM, Ermentrout GB, White JA (2010) Phase-response curves and synchronized neural networks. *Philos T R Soc B* 365:2407-2422.
- Sohal V, Zhang F, Yizhar O, Deisseroth K (2009) Parvalbumin neurons and gamma rhythms enhance cortical circuit performance. *Nature* 459:698-702.
- Somogyi P, Klausberger T (2005) Defined types of cortical interneurone structure space and spike timing in the hippocampus. *J Physiol* 562:9-26.
- Song K, Meng M, Chen L, Zhou K, Luo H (2014) Behavioral Oscillations in Attention: Rhythmic alpha Pulses Mediated through theta Band. *J Neurosci* 34:4837-4844.
- Song S, Miller KD, Abbott LF (2000) Competitive Hebbian learning through spike-timing-dependent synaptic plasticity. *Nat Neurosci* 3:919-926.
- Soteropoulos DS, Baker SN (2006) Cortico-cerebellar coherence during a precision grip task in the monkey. *J Neurophysiol* 95:1194-1206.
- Spencer KM, Nestor PG, Niznikiewicz MA, Salisbury DF, Shenton ME, McCarley RW (2003) Abnormal neural synchrony in schizophrenia. *J Neurosci* 23:7407-7411.
- Steriade M (2001) Impact of network activities on neuronal properties in corticothalamic systems. *J Neurophysiol* 86:1-39.
- Steriade M, Deschenes M (1984) The thalamus as a neuronal oscillator. *Brain Res* 320:1-63.
- Steriade M, Timofeev I (2003) Neuronal plasticity in thalamocortical networks during sleep and waking oscillations. *Neuron* 37:563-576.
- Steriade M, Nunez A, Amzica F (1993) A novel slow (< 1 Hz) oscillation of neocortical neurons in vivo: depolarizing and hyperpolarizing components. *J Neurosci* 13:3252-3265.
- Steriade M, Gloor P, Llinas RR, Lopes de Silva FH, Mesulam MM (1990) Basic mechanisms of cerebral rhythmic activities. *Electroen Clin Neuro* 76:481-508.



- Stickgold R, James L, Hobson JA (2000) Visual discrimination learning requires sleep after training. *Nat Neurosci* 3:1237-1238.
- Stiefel KM, Gutkin BS, Sejnowski TJ (2008) Cholinergic Neuromodulation Changes Phase Response Curve Shape and Type in Cortical Pyramidal Neurons. *PLoS One* 3.
- Stiefel KM, Gutkin BS, Sejnowski TJ (2009) The effects of cholinergic neuromodulation on neuronal phase-response curves of modeled cortical neurons. *J Comput Neurosci* 26:289-301.
- Swettenham JB, Muthukumaraswamy SD, Singh KD (2009) Spectral properties of induced and evoked gamma oscillations in human early visual cortex to moving and stationary stimuli. *J Neurophysiol* 102:1241-1253.
- Tallon-Baudry C, Bertrand O (1999) Oscillatory gamma activity in humans and its role in object representation. *Trends Cogn Sci* 3:151-162.
- Tamas G, Somogyi P, Buhl EH (1998) Differentially interconnected networks of GABAergic interneurons in the visual cortex of the cat. *J Neurosci* 18:4255-4270.
- Tamas G, Buhl EH, Lorincz A, Somogyi P (2000) Proximally targeted GABAergic synapses and gap junctions synchronize cortical interneurons. *Nat Neurosci* 3:366-371.
- Tateno T, Robinson HP (2007) Phase resetting curves and oscillatory stability in interneurons of rat somatosensory cortex. *Biophys J* 92:683-695.
- Tateno T, Harsch A, Robinson HPC (2004) Threshold firing frequency-current relationships of neurons in rat somatosensory cortex: Type 1 and type 2 dynamics. *J Neurophysiol* 92:2283-2294.
- Terman D, Kopell N, Bose A (1998) Dynamics of two mutually coupled slow inhibitory neurons. *Physica D* 117:241-275.
- Terman D, Lee E, Rinzel J, Bem T (2011) Stability of anti-phase and in-phase locking by electrical coupling but not fast inhibition alone. *SIAM J Appl Dyn Syst* 10:1127-1153.
- Theyel BB, Llano DA, Sherman M (2010) The corticothalamocortical circuit drives higher-order cortex in the mouse. *Nat Neurosci* 13:84-U246.
- Thut G, Miniussi C, Gross J (2012) The Functional Importance of Rhythmic Activity in the Brain. *Curr Biol* 22:R658-R663.
- Tiesinga P, Sejnowski TJ (2009) Cortical enlightenment: Are attentional gamma oscillations driven by ING or PING? *Neuron* 63:727-732.
- Tiesinga PHE, Fellous JM, Sejnowski TJ (2002) Spike-time reliability of periodically driven integrate-and-fire neurons. *Neurocomputing* 44:195-200.
- Tiesinga PHE, Fellous JM, Jose JV, Sejnowski TJ (2001) Computational model of carbachol-induced delta, theta, and gamma oscillations in the hippocampus. *Hippocampus* 11:251-274.

- Tikidji-Hamburyan RA, Martinez JJ, White JA, Canavier CC (2015) Resonant Interneurons Can Increase Robustness of Gamma Oscillations. *J Neurosci* 35:15682-15695.
- Timme M, Wolf F, Geisel T (2003) Unstable attractors induce perpetual synchronization and desynchronization. *Chaos* 13:377-387.
- Timofeev I, Steriade M (1996) Low-frequency rhythms in the thalamus of intact-cortex and decorticated cats. *J Neurophysiol* 76:4152-4168.
- Traub R, Whittington M, Colling S, Buzsáki G, Jefferys J (1996a) Analysis of gamma rhythms in the rat hippocampus in vitro and in vivo. *J Physiol-London* 493 ( Pt 2):471-484.
- Traub RD, Jefferys JGR, Whittington MA (1997) Simulation of gamma rhythms in networks of interneurons and pyramidal cells. *J Comput Neurosci* 4:141-150.
- Traub RD, Whittington MA, Stanford IM, Jefferys JGR (1996b) A mechanism for generation of long-range synchronous fast oscillations in the cortex. *Nature* 383:621-624.
- Traub RD, Kopell N, Bibbig A, Buhl EH, LeBeau FEN, Whittington MA (2001) Gap junctions between interneuron dendrites can enhance synchrony of gamma oscillations in distributed networks. *J Neurosci* 21:9478-9486.
- Traub RD, Draguhn A, Whittington MA, Baldeweg T, Bibbig A, Buhl EH, Schmitz D (2002) Axonal gap junctions between principal neurons: a novel source of network oscillations, and perhaps epileptogenesis. *Rev Neurosci* 13:1-30.
- Tsubo Y, Takada M, Reyes AD, Fukai T (2007) Layer and frequency dependencies of phase response properties of pyramidal neurons in rat motor cortex. *Eur J Neurosci* 25:3429-3441.
- Tukker J, Fuentealba P, Hartwich K, Somogyi P, Klausberger T (2007) Cell type-specific tuning of hippocampal interneuron firing during gamma oscillations in vivo. *J Neurosci* 27:8184-8189.
- Uhlhaas PJ, Singer W (2006) Neural synchrony in brain disorders: Relevance for cognitive dysfunctions and pathophysiology. *Neuron* 52:155-168.
- Uhlhaas PJ, Pipa G, Lima B, Melloni L, Neuenschwander S, Nikolic D, Singer W (2009) Neural synchrony in cortical networks: history, concept and current status. *Front Integr Neurosci* 3:17.
- van Rossum MCW, Bi GQ, Turrigiano GG (2000) Stable Hebbian learning from spike timing-dependent plasticity. *J Neurosci* 20:8812-8821.
- van Vreeswijk C (1996) Partial synchronization in populations of pulse-coupled oscillators. *Phys Rev E* 54:5522-5537.
- van Vreeswijk C, Abbott LF, Ermentrout GB (1994) When inhibition not excitation synchronizes neural firing. *J Comput Neurosci* 1:313-321.

- Vanderwolf CH, Zibrowski EM (2001) Pyriform cortex beta-waves: odor-specific sensitization following repeated olfactory stimulation. *Brain Res* 892:301-308.
- Vanhatalo S, Palva JM, Holmes MD, Miller JW, Voipio J, Kaila K (2004) Infraslow oscillations modulate excitability and interictal epileptic activity in the human cortex during sleep. *Proc Natl Acad Sci U S A* 101:5053-5057.
- Varela F, Lachaux JP, Rodriguez E, Martinerie J (2001) The brainweb: Phase synchronization and large-scale integration. *Nat Rev Neurosci* 2:229-239.
- Vertes RP (2004) Memory consolidation in sleep; dream or reality. *Neuron* 44:135-148.
- Vertes RP, Kocsis B (1997) Brainstem-diencephalo-septohippocampal systems controlling the theta rhythm of the hippocampus. *Neuroscience* 81:893-926.
- Vicente R, Gollo LL, Mirasso CR, Fischer I, Pipa G (2008) Dynamical relaying can yield zero time lag neuronal synchrony despite long conduction delays. *Proc Natl Acad Sci U S A* 105:17157-17162.
- Viriyopase A, Memmesheimer RM, Gielen S (2016) Cooperation and competition of gamma oscillation mechanisms. *J Neurophysiol* 116:232-251.
- Viriyopase A, Bojak I, Zeitler M, Gielen S (2012) When Long-Range Zero-Lag Synchronization is Feasible in Cortical Networks. *Front Comput Neurosci* 6:49.
- Volgushev M, Chistiakova M, Singer W (1998) Modification of discharge patterns of neocortical neurons by induced oscillations of the membrane potential. *Neuroscience* 83:15-25.
- von Stein A, Sarnthein J (2000) Different frequencies for different scales of cortical integration: from local gamma to long range alpha/theta synchronization. *Int J Psychophysiol* 38:301-313.
- von Stein A, Chiang C, Konig P (2000) Top-down processing mediated by interareal synchronization. *Proc Natl Acad Sci U S A* 97:14748-14753.
- Vyazovskiy VV, Harris KD (2013) Sleep and the single neuron: the role of global slow oscillations in individual cell rest. *Nat Rev Neurosci* 14:445-453.
- Walberg F (1965) Axoaxonic contacts in the cuneate nucleus, probable basis for presynaptic depolarization. *Exp Neurol* 13:218-231.
- Wan Q, Xiong ZG, Man HY, Ackerley CA, Braunton J, Lu WY, Becker LE, MacDonald JF, Wang YT (1997) Recruitment of functional GABA(A) receptors to postsynaptic domains by insulin. *Nature* 388:686-690.

- Wang L, Narayan R, Graña G, Shamir M, Sen K (2007) Cortical Discrimination of Complex Natural Stimuli: Can Single Neurons Match Behavior? *J Neurosci* 27:582-589.
- WANG Q, LU Q, CHEN G (2008) SYNCHRONIZATION TRANSITION INDUCED BY SYNAPTIC DELAY IN COUPLED FAST-SPIKING NEURONS. *Int J Bifurcat Chaos* 18:1189-1198.
- Wang S, Musharoff MM, Canavier CC, Gasparini S (2013) Hippocampal CA1 pyramidal neurons exhibit type 1 phase-response curves and type 1 excitability. *J Neurophysiol* 109:2757-2766.
- Wang S, Chandrasekaran L, Fernandez FR, White JA, Canavier CC (2012) Short conduction delays cause inhibition rather than excitation to favor synchrony in hybrid neuronal networks of the entorhinal cortex. *PLoS Comput Biol* 8.
- Wang XJ (1993) Ionic basis for intrinsic 40 Hz neuronal oscillations. *Neuroreport* 5:221-224.
- Wang XJ (1999) Fast burst firing and short-term synaptic plasticity: A model of neocortical chattering neurons. *Neuroscience* 89:347-362.
- Wang XJ, Rinzal J (1992) Alternating and synchronous rhythms in reciprocally inhibitory model neurons. *Neural Comput* 4:84-97.
- Wang XJ, Buzsáki G (1996) Gamma oscillation by synaptic inhibition in a hippocampal interneuronal network model. *J Neurosci* 16:6402-6413.
- Welch PD (1967) The use of fast Fourier transform for the estimation of power spectra: A method based on time averaging over short, modified periodograms. *IEEE Trans Acoust* 15:70-73.
- Wernicke C (1910) The symptom-complex of aphasia. In: *Diseases of the nervous system*, pp 265-324. New York: D. Appleton.
- Whishaw IQ, Vanderwolf CH (1973) Hippocampal EEG and behavior: changes in amplitude and frequency of RSA (theta rhythm) associated with spontaneous and learned movement patterns in rats and cats. *Behav Biol* 8:461-484.
- White JA, Klink R, Alonso A, Kay AR (1998a) Noise from voltage-gated ion channels may influence neuronal dynamics in the entorhinal cortex. *J Neurophysiol* 80:262-269.
- White JA, Chow CC, Ritt J, Soto-Trevino C, Kopell N (1998b) Synchronization and oscillatory dynamics in heterogeneous, mutually inhibited neurons. *J Comput Neurosci* 5:5-16.
- Whittingstall K, Logothetis NK (2009) Frequency-Band Coupling in Surface EEG Reflects Spiking Activity in Monkey Visual Cortex. *Neuron* 64:281-289.
- Whittington M, Cunningham M, LeBeau F, Racca C, Traub R (2011) Multiple origins of the cortical  $\gamma$  rhythm. *Dev Neurobiol* 71:92-106.

- Whittington MA, Traub RD, Jefferys JGR (1995) Synchronized oscillation in interneuron networks driven by metabotropic glutamate receptor activation. *Nature* 373:612-615.
- Whittington MA, Jefferys JG, Traub RD (1996) Effects of intravenous anaesthetic agents on fast inhibitory oscillations in the rat hippocampus in vitro. *Br J Pharmacol* 118:1977-1986.
- Whittington MA, Faulkner HJ, Doheny HC, Traub RD (2000a) Neuronal fast oscillations as a target site for psychoactive drugs. *Pharmacol Therapeut* 86:171-190.
- Whittington MA, Stanford IM, Colling SB, Jefferys JGR, Traub DR (1997) Spatiotemporal patterns of  $\gamma$  frequency oscillations tetanically induced in the rat hippocampal slice. *J Physiol* 502:591-607.
- Whittington MA, Traub RD, Faulkner HJ, Jefferys JG, Chettiar K (1998) Morphine disrupts long-range synchrony of gamma oscillations in hippocampal slices. *Proc Natl Acad Sci U S A* 95:5807-5811.
- Whittington MA, Traub RD, Kopell N, Ermentrout B, Buhl EH (2000b) Inhibition-based rhythms: Experimental and mathematical observations on network dynamics. *Int J Psychophysiol* 38:315-336.
- Williams RW, Herrup K (1988) The control of neuron number. *Annu Rev Neurosci* 11:423-453.
- Winfree AT (1967) *Biological Rhythms and Behavior of Populations of Coupled Oscillators*. *J Theor Biol* 16:15-&.
- Winfree AT (2001) *The geometry of biological time*. New York: Springer.
- Witham CL, Wang M, Baker SN (2007) Cells in somatosensory areas show synchrony with beta oscillations in monkey motor cortex. *Eur J Neurosci* 26:2677-2686.
- Womelsdorf T, Schoffelen JM, Oostenveld R, Singer W, Desimone R, Engel AK, Fries P (2007) Modulation of neuronal interactions through neuronal synchronization. *Science* 316:1609-1612.
- Woodman MM, Canavier CC (2011) Effects of conduction delays on the existence and stability of one to one phase locking between two pulse-coupled oscillators. *J Comput Neurosci* 31:401-418.
- Woolley DE, Barron BA, Timiras PS (1966) Spectral components in prepyriform electrical activity and changes at high altitude. *Electroen Clin Neuro* 20:175-180.
- y Cajal SR (1892) El nuevo concepto de la histología de los centros nerviosos. *Rev Ciencias Médicas (Barcelona)* 18:457-476.
- Zeitler M, Daffertshofer A, Gielen CC (2009) Asymmetry in pulse-coupled oscillators with delay. *Phys Rev E Stat Nonlin Soft Matter Phys* 79:065203.

# Dankwoord

**F**irst of all, I would like to thank Stan Gielen for giving me the precious opportunity to pursue one of my important journey, a Ph. D. During my first year, I conducted my research about mathematically understanding a mechanism of epilepsy under main supervision of Magteld Zeitler and Ingo Bojak, whom I shall thank for the excellent educational trainings despite the relatively short period. To succeed my research, I would like to thank Geertjan Huiskamp for his hospitality and for providing me the experimental data as well as Stephan van Gils and Hil Meijer for their mathematics consultancy. After my first year, Raoul-Martin Memmesheimer has become my new co-supervisor, whom I am overwhelmed with gratitude for his constructive critiques, questioning, time, and patience. Furthermore, I would like to thank Paul Tiesinga and Francesco Battaglia for fruitful discussions as well as Günter Windau, Judith Fontaine, Gea Hulzebos, and José Jansen for their effective administration. Above all, I would like to heartily thank Stan for his excellent guidance. Additionally, I would like to thank John van Opstal, Donders Institute, and NWO for the research funding.

I would like to thank my colleagues Charl Linssen for spending his Sunday's afternoon on my important rehearsal and Juan Vasquez, Linsey Roijendijk, Marije ter Wal, Marijn Martens, Martin Kruppa, Natalia Bielczyk, as well as Rembrandt Bakker for sharing a good time at the office.

For the wonderful graphics on the cover page, I would like to thank Alfred Anwander and Freepik from [www.flaticon.com](http://www.flaticon.com).

Last but not least, I would like to thank my family and friends Chalernpol Nakswun, Chayada Chotsrisuparat, Jit and Patrick Engels, Kukiattudpor, Sasinee Khuankaew, Sitaporn Youngkong, Yodying Uefue for their supports and accompanying during my bad and good times: especially Chayada Chotsrisuparat and Yodying Uefue for being my paranympths.

Particularly thanks my beloved Siraprapa Yukaew very much!!!



# Curriculum Vitae

**A**tthaphon Viriyopase was born on 4 November 1978, Bangkok, Thailand. His curiosity about mathematics and physics stemmed from his years in high school at Debsirin. He went to King Mongkut's Institute of Technology Ladkrabang for his bachelor degree in computer engineering, after which he continued his study in applied mathematics at the Technical University of Kaiserslautern, Germany, where he grew interest in using mathematics as a primary tool to investigate problems appearing in various fields. He had a chance to pursue his determined interest as a consultant at Mathematics for Industry, Eindhoven University of Technology, where he worked in the field of transport phenomena. He continued his resolute interest by pursuing PhD in the field of computational neuroscience.

## Publications

- Viriyopase A, Bojak I, Zeitler M, Gielen S (2012) When long-range zero-lag synchronization is feasible in cortical networks. *Front Comput Neurosci* 6:49.
- Viriyopase A, Memmesheimer RM, Gielen S (2016) Cooperation and competition of gamma oscillation mechanisms. *J Neurophysiol* 116:232-251.
- Viriyopase A, Memmesheimer RM, Gielen S (2017) Analyzing the competition of gamma rhythms with delayed pulse-coupled oscillators in phase representation. Submitted to *Physical Review E*.

## Conferences, Events, and Schools

- Viriyopase A**, Bojak I, Zeitler M, Gielen S (2010) Synaptic plasticity improves the long-range synchronization. Poster. Donders Discussion. Nijmegen, the Netherlands.
- Viriyopase A**, Bojak I, Zeitler M, Gielen S (2012) Feasibility of long-range synchronization with zero phase lag in a relay network. Poster. the DCN program with a lunch and poster session. Nijmegen, the Netherlands.
- Viriyopase A**, Zenke F (2012) Brain circuits for the liquid state machine. Oral. Advanced Course in Computational Neuroscience. Bedlewo, Poland
- Viriyopase A, **Memmesheimer RM**, Gielen S (2013) Cooperation and competition of gamma oscillation mechanisms. Poster. Bernstein Conference. Tübingen, Germany.
- Viriyopase A**, Memmesheimer RM, Gielen S (2016) Cooperation and competition of gamma oscillation mechanisms. Oral. Organization for Computational Neurosciences Annual Meeting. Jeju, South Korea.



